THÈSE

En vue de l'obtention du

DOCTORAT DE L'UNIVERSITÉ DE TOULOUSE

Délivré par :

Institut National Polytechnique de Toulouse (Toulouse INP)

Discipline ou spécialité :

Dynamique des Fluides

Présentée et soutenue par :

M. CLEMENT TOUPOINT

le jeudi 29 novembre 2018

Titre :

Path and wake of cylinders falling in a liquid at rest or in a bubble swarm towards the hydrodynamical modeling of ebullated bed reactors

---

Ecole doctorale :

Mécanique, Energétique, Génie civil, Procédés (MEGeP)

Unité de recherche :

Institut de Mécanique des Fluides de Toulouse (I.M.F.T.)

Directeur(s) de Thèse :

MME PATRICIA ERN

MME VERONIQUE ROIG

Rapporteurs :

M. JEAN-PIERRE HULIN, CNRS PARIS

M. ROMAIN VOLK, ECOLE NORMALE SUP LYON ENS DE LYON

Membre(s) du jury :

M. JACQUES MAGNAUDET, CNRS TOULOUSE, Président

M. CRISTIAN MARCHIOLI, UNIVERSITE D'UDINE, Membre

M. FRANCISCO HUERA-HARTE, UNIVERSITAT ROVIRA I VIRGILI TARRAGONA, Membre

Mme PATRICIA ERN, CNRS TOULOUSE, Membre

Mme RIM BRAHEM, IFPEN, Membre

Mme VERONIQUE ROIG, INP TOULOUSE, Membre

Résumé

L'étude des Réacteurs à Lit Bouillonnant (RLB) est à l'origine de ce projet de thèse. Ce type de réacteur chimique est très étudié en génie des procédés, en raison notamment de son utilisation pour l'hydrocraquage des charges lourdes. Des phénomènes complexes ont lieu dans un RLB, ce qui rend leur design et leur optimisation difficiles. Certains des mécanismes physiques prenant place dans les RLBs sont également des champs de recherche actifs en mécanique des fluides. Par conséquent, cette étude se concentre sur des mécanismes locaux participant à l'hydrodynamique des RLBs avec des catalyseurs cylindriques.

Dans un premier temps, l'impact de l'anisotropie du catalyseur sur sa chute est étudié. Nous réalisons une étude expérimentale de la chute libre d'un cylindre en fluide au repos, afin de déterminer l'effet de l'anisotropie du corps sur sa dynamique. Les paramètres d'intérêt du problème sont le nombre d'Archimède du cylindre (Ar) et son rapport d'élongation (L/d). Les expériences sont menées avec deux caméras orthogonales, et des techniques de traitement d'images avancées sont développées pour parvenir à une mesure précise de la position et de l'orientation du corps en 3D. Pour ($200 < \mathrm{Ar} < 1100$, $2 < \mathrm{L/d} < 20$), les cylindres adoptent différents types de trajectoire. Les deux principaux sont la chute rectiligne, durant laquelle l'axe du cylindre reste horizontal, et un mouvement de fluttering, qui est analysé en détail. D'autres types de mouvement plus complexes sont observés et discutés. De surcroît, le sillage du cylindre est analysé et caractérisé.

De nombreuses particules sont présentes dans un RLB (40% de fraction massique environ). Les interactions entre ces corps multiples ont un impact fort sur le mouvement de chacun d'entre eux, mais sont très complexes. En première approximation, nous rendons compte de la présence de multiples particules en introduisant un milieu confiné. Nous étudions expérimentalement la chute d'un seul cylindre dans une cellule confinée verticale, dans laquelle le cylindre n'est libre de se mouvoir que dans deux directions. Le rapport d'élongation du cylindre ($3<\mathrm{L/d}<40$) et son rapport de densité ($\rho_c/\rho_f = 1{,}16,\ 2{,}70,\ 4{,}50$) sont les deux paramètres d'intérêt. Le nombre d'Archimède du cylindre se trouve entre les mêmes bornes qu'en milieu non confiné, et les deux modes principaux de mouvement sont aussi la chute rectiligne et le fluttering. Cependant, pour des paramètres (Ar,L/d) comparables, il existe des différences importantes dans le déplacement du cylindre comparé au cas non confiné.

Nous avons également étudié l'interaction entre un cylindre en chute libre et un nuage de bulles ascendantes. Cette étude a été menée expérimentalement dans la cellule confinée utilisée pour la seconde partie de la thèse. Des cylindres de plusieurs rapports de densité ($\rho_c/\rho_f = 1{,}16,\ 2{,}70,\ 4{,}50$) and rapports d'élongation ($3<\mathrm{L/d}<20$) ont été lâchés dans un nuage de bulles de fraction volumique de gaz comprise entre 2% et 5%. Plusieurs mécanismes d'interaction entre le cylindre et les bulles ont été identifiés (contact direct, interaction avec des perturbations du fluide...), et leur effet a été caractérisé. Nous avons effectué une étude statistique du mouvement du cylindre dans le nuage de bulles, et nous l'avons comparée aux résultats obtenus en milieu confiné et en fluide au repos. Les rapports de densité et d'élongation du cylindre jouent tous deux un rôle important dans son mouvement au sein du nuage de bulles. Des statistiques conditionnelles nous permettent d'approfondir notre analyse du contact entre le cylindre et les bulles, ainsi que du rôle de l'orientation du cylindre. Enfin, la dispersion du mouvement du cylindre dans le nuage est caractérisée. Un des principaux effets du nuage de bulles est d'accroître, via

les contacts bulle-cylindre, l'orientation du cylindre jusqu'à-ce qu'il soit presque vertical, ce qui a un effet très fort sur sa cinématique en comparaison avec le fluide au repos.

Abstract

The origin of this PhD thesis lies in the study of Ebullated Bed Reactors (EBRs). These chemical reactors are very active research topics in chemical processes, notably thanks to their usage in heavy oil processing. Many complex phenomena take place within EBRs, and make their design and optimization difficult. In fluid mechanics, a lot of physical mechanisms present in EBRs are active fields of study (three-phase flow, fluid-body interaction...). Hence, in the present work, a study of the mechanisms participating in the hydrodynamics of an EBR with cylindrical catalysts is performed.

In a first part, the impact of the catalyst anisotropy on its fall is investigated. In order to gain insight on the effect of the body anisotropy on its fall dynamics, we investigate experimentally the free fall of a solid cylinder in a fluid at rest. The sensitivity to two dimensionless parameters, the Archimedes number (Ar) and the aspect ratio of the cylinder (L/d) is examined. Experiments are conducted with two orthogonal cameras, and advanced image processing techniques are developed in order to measure the position and orientation of the cylinder in 3D. Within the range of parameters studied ($200 < Ar < 1100$, $2 < L/d < 20$), the cylinders adopt different types of falling motion. Two main types of paths are observed, the first one is a rectilinear fall of the cylinder that keeps its axis horizontal, and the second one is a fluttering oscillatory motion. Other more complex types of motion are observed and discussed. The fluttering motion of the cylinder is analyzed in details. On top of the study of the body motion, the cylinder wake is also visualized and characterized.

A large number of particles are present at the same time inside an EBRs (about 40% of the mass). Interactions between multiple objects have a strong impact on the motion of each individual particle, but are very complex. In a first approximation, we take into account the presence of numerous particles by introducing a confined medium. We study experimentally the fall of a single cylinder in a confined vertical thin-gap cell, where the cylinders are free to move in only two directions. The cylinder elongation ratio ($3<L/d<40$) and density ratio ($\rho_c/\rho_f = 1.16, 2.70, 4.50$) are the two parameters of interest. The Archimedes number of the cylinder lies within the same range as in the unconfined medium, and the two main modes of motion of the cylinder are a rectilinear motion, and a fluttering one. However, for the same parameters (Ar,L/d), the motion of the cylinder in the confined cell is strongly different in form to that in the unconfined medium.

We also studied the interaction between a freely falling cylinder and a rising swarm of bubbles. This investigation was performed experimentally, in the confined cell used in the second part. Cylinders of various density ratio ($\rho_c/\rho_f = 1.16$, 2.70, 4.50) and elongation ratio ($3<L/d<20$) are released in a bubble swarm of gas volume fraction between 2% and 5%. The cylinder motion is greatly modified by the bubble swarm. Several mechanisms of interaction between the cylinder and the bubbles are identified (direct contact, interactions with fluid perturbations...), and their effect is characterized. We perform a statistical analysis of the cylinder motion in the swarm, and compare it to results in the confined fluid at rest. The cylinder density ratio and elongation ratio both play an important role in its motion in the bubble swarm. Conditional statistics allow us to further investigate the effect of the contact between the cylinder and a bubble, and of the cylinder orientation in the swarm. Finally, the dispersion of the cylinder motion in the swarm is characterized. A major effect of the bubble swarm is to increase, through bubble-cylinder contacts, the

probability of the cylinder to be in nearly vertical orientations. This drastically changes the kinematics of the cylinder as compared to its motion in the fluid at rest.

Remerciements

Je tiens tout d'abord à remercier les membres de mon jury de thèse pour leur évaluation de mes travaux, ainsi que pour les discussions qui ont suivi ma présentation lors de ma soutenance. En particulier, je suis reconnaissant à Jean-Pierre Hulin et Romain Volk pour leur lecture détaillée de mon manuscrit de thèse, ainsi qu'à Jacques Magnaudet pour avoir présidé le jury.

J'exprime tout particulièrement ma gratitude à Patricia Ern et Véronique Roig pour leur soutien, leur ethousiasme et leur investissement tout au long de ces trois années de travail. Merci de vous être tant impliquées pour que ma thèse se déroule bien, et d'avoir toujours été présentes lorsque j'en avais besoin.

Je suis également reconnaissant à Claudio Pereira da Fonte et Daniel Ferré pour avoir participé à la naissance de ce projet de thèse, et pour m'avoir accompagné durant la première motité de mon travail. Par la suite, je remercie également Rim Brahem et Lionel Gamet pour avoir pris la relève et s'être si rapidement investis dans ma thèse. J'adresse également mes remerciements à Jean-Lou Pierson pour son intérêt et son suivi de mon travail.

Les nombreuses expériences présentées dans ce manuscrit de thèse n'auraient pu voir le jour sans la participation et l'engagement de Grégory Ehses et Sébastien Cazin. Leur expertise m'a permis d'obtenir des résultats expérimentaux de grande qualité. Je souligne également la participation de Rudy Sopaerno, pour m'avoir apporté son aide dans la fabrication de mes cylindres, et pour avoir contribué, avec Frédéric Bergame, à la mesure de l'entrefer de ma cellule. Je remercie également Gilles Albert pour la fabrication des pièces de mon dispositif expérimental.

Je remercie l'IMFT pour l'accueil que j'ai reçu au sein du laboratoire, ainsi que pour les importants moyens techniques qui ont été mis à ma disposition. Je remercie également tous les membres des groupes Interface et EMT2 pour les moments de convivialité que nous avons partagés.

Merci enfin à toutes celles et ceux qui m'ont soutenu et accompagné dans le reste de ma vie. J'adresse une pensée particulière à Loïc et Karim pour leur soutien sans faille. Un grand merci également à mes parents qui ont su être toujours présents.

Contents

Chapter 1

Introduction

1.1 Industrial context and issues, scientific strategy

The World's increasing energetic demands are causing a rapid consumption of fossil reserves. To reply to this problematic, the main route followed by industry may comprise the upgrading of heavy crude oils or the increasing use of biomass resources like bio-oils. Ebullated Bed Reactors (EBRs) can be used in various chemical processes, but have their main field of application in petroleum refining. More specifically, the hydro-cracking of heavy petroleum feedstock greatly benefits from the use of EBR, because of the difficulties encountered when using conventional technologies, as stated by Martinez et al. [28], or [24, 35]. This PhD. thesis has been financially supported by IFP Energies nouvelles (IFPEN) and aims at improving fundamental knowledge related to hydrodynamics of Ebullated Bed Reactors. The initial promoters of IFPEN for this research were Claudio Pereira da Fonte and Daniel Ferré, who were then replaced by Lionel Gamet and Rim Brahem.

Figure 1.1 shows a schematic view of an ebullated bed reactor. It consists in a fluidized bed with three different phases. The liquid phase is mostly composed of hydrocarbons, the gas phase is a mixture of vaporized hydrocarbons and injected hydrogen, and the solid phase is formed by catalytic particles of cylindrical shape. The operating principle of an EBR is the fluidization of the solid phase thanks to the upward flow of liquid and gas, along with specific physical properties of the catalytic particles. Contrary to a Fixed Bed Reactor (FBR), in which the catalytic particles are fixed, in an EBR the catalytic particles are free to move within the reactor. They can also be added or removed at any moment during the process, to handle catalyst deactivation.

In Ebullated Bed Reactors, bubbles and liquid agitation contribute to distribute the catalysts and the reactant efficiently in the reactor. The heat created in exothermic reactions is also spread evenly in the reactor thanks to its efficient mixing capacities. Fluidization of the bed also helps preventing the accumulation of impurities on the catalyst particles and slows down their deactivation. However, during the process, new catalysts have to be regularly added in the reactant liquid phase. Fixed Bed Reactors (FBR) technology is also used for petroleum processes, and is simpler to model and scale-up than EBRs, but it proves to be less efficient in dealing with these specific problems related to mixing and catalyst consumption (see [28]). Even if Ebullated Bed Reactors have several advantages over Fixed Bed Reactors, one of their main drawbacks is the heavy consumption of catalyst particles, which plays an important role in the operating costs of EBRs (several thousands of dollars per day for a single refinery). Moreover, a constant monitoring is needed to avoid the appearance of stagnant zones capable of destabilizing the process. Finally, the scale-up and design is more difficult for EBRs than

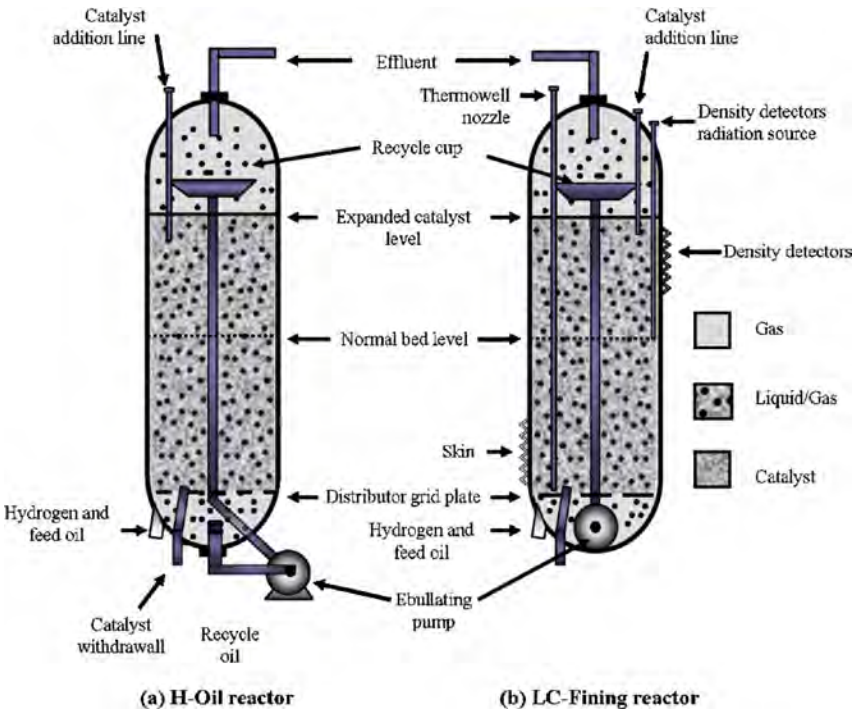

Figure 1.1 – Schematic view of an ebullated bed reactor, as found in [28]

for FBRs, as the hydrodynamics of the process is multiscale and much more complex, but their noticeable efficiency renders their use particularly valuable.

The complexity of ebullated bed reactors is due to the presence of three different phases in relative motion and to operating conditions at high temperature and high pressure (temperature is comprised between 410 and 440°C, while pressure is between 10 and 20 MPa). The solid volume fraction α_s can go up to 0.50, and the gas volume fraction is typically between $\alpha_g = 0.10$ and 0.30. There is a large concentration of solid particles, which interact with the liquid and between each other, as well as with the gas phase. Catalyst particles are most commonly extrudate cylinders, of constant diameter but of varying length, depending on the length of the particle when it was cut, and on successive breakups when the reactor is running. The chemical reaction taking place in the reactor generates heat, and causes a modification of the physical properties of the catalyst particles during the process, as impurities accumulate on them, making them heavier and limiting the reaction rate. The result is a highly complex system concerning as well thermodynamics and chemistry as hydrodynamics, where the population of catalysts evolves in time. The hydrodynamical questions raised by the EBR are numerous, and their understanding at local scales is poor, despite being crucial for the optimization of the process. Some work has been done on specific aspects of EBRs. For example, Ruiz et al. [33] studied the impact of pressure and temperature on some key features of the EBR. Luo et al. [27] specifically investigated the influence of pressure on the bubble characteristics in the bed. However, most researches were devoted to experimental macro-scale analysis, where parameters averaged in the reactor volume (volume fractions, pressure gradients, fluidization velocities...) were measured and analyzed, in order to provide correlations useful for the design and global operation of EBRs.

Since local descriptions using numerical codes are not available, optimization of EBRs using such numerical simulations is currently out of reach. In order to progress towards the building of models for local numerical prediction of the dynamics of EBRs, it is necessary to develop a multi-scale modeling strategy. The aim of this PhD research was thus defined

as a first step to disentangle part of the complexity of such hydrodynamics. Indeed, focusing on the hydrodynamics and leaving out supplementary difficulties originating from complex geometries of industrial systems, we find various sources of complexity that combine themselves and can be listed: *(i)* as any fluidized bed, EBRs involve *turbulent multi-scale flows*, *(ii)* EBRs primarily involve *liquid-solid interactions* which have been less studied than gas-solid ones, *(iii)* they are however *three-phase flows* as the bubbles also act on the dynamics of the other phases, *(iv)* they involve *dense dispersed phases* with high volume fractions and *(v)* the solid *particles are anisotropic* as they consist in cylinders.

The EBR is a *turbulent multi-scale flow* where various mechanisms happen at scales spanning from local – typically the scale of the cylinder – to macroscopic one, corresponding to the size of the reactor, which can reach several tens of meters. In between these scales, other mechanisms may control the meso-scale dynamics associated to groups of particles. Powerful methodologies of upscaling have already been developed, that lead to models able to predict macro-systems while taking into account all the mechanisms present on different scales. Most often, such multi-level modeling approach intends to generate closure information from DNS or physical experimentation at a local scale. In turn, this closure information is to be used primarily in meso-scale models named Discrete Particle Models (DPM) or Discrete Element Method-CFD (DEM) models or also Euler-Lagrange (EL) models. DPM models themselves are then a stage of the multi-level modeling approach. They are used to generate closure information, that are required in more coarse-grained models such as Euler-Euler models based on the kinetic theory of granular flow (KTGF), which are finally used to simulate larger systems and more complex industrial processes. Multi-scale approaches for the study of particles-fluid interaction have been developed over the last years, especially for *gas-solid flows* involving *spherical particles*. In particular, van der Hoef et al. [40] discuss the whole upscaling from micro to macro scales. In spite of their importance in industrial applications, *liquid-solid flows* have been far less studied. A major difference between gas-solid and liquid-solid fluidized beds can be highlighted. Global observations show clearly that liquid-solid systems are less chaotic than gas-solid ones and more often exhibit homogeneous fluidization regimes (see [14, 20]). This emphasizes the need to build specific closure laws for liquid-solid-gas fluidized beds in numerical codes such as Euler-Lagrange or Euler-Euler codes originally developed for gas-solid systems. This is a long-term research program, that requires several studies, each ideally devoted to successive larger scales or intermediate scales.

In order to start with this long-term program, it was decided with Daniel Ferré and Claudio Pereira da Fonte, that first promote this PhD thesis at IFPEN, that it was essential to develop comprehensive experiments at the local scale. Furthermore, the choice was made to focus on the catalyst motion at local scale. It is interesting from an operational point of view because cylindrical catalysts are one of the key elements of EBRs, and also one of the main causes of the problems that can be encountered during the use of such reactors. Studying the behaviour of catalytic particles from a fluid mechanics point of view at local scale is also the logical first step of an upscaling methodology.

An approach of increasing complexity has been chosen to study some fundamental mechanisms governing the motion of cylinders in an EBR. It is first important to understand how an anisotropic solid particle modifies the liquid flow around it, how it moves in a fluid at rest, how any imposed local liquid flow acts on its motion, or how the bubble-induced agitation modifies this motion. It is also important to study the way in which two cylinders come into contact and interact with bubbles.

All these open questions cannot be tackled in a 3 years research. We thus decided to

study two fundamental problems: (i) the free fall of a cylinder in a fluid at rest of infinite dimensions to understand the effect of the body anisotropy on its kinematics and (ii) the free fall of a cylinder in an homogeneous bubble swarm rising in a fluid otherwise at rest in a confined planar cell. This thesis is thus divided in three parts that will be presented later on, each focusing on specific mechanisms contributing to complexity in an EBR. The finishes of the various parts are different because of the great research program we had to face. Concerning the study of the free fall in the unconfined flow, it is a complex problem that already required two years of investigation. As for the study of the motion of the cylinder in a bubble swarm confined in a thin-gap cell, we first faced technical difficulties to produce a well-controlled thin-gap cell and definitive experiments were performed from September 2017. The processing and analysis of these results was performed in the year preceding the PhD. defense.

The geometry of catalysts plays an important role in their behaviour. While its effect on the global behaviour of the reactor has been reported (see [23]), to the knowledge of the authors, no study has investigated in detail its specific effect on the hydrodynamics of EBRs. In fluid mechanics, the impact of the geometry of a solid body on its behaviour when moving in a fluid is an open topic of research. Indeed, when a solid object falls into a fluid, a complex interaction takes place between the motion of the body and the motion generated in the fluid. The fluid, disturbed by the passage of the body, generates hydrodynamical forces and torques that govern the body motion. This complex coupling has been a very active research topic in the last 15 years, thanks to advances in numerical simulations and experimental tools, but is still not fully understood even for simple geometries. Most works focused on the study of spheres, or axisymmetric bodies such as disks and plates (see [13]). The trajectory and wake of a free cylinder of finite length have only been investigated in few studies (see [9], and the introduction of part I). Yet, none of these studies offers a complete description of the behaviour of freely falling cylinders over a large range of parameters. Hence, the *first part of the thesis* focuses on the study of the trajectory and wake of a freely falling cylinder, in a three dimensional environment. This experimental investigation is the first step towards better understanding of the role of the cylinder anisotropy in its motion.

Lots of catalytic particles co-exist inside the ebullated bed reactors. Each individual one is constantly in contact with other particles, making its motion effectively restricted by the bodies around it. While our study focuses on a single particle, we can roughly represent the effect of the high solid volume fraction by a strong confinement acting on the cylinder motion. In the *second part of the thesis*, we study the free fall of a cylinder in a confined medium. This medium consists in a vertical confined cell (sometimes referred to as a Hele-Shaw cell), for which the cell thickness is very low compared to the other dimensions (800 mm in height, 400 mm in width and 1.1 mm in thickness). The cylinder is released in the cell with its axis parallel to the walls, and with its diameter close to the thickness of the cell. Close configurations have already been investigated (see for instance [36, 37] on the study of a tethered cylinder, or [10, 19] for a free cylinder), and have highlighted a strong effect of such confinement on the cylinder motion. D'Angelo et al. [11] have investigated the oscillating motion of cylinders in a setup in which the cylinder is confined both along its diameter and length. Our goal is to characterize the effect of the confinement of the cylinder along its diameter for a planar thin-gap cell of otherwise large dimensions as compared to the cylinder length. Therefore, we conduct experiments to study the behaviour of the cylinder in this confined cell, and investigate the effect of the cylinder geometry and density ratio.

In the *third part of this thesis*, an additional degree of complexity is taken into account. The interactions between the three different phases play a major role in the dynamics of

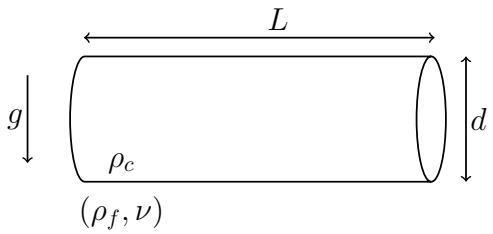

Figure 1.2 – Schematic view of a cylinder, along with the important parameters

an EBR. The gas is responsible for a large part of the agitation in the liquid, and also of the solid particles. The rising of bubbles in a fluid generates a lot of turbulence and mixing within the liquid phase. Obviously, complex interactions take place between the bubble-induced agitation, the bubbles themselves, and the falling solid bodies. The confined cell used in part II is an ideal flow configuration to study the interactions between a falling cylinder and a rising swarm of bubbles. Indeed, if bubbles of a diameter greater than the gap width are injected in the cell, they are confined between the walls of the cell. This facilitates experimental observation, as it becomes possible to observe multiple objects in motion with no optical obstruction. The bubbles rise at high Reynolds number, and generate a strong agitation in the liquid, already explored in 2014 for a homogeneous bubble swarm by Bouche et al. [6].

1.2 Setting up the problem of free fall of a cylinder

1.2.1 Definition of the parameters of interest

Based on the physical parameters of the problem studied, non-dimensional parameters are defined, and will be used to work partly in similarity conditions between our experiment and the industrial case.

We consider a cylinder of diameter d, length L and density ρ_c, freely falling in a fluid of density ρ_f and of kinematic viscosity ν. The moving force will be the gravity, and the acceleration of gravity is denoted g. These 6 parameters involve 3 different units (of mass, length and time), so that 3 non-dimensional parameters can be defined to characterize the problem. The first one is the elongation ratio, $\xi = L/d$, which characterizes the body geometry. The density ratio between the body and the fluid, ρ_c/ρ_f, is also introduced.

The Archimedes number is a non-dimensional parameter that compares the effect of buoyancy with viscous effects. For a given characteristic length d_{eq}, it can be written,

$$Ar = \sqrt{\frac{\rho_c - \rho_f}{\rho_f} g d_{eq}} \quad \frac{d_{eq}}{\nu} \tag{1.1}$$

Instead of using the cylinder length L or diameter d, we use d_{eq}, defined as the equivalent diameter of a sphere having the same volume than the cylinder studied. Hence, by setting an Archimedes number, and varying L/d, it is possible to study directly the influence of L/d on bodies having the same volume, and therefore the same driving force associated to buoyancy.

Based on the parameters ρ_c/ρ_f, L/d, and Ar, and on their values in the ebullated beds used by IFPEN, we can find the range of parameters that will be explored.

1.2.2 Case studied to match the industrial problem

We wish to mimic the conditions found in ebullated bed reactors. The characteristics of the bodies and fluid used by IFPEN allow us to determine the range of parameters that needs to be explored. L/d, the elongation parameter for the catalytic particles used in EBRs, is estimated to be comprised between 2 and 10. These particles are made of a material of density 4000 kg.m^{-3}, with a porosity of 0.4, and immersed in a fluid of density 700 kg.m^3. We can therefore estimate a range of density for the solid particles, with the lowest density being the case of a porous particle full of air, and the higher, of a porous particle full of liquid, leading to $2 < \frac{\rho_c}{\rho_f} < 3$. This enables to restrict $\Delta\rho$, so that bodies in the required range of Archimedes number are not too small.

Namkoong et al. [30] observed that for an infinite cylinder, the density ratio had little impact on the body dynamics in the range $1 < \frac{\rho_c}{\rho_f} < 4$.

With a diameter of about ~ 1 mm, L/d ranging from 2 to 10, and a fluid of kinematic viscosity $\nu = 5.7.10^{-7}$ m^2.s^{-1}, we can estimate an equivalent diameter for the case of interest for IFPEN, yielding 1.4 mm$\leqslant d_{eq} \leqslant$ 2.5 mm, and then build the corresponding Archimedes number,

$$200 \leqslant Ar \leqslant 800 \tag{1.2}$$

Therefore, cases covering $2 < L/d < 10$, $\rho_c/\rho_f > 1$ and $200 < Ar < 800$ will be studied.

1.3 Setting up the problem of a cylinder freely falling in a homogeneous confined bubble swarm

The effect of the high volume fractions of solid and gas in EBR on the dynamics is primarily to induce a strong confinement of all the phases. The liquid being strongly confined, the agitation in the liquid phase at small scale is expected to be modified by this confinement and by regular and high frequency solid or bubble crossings. Dynamics of all phases at such scales are thus expected to be more dependent on the confinement than on any turbulent cascade inducing agitation at small scale as in single-phase flows. Of course in an EBR the respective mobility of the solid and gas phases arrangements at a macro-scale participate to the dynamics. But, in order to study the primary effect of high volume fractions α_s and α_g consisting in confinement, we proposed to study the free fall of a cylinder in a homogeneous high Reynolds number bubble swarm rising in a vertical thin gap cell.

The size of the gap is chosen millimetric in relation with the industrial case (as explained in a following part) where catalytic particles and bubbles sizes are about a millimeter with an important volume fraction of the solid (0.4) leading to millimetric characteristic distance between the inclusions. The agitation induced by a homogeneous bubble swarm rising at high Reynolds number in water at rest confined in a vertical thin gap cell (of 1 mm thickness) has been investigated by Bouche et al. ([5], [6]). We can therefore use the knowledge about the agitation induced in such a flow to explore further its effect on the motion of a free falling cylinder. In this flow bubbles have a size greater than the gap so that they are flattened between the walls with thin liquid films existing between the bubble and the walls. In the regime we are interested in, the bubbles have an ellipsoidal in-plane projected shape. Their relative motions generate in-plane motions in the liquid phase. The flow can thus be mainly characterized by the motions averaged through the gap (a 2D characterization). The perturbations in the liquid mainly consists in a potential

flow in front of the bubbles and a unsteady wake behind them that are rapidly dampened by the shear stress at the walls. They produce a strong random bubble-induced agitation in the liquid phase of this confined bubble swarm.

In the following we present the arguments leading to the choice of the experimental conditions that were explored.

1.3.1 Parameters of interest

When a cylinder falls into a swarm of bubbles confined in a vertical cell, its dynamic depend on 13 physical parameters. For the solid phase, we have cylinders of diameter d_c, length L and density ρ_c. The liquid phase has a density ρ_l, a kinematic viscosity ν_l and a surface tension σ. The gas phase is made of gas bubbles, of density ρ_g and kinematic viscosity ν_g. The dimensions of the bubbles are larger than the gap of the cell (typically about 4 mm), thus, they are compressed between the two glass plates. Their shape can therefore be approximated by a flattened cylinder of ellipsoidal cross-section. The size of the bubbles will be defined as the equivalent diameter of the in-plane projected area of the bubble, noted d_b. In order to take the confinement into account, the size of the horizontal gap, H needs to be added, as can be seen on Figure 1.3. H is chosen equal to 1 mm, lower than the capillary length, so that the flow remains mainly an in-plane flow even for deformable bubbles because they preferentially deform in the plane of the cell. The width W of the cell in the in-plane horizontal direction also characterizes the geometrical confinement. The moving force is the gravitational force, denoted g. It should be noted that the coalescence of bubbles will be inhibited so that a stable nearly mono-dispersed swarm of bubbles can be created. The gas volume fraction α_G is the last important parameter of the problem which is already non-dimensional.

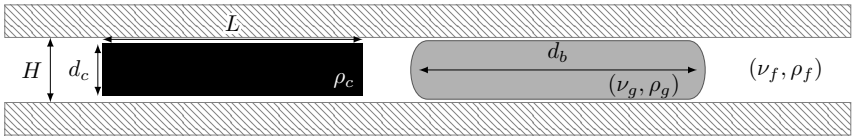

Figure 1.3 – Schematic top view of the cell, featuring a cylinder of dimensions L and d_c alongside a bubble of diameter d_b.

Based on these physical parameters, it is possible to build a set of 10 non-dimensional parameters : ν_g/ν_l, ρ_g/ρ_l, Bo, Ar_b, α_G, L/d_c, ρ_c/ρ_f, Ar_c, d_c/H, L/W. They will be defined in the following.

We do not intend to change neither the liquid, which will be water, nor the gas, which will be air, in our experiments. Therefore, both ν_g/ν_l and ρ_g/ρ_l will remain constant, and negligible. A Bond number can be built to characterize the deformations of the bubbles, $Bo = \frac{\Delta\rho g d_b}{\sigma}$ with $\Delta\rho$ being the density difference between both phases, and σ the surface tension between liquid and gas phases. The Bond number will remain constant across all our experiments. In fact the bubble size d_b is weakly dependent on α_G, as found by Bouche et al [6]. An Archimedes number can be built to compare the effects of buoyancy and viscosity on the dynamics of the bubble $Ar_b = \frac{\sqrt{\Delta\rho/\rho_f g} d_b^{3/2}}{\nu_f}$. It will also remain constant when varying α_G.

As for the unconfined study, the effect of the aspect ratio of the cylinders L/d_c will be studied. The effect of the ratio of the cylinder density over the fluid density, ρ_c/ρ_f, will also be investigated. An Archimedes number $Ar_c = \frac{\sqrt{\Delta\rho/\rho_f g} d_c^{3/2}}{\nu_f}$ can also be defined, similarly to the unconfined study. The ratio of the cylinder diameter over the size of the

gap d_c/H will be kept constant. Indeed, it was shown by D'Angelo et al. (2013) [10] that in the case of a cylinder falling in a 2D cell, oscillations could occur across the gap. As it is not the case we wish to study, it is necessary to ensure conditions where they do not occur, which is by keeping d_c/H above 0.7 [10]. Hence, the ratio d_c/H will remain constant and larger than 0.7 for all our experiments. Similarly, it is important in our study that the cylinder can move freely along its axis, so that it is free to flutter. Therefore, the ratio of the length of the cylinder over the well width, L/W will be kept extremely low ($L/W \leqslant 0.08$).

1.3.2 Definition of the experimental case from similarity arguments

In industrial applications such as EBR, the presence of two dense dispersed phases with solid volume fraction of about 50% and gas volume fraction up to 10% induces a confinement which length scale can be estimated for example assuming that cylinders could be in a cubic arrangement of size H. Ignoring the gas volume fraction, for cylinders of diameter equal to 1 mm and length ratio $\xi \approx 5$, the value of H is around 2 mm which is similar to the capillary length ($l_c = \sqrt{\sigma/(\rho_l g)}$ surface tension being about $\sigma \approx 0.03$ N.m^{-1}). Moreover in EBR a crude estimation of bubble diameter can be given as 4 mm. We thus decided to mimic the confinement effect in an EBR by studying the motion of a cylinder in a swarm of bubbles confined in a cell between two plates using water and air. The size of the gap cell was chosen equal to 1 mm so that we could benefit from previous knowledge of the agitation generated in such a confined bubble swarm (Bouche et al [6]).

The non-dimensional parameters related to the bubbles in an EBR are then estimated as $Bo \approx 3.7$, $Ar_b \approx 1400$ and $H/d_b \approx 0.5$. In the confined cell they will be $Bo \approx 1.13$, $Ar_b \approx 500$ and $H/d_b \approx 0.35$. We can notice that a perfect similarity cannot be achieved but the confinement ratios H/d_b are comparable. Furthermore, for these high Archimedes numbers the inertial effects will be present and similar in the cell as in an EBR. Finally a Bond number slightly higher in an EBR can lead to more deformable bubbles than in the cell, where deformation will be nevertheless present. The gas volume fraction will be varied in the experiments up to 5% due to technical limitations but it is a value near the one commonly found in EBR.

The ratio of confinement for the solid cylinders $d_c/H \approx 0.5$ in the EBR, while it is chosen at about 0.72 in the present study. The values are not identical, but are similar. And we chose the value of 0.72 to avoid complex 3D motions in the gap as explained in [10, 19].

Simplifying the problem of confinement in an EBR by allowing motions in a thin plane cell is a strong simplification because it restricts the degrees of freedom of the motions. But it makes sense because it is a way to simultaneously impose a confinement due to solid phase and simulate correctly the bubble-induced agitation in a confined bubble swarm where bubbles are free to move. The motions of a cylinder in such a flow is expected to share common properties with those of a test cylinder in an EBR. This flow configuration also simplifies the measurements of the cylinder trajectories which are otherwise particularly difficult to obtain except with complex methods such as computed tomography (CT) or computer-automated radioactive particle tracking (CARPT)(as presented by Chen et al. [8]).

1.4 Organization of the dissertation

Part 1 reports the results of the research on paths and wakes of cylinders free to move in a fluid at rest that are synthesized in an article accepted in the Journal of Fluid Mechanics. The specific image processing developments that were necessary to detect the precise position of a small cylinder in a large volume of fluid are also reported as they are not so often explained in literature.

Part 2 presents the set-up for the study in the thin-gap cell and reports the experimental results concerning the kinematics and wakes of an isolated confined cylinder falling in the liquid at rest.

In part 3 finally describes the complex response of cylinders free to move to a random agitation generated by a confined bubble swarm.

Part I

Free fall of a cylinder in a three-dimensional medium

Kinematics and wake of freely falling cylinders at moderate Reynolds numbers

Clément Toupoint[1, 2], Patricia Ern[2]† and Véronique Roig[2]

[1]IFP Energies Nouvelles, Rond-point de l'échangeur de Solaize, BP 3, 69360 Solaize, France
[2]Institut de Mécanique des Fluides de Toulouse (IMFT), Université de Toulouse, CNRS, Toulouse, France

(Received 9 July 2018; revised 31 October 2018; accepted 13 December 2018)

We investigated experimentally the motion of elongated finite-length cylinders (length L, diameter d) freely falling under the effect of buoyancy in a low-viscosity fluid otherwise at rest. For cylinders with densities ρ_c close to the density ρ_f of the fluid ($\overline{\rho} = \rho_c/\rho_f \simeq 1.16$), we explored the effect of the body volume by varying the Archimedes number Ar (based on the body equivalent diameter) between 200 and 1100, as well as the effect of their length-to-diameter ratios L/d ranging from 2 to 20. A shadowgraphy technique involving two cameras mounted on a travelling cart was used to track the cylinders along their fall over a distance longer than $30L$. A dedicated image processing algorithm was further implemented to properly reconstruct the position and orientation of the cylinders in the 3D space. In the range of parameters explored, we identified three main types of paths, matching regimes known to exist for three-dimensional bodies (short-length cylinders, disks and spheres). Two of these are stationary, namely, the rectilinear motion and the large-amplitude oscillatory motion (also referred to as fluttering or zigzag motion), and their characterization is the focus of the present paper. Furthermore, in the transitional region between these two regimes, we observed irregular low-amplitude oscillatory motions, that may be assimilated to the A-regimes or quasi-vertical regimes of the literature. Flow visualization using dye released from the bodies uncovered the existence of different types of vortex shedding in the wake of the cylinders, according to the style of path.

The detailed analysis of the body kinematics in the fluttering regime brought to light a series of remarkable properties. In particular, when normalized with the characteristic velocity scale $u_0 = \sqrt{(\overline{\rho}-1)gd}$ and the characteristic length scale $l_0 = \sqrt{dL}$, the mean vertical velocity $\overline{u_Z}$ and the frequency f of the oscillations become almost independent of L/d and Ar. The use of the length scale l_0 and of the gravitational velocity scale to build the Strouhal number $St^* = fl_0/u_0$ allowed us to generalize to short ($0.1 \leqslant L/d \leqslant 0.5$) and elongated cylinders ($2 \leqslant L/d \leqslant 12$), the result $St^* \simeq 0.1$. An interpretation of l_0 as a characteristic length scale associated to the oscillatory recirculation thickness generated near the body ends is proposed. In addition, the rotation rate of the cylinders scales with u_0/L, for all L/d and Ar investigated. Furthermore, the velocity component u along the cylinder axis oscillates about $5\pi/4$ in advance of phase relative to the inclination angle θ of the cylinder, whatever the elongation ratio L/d and the Archimedes number Ar.

† Email address for correspondence: ern@imft.fr

1. Introduction

Three-dimensional bodies falling or rising under the effect of buoyancy in a fluid at rest have been a subject of continuous interest for the variety and attractiveness of the types of path that they display. Non-vertical (*e.g.* oblique) or non-rectilinear (*e.g.* periodic, chaotic, ...) paths are known to be the result of the complex coupling between the flow generated by the body motion (in particular, the wake structure) and the degrees of freedom in translation and rotation of the body. The case of the freely moving sphere illustrates the strong influence of the control parameters on the coupling between the fluid and the moving body, providing a remarkable diversity in the styles of path and associated wakes (see Auguste & Magnaudet 2018, and references therein). For this singular geometry, the control parameters are the body to fluid relative density $\overline{\rho}$, and the Archimedes number Ar comparing buoyancy and viscosity effects, defined as

$$\overline{\rho} = \frac{\rho_c}{\rho_f} \quad \text{and} \quad Ar = \left(\frac{\rho_c - \rho_f}{\rho_f} g D \right)^{1/2} \frac{D}{\nu},$$

where ρ_c is the density of the solid body, ρ_f is the fluid density, ν is the fluid kinematic viscosity, $g = 9.81$ m.s^{-2} is the magnitude of the gravitational acceleration, and D is a characteristic dimension of the body, the diameter in the case of a sphere. Once the mean rise/fall velocity of the body is known, a Reynolds number Re can be defined, enabling the comparison with the case of a fixed body, the corresponding velocity being then the upcoming mean flow velocity. In the case of non-spherical bodies, the anisotropy of the body has also an influence on the fluid-body coupling, by impacting the flow structure as well as the response of the body to the hydrodynamic loads. Wake instability depends on the body geometry and vortex formation is modified as soon as the symmetry axis of the body changes its orientation with respect to the body velocity. As well, non-sphericity makes anisotropic the generalized inertia tensors, involving proper and added-mass contributions, so that the ability of the body to react to hydrodynamic efforts is anisotropic. The influence of a control parameter characterizing the body non-sphericity on the properties and characteristics of the different paths, as well as on the transitions between them, is emphasized in the investigations on freely moving disks of various thickness-to-diameter ratio or two-dimensional plates of various thickness-to-width ratio (see Ern *et al.* 2012). At variance with the latter geometries, the free motion of elongated finite-length circular cylinders received until now little attention. It is however one of the simplest three-dimensional geometry, characterized by the elongation ratio, L/d, where d is the diameter and L the length of the cylinder. Moreover, this geometry arouse the surge of developments concerning wake instability and three-dimensional aspects of nominally two-dimensional wake flows about fixed cylinders (see Williamson 1996; Inoue & Sakuragi 2008) or elastically mounted cylinders undergoing vortex-induced vibrations (see Williamson & Govardhan 2004). It is therefore the focus of the present investigation.

The problem of an infinitely long circular cylinder free to move in any direction perpendicular to its axis is a two-dimensional counterpart to the case of the sphere, and its characteristic dimension D is the cylinder diameter. To investigate the coupling between the wake instability and path oscillations, Namkoong *et al.* (2008) performed numerical simulations of the two-dimensional motion of a freely falling/rising infinitely-long circular cylinder in an infinite fluid, but considered also situations of partially restrained motion in translation and rotation of the body. They focused on density ratios $0.5 < \overline{\rho} < 4$ and Reynolds numbers between 65 and 185, corresponding to an unsteady wake exhibiting periodic vortex shedding in the case of a fixed cylinder. They observed that vortex shedding induces a low-amplitude periodic motion of the cylinder, both in translation

and rotation, with transverse displacements typically lower than $0.1\,D$ (for instance $0.08\,D$ for $Re \simeq 160$ and $\overline{\rho} = 1.01$). By partially restraining the cylinder translation or rotation, they further showed that the transverse motion of the cylinder delays the onset of vortex shedding, thus reducing the Strouhal number (of less than 15%), whereas rotation has a negligible effect. A similar behaviour is found experimentally by Horowitz & Williamson (2006, 2010) for cylinders with also two degrees of freedom in translation and one in rotation, though at much higher Reynolds numbers ($3500 < Re < 7000$). For density ratios $\overline{\rho} > 0.54$, they observed small amplitude oscillations (about $0.05\,D$ for $Re \simeq 3800$ and $\overline{\rho} = 2.0$), occurring at a frequency equal to the vortex shedding frequency for a stationary cylinder, and consistent with the Bénard-von Kármán vortex street observed in the wake of the body. This path was considered rectilinear by the authors owing to the negligible amplitudes involved, but also in contrast to the large amplitude oscillatory motion observed for light cylinders ($\overline{\rho} < 0.54$). In the latter case, they recorded displacement oscillations of amplitude of the order of D in the transverse direction at a frequency about 1.3 times smaller (and $0.3\,D$ in the vertical direction at twice this frequency), in association with a wake structure comprising two vortex pairs generated per cycle. In the same configuration, Mathai *et al.* (2017) investigated numerically the effect of both $\overline{\rho}$ and $I^* = I_p/I_f$, the particle moment of inertia I_p relative to that of the fluid I_f, by varying them separately in the range $[0.1, 10]$, thus covering heavy ($\overline{\rho} \simeq 10$) to light ($\overline{\rho} \simeq 0.1$) cylinders. They separate for $Ar \simeq 220$ (the corresponding Re is not specified) a regime of cylinder oscillation with weak to intermediate displacement amplitudes, $0 < A < 0.3D$, dominated by the effect of the parameter $\overline{\rho}$, from a regime dominated by the effect of the moment of inertia and the rotational degree of freedom, corresponding to higher amplitudes, $0.4D < A < 0.75D$. For $Ar \simeq 500$, the mass dominated regime extends until $A \simeq 0.5D$, and in the moment of inertia dominated regime, amplitudes almost double (ranging from $0.6D$ to $1.2D$) when I^* is varied. They also noted that the gradual transition from one regime to the other is accompanied by a change in the wake shedding pattern, from the two single vortex mode to the two pair vortex mode identified by Horowitz & Williamson (2010). They concluded that the rotational degree of freedom can have a significant influence on the trajectories, in particular on the frequency and amplitude of the body displacement, and on the wakes of freely rising isotropic bodies.

A question that can now be asked is whether the additional degrees of freedom associated to the free ends of a finite-length cylinder would result in different paths. In other words, what would be the effect of leaving free the cylinder ends; and of allowing the six degrees of freedom of the body to be excited by the surrounding flow structure, and to be coupled with it? Two lengths now characterize the body geometry, the diameter d and the length L. The behaviour of circular cylinders of finite span-length moving through still water by buoyancy was studied by Marchildon *et al.* (1964) for $70 < Re < 2400$ (Re is based on d) and $1.46 < L/d < 35$, and by Chow & Adams (2011) for $200 < Re < 6000$ and $1 \leqslant L/d \leqslant 90$, in both cases for a wide range of cylinder materials and therefore densities, ranging from wood ($\rho_c = 0.74$ g/cm^3) to gold alloy ($\rho_c = 11.7$ g/cm^3). For these extensive ranges of parameters, both studies record a periodic motion of the cylinder consisting of an angular oscillation of the symmetry axis (of amplitude larger than 20° in Chow & Adams (2011)) associated to a periodic lateral deviation of the center of gravity, about the cylinder configuration corresponding to the rectilinear path with the symmetry axis perpendicular to the mean fall velocity. Numerical simulations by Romero-Gomez & Richmond (2016) reproduced the results of Chow & Adams (2011). Jayaweera & Mason (1965) investigated small cylinders made either of perspex, steel, or aluminium falling in liquid paraffin, sugar solutions of different concentrations, or water,

for Reynolds numbers ranging from less than 0.01 to about 1000. They observed that when eddies break away from the edges as well as the sides, the cylinder flutters with an amplitude of oscillation comparatively large for shorter cylinders, but decreasing as the length increases, so that longer cylinders fall stably. They further mentioned that the transition from steady fall to fluttering is not abrupt. They however observed that it depends on $\overline{\rho}$, and that the critical value of Re above which fluttering occurs increases with increasing L/d; for steel cylinders with L/d about 10, their critical value of Re is about 50. Marchildon *et al.* (1964) observed the secondary motion for Re greater than 300, and in some cases as low as 80. It is worth pointing out that the latter value is higher than the critical Reynolds number corresponding to the onset of unsteadiness in the wake behind a fixed two-dimensional cylinder of infinite span, $Re_c \simeq 47$. However, for a cylinder hold in an upcoming flow, the transition of its wake from a stationary to a periodic state is strongly dependent on the elongation ratio L/d of the cylinder. The experiments by Schouveiler & Provansal (2001) and Provansal *et al.* (2004) for cylinders with free hemispherical ends and the numerical simulations by Inoue & Sakuragi (2008) for cylinders with free flat faces indicate that this transition occurs at increasing critical Reynolds numbers Re_c when the elongation ratio decreases, typically $Re_c \simeq 100$ for $L/d = 5$ and $Re_c \simeq 200$ for $L/d = 1$. Furthermore, the numerical investigation by Inoue & Sakuragi (2008) disclose the existence of a variety of wake structures for $40 \leqslant Re \leqslant 300$ and $1 < L/d < 100$. Depending on the governing parameters, they identify five different vortex shedding patterns, corresponding to different equilibria reached from the vortical contributions generated from the flat bases or from the circular side of the cylinder. A question thus arises on what would be the paths associated to these different wake structures, or how would these be modified by the degrees of freedom of the cylinder.

Besides the diversity of paths that could be observed, we have seen that the question of the existence of contrasted periodic motions of either low or large amplitude associated with different types of wake structure, permeates the literature on freely moving two-dimensional cylinders. As this feature is shared with disks, or spheres, conviction has grown steadily stronger that it constitutes a central question concerning the behaviour of freely moving bodies (Ern *et al.* 2012). A decisive step forward to clarify this question was achieved recently for short-length cylinders ('disks' of variable thickness), by a joint effort in both direct numerical simulations (Auguste *et al.* 2013; Chrust *et al.* 2013) and stability analysis of the fluid-body system (Tchoufag *et al.* 2014). Tchoufag *et al.* (2014) showed that instability of the fluid-body system leads to contrasted instability modes corresponding to different strengths of coupling between the body and the fluid depending on the time scales involved, resulting in different types of paths, in particular periodic motions of contrasted amplitude, but also involving different symmetry properties, embodied in planar or spiraling paths, or intermediate paths. The existence of modes corresponding to different strengths of coupling between the fluid and the body may also be expected to occur for finite-length elongated cylinders. Furthermore, these complex regimes are more likely to happen close to the onset of path instability where the rectilinear path gives place to periodic paths.

With the aim to shed some light on the questions raised in this Introduction, the present paper addresses experimentally the problem of freely falling finite-length cylinders for a large range of elongation ratios and Archimedes numbers corresponding to paths transitioning from rectilinear to periodic. The general guideline of this work is the following. We first present the experimental approach, in particular the experimental set-up allowing us to track the motion of the cylinders, and the image processing procedure implemented to have a non-biased and accurate description of it. A technical appendix complements the latter. We then present an overview of the different paths observed. The

following sections are devoted to the quantitative characterization of the rectilinear and fluttering paths, presenting the measurement results and the corresponding scaling laws for the mean vertical motion as well as for the oscillatory translational and rotational motion of the body. A qualitative description is further provided, when possible, of the wake structure associated to the different paths. The paper ends with a discussion and concluding remarks.

2. Experimental tools

The bodies used in the experiments are 3D printed elongated circular cylinders of length L and diameter d (figure 1a). The 3D printer was a ProJet®3510HD, and the material, VisiJet®M3-X, an ABS-like plastic. The choice of 3D printing allowed us for a very good control of the dimensions of the cylinders, with a resolution of 32 μm and an accuracy of $\pm 2‰$. When possible, cylinders were printed with their axis pointing upwards, so that the layers of material were deposited along the length of the cylinder, which allowed for a better accuracy when printing the rounded sides of the cylinder. However, this could not be done for very long cylinders ($L/d = 20$), for they would bend during the printing process. Consequently, the latter were printed with their axis horizontal. The diameter of the cylinders ranged from 1.17 mm to 5.47 mm, and their lengths from 5.26 mm to 50.86 mm. The elongation ratio of the cylinders L/d ranged from 2 to 20 and was known up to $\pm 4.3.10^{-2}$. The mass of all cylinders was measured using a scale accurate up to 10^{-4} g, which allowed us to know the density ρ_c of the cylinders with an accuracy of ± 0.2 kg.m^{-3}. The measured densities ranged from 1140.0 kg.m^{-3} to 1190.0 kg.m^{-3}, with 2 cylinders out of 163 having a measured density of 1111.0 kg.m^{-3}. The cylinders were kept submerged in water at all times to ensure that the porosity of the 3D printing material was constantly saturated with water, so that the body density would not change during the course of the experiments. At the minimum three different cylinders were printed for each couple of parameters (L, d). No significant difference in behaviour was observed across all bodies having same dimensions (L, d), which ensures that the 3D printing was consistent both with dimensions and density of the bodies.

The experiments were performed in a 1.70 m high glass tank with a square cross-section of 0.4 m (eight to eighty times larger than the particle length), filled with filtered tap water. The tank was located in an air-conditioned laboratory at 19 ± 1°C. Water temperature was measured everyday using two thermocouples located at the top of the tank below the free surface, and at the bottom of the tank. Temperature differences between the top and the bottom of the tank were always smaller than 1.1°C. The water density was assumed to be $\rho_f = 1000$ kg.m^{-3}, giving a density ratio of $\overline{\rho} = \rho_c/\rho_f = 1.16 \pm 1\%$ for all experiments.

In addition to the density ratio $\overline{\rho}$ and the elongation ratio L/d, the problem also depends on the Archimedes number, introduced previously and defined as,

$$Ar = \left(\frac{\rho_c - \rho_f}{\rho_f} g D\right)^{1/2} \frac{D}{\nu} \quad \text{with} \quad D = \left(\frac{3}{2} d^2 L\right)^{1/3},$$

where the diameter of the sphere having a volume equal to that of the cylinder is taken here as the characteristic dimension of the body D. With this definition of Ar based on D, experiments performed for various L/d at given Ar and $\overline{\rho}$ allow us to investigate for given volume, and thus given buoyancy force, the influence of the cylinder elongation ratio on its behaviour.

The cylinders were released at the top of the tank, below the free surface, using tweezers. The release conditions were found to have no effect on the final behaviour

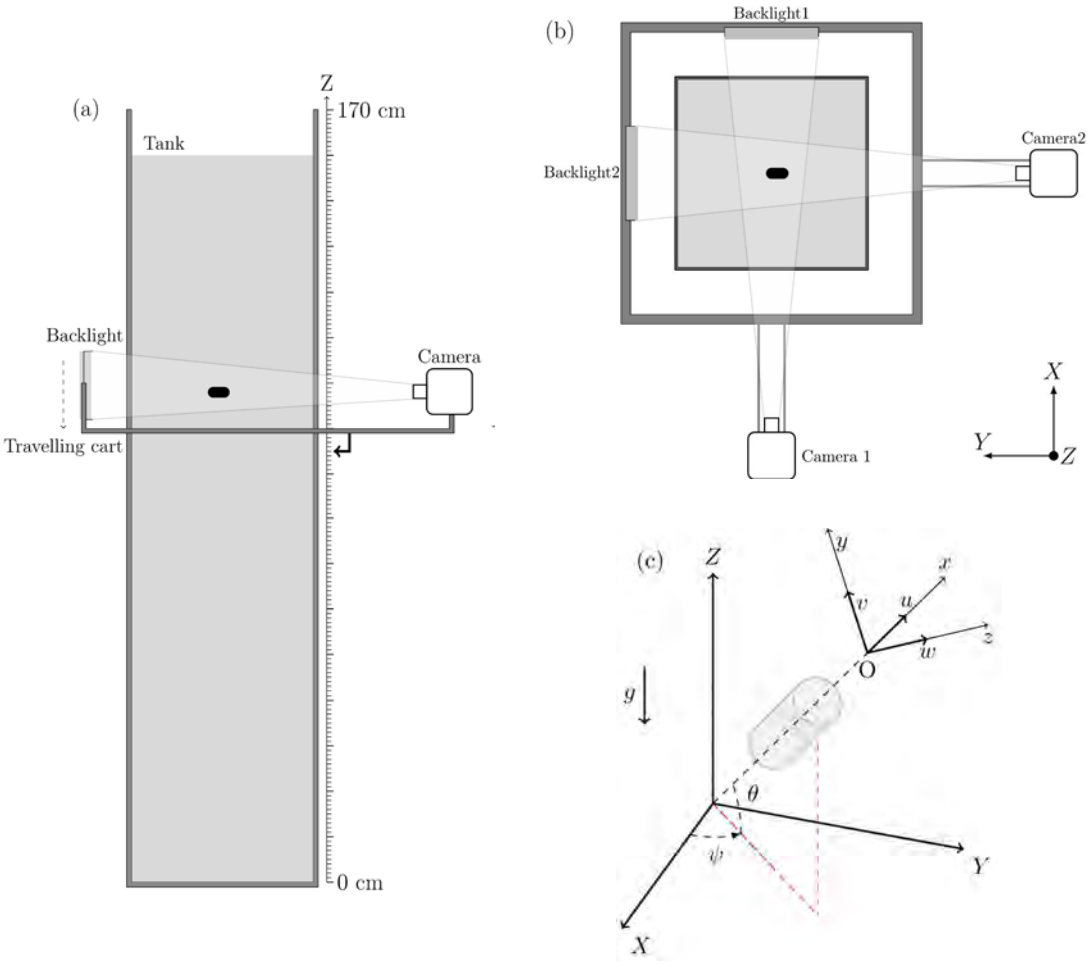

Figure 1: (a-b) Lateral and top view of the experimental setup; (c) Schematic view of the cylinder; (b-c) Definition of the coordinate systems. Z labels the vertical coordinate, (X, Y) the horizontal plane defined by the positions of the cameras. Origin O is fixed; axis (Ox) is parallel to the cylinder axis; (Oz) is parallel to the horizontal plane (X, Y); Plane (x, y) is vertical.

of the cylinder. Even when released with their axis vertical, the cylinders rotated so that their axis was horizontal after a transient distance of fall less than $10d$. The time between two releases was kept above 5 min, so that fluid perturbations in the tank caused by the fall of the previous cylinder could dissipate.

The cylinders were tracked along their fall with a travelling cart embarking two orthogonal cameras and the corresponding backlights allowing the observation of the bodies by shadowgraphy (figures 1a and b). Travelling followed the cylinders over a distance of at least $200d$. The elevation of the cart was recorded using a magnetic encoder with an accuracy of $\pm 5\mu$m and an acquisition frequency of 1000 Hz.

Since the shadowgraphy technique could not provide any information on the cylinder rotation about its axis, a pattern of random dots was drawn on a single cylinder out of the three available for each set of parameters $(Ar, L/d, \overline{\rho})$. Use of front lightning allowed visualization of these patterns. No significant rotation of the cylinders about their axis was observed across all experiments, except in some cases during the short transient period following the release of the body from rest.

In addition, specific experiments were carried out to uncover the wake associated with the different types of path. The wake of the falling cylinders was visualized by coating the bodies with ink before releasing them in the tank. The ink chosen was highly concentrated

and miscible in water. The cylinders were left submerged in pure ink during 15 to 30 min before being released in the tank, to ensure that the amount of ink on the cylinder surface was sufficiently high so that it would be released during a satisfactory amount of time. The ink trail left by the cylinders during their fall was recorded with the same cameras and backlights used for shadowgraphy.

3. Image and signal processing

The images were acquired by two orthogonal cameras using shadowgraphy, i.e. by shedding light from behind the cylinder, which projects its shadow on the camera (figure 1b). The output of the cameras is two greyscale image sequences in the planes (X, Z) and (Y, Z), where Z is the vertical coordinate and (X, Y) map the horizontal plane. Two different sets of cameras were used. PCO2000 ® acquired 2048×2048 pixels images at 14 Hz for recording slow periodic motions, and LaVision ® sCMOS acquired 2560×2160 pixels images at 50 Hz for faster oscillations. The greyscale images were converted to black and white images using a thresholding operation. After binarization, the cylinder shadows on both cameras appear as a black area on a white background. The list of pixels belonging to the borders between black and white regions was then retrieved and labelled as the projection contours of the cylinder. Following the routine described in Fernandes *et al.* (2007), camera calibration was performed using a metallic cylinder of known diameter, which was placed at different known positions (X_{cal}, Y_{cal}) in the cameras field of view. The optical scale factor obtained with the camera calibration was used to convert the pixel data of the images in meters. Then, an iterative procedure crossing the information provided by the two cameras allowed the estimation of the 3D coordinates of the cylinder center of gravity as those of the isobarycentres of the contour points of the cylinder projections.

This method is however not sufficient to determine accurately the center of gravity and orientation of the body, as it does not account for the deformations of the cylinder contour induced by the perspective projections onto the image plane of the cameras. It provides however a first estimation of the distance of the body centre to the camera which is used as an initialization of the refined following step implemented to correct perspective effects. This advanced technique, described in more details in appendix A, is based on a geometric reprojection of the cylinder contour (Huang *et al.* 1996). It outputs the center of the two flat faces of the cylinder, denoted S and T, in a frame tied to the camera position. Using the vertical position of the travelling cart embarking the cameras, given by the magnetic encoder, the positions of S and T can then be expressed in a frame tied to the tank (thereafter termed the laboratory frame), which is independent of the position of the travelling cart, and corresponding to the coordinate system (X, Y, Z).

From the 3D coordinates of S and T, the position of the cylinder center of gravity can easily be deduced, as well as the angle θ between the cylinder axis and the horizontal, and the azimuthal angle ψ (see figure 1c). Note that as mentioned in section 2, experiments showed that no rotation of the cylinder about its axis (Ox) could be observed, apart from the initial transient in some cases. However, transients, mainly related to the release of the body from rest, are discarded in the analysis and results that follow. The 3D coordinates of the cylinder centre of gravity in the laboratory frame are hereafter denoted (X, Y, Z), and the corresponding velocities (u_X, u_Y, u_Z). An example of the time evolution of the quantities characterizing the cylinder position and orientation can be seen on figure 2b-d. In addition to the oscillatory behaviour, a slight drift is observed for the spatial coordinates X and Y, as well as for the azimuthal angle ψ. This drift was measured to be always less than 6% of the total falling height, to be not reproducible, and could

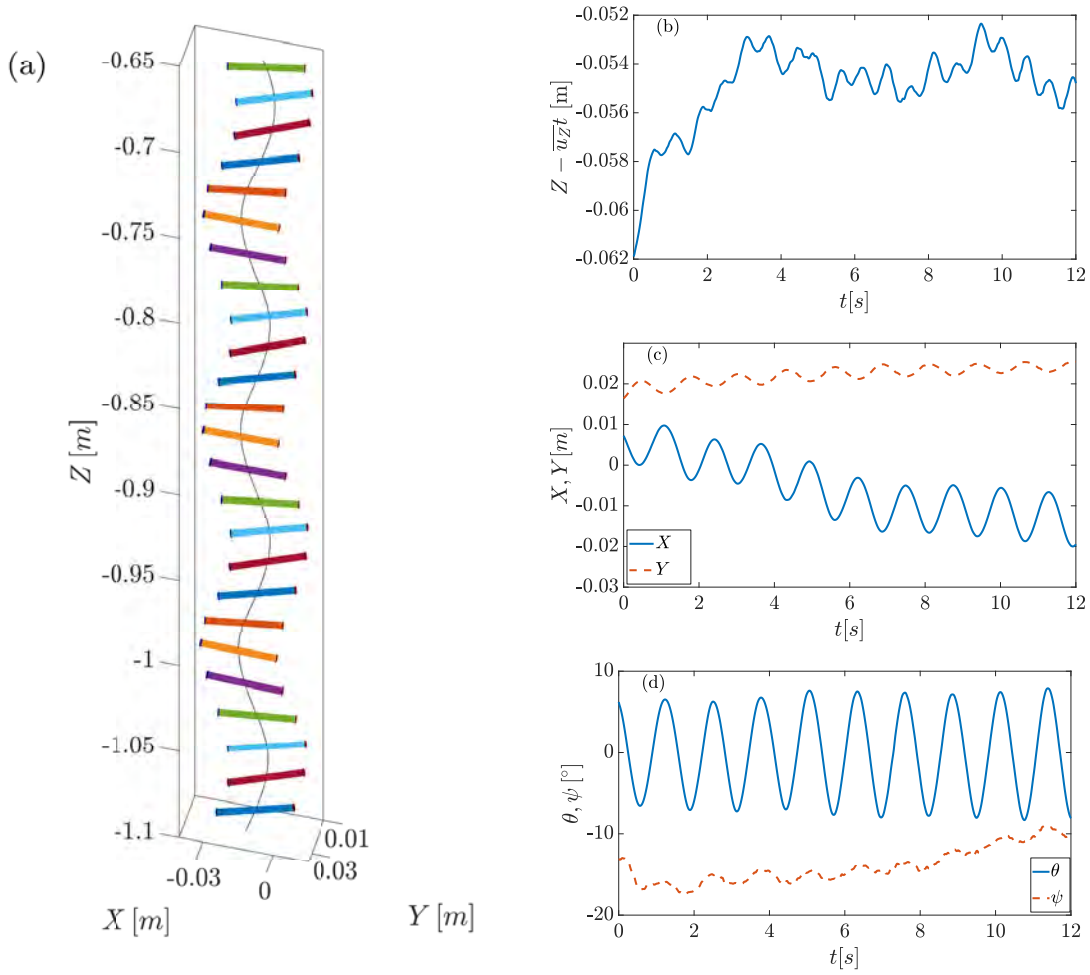

Figure 2: Illustration of the cylinder motion in the fluttering regime: (a) Three-dimensional plot, with an angle of view chosen close to perpendicular to the azimuthal plane to avoid perspective effects; corresponding time period 5.5 s to 10.5 s; the cylinder is plotted every 0.18 s; (b-d) Typical evolutions in time of the: (b) vertical displacement, (c) horizontal coordinates, (d) angles θ and ψ; $Ar = 800$, $L/d = 10$, $d = 3$ mm, $\overline{u_Z} = 10$ cm/s.

not be linked to any of the governing parameters. Its existence is attributed to large-scale low-velocity fluid motions in the tank, as they are difficult to avoid in a large tank. Similar irregular weak motions were observed in other experiments, and are mentioned in particular by Fernandes *et al.* (2007) for the study of rising disks. Following their approach that considers this drift as uncoupled with the main oscillatory motion of the body, a low-frequency filtering is applied to the time evolutions of the quantities characterizing the oscillatory behaviour of the body. The amplitude and phases of the periodic signals are then obtained using the Hilbert transform.

The coordinate system provided by the cameras being arbitrary, it is not the best suited to describe the body motion. Several coordinates systems can be introduced to get a better characterization of the body motion. For planar trajectories of the cylinders, a simpler and good description of their path is in fact manifest in the azimuthal plane defined by the cylinder axis and the vertical direction, and obtained by rotating the

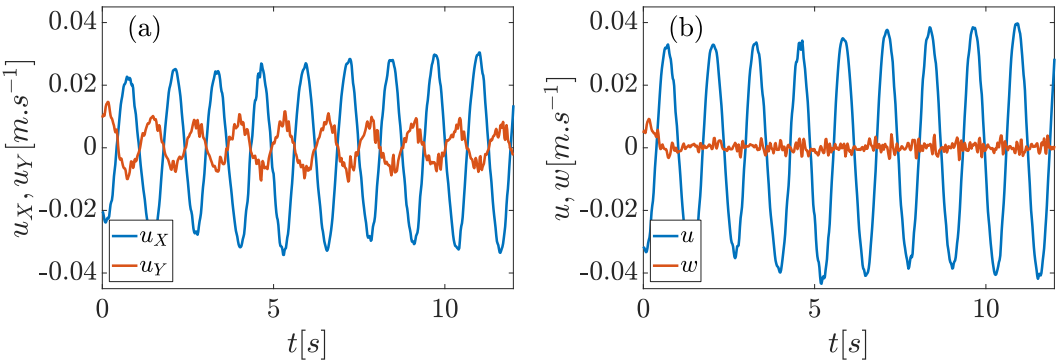

Figure 3: Comparison for a cylinder ($Ar = 800, L/d = 10$) of the velocity components (a) in the laboratory frame, and (b) in the system of axes rotating with the body defined in figure 1c.

laboratory frame coordinates (X, Y, Z) by the angle ψ, as

$$\begin{bmatrix} X_{azi} \\ Y_{azi} \\ Z_{azi} \end{bmatrix} = R_\psi \begin{bmatrix} X \\ Y \\ Z \end{bmatrix} \qquad \text{with} \quad R_\psi = \begin{pmatrix} cos\psi & sin\psi & 0 \\ -sin\psi & cos\psi & 0 \\ 0 & 0 & 1 \end{pmatrix} \tag{3.1}$$

However, while it is often the case, we will see later that not all trajectories lie in this plane. We therefore opt to work within the frame, hereafter termed the body frame, having its origin O fixed and axes (x, y, z) rotating with the body (Lamb 1993). Axis (Ox) is chosen parallel to the cylinder axis and the plane (x, y) vertical (see figure 1c). In this frame, the cylinder velocity components are denoted (u, v, w) and are deduced from the velocity components in the laboratory frame (u_X, u_Y, u_Z) by two rotations of angle θ and ψ respectively,

$$\begin{bmatrix} u \\ v \\ w \end{bmatrix} = R_\theta R_\psi \begin{bmatrix} u_X \\ u_Y \\ u_Z \end{bmatrix} \qquad \text{with} \quad R_\theta = \begin{pmatrix} cos\theta & 0 & sin\theta \\ 0 & 1 & 0 \\ -sin\theta & 0 & cos\theta \end{pmatrix} \tag{3.2}$$

Note that the axis z, corresponding to the velocity component w, has been chosen perpendicular to the vertical plane (Ox, Oy) containing the cylinder axis, and is therefore horizontal. As can be seen on the example in figure 3, the body frame provides a simpler and more relevant description of the body motion than the laboratory frame, figure 3b indicating that in this case, the trajectory is nearly planar and contained in the azimuthal plane.

4. Overview of the different paths observed

In this section we provide an overview of the different types of path observed within the space of parameters $(Ar, L/d)$ investigated for 195 cylinders. As can be seen in figure 4, three main types of motion are observed in the range $Ar \in [200, 1100]$, $L/d \in [2, 20]$. The first two correspond to stationary regimes: the rectilinear fall and the regular oscillatory motion called fluttering. In addition, in the transitional region of parameters separating the domains of occurrence of these regimes, oscillatory motions of weak and irregular amplitude are detected. Based on their distinctive features, we separate them in three types (termed Irregular I to III).

The fluttering motion is a periodic oscillatory motion of regular amplitude, observed here for Archimedes numbers ranging from 490 to 1080, and L/d from 2 to 12 (figure 4).

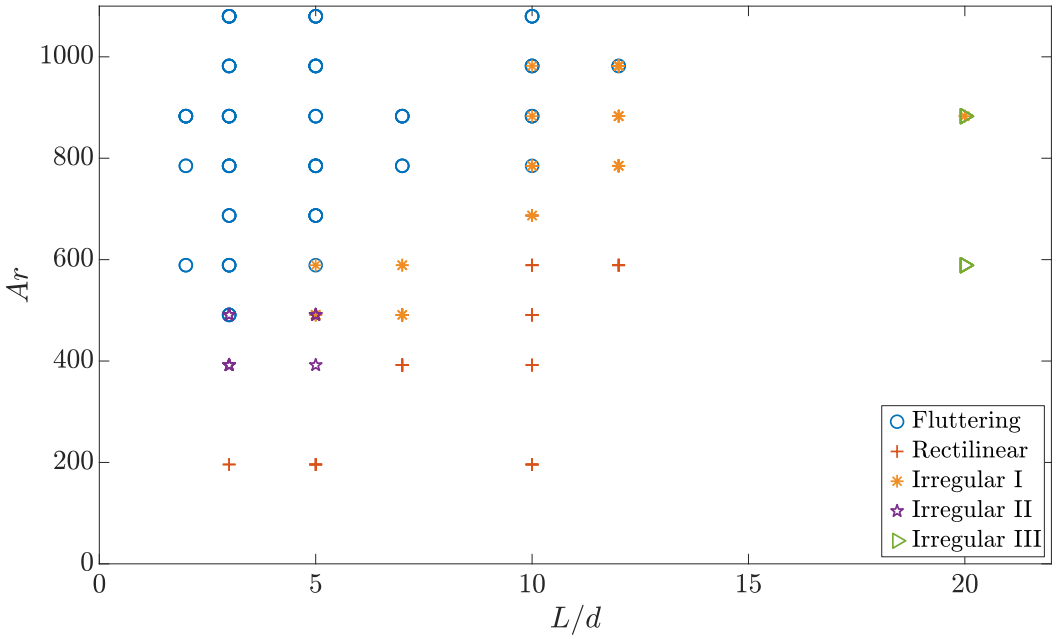

Figure 4: Map of the different paths observed in the plane $(Ar, L/d)$ for $\rho_c/\rho_f \simeq 1.16$. For all $(Ar, L/d)$, each type of path is observed using different cylinders. For some $(Ar, L/d)$, different types of path can be observed with the same cylinder in different runs.

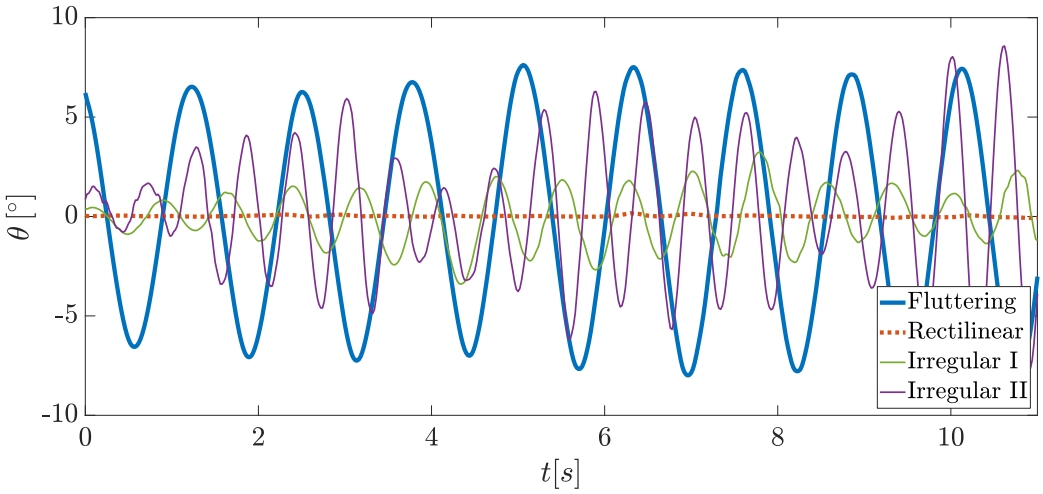

Figure 5: Examples of the time evolution of θ for a cylinder with $(Ar = 785, L/d = 10)$ for the fluttering motion, $(Ar = 200, L/d = 3)$ for the rectilinear motion, $(Ar = 500, L/d = 5)$ for the Irregular I motion and $(Ar = 400, L/d = 3)$ for the Irregular II motion.

An illustration of this path is shown in figures 2b-d, where the evolution in time of the five measured degrees of freedom are plotted. The evolution of the body along its path is also displayed in the three-dimensional plot of figure 2a. Fluttering typically occurs for heavier and shorter cylinders, at a frequency of about 1 Hz. It is characterized by oscillations of the cylinder centre of gravity (horizontal displacement in the azimuthal direction ranging approximately from $0.1L$ to $0.3L$, or $0.35d$ to $2.8d$) coupled with oscillations of the inclination angle θ (ranging from 7° to 20°). Oscillations of horizontal velocity components (u_X,u_Y) and of θ occur at the same frequency f and their amplitudes

remain constant during the fall. Owing to symmetry properties, oscillations of the vertical velocity component u_Z occur at twice the fluttering frequency, $2f$. Weak oscillations of ψ (typically lower than 6°) can also be observed at the fluttering frequency, and are stronger for cylinders with smaller elongation ratios ($L/d < 5$). The kinematics of the fluttering regime will be described in detail in section 6. Similar zigzag periodic motions were observed for finite-length cylinders covering a large range of density ratios by Marchildon *et al.* (1964) and Chow & Adams (2011), and are also known to exist for plates (see for instance Belmonte *et al.* 1998; Andersen *et al.* 2005*b*) and disks (see for instance Fernandes *et al.* 2007; Auguste *et al.* 2013).

During the rectilinear vertical fall, the cylinder axis remains horizontal. This kind of motion is observed in a subspace of $Ar \in [200, 1000]$ and $L/d \in [3, 12]$ (figure 4). For this type of path, a slight horizontal drift might be observed on the motion of the centre of gravity, but it is weak (for all cases it is lower than 3% of the total falling height), non reproducible and does not present a preferential direction related to the body geometry. No significant and regular horizontal motion could be observed for these cylinders so that their path is termed rectilinear. However, low-amplitude high-frequency oscillations (about six times larger than typical fluttering frequencies f) were detected on the vertical velocity u_Z (or on v) in the range $L/d \in [2, 12]$ and $Ar \in [390, 1080]$ investigated with a 50 Hz acquisition frequency of the camera, and covering both some rectilinear and fluttering paths. These oscillations will be discussed in more detail in section 7.

In the transitional region separating the rectilinear fall and the fluttering regime, different types of weak irregular oscillations can be observed, markedly in contrast with the rectilinear and fluttering regime. Though they are hard to disentangle from noise, some distinctive features can be pointed out to suggest a classification. The regime Irregular I is attributed to cylinder oscillations of weak and irregular amplitude in both displacement and inclination angle θ. These occur at frequencies close to those of the fluttering motion but with amplitudes significantly smaller (typically $\theta < 3°$) and less regular than the ones observed for fluttering cylinders. An illustration is provided in figure 5. In the regime Irregular II observed here for $Ar \in [400, 500]$ and $L/d \in [3, 5]$, the oscillations of the cylinder axis (close to the fluttering frequency f) are modulated by a low-frequency oscillation (for instance, 6 times slower), as shown in figure 5. The amplitude reached in the bursts is higher than that observed in the Irregular I regime (for instance, an amplitude of 10° can be reached). As for now, the origin of this mode is unclear, but it might be related to a complex wake structure occurring for this range of parameters. In fact, it is worth pointing out that low-frequency modulations of wake oscillations have been observed in several studies for *fixed* finite-length cylinders with free ends in comparable ranges of L/d and Re. Dauchy *et al.* (1997) observed a slow modulation of the oscillations in the wake of cylinders with L/d about 10 and 20 for $52 \leqslant Re \leqslant 100$, as the result of a secondary instability setting in at about 20% above the primary-instability threshold. Numerical simulations by Inoue & Sakuragi (2008) for cylinders with $20 \leqslant L/d \leqslant 50$ and $Re = 60$ also revealed the existence of a low-frequency modulation in the wake signal, but the beat in this case was attributed to bistability of the flow and the alternate appearance of two different modes of instability (namely *Type II* and *III* described in section 7). Note that the frequency of the wake primary instability is different in both studies, both values being about seven times larger than the frequency f of the modulated oscillation observed here. Modes Irregular I and II are difficult to distinguish from what would be the fluttering regime when it sets in. And in fact, figure 4 shows that for different cylinders having same $(Ar, L/d)$, different types of path (Fluttering, Irregular I or II) can be observed. This underlines the difficulty of experimentation for these parameters. However, as will be seen later in figure 12, there is a

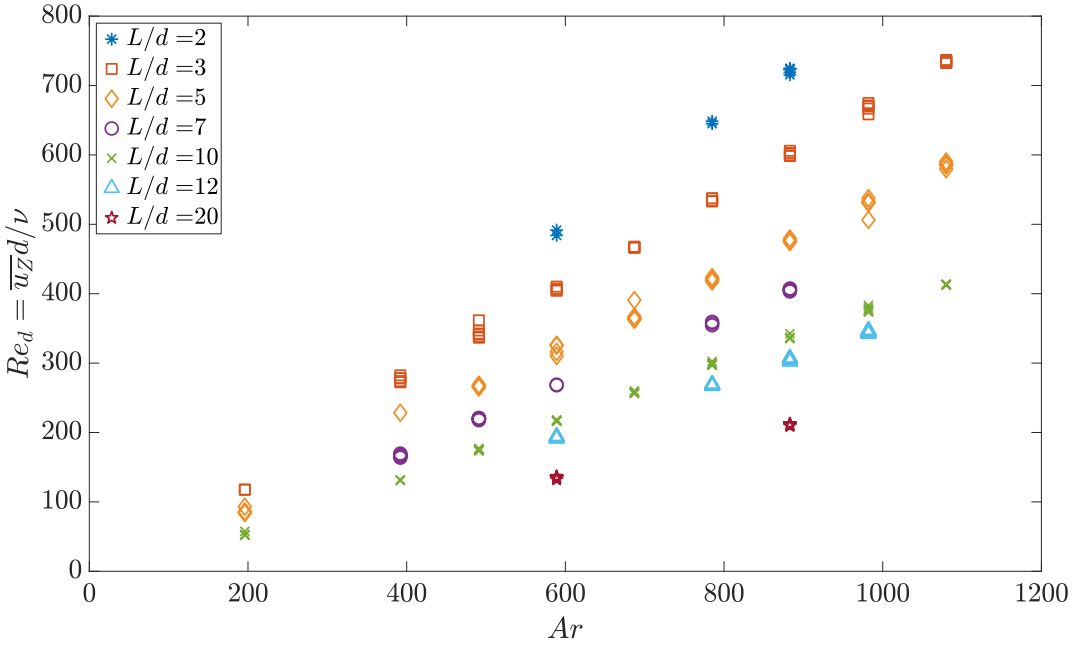

Figure 6: Reynolds number versus Archimedes number for various elongation ratios.

significative jump in the oscillation amplitude of θ between the Irregular I regime and the fluttering one. Finally, in the case of long cylinders ($L/d = 20$, $Ar = 590$ and $Ar = 890$), a different rotational low-amplitude oscillatory mode is observed, called Irregular III. At variance with the fluttering mode that affects the inclination angle θ, oscillations in the azimuthal angle of the cylinder, ψ, are detected at a higher frequency than the fluttering one, about 4 Hz. The amplitude of this motion is of extremely low amplitude, about 0.2°.

We have seen that a wide variety of paths occurs for cylinders in the range of parameters investigated here. The existence of low-amplitude oscillatory motions and the subsequent transition to stronger oscillations, when control parameters are changed (in this case for given L/d when increasing the volume of the body, *i.e.* when increasing Ar) has been observed in previous works for bodies with contrasted geometries (disks, short-length cylinders, two-dimensional cylinders, spheres, etc...) as reviewed by Ern *et al.* (2012). As the experimental determination of these motions, termed A-regimes or quasi-vertical regimes in the literature, may be hindered or modified by noise or residual disturbances in the fluid, numerical simulations appear today as the most suitable tool for their investigation (Auguste *et al.* 2013; Chrust *et al.* 2013). We therefore turn now our attention to the quantitative analysis of mean fall velocity and mean drag (section 5), before focusing on the properties of the large-amplitude oscillatory motion corresponding to the fluttering regime (section 6).

5. Mean fall velocity of the cylinder

After the initial transient following the release of the body from rest, a mean vertical velocity of the body can be determined. Its absolute value, denoted $\overline{u_Z}$, typically ranges from 4 cm/s to 13.5 cm/s. For a given couple $(Ar, L/d)$, data scattering between different runs indicates on average a relative error for $\overline{u_Z}$ less than 1% for the whole data, with a maximum of dispersion of 4.5%. The velocity $\overline{u_Z}$ can be used to create the Reynolds number $Re_d = \overline{u_Z} d/\nu$ based on the cylinder diameter, which is particularly useful for the comparison with fixed or with two-dimensional cylinders, as will be done in section 7.

Figure 6 shows Re_d plotted versus the Archimedes number for various L/d. For a given volume of the body, corresponding to a given Archimedes number, a strong effect of the elongation ratio is visible, lower L/d corresponding to higher Re_d. For all elongation ratios and all types of motion, the evolution of Re_d versus Ar is very close to linear, though for $L/d \leqslant 5$ and $Ar \leqslant 500$, data more notably separate from the global trend.

A drag coefficient can also be deduced from $\overline{u_Z}$, via a force balance between the drag force and the buoyancy force, as

$$\frac{1}{2}\rho_f C_d L d\, \overline{u_Z}^2 = (\rho_c - \rho_f)\, \frac{\pi}{4} d^2 L g, \tag{5.1}$$

$$\text{giving} \quad C_d = \frac{\pi}{2} \frac{\rho_c - \rho_f}{\rho_f} \frac{gd}{\overline{u_Z}^2}. \tag{5.2}$$

Figure 7 shows the evolution of C_d with the Reynolds number for the different types of motion. The drag coefficients are nearly constant at 0.70 for the fluttering and Irregular I regime, for the Reynolds numbers and elongation ratios considered here, and for rectilinear paths with $Re_d > 250$. Irregular II paths also correspond to comparable values of C_d. For rectilinear paths with Re increasing from 50 to 250, the drag coefficient decreases from about 1.45 to 0.70. Cylinders undergoing Irregular III oscillations have a higher C_d than those falling rectilinearly at the same Re_d, an increase of about 0.1 being observed for $Re_d \simeq 100$ and of 0.15 for $Re_d \simeq 200$. For comparison, we also plot the drag coefficients obtained experimentally by Jayaweera & Mason (1965) for metal cylinders with $L/d > 100$ falling through liquid paraffin, sugar solutions or water. The trend is similar, but the two sets of measurements separate on parallel curves for $Re_d > 50$, a difference that may come from the differences in $\overline{\rho}$ and L/d. For $10 < Re_d < 50$, we also compare with the coefficients provided by the numerical simulations of Vakil & Green (2009) for fixed finite-length cylinders. Their results are consistent with those of Jayaweera & Mason (1965) and with the trend of our data. In this range of Re, no significant effect of L/d is observed by Vakil & Green (2009). In their experimental study on the drag coefficient of freely falling cylinders for $200 < Re_d < 6000$, Chow & Adams (2011) review the different correlations of the literature based on $\overline{\rho}$ and L/d, and propose an expression depending on $I^* = \sqrt{\overline{\rho}/(L/d)}$. In the present study, the drag coefficient depends on the Reynolds number for $Re_d < 200$, which lies outside the range of Re_d studied by Chow & Adams (2011). However, significant differences in C_d are also observed with this work for $Re_d > 200$ for the same values of $\overline{\rho} = \rho_c/\rho_f$ and L/d. Chow & Adams (2011) measured C_d ranging from about 0.8 to 1 for I^* ranging from 0.25 to 1, whereas the present C_d is nearly constant at 0.7 over the same range of I^*. This difference might be linked with the fact that the fluttering motion observed by Chow & Adams (2011) is of a much greater amplitude ($20° < \tilde{\theta} < 50°$) than the one observed in the present study, where $\tilde{\theta} < 25°$.

The remarkable trend displayed by the evolution of C_d with Re_d in figure 7 allows us to infer from equation (5.2) that the characteristic velocity scale for the mean fall is given by the gravitational velocity $u_0 = ((\rho_c/\rho_f - 1)gd)^{1/2}$. The dimensionless mean fall velocity $\overline{u_Z}/u_0$ is shown in figure 8 for all the Archimedes numbers and elongation ratios investigated. For fluttering and Irregular I regimes, as well as rectilinear paths with $Ar > 600$, the dimensionless velocity is remarkably independent of the Archimedes number; $\overline{u_Z}/u_0$ is almost constant at about 1.46 for all the Ar and L/d considered here. In the case of cylinders falling rectilinearly with Archimedes numbers rising from about 200 to 600, the fall velocity increases from about 1 to 1.5 and depends on the elongation ratio, as can be seen in the inset of figure 8. The effect is stronger at lower Ar. For $Ar = 200$, a difference of about 0.2 is observed between $L/d = 10$ and $L/d = 3$,

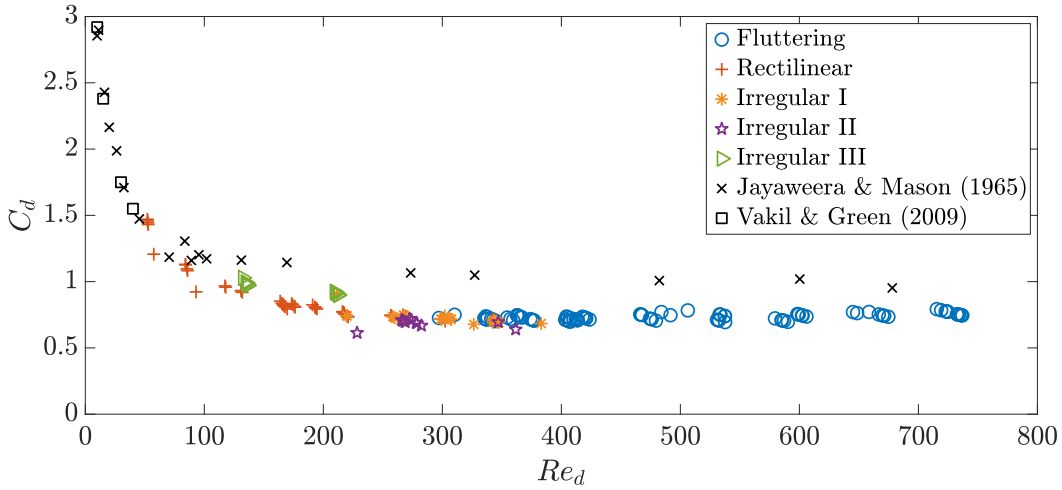

Figure 7: Drag coefficient of the cylinders versus Reynolds number $Re_d = \overline{u_Z}d/\nu$ for the different types of motion.

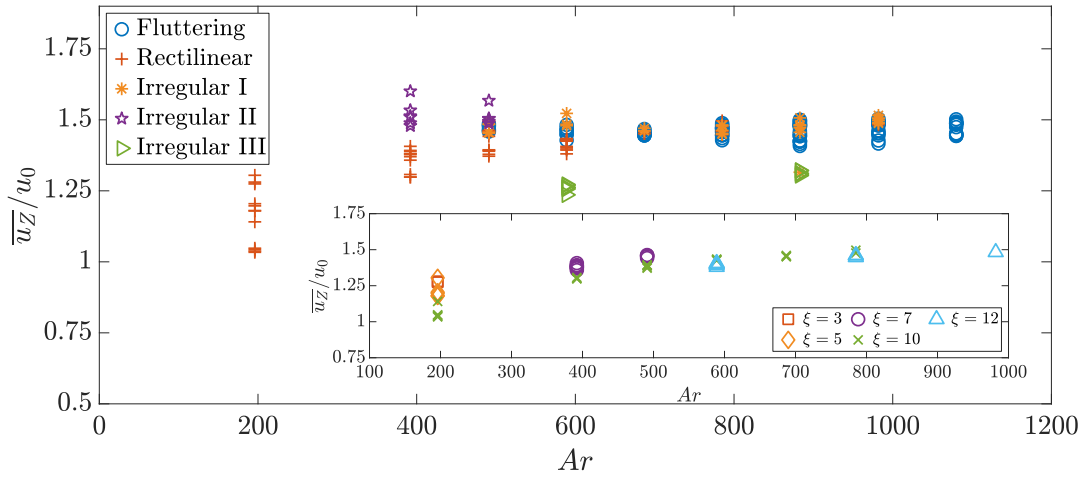

Figure 8: Average vertical velocity scaled by the gravitational velocity versus the Archimedes number for the different types of motion. The inset shows the effect of the elongation ratio on the velocities of cylinders displaying a rectilinear motion.

the longer cylinders being the slower ones. A slight effect of the type of motion is also visible. Cylinders undergoing modulated oscillations (Irregular II regime) have a slightly higher dimensionless fall velocity than those displaying fluttering and rectilinear paths (difference of about 10% for Ar=400 and 5% for Ar=500), while cylinders undergoing weak azimuthal oscillations (Irregular III regime) have a lower (about 20%) dimensionless fall velocity than the other ones. Interestingly, the fall velocity of the elongated finite-length cylinders considered here scales with the gravitational velocity u_0 based on their diameter d independently of their length L, in the same way the fall/rise velocity of short-length cylinders (disks of finite thickness) scales with the gravitational velocity based on their length or thickness L, independently of the body diameter (Fernandes *et al.* 2007).

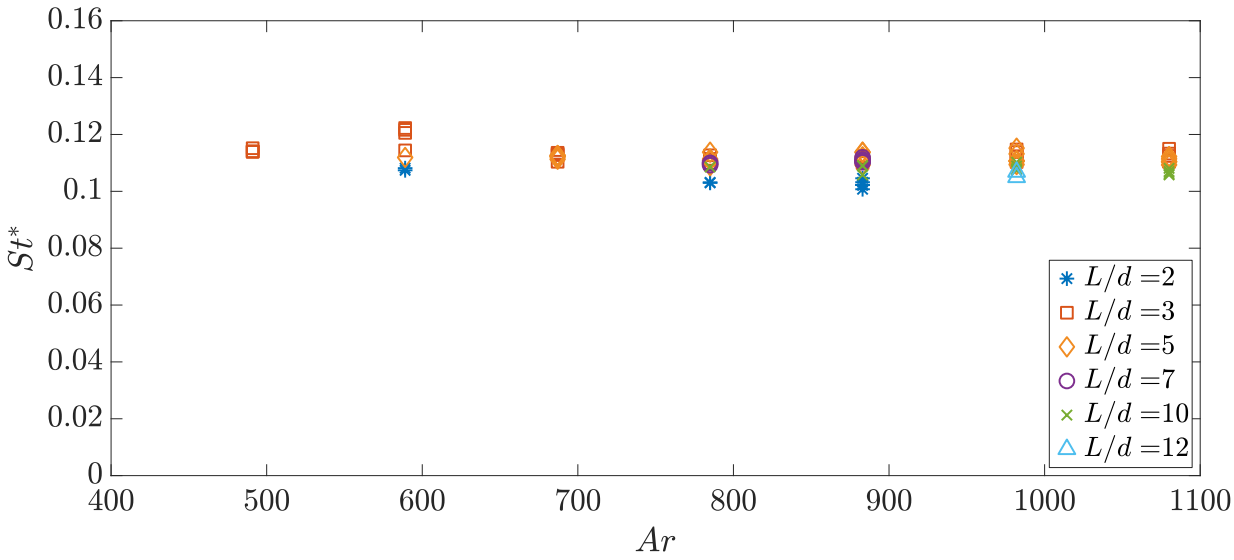

Figure 9: Strouhal number $St^* = f\sqrt{Ld}/u_0$ of the fluttering motion versus the Archimedes number Ar for various elongation ratios.

6. Fluttering regime of the cylinders

This section focuses on the study of the body kinematics in the oscillatory regime, called fluttering in section 4, and characterized by oscillations of the body center of gravity and of the body inclination, θ. These oscillations occur at the frequency f with $\omega = 2\pi f$, while oscillations at 2ω are observed on the vertical velocity of the body. The fluttering frequency f was measured via a spectral analysis of the oscillations of θ over the time span of constant amplitude. The frequency ranges from 0.65 to 1.5 Hz and decreases as Ar increases, whatever the elongation ratio. For $L/d = 2$, a frequency decrease from about 1.5 to 1.2 Hz is observed for Ar going from about 590 to 880. For $L/d = 10$, f goes from 0.80 to 0.75 Hz for Ar increasing from 785 to 1090. To built a Strouhal number, a characteristic length scale has to be chosen as a complement to the gravitational velocity scale determined in the previous section, u_0. Considering the classical interpretation of the Archimedes number as a Reynolds number, we get $Ar = \sqrt{3/2}\, u_0 l_0/\nu$, with $l_0 = \sqrt{dL}$. The characteristic length and velocity scales, l_0 and u_0, can then be used to form the Strouhal number,

$$St^* = f l_0/u_0 = f\sqrt{dL}/u_0.$$

Figure 9 shows that St^* is nearly independent of Ar and L/d in the range considered, with $St^* \simeq 0.115$. Furthermore, this result turns out to be general for short and elongated finite-length cylinders. For short-length cylinders with L/d ranging from 0.1 to 0.5 and a density contrast close to 1, Fernandes *et al.* (2007) obtained the relation $St^* = fd/\left((\rho_c/\rho_f - 1)gd\right)^{1/2} \simeq 0.1$ which is retrieved from the expression proposed here, considering that the gravitational velocity scale u_0 for these bodies is $\left((\rho_c/\rho_f - 1)gL\right)^{1/2}$, L being the cylinder length or disk thickness. It is worth pointing out that the Strouhal number St_L based on the inertial time scale L/u_0 is also nearly independent of Ar for all L/d but contrastingly shows a strong dependence in L/d, increasing from about 0.15 for $L/d = 2$ to about 0.4 for $L/d = 12$. In fact, St_L scales with $(L/d)^{1/2}$, so that $St_L/(L/d)^{1/2} \simeq 0.115$ for all elongation ratios and Ar considered here. A similar expression can be straightforwardly obtained for the Strouhal number based on the diameter d.

This result can be compared with the expression $f_{lit} \simeq 0.126\sqrt{(\overline{\rho} - 1)\, g/\overline{\rho} L}$ proposed

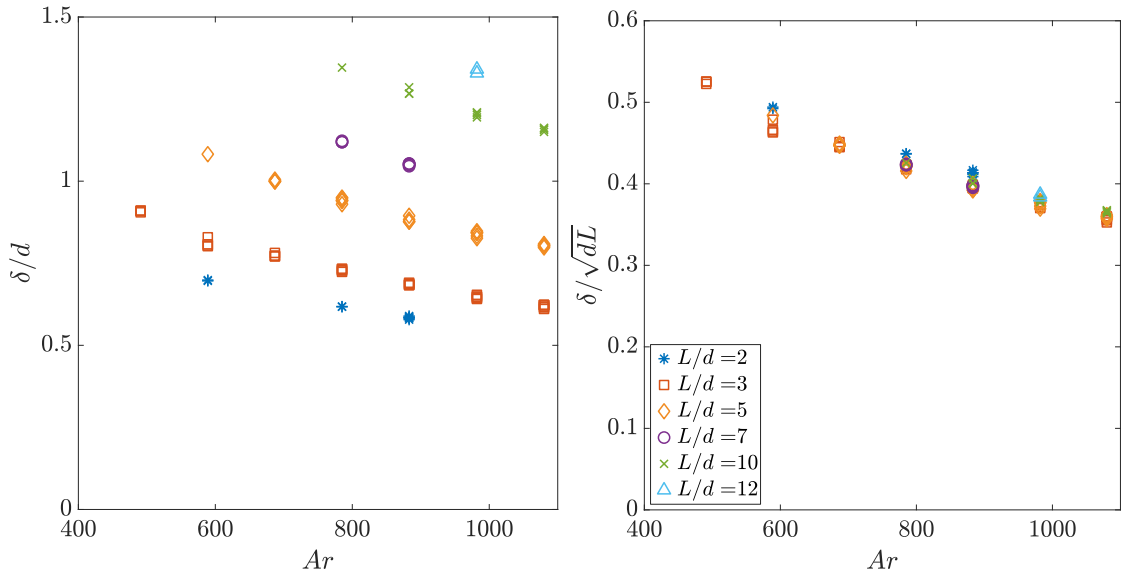

Figure 10: Stokes layer thickness δ versus Ar for various elongation ratios, normalized with (a) the cylinder diameter d ; (b) $l_0 = \sqrt{dL}$. Same legend for both figures.

by Marchildon *et al.* (1964) to represent the oscillation frequencies they measured experimentally for cylinders with $\overline{\rho} \in [1.14, 11.7]$ and by Chow & Adams (2011) for cylinders with $\overline{\rho} \in [1.13, 8.51]$. This expression fits, with only a very slight overestimation, the measured oscillation frequencies f of the present paper, since $f_{lit} \simeq 1.1 f/\sqrt{\overline{\rho}} \simeq 1.02\, f$ for $\overline{\rho} = 1.16$. However, the two predictions significantly depart from each other for stronger density contrast $\overline{\rho}$. A factor 2 between the two expressions would typically be found for metal cylinders falling in water. It is therefore worth pointing out that both expressions have to be considered with caution. The expression proposed here, which also applies to short-length cylinders, was only determined for bodies with density close to that of the surrounding liquid. As in the case of short-length cylinders (or disks), at different $\overline{\rho}$, different modes of oscillatory motion may be expected to occur (Tchoufag *et al.* 2014). As regards the expression for f_{lit}, it is based on a torque balance on the body, assuming that the moment of momentum of the cylinder compensates for a pressure torque due to the asymmetry of the flow surrounding the cylinder, as soon as its axis is no longer perpendicular to its velocity. However, this balance omits the added-mass torque related to the existence of both axial and transversal velocity components, and which has been lately shown to provide a crucial contribution for anisotropic bodies, for instance for plates (Andersen *et al.* 2005*a*) and short-length cylinders (Fernandes *et al.* 2008). Like for these bodies, the selection of the fluttering frequency is therefore concealed in the intricate equilibrium between the proper and added inertia terms and the vortical contributions accounting for viscous and wake effects.

Following this line, the analysis can be pushed ahead by investigating the characteristics of the unsteady boundary layer existing at the surface of a body oscillating in a fluid otherwise at rest at the fluttering frequency $\omega = 2\pi f$. This frequency is much larger than the viscous diffusion frequency ν/d^2 (typically 50 times for $L/d = 2$ and 200 times for $L/d = 10$), so that viscous diffusion of vorticity away from the body surface is strongly limited, the velocity changing sharply to adapt to the no-slip condition. The associated characteristic length scale can be introduced in the form of the oscillatory viscous wavelength, $\delta = 2\pi\sqrt{2\nu/\omega}$. Figure 10a shows that δ is here of the order of the diameter d of the cylinder and depends both on Ar and L/d. Furthermore, figure 10b shows that it scales with $l_0 = \sqrt{dL}$, since δ/l_0 is independent of the elongation ratio,

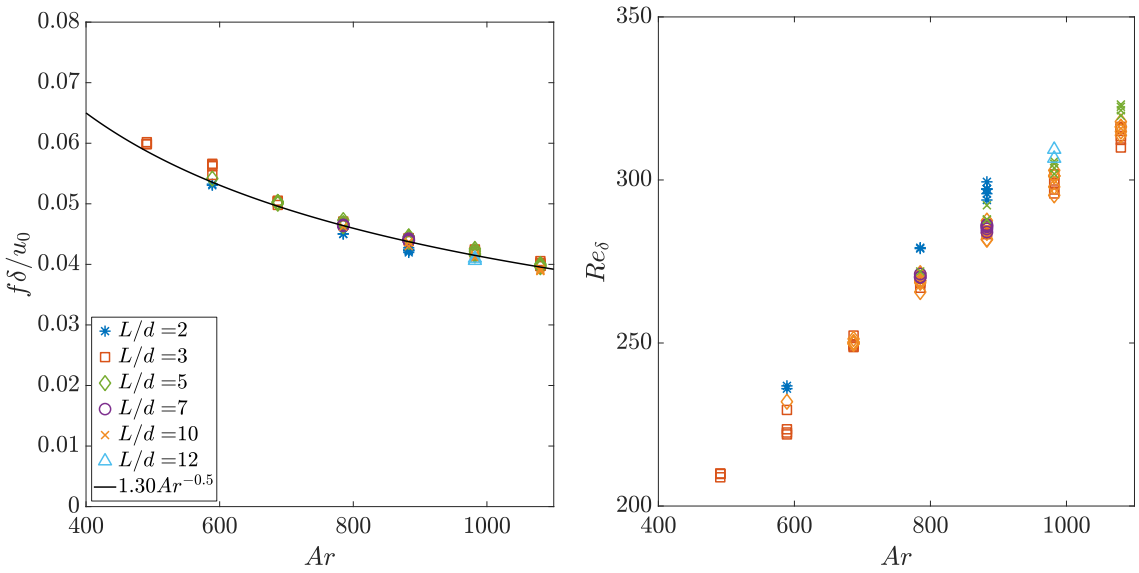

Figure 11: (a) Strouhal number, $f\delta/u_0$, versus Ar for various elongation ratios, indicating an evolution close to $Ar^{-0.5}$; (b) Reynolds number $Re_\delta = u_0\delta/\nu$ based on the Stokes layer thickness for various elongation ratios as a function of the Archimedes number Ar.

within experimental accuracy. This provides a possible physical interpretation for the length scale l_0. Since the effect of the elongation ratio is well captured by the length scale l_0 as well as by the length scale δ, the results presented in figures 9 and 10 can then be expressed in two other forms. The first, illustrated in figure 11a, is that the Strouhal number based on the thickness δ is independent of the elongation ratio. It displays an evolution with Ar that can be modeled by $1.3Ar^{-0.5}$, leading to the scaling $St^* \simeq 0.115$. The second is that the Reynolds number based on the thickness of the unsteady boundary layer $Re_\delta = u_0\delta/\nu$ is also independent of L/d, as shown in figure 11b. The result is highlighted by contrasting this figure with figure 6. The dependence on Ar and independence of L/d observed in figures 11a and b indicate that for these quantities the volume of the body is important as expected (buoyancy being the driving force), yet no longer the exact shape of the body (*i.e.* its elongation ratio), suggesting a crucial role of the sharp edges of the cylinder (formed where its flat bases join its circular side) in the control of the extension of the unsteady boundary layers created by viscosity in the vicinity of the moving body.

We now turn our attention to the amplitudes of the translational and rotational oscillatory motion of the cylinder. During the fluttering regime, the inclination of the cylinder axis relative to the horizontal, θ, oscillates periodically and regularly, so that it can be modeled by an harmonic function, $\theta = \tilde{\theta} sin\,(\omega t - \phi_\theta)$. Figure 12 shows that the amplitude $\tilde{\theta}$ depends both on Ar and L/d, ranging from about 20° for $L/d = 2$ to about 7° for $L/d = 12$, shorter cylinders displaying a greater oscillation amplitude of their axis. For a given elongation ratio, $\tilde{\theta}$ increases slightly with Ar. A larger increase, of about 2.5°, is observed for $L/d = 3$ and Ar going from 490 to 590, which is not observed for higher elongation ratios for the values of Ar that could be explored. For $L/d \geqslant 5$, a jump is in fact observed in a short interval of Ar from the values corresponding to the Irregular I regime, $\tilde{\theta} < 3°$, to those of the fluttering regime, $\tilde{\theta}$ growing further slowly and nearly linearly with Ar.

Chow & Adams (2011) measured $\tilde{\theta}$ in their experiments for freely falling cylinders with $\overline{\rho} \in [1.13, 8.5]$, $L/d \in [1, 90]$ and $Ar \in [200, 6000]$. By considering that the oscillation velocity of the ends of the cylinders is of the same order of magnitude than the mean

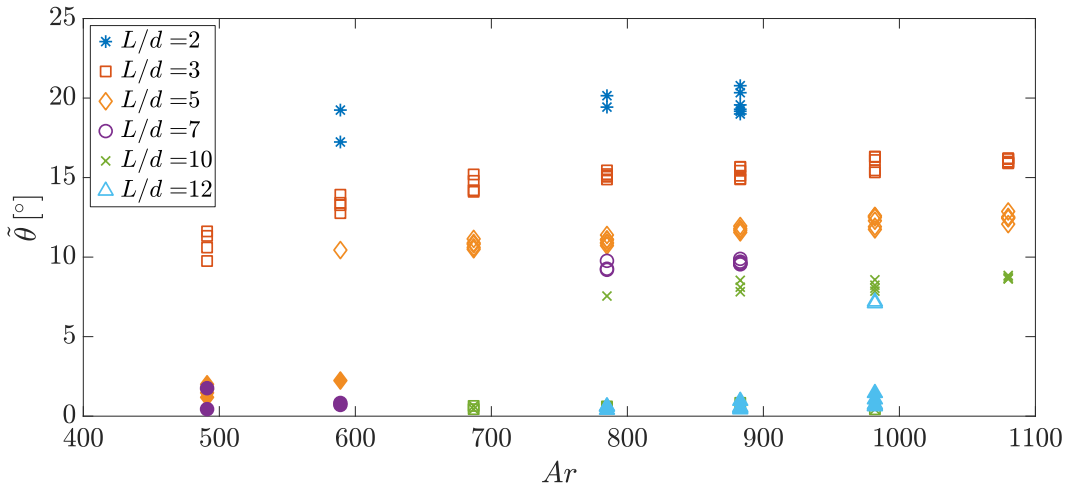

Figure 12: Amplitude $\tilde{\theta}$ of the oscillations of θ versus Ar for various elongation ratios for the fluttering and Irregular I regimes. Cylinders corresponding to the latter regime are plotted using filled markers, except those for $L/d = 10$ which are plotted using ticked boxes.

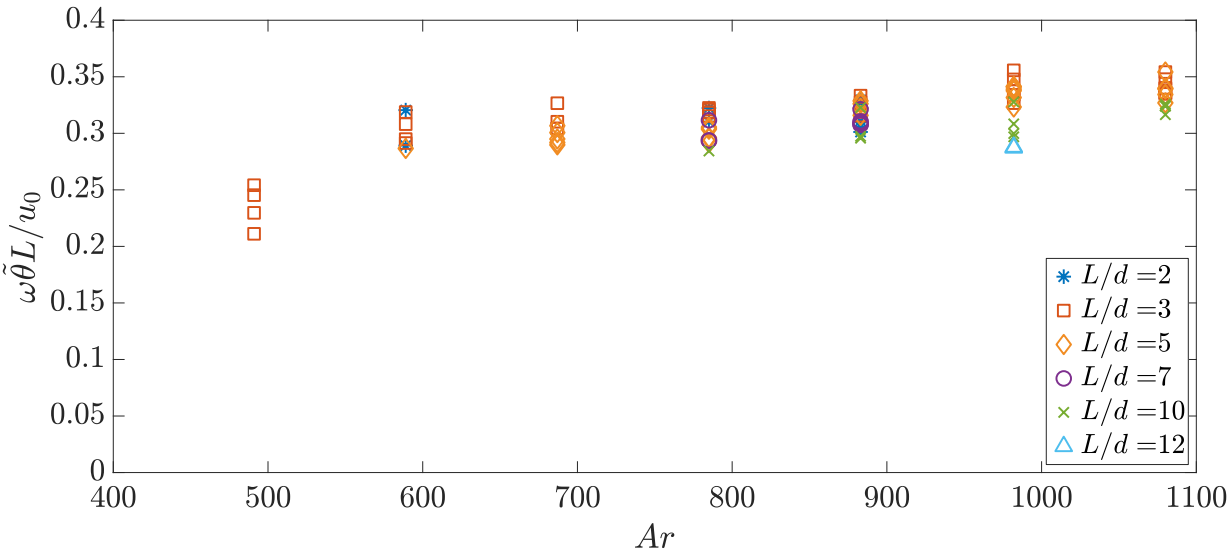

Figure 13: Angular velocity of the cylinder $\tilde{\omega\theta}L$ normalized with the gravitational velocity u_0 as a function of Archimedes number Ar for various L/d.

fall velocity, and that it scales as its excursion over its period, $f_{lit}L\tilde{\theta}$, they propose that $\tilde{\theta}$ is only dependent on the density and elongation ratio, $\tilde{\theta} \sim \sqrt{\overline{\rho}/(L/d)}$. They measured $20° < \tilde{\theta} < 40°$ for $0.3 < \sqrt{\overline{\rho}/(L/d)} < 0.9$. In the present study, $\tilde{\theta}$ can not be determined using only $\sqrt{\overline{\rho}/(L/d)}$, as it is also dependent on the Archimedes number. Moreover, the amplitude of the oscillations are here significantly smaller than those obtained by Chow & Adams (2011) for similar $\sqrt{\overline{\rho}/(L/d)}$ (ranging here from 0.30 to 0.75).

From the inclination angle of the body, we can determine the rotation rate of the body and its amplitude $\tilde{\omega\theta}$, which is expected to scale with the inertial frequency associated to the mean fall, u_0/L. This scaling is displayed on figure 13, versus the Archimedes number, showing a remarkable gathering of the data points independently of the elongation ratio L/d. Furthermore, the evolution with the Archimedes number is close to a constant,

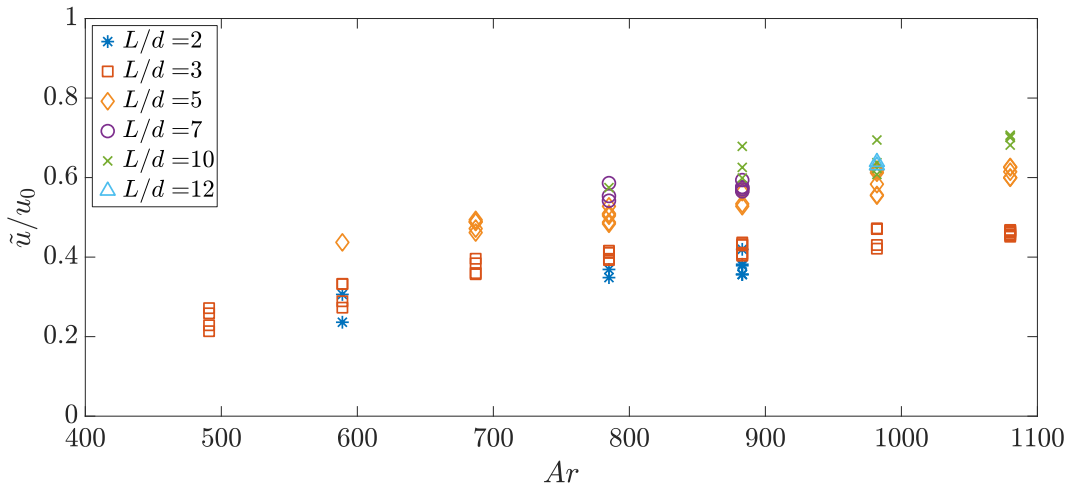

Figure 14: Amplitude of the oscillations of u normalized with u_0 versus Ar for various elongation ratios.

except for $Ar \simeq 500$ at $L/d = 3$, for which the rotation rate is in fact slightly lower, as seen previously for the inclination angle $\tilde{\theta}$.

During the periodic motion, the oscillations of θ are coupled with oscillations of the cylinder center of gravity. These can be characterized by the component of the body velocity along the cylinder axis, u, which oscillates at the fluttering frequency f, and similarly to θ, can be accurately represented by an harmonic function, $u = \tilde{u}sin(\omega t - \phi_u)$, $\tilde{u}$ being the oscillation amplitude and ϕ_u the phase. Figure 14 shows that the amplitude $\tilde{u}$ normalized with u_0 ranges between 0.2 and 0.7 for all the cases investigated. For a given elongation ratio, $\tilde{u}/u_0$ increases with Ar. At variance with the amplitude $\tilde{\theta}$, it also increases with L/d. The periodic motion of cylinders with increasing elongation ratios is therefore characterized by stronger axial velocity components and lower inclination angles. The phase difference, $\phi_u - \phi_\theta$, between the oscillations of u and θ is plotted as a function of Ar for various L/d in figure 15. Values remarkably gather along a master curve increasing slightly from about $9\pi/8$ to a constant value about $5\pi/4$ for $Ar \geqslant 690$. In the range of parameters considered here, no significant effect of Ar nor of the elongation ratio L/d is observed on the phase difference between the oscillations of body inclination and axial velocity, at variance with the results for short-length cylinders (Fernandes *et al.* 2007).

As mentioned in section 2, not all trajectories in the fluttering regime are planar zigzag paths contained in the azimuthal frame. The ellipticity of the path can be characterized by the ratio of $\tilde{w}/\tilde{u}$, $\tilde{w}$ being the amplitude of the oscillations of the velocity component w in the direction perpendicular to the azimuthal plane (see figure 1c). This quantity is displayed in figure 16. Mean values of $\tilde{w}/\tilde{u}$ are plotted in the inset of figure 16 versus L/d. The figures indicate that the elongation ratio has a decisive impact on the type of trajectory observed. For long cylinders ($L/d = 7$, 10 and 12), the trajectory is very close to a planar zig-zag, with $\tilde{w}/\tilde{u} < 7\%$ for all cases. This behaviour changes with decreasing L/d, with $\tilde{w}/\tilde{u} \sim 0.1$ for all cylinders at $L/d = 5$. For $L/d = 3$, we find $\tilde{w}/\tilde{u} \sim 0.2$, and for $L/d = 2$, $\tilde{w}/\tilde{u} \sim 0.3$. A slight increase of $\tilde{w}/\tilde{u}$ with Ar can be seen for $L/d = 3$, even though the data is dispersed due to difficulties in measuring w, which remains small (typically, lower than 1.5 cm/s). The body motion gets more complex and three-dimensional as the elongation ratio decreases. The existence of the w component in the fluttering regime is probably related to the existence of oscillations in the azimuthal

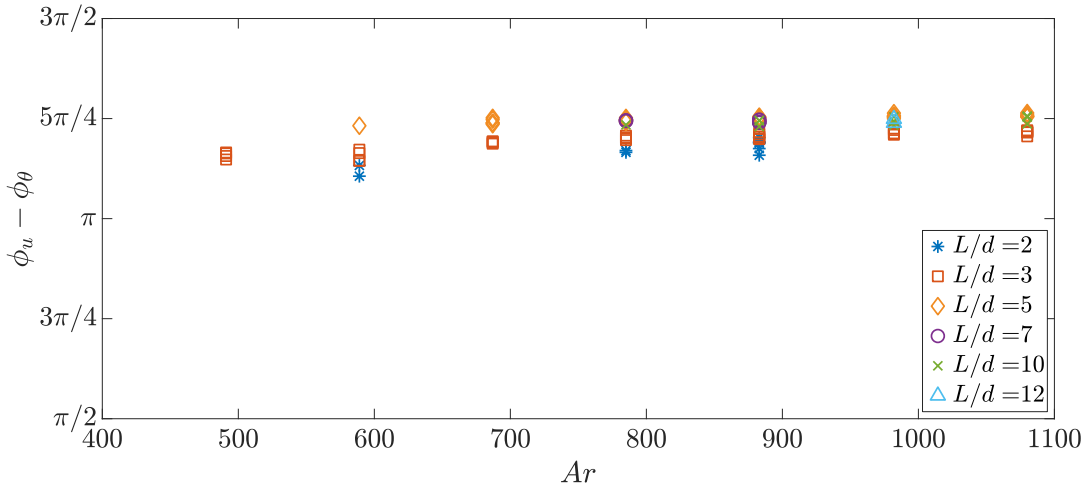

Figure 15: Phase difference between the oscillations of u and θ versus the elongation ratio L/d for various Archimedes numbers.

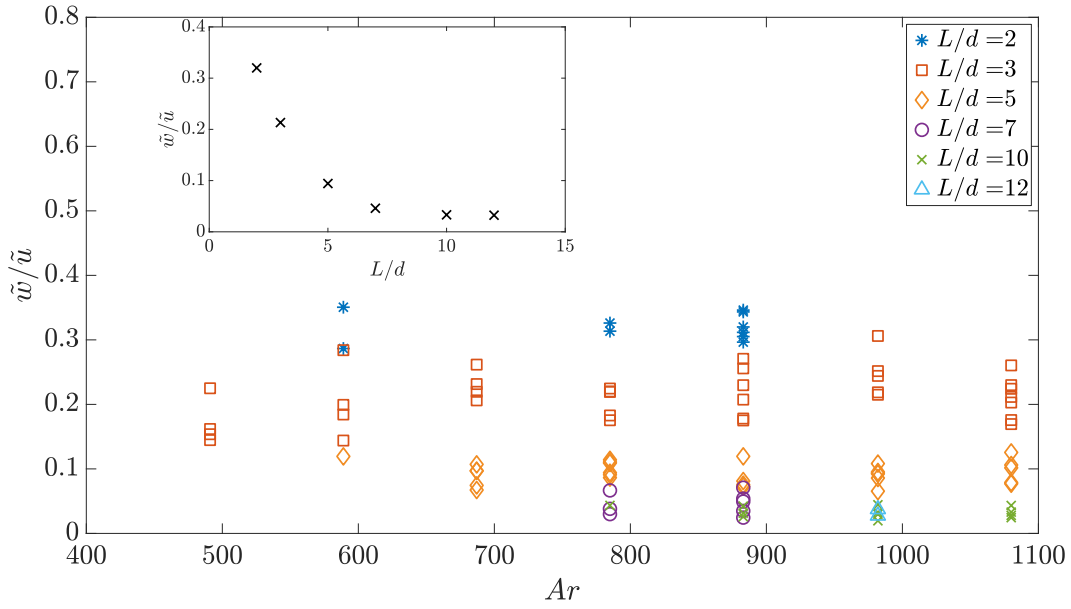

Figure 16: Ratio between the amplitude of the oscillations of u and w, versus Ar for various elongation ratios. The inset shows the mean values of $\tilde{w}/\tilde{u}$ for each L/d as a function of L/d.

angle ψ. We were able to detect weak oscillations of amplitude slightly increasing with Ar, about 6° for $L/d = 2$, dispersed between 3 and 7° for $L/d = 3$, lower than 4° for $L/d = 5$ and than 2° for $L/d = 10$. However, the trajectory of short cylinders ($L/d = 2$ and 3) could not be fully described, owing to the difficulty in determining properly the phase of w and of ψ relative to those of u and θ.

7. Wake visualization and analysis

We now turn our attention to the structure and nature of the wake associated to the various paths observed here for freely falling cylinders. Wake visualization was performed by coating the cylinders in ink before releasing them into the tank. This

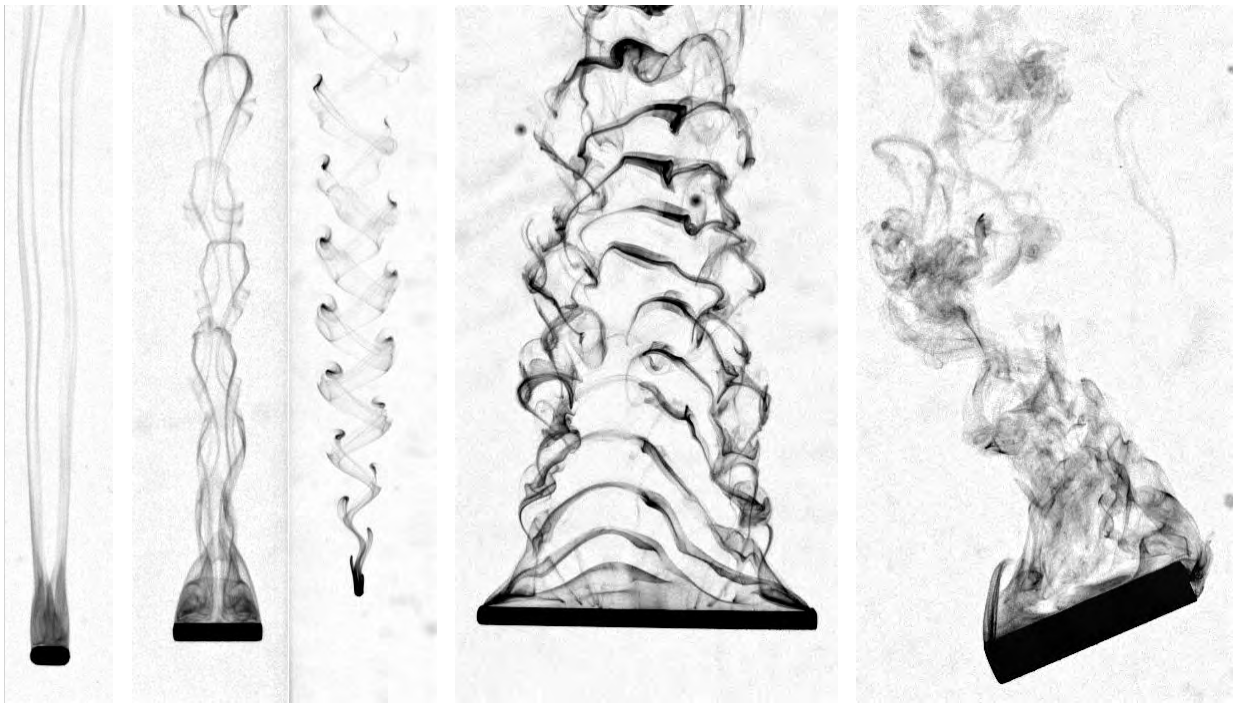

(a) (b) (c) (d)

Figure 17: Different types of wake observed. (a) Steady wake with two pairs of longitudinal vortices observed for a cylinder in rectilinear motion with $(Ar = 200, L/d = 3)$. (b) Periodic release of hairpin vortices observed for cylinders following rectilinear paths with $(Ar = 200, L/d = 5)$ on the left and $(Ar = 200, L/d = 10)$ on the right. (c) Wake for long cylinders $(Ar = 600, L/d = 20)$ displaying weak azimuthal oscillations. (d) Fluttering regime $(Ar = 1100, L/d = 5)$.

provides a good qualitative visualization of the wake of the cylinders, as can be seen on figure 17. Several different types of wake are observed in the space of parameters $(Ar, L/d)$ covered here, for cylinders undergoing a rectilinear fall (figure 17a and 17b), Irregular III oscillations (figure 17c) or strong fluttering (figure 17d). In the case of cylinders presenting a rectilinear motion, a comparison can directly be done with the numerical study by Inoue & Sakuragi (2008) for fixed cylinders with finite length and free ends.

We observe a single case of steady wake for $Ar = 200$ and $L/d = 3$, corresponding to $Re_d = 120$ and to the lightest cylinder tested in our experiment which displays a rectilinear fall (see figure 17a). This wake is characterized by the formation of four longitudinal dye streaks, alike the steady wake observed numerically by Inoue & Sakuragi (2008) for $Re_d = 150$ and $L/d = 1$ (denoted *Type IV* in their work) and composed of two pairs of counter-rotating longitudinal vortices (see their figure 5b and 6). To our knowledge, this is the first experimental evidence of the existence of the wake structure uncovered numerically by Inoue & Sakuragi (2008) for cylinders with slightly different parameters, and corresponding to the shedding of two steady counter-rotating vortex pairs behind the cylinder.

For $Ar = 200$, $L/d = 5$ and 10 (corresponding to $Re_d = 80$ and 50 respectively), we observe a periodic double-sided shedding of hairpin vortices (figure 17b). It should be noted that in both cases, no significant horizontal displacement of the body was detected. The vortex shedding frequency was estimated to be about $7Hz$. Inoue & Sakuragi (2008) observed similar shedding of vortices for $Re_d = 150$ and $L/d = 5$, for $Re_d = 100$ and

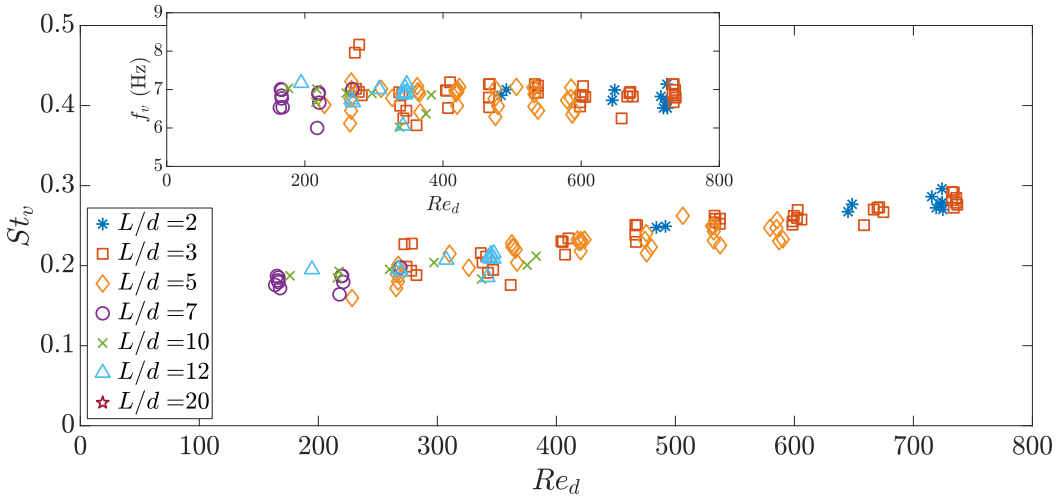

Figure 18: Strouhal number based on the high-frequency vertical oscillation of v, $St_v = f_v d/\overline{u_Z}$, versus the Reynolds number.

$L/d = 10$, and for $Re_d = 60$ and $L/d = 13$, referenced as *Type III* (see their figure 5a). This type of wake is according to Inoue & Sakuragi (2008) characterized by disconnected hairpin-shaped vortices shed alternatively from opposite sides of the curved surface of the cylinder, in contrast to vortices shed in *Types I* and *II*, to be discussed hereafter. An experimental illustration of a similar wake is also provided by Jayaweera & Mason (1965) for $Re_d = 70$ and $L/d = 10$.

Figure 17c shows the wake of a cylinder with $Ar \simeq 600$ and $L/d = 20$ ($Re_d \simeq 130$). The wake for this freely-moving long cylinder can be compared to the observations for fixed long cylinders, with free ends from the numerical study by Inoue & Sakuragi (2008) and without free ends from the experimental results by Williamson (1989). The instantaneous structure of the wake observed in this case is similar to that referred to as *Type II* by Inoue & Sakuragi (2008), and as oblique vortex shedding by Williamson (1989). However, the cylinder shown in figure 17c presents weak regular azimuthal oscillations, which are coupled to the wake. A periodic beating of the wake is in fact observed here near the ends of the cylinder, at the oscillation frequency of the azimuthal angle ψ.

In the case of fluttering cylinders, the coupling between the wake and the motion of the body leads to a significantly different wake structure, strongly influenced by the orientation of the body and of its flat faces relative to its velocity. An example is shown on figure 17d for $Ar \simeq 1100$ and $L/d = 5$ ($Re_d \simeq 585$) for a body displaying a fluttering motion of amplitude $\theta \simeq 12°$.

Flow visualization thus revealed that an unsteady wake is observed even for bodies maintaining a rectilinear motion. A deeper analysis of the cylinder kinematics was therefore carried out in order to uncover possible effects of the wake unsteadiness in their path. This revealed that high-frequency oscillations of the vertical velocity of the cylinder (which can be seen on v, as $v \simeq u_Z$ for all cases) are observed on most cylinders recorded with an acquisition frequency of 50Hz. These oscillations occur at a frequency $f_v \sim 7Hz$ measured by the spectral analysis of v (figure 18), and are observed for cylinders presenting rectilinear as well as fluttering paths. The amplitude of this vertical oscillation is very low, less than $4\%\,\overline{u_Z}$ for all cases, and was difficult to measure accurately. f_v is remarkably constant with Re_d, with 6Hz $< f_v <$ 7.2Hz for all cases but 2, being at about $8Hz$. No effect of L/d was detected on f_v. Vortex shedding from the curved side of the cylinder is a plausible cause for these oscillations, as they occur for all

cylinders independently of their path, L/d and Re_d. Furthermore, this frequency is close to the estimated vortex shedding frequency from wake visualization videos for instance for $Re_d = 50$ and $L/d = 10$ (figure 17b).

A corresponding Strouhal number can be built as $St_v = f_v d/\overline{u_Z}$. St_v increases with Re_d and ranges from about 0.16 to 0.30 (figure 18). The elongation ratio has seemingly no impact on St_v in the range explored. Comparison of St_v with previous results of the literature can be seen in figure 19. Williamson & Brown (1998) proposed a fit in series of $Re_d^{-1/2}$ for the Strouhal number corresponding to the Bénard-von Kármán instability about a fixed cylinder, $St_{BvK} = 0.2731 - 1.1129Re_d^{-1/2} + 0.4821Re_d^{-1}$ for $Re_d \leqslant 1000$. For about $160 < Re_d < 400$ corresponding to rectilinear and Irregular I paths (figure 7), the present results for St_v are in good agreement with this expression. The Strouhal number values, computed by Inoue & Sakuragi (2008) for fixed cylinders with free ends at $Re_d = 100$, are also plotted in figure 19. They are significantly smaller than the results for infinite cylinders, ranging from about 0.08 for $L/d \simeq 3$ to 0.13 for $L/d \simeq 20$. Qu *et al.* (2013) and Gioria *et al.* (2011) performed numerical studies of the flow past a cylinder using domains of varying spanwive length. Although measuring St_{BvK} was not the primary aim of their work, they provided values of St_{BvK} for some Reynolds number. Qu *et al.* (2013) studied cylinders of spanwise length $L = 10d$ and $12d$ at $Re_d = 200$ providing $St_{BvK} \simeq 0.18$, and Gioria *et al.* (2011) cylinders of spanwise length $L = 6d$ and $12d$ at $Re_d = 400$ yielding $St_{BvK} \simeq 0.21$. Both St_{BvK} values are in good agreement with the present experimental results. It should be noted that Qu *et al.* (2013) also performed numerical simulations on infinite cylinders, and that the values of St_{BvK} they found were in remarkable agreement with the model of Williamson & Brown (1998). For the same Re_d, the Strouhal number values they computed were thus lower for cylinders of fixed spanwise length. Finally, it can be pointed out that Namkoong *et al.* (2008) observed numerically that for $66 < Re_d < 185$ the degrees of freedom in rotation and translation of an infinitely long (*i.e.* two-dimensional) cylinder lead to a slight decrease in the frequency of vortex shedding and of the associated oscillatory motion of the cylinder, with typically $St_{BvK} \simeq 0.17$ for $\overline{\rho} = 1.01$ and $Re_d = 156$, corresponding to the trend observed here for lower Re_d (figure 19). For Re_d larger than about 400, corresponding to cylinders displaying in our configuration a fluttering motion (figure 7), we find values for the Strouhal number St_v higher than those of St_{BvK}. The high-frequency mode is therefore observed to coexist, and most possibly is coupled, with the fluttering mode, as oscillations of v at St_v are detected to be superimposed to those at twice the fluttering frequency.

The correspondence between the Strouhal numbers provided by the oscillations of v measured in our experiments, by the wake visualizations and by various numerical and experimental data on vortex shedding in the wake of fixed cylinders suggests that vortex shedding from the curved side of the cylinder may be responsible for the weak oscillations of the vertical velocity observed here for freely falling cylinders. An associated rotation of the cylinder about its axis could possibly exist along with the high-frequency vertical oscillation of the body, as observed by Namkoong *et al.* (2008). In our experiments, no such motion could be detected across all experiments outside the transient period following the release of the body from rest. However, the measurement method for the rotation is not accurate enough to determine such low-amplitude motions (rotational and translational oscillation of amplitudes respectively about $0.7°$ and $0.1d$ for $\overline{\rho} = 1.01$ and $Re_d = 156$ in the simulations by Namkoong *et al.* (2008) for freely falling two-dimensional cylinders). Numerical simulation may be a more adapted and accurate tool

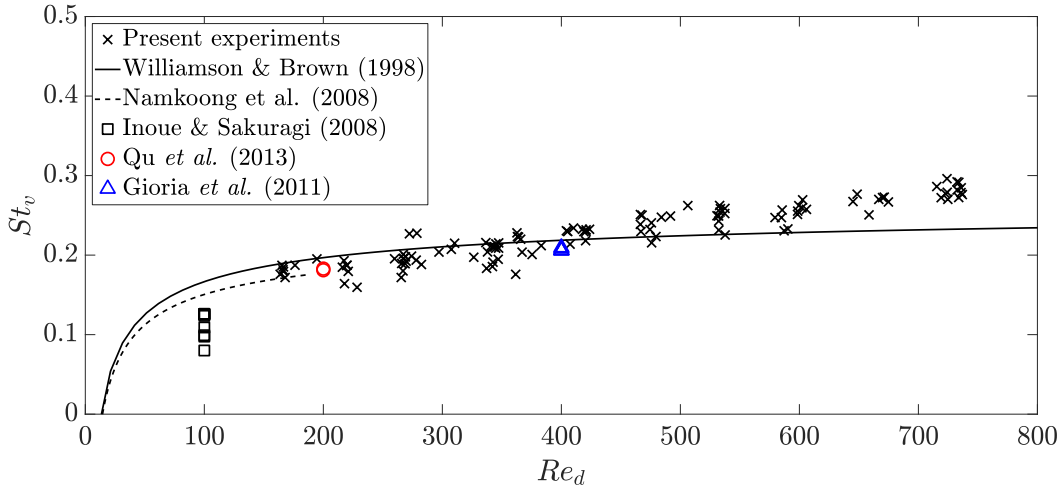

Figure 19: Strouhal number based on the high-frequency vertical oscillation of v, $St_v = f_v d/\overline{u_Z}$, versus Re_d, comparison with results from Williamson & Brown (1998); Qu *et al.* (2013); Gioria *et al.* (2011). The dashed line corresponds to the expression $St_v = 0.2429 - 0.9238 Re_d^{-1/2}$ from Namkoong *et al.* (2008).

to carry further the investigation of the different regimes of low-amplitude oscillations of the cylinders.

8. Conclusion

We investigated the motion of freely falling elongated cylinders (length-to-diameter ratio ranging from 2 to 20) in a liquid otherwise at rest, for the density ratio $\overline{\rho} \simeq 1.16$ and for Archimedes numbers ranging from 200 to 1100. The Archimedes numbers are based on the body equivalent diameter, enabling us to investigate at given Ar, and therefore at given volume of the body and given buoyancy force ($\overline{\rho}$ being fixed), the effect of the elongation ratios of the cylinders on their behaviour. A shadowgraphy technique involving two cameras and two backlights mounted on a travelling cart was used to track the cylinders along their fall. A dedicated image processing algorithm was further implemented to properly reconstruct the position and orientation of the cylinder in the 3D space. In the range of parameters explored, we identified three main types of paths, matching regimes known to exist for three-dimensional bodies (disks and spheres). Two of these are stationary, the rectilinear motion and the large-amplitude oscillatory motion (also referred to as fluttering or zigzag motion). The third one comprises irregular oscillatory motions of low-amplitude (denoted here Irregular I to III) that may be assimilated to A-regimes or quasi-vertical regimes of the literature. The rectilinear motion observed here is twofold. On the one hand, a steady vertical fall associated with a steady wake composed by two pairs of longitudinal vortices generated behind the cylinder is observed (here, only for $Ar = 200$ and $L/d = 3$). On the other hand, a vertical rectilinear motion with very light vertical oscillations at a Strouhal number St_v (frequency f_v) close to that of the Bénard-von Kármán instability is observed in association with an unsteady wake, displaying in some range of parameters a periodic shedding of hairpin vortices. No additional motion of the body could be detected here experimentally, but horizontal or rotational motions of the body could possibly occur for these bodies. Their path would then belong to the second class of paths identified here, the low-amplitude rotational oscillatory regimes. The low-amplitude rotational regimes

observed here present oscillations of irregular amplitude, that are difficult to disentangle from noise. Nevertheless, we tried to grasp some distinctive features and classified them in three groups. Irregular III corresponds to oscillations essentially of the azimuthal angle ψ of the cylinder at Strouhal numbers about St_v for long cylinders ($L/d = 20$). Irregular I and Irregular II present irregular oscillations of the inclination angle θ and of the body center of gravity position at a frequency close to the fluttering frequency f, that stay weak (lower than 3°) over the whole time sequence (Irregular I) or are low-frequency modulated (Irregular II), amplitudes varying in this case from less than 3° to sometimes about 10°. These salient features are proposed here as a basis for future developments and improved analysis of these paths, as it must be stressed that experimentation, at least the one carried out here, is not accurate enough to elaborate a full characterization of these complex paths. A sharp distinction between these regimes and the fluttering regime is conspicuous, for large-amplitude oscillations in both orientation and translation of the body are manifest in the latter. In the whole range of parameters investigated here, a significant agitation due to wake unsteadiness is present in the liquid, featuring in particular three-dimensional vortex shedding, even when no significant oscillatory motion of the cylinder is clearly visible. In the fluttering regime, the rotation of the body as well as its tendency to slide along its symmetry axis are strongly coupled with an unsteady wake that has a distinct outline, and whose characteristic features are related to the fact that the flat sides of the cylinder contoured by sharp edges tend now to face the direction of motion. Still, closer examination of the temporal signals of the body vertical motion revealed coexistence in the fluttering regime of oscillations at frequencies $2f$ (fluttering behaviour) and f_v, suggesting a complex shedding of vortices originating both from the curved side of the cylinder and from the flat faces.

The detailed analysis of the body kinematics in the fluttering regime brought to light a series of remarkable properties of this motion. In the range of parameters Ar and L/d investigated here for $\overline{\rho} \simeq 1.16$, the values of the mean vertical velocity of the body gather together into the relation $\overline{u_Z} \simeq 1.46\, u_0$, where $u_0 = ((\overline{\rho} - 1)gd)^{1/2}$ is the gravitational velocity based on the cylinder diameter d. The mean fall velocity of the cylinder appears therefore independent of its length, depending solely on its diameter, in the same way the mean velocity of the finite-length disk is independent of its diameter, depending solely on its length or thickness (see for instance Fernandes *et al.* 2007, where $u_0 = (|\overline{\rho} - 1|gL)^{1/2}$, $\overline{\rho} \simeq 0.99$ and $0.1 \leqslant L/d \leqslant 0.5$). Proceeding along with this parallel, a unified view of the fluttering frequency f of finite-length cylinders (either short or elongated) with density ratios close to unity is provided by the Strouhal number,

$$St^* = f l_0/u_0 \quad \text{with} \quad l_0 = \sqrt{dL},$$

featuring the length scale l_0 and the gravitational velocity scale based on the dimension of the cylinder corresponding to the direction of its mean vertical motion (the length for a short-length cylinder and the diameter for an elongated cylinder), yielding $St^* \simeq 0.115$ for elongated cylinders, and $St^* \simeq 0.1$ for disks in Fernandes *et al.* (2007). These results bring to the fore that the characteristic length and velocity scales of the body motion are respectively l_0 and u_0. When made dimensionless using these scales, the mean vertical velocity and the frequency of the oscillations are almost independent of L/d and Ar. Their relevance is further intensified by considering that the Archimedes number defined using the equivalent diameter of the cylinder D as mentioned previously, can be expressed as the Reynolds number built with u_0 and l_0, $Ar = \sqrt{3/2}\, u_0 l_0/\nu$.

Moving beyond this point to improve our understanding is not an easy task with the results at hand. The scaling proposed for the fluttering frequency appears as purely

inertial, based on the inertial time scale l_0/u_0. However, primary causes of frequency selection could lie deeper in the flow organization in the vicinity of the body due to the effect of viscosity. The fluttering period is an order of magnitude shorter than the viscous diffusion time scale d^2/ν, so that the liquid velocity changes sharply to satisfy the no-slip condition on the cylinder surface and viscous effects are responsible for flow reversal in the vicinity of the cylinder. The extension of the recirculation region can be estimated with the oscillatory viscous wavelength, $\delta = 2\pi\sqrt{2\nu/\omega}$, which scales with $l_0 = \sqrt{dL}$, since δ/l_0 is found to be, within experimental accuracy, independent of the elongation ratio for given Ar. We therefore suggest that the origin of the length scale l_0 is related to viscosity, as a characteristic recirculation length scale. For the unsteady boundary layers at rather high-frequencies involved here, flow reversal may be expected to occur simultaneously both on the face and side of the cylinder surface, coupling therefore the two characteristic dimensions of the body, d and L.

We further explored the characteristics of the amplitudes of oscillation in translation and rotation of the body and showed that cylinders with higher elongation ratios display higher axial velocity component u and lower inclination angle θ. The rotation rate of the cylinders scales with the inertial frequency scale, u_0/L, depending only slightly on Ar and L/d. One of the most remarkable results is however provided by the phase difference $(\phi_u - \phi_\theta)$ between the oscillations of u and θ, which increases slightly from about $9\pi/8$ to a constant value of $5\pi/4$ for larger Ar, whatever the elongation ratio L/d. This result is markedly at variance with the behaviour of disks, where a strong influence of the disk aspect ratio on the phase difference is observed, changing by about $\pi/2$ when L/d varies between 0.1 and 0.5 (Fernandes *et al.* 2007). In spite of these properties, it is worth pointing out that the path of the cylinders remains complex. The fluttering motion is moderately three-dimensional (ellipticity lower than 0.3), becoming more planar as the elongation ratio of the body increases, tending towards a path contained in the plane formed by the body symmetry axis and the vertical. Since the motion in the perpendicular direction to this plane is weak, its characterization requires a specific investigation, which is beyond the scope of the present paper.

Appendix A. Three-dimensional reconstruction of a cylinder using its projected contour

When observing a 3D object through a camera using shadowgraphy, only the 2D projection of its contour is seen. This projected contour loses some properties of the 3D object, such as symmetries. In our study, we need to determine accurately the pose, i.e. the accurate position in a 3D space, of the cylinders. In the case of a cylinder, the projected contour on the camera plane loses the planar symmetry property of the cylinder. Moreover, the distortion is not even for all contour points, and the ones further from the camera axis are more distorted. As a result, the shape and orientation of the projected cylinder contour are vastly different from its physical ones. Furthermore, no contour point is easily matchable to a physical point of the cylinder. In consequence, determining the exact features of the 3D object using solely its projection is not a trivial matter. The 3D reconstruction (also called pose estimation) of a cylinder using its projected contour is a problem investigated by several computer vision studies due to its difficulty and numerous applications (Huang *et al.* 1996; Doignon & de Mathelin 2007; Shiu & Huang 1993; Navab & Appel 2006).

Huang *et al.* (1996) presented a pose determination method using only the straight line projection of the sides of the cylinder, based on the image from a single camera. Being based on a geometric transformation, it can be implemented directly on the cylinder

contour (versus on the images, which is more computational heavy), it runs fast and could be modified to work on a two-cameras system. Consequently, the method of Huang *et al.* (1996) was chosen in the present work to solve the problem of the 3D reconstruction of the cylinder.

As mentioned before, the perspective distortion of a cylinder depends on its position in the camera field of view. Features of the cylinder can only be accurately extracted when its axis is perfectly orthogonal to the camera optical axis. In our experiments, the rotation and falling velocity of the cylinder made it impossible to keep it in that configuration at all times. Additionally, the projected contour of the cylinder only has smooth surfaces, and no angular point can be identified and matched to a physical point of the cylinder. Therefore, we need to find other geometric properties of the cylinder contour that can be easily identified. Huang *et al.* (1996) chose to use the projection of the straight sides of the cylinder as such features. Once the contour points belonging to the cylinder straight sides have been properly identified, it is possible to determine the equation of the two planes containing each the centre of projection of the camera and one of these lines. Then, a new image plane, called the canonical image plane, is created. The cylinder contour points in this new plane correspond to what would have appeared on the original image plane if the cylinder axis had been orthogonal to the camera optical axis. Specific features of cylinder contour in the canonical image plane can be used to determine the position and orientation of the cylinder in the laboratory frame. Once these points have been identified, they are located in the original image plane using the inverse projection transformation to the one used to go from the original image plane to the canonical one. Then, their position the laboratory frame are deduced from the camera calibration. The output from this method is the center of the two flat faces of the cylinder.

The method described in Huang *et al.* (1996) was developed to be used with a single camera. In our experimental set-up, we have two orthogonal cameras. Given the nature of a camera, the method of Huang *et al.* (1996) is very accurate to determine the 2 coordinates corresponding to its image plane, but less so for the third one, corresponding to its depth of field. In the present work, the method of Huang *et al.* (1996) was adapted so that for each frame, a camera was used to give the two coordinates corresponding to its image plane, and the remaining coordinate was given by the other camera. The camera outputting 2 coordinates was chosen to be the one having the best view angle of the cylinder. This adaptation proved to increase significantly the accuracy of the reconstruction method.

Given the vast number of operations involved in the method of Huang *et al.* (1996), it is difficult to estimate quantitatively its accuracy. Huang *et al.* (1996) suggest to use the computed cylinder length, deduced from the coordinates of the two flat faces of the cylinder, and to compare it to the actual cylinder length to have an estimation of the accuracy. All the data we provide in this work have an associated mean relative error of 4.5% for the length, with a maximum error of 10% and a RMS value of 4%. When the error was greater than 10%, the data was discarded. This occurred in 22 out of 248 runs.

Acknowledgments

The authors are grateful to S. Cazin, G. Ehses and R. Soeparno for the technical support provided for the experiments. They also gratefully acknowledge financial support by IFP Energies Nouvelles, Solaize, France and warmly thank D. Ferré and R. Brahem (from department R1240S), C.P. da Fonte and L. Gamet (R1510S), as well as J.L. Pierson (R04) for their interest in the problem.

REFERENCES

Andersen, A., Pesavento, U. & Wang, Z.J. 2005*a* Analysis of transitions between fluttering, tumbling and steady descent of falling cards. *J. Fluid. Mech.* **541**, 91–104.

Andersen, A., Pesavento, U. & Wang, Z.J. 2005*b* Unsteady aerodynamics of fluttering and tumbling plates. *J. Fluid. Mech.* **541**, 65–90.

Auguste, F. & Magnaudet, J. 2018 Path oscillations and enhanced drag of light rising spheres. *J. Fluid Mech.* **841**, 228–266.

Auguste, F., Magnaudet, J. & Fabre, D. 2013 Falling styles of disks. *J. Fluid Mech.* **719**, 388–405.

Belmonte, A., Eisenberg, H. & Moses, E. 1998 From flutter to tumble: inertial drag and Froude similarity in falling paper. *Phys. Rev. Lett.* **81** (2), 345.

Chow, A.C. & Adams, E.E. 2011 Prediction of drag coefficient and secondary motion of free-falling rigid cylindrical particles with and without curvature at moderate Reynolds number. *J. Hydraul. Eng.* **137** (11), 1406–1414.

Chrust, M., Bouchet, G. & Dušek, J. 2013 Numerical simulation of the dynamics of freely falling discs. *Phys. Fluids* **25**, 044102.

Dauchy, C., Dušek, J. & Fraunié, P. 1997 Primary and secondary instabilities in the wake of a cylinder with free ends. *J. Fluid Mech.* **332**, 295–339.

Doignon, C. & de Mathelin, M. 2007 A degenerate conic-based method for a direct fitting and 3-D pose of cylinders with a single perspective view. In *IEEE Int. Conf. Robot.*, pp. 4220–4225.

Ern, P., Risso, F., Fabre, D. & Magnaudet, J. 2012 Wake-induced oscillatory paths of bodies freely rising or falling in fluids. *Annu. Rev. Fluid Mech.* **44**, 97–121.

Fernandes, P.C., Ern, P., Risso, F. & Magnaudet, J. 2008 Dynamics of axisymmetric bodies rising along a zigzag path. *J. Fluid Mech.* **606**, 209–223.

Fernandes, P.C., Risso, F., Ern, P. & Magnaudet, J. 2007 Oscillatory motion and wake instability of freely rising axisymmetric bodies. *J. Fluid Mech.* **573**, 479–502.

Gioria, R.S., Meneghini, J.R., Aranha, J.A.P., Barbeiro, I.C. & Carmo, B.S. 2011 Effect of the domain spanwise periodic length on the flow around a circular cylinder. *J. Fluids Struct.* **27** (5), 792–797.

Horowitz, M. & Williamson, C. H. K. 2006 Dynamics of a rising and falling cylinder. *J. Fluids Struct.* **22**, 837–843.

Horowitz, M. & Williamson, C. H. K. 2010 Vortex-induced vibration of a rising and falling cylinder. *J. Fluid Mech.* **662**, 352–383.

Huang, J.B., Chen, Z. & Chia, T.L. 1996 Pose determination of a cylinder using reprojection transformation. *Pattern Recogn. Lett.* **17** (10), 1089–1099.

Inoue, O. & Sakuragi, A. 2008 Vortex shedding from a circular cylinder of finite length at low Reynolds numbers. *Phys. Fluids* **20** (3), 033601.

Jayaweera, K.O.L.F. & Mason, B.J. 1965 The behaviour of freely falling cylinders and cones in a viscous fluid. *J. Fluid Mech.* **22** (4), 709–720.

Lamb, H. 1993 *Hydrodynamics*. Cambridge University Press.

Marchildon, E.K., Clamen, A. & Gauvin, W.H. 1964 Drag and oscillatory motion of freely falling cylindrical particles. *Can. J. Chem. Eng.* **42** (4), 178–182.

Mathai, V., Zhu, X., Sun, C. & Lohse, D. 2017 Mass and moment of inertia govern the transition in the dynamics and wakes of freely rising and falling cylinders. *Phys. Rev. Lett.* **119**, 054501.

Namkoong, K., Yoo, J.Y. & Choi, H.G. 2008 Numerical analysis of two-dimensional motion of a freely falling circular cylinder in an infinite fluid. *J. Fluid Mech.* **604**, 33–54.

Navab, N. & Appel, M. 2006 Canonical representation and multi-view geometry of cylinders. *Int. J. Comput. Vision* **70** (2), 133–149.

Provansal, M., Schouveiler, L. & Leweke, T. 2004 From the double vortex street behind a cylinder to the wake of a sphere. *Eur. J. Mech. B/Fluids* **23**, 65.

Qu, L., Norberg, C., Davidson, L., Peng, S.-H. & Wang, F. 2013 Quantitative numerical analysis of flow past a circular cylinder at Reynolds number between 50 and 200. *J. Fluids Struct.* **39**, 347–370.

Chapter 3

Reconstruction of the cylinder based on its projected contours

In the reference above, we present an experimental investigation of the motion of a cylinder freely falling in a fluid otherwise at rest. One of the main technical challenge of this study was to properly acquire the 3D position and orientation (also called pose) of the cylinder. Indeed, because of the body anisotropy, the projected contour of the object on the cameras is heavily distorted by perspective. This distortion depends on the position of the cylinder in the camera field of view, and on its orientation. Whilst we have briefly described the image processing techniques we used in the reference above (see 2.8), we provide here a more thorough explanation of the technical challenge to overcome, and of the different steps of our algorithm.

3.1 Calibration

The coordinates resulting from the raw outputs of the cameras are expressed in pixels. It is necessary to find the link between these coordinates taken in the camera frames, and coordinates in the laboratory frame expressed in international units. It exists, for each camera, a relationship between the apparent size of an object in the camera frame, and the actual size of it, depending on the distance between the object and the camera. This relationship is linear.

Despite both cameras sharing the same characteristics and manufacturer, calibration needs to be performed on each one of them independently. In order to determine these two relationships, an object of controlled dimensions is filmed by both cameras in different positions inside the tank, each time at a known distance from the cameras. The volume explored with this body needs to encompass the volume in which measurements will be carried out, as can be seen on figure 3.1a.

The simple fit of a degree 1 polynomial on the data points gives us, for each camera, the relationship between the size of the object in pixels in the image plane and the distance form the camera in the form :

$$\gamma = \gamma_0 + \beta x \tag{3.1}$$

where x is the distance between the object and the camera in cm, γ is the scaling factor in cm/px^{-1}, and $\gamma_0 = \gamma(x = 0)$.

This law links the size of an object in pixels in the image plane to its actual size in the laboratory frame. Therefore, knowing the actual size of the cylinder, and crossing the information given by the 2 cameras, it should be possible to find out the position of the cylinder in the laboratory frame.

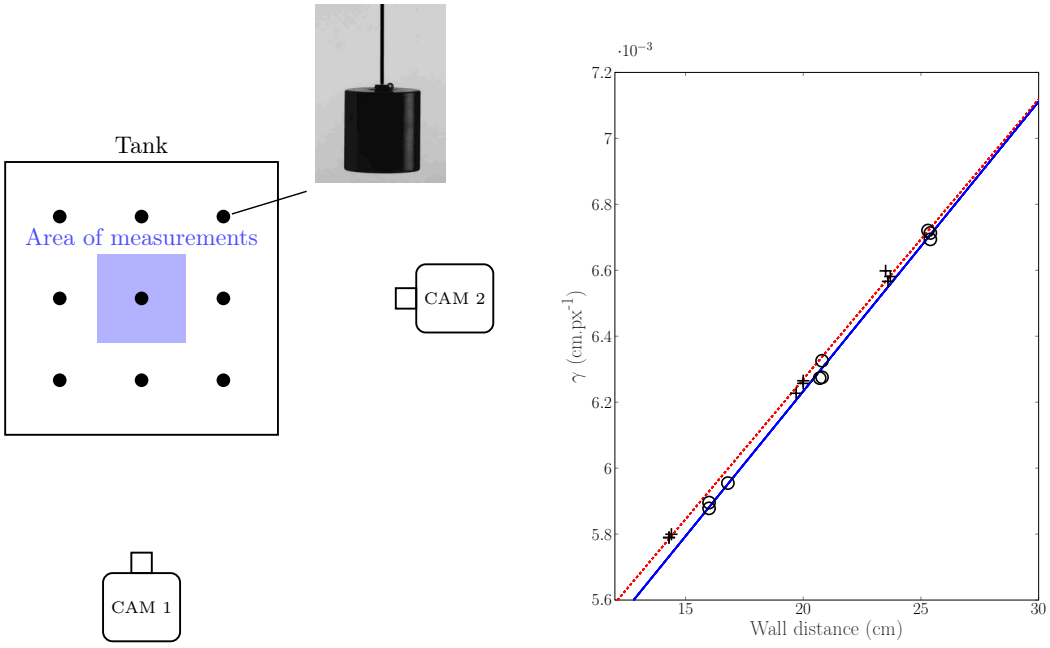

(a) (b)

Figure 3.1 – (a) Top view of the tank during the calibration process. Black dots inside the tank represent the positions in which the calibration object was placed. (b) Calibration law for both cameras, black crosses (+), respectively circles (◯) show the measured points for CAM1, respectively CAM2, and the dashed line, respectively plain line, show the fitted law for CAM1, respectively CAM2.

The 2 calibrations laws for the 2 different cameras can be written :

$$\gamma_1 = 4.57.10^3 + 8.49.10^{-5}x \tag{3.2}$$
$$\gamma_2 = 4.48.10^3 + 8.79.10^{-5}x \tag{3.3}$$

Each cameras has its own set of coordinates (x_1, y_1), and (x_2, y_2), as can be seen on figure 3.2. It is obtained after translation and rotation of the image frame whose origin is located in the top left corner of the frame (frame (R_0) in fig. 3.2). Coordinates (x_1, y_1), and (x_2, y_2) are expressed in pixels in their respective image plane. The laboratory frame is defined arbitrarily as an orthonormal (X, Y, Z) frame (frame (R_{lab}) in fig. 3.2), whose origin is situated on a known point of the physical space, denoted K, and whose axis are defined as seen in figure 1 of the reference above. The camera labeled as CAM1 will output coordinates Y and a first value of Z, noted $Z1$, while the one labelled as CAM2 will output X and another measurement of Z.

Using both cameras, it is possible to transform both set of pixel coordinates into coordinates in the laboratory frame. Several steps are needed in order to achieve a correct transformation.

The pose of the camera, i.e. its 3D position and orientation, is obviously crucial in this approach. The distance between the cameras and the tank has been measured, as well as their orientation in the laboratory frame. Images of a plumb line were also recorded by both cameras, giving us the means to check their orientation with respect to the vertical.

We need to ensure that the origin of the two image planes corresponds to a single point in the laboratory frame. During the calibration process described in 3.1a, an object of known dimensions was filmed at different locations inside the tank. An identifiable point

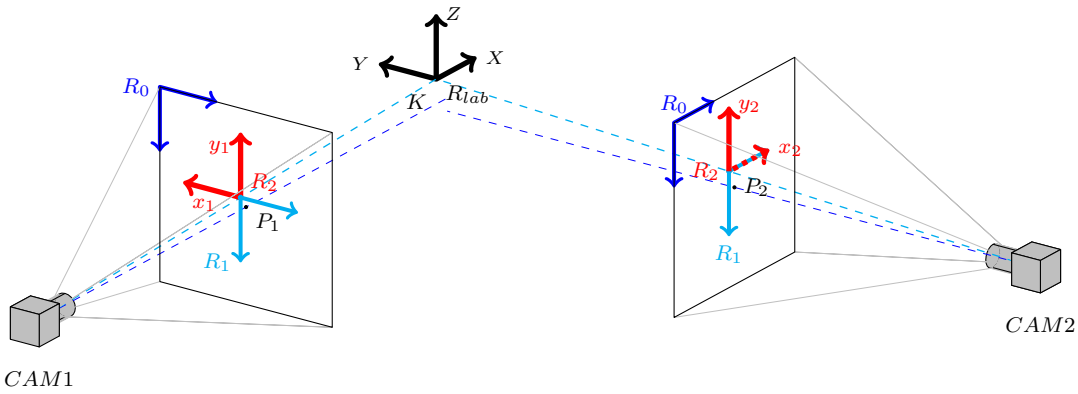

Figure 3.2 – Schematic views of the two cameras system, along with the different transformations applied to the image coordinates. Points P_1 and P_2 belong to the axis of cameras 1 and 2. The original frame is R_0, whose origin is the top left corner of the images. The origin of the frame is then translated so that both camera systems have their origin on a common point of the physical space K (frame R_1). Then, the pixel coordinates are rotated when needed, in order to create an orthonormal frame with both cameras frames (R_2), corresponding to R_{lab} in the physical space. The origin of frames (R_2) and (R_1) are the images of K in both image planes.

of this object, here the intersection point between the wire and the cylinder, will be used as an origin for both image frames.

MATLAB®is able to output the coordinate of the barycentre of the projected contours of the cylinder. It should be noted that the barycentre of the projected contour may differ from the barycentre of the 3D cylinder , depending on the position of the cylinder in the image frame. More details will come on this part in the following. This rough measure will be used to have a first estimate of the distance between the cylinder and each of the cameras. Using both (3.2) and (3.3), we need to have the coordinates $(X, Y, Z1, Z2)$ satisfying the relationship :

$$\frac{\text{actual size of the object}}{\text{apparent size of the object}} = \gamma_{0,1} + \alpha_1 X$$
$$\frac{\text{actual size of the object}}{\text{apparent size of the object}} = \gamma_{0,2} + \alpha_2 Y$$

An iterative procedure is used. A first estimation of the distances (X, Y) is performed, using $\gamma_{0,1}$ and $\gamma_{0,2}$ as the scaling factors.

$$Y_0 = \gamma_{0,1} x_1$$
$$Z1_0 = \gamma_{0,1} y_1$$
$$X_0 = \gamma_{0,2} x_2$$
$$Z2_0 = \gamma_{0,2} y_2$$

Once (X_0, Y_0) is found, the following iterations are :

$$
\begin{aligned}
Y_{i+1} &= x_1(\gamma_{0,1} + \alpha_1 X_i) \\
Z1_{i+1} &= y_1(\gamma_{0,1} + \alpha_1 X_i) \\
X_{i+1} &= x_2(\gamma_{0,2} + \alpha_2 Y_i) \\
Z2_{i+1} &= y_2(\gamma_{0,2} + \alpha_2 Y_i)
\end{aligned}
$$

The value of (X, Y) found in each iteration is used for the subsequent one, until the difference between (X_i, Y_i) and (X_{i+1}, Y_{i+1}) is low enough (an arbitrary threshold of $1.10^{-5}cm$ is used). There may be differences between $Z1$ and $Z2$, depending on the position of the object in the image frame of both cameras due to the perspective deformation of the cylinder contour, and to the translation of the origins of (R_1) and (R_2). another way of managing this problem will be addressed in 3.2.1. In a first approximation, a coordinate Z, calculated using the average of $Z1$ and $Z2$, is used. The reader must keep in mind that the values $(x1, z1)$ and $(x2, z2)$ used in this procedure are the pixel coordinates of the apparent barycentre of the cylinder contour, which, due to perspective, is not the actual barycentre of the physical object. Hence the coordinates (X, Y, Z) found in the laboratory frame are mere estimations of the 3D positions of the object. This estimation will be necessary in the following procedure, but cannot be easily linked to the precise pose of the cylinder. A more complex method needs to be used, and will be described in detail in section 3.2.

3.2 Image processing : pose determination

The introduction of the effect of perspective on the cylinder contour is explained in detail in the Appendix A of Toupoint et al. (2018). In this seciton, we focus on the technical implementation of the algorithm by Huang et al. [21], which was used in our work to determine the cylinder position and orientation in the laboratory frame.

3.2.1 Reprojection transformation

Figure 3.3 presents a schematic view of the contour of a cylinder of arbitrary orientation, as it can be seen by a camera. Our aim is to recover the position in the laboratory frame of points S and T , center of the two flat faces of the cylinder, as they will allow the 3D reconstruction of a cylinder of known diameter. However, we can see on fig. 3.3 that these points are not directly visible, and that we have no means of knowing their position. Points I and J, however, can be detected using the apparent axis of the cylinder, but cannot be matched with specific points of the 3D cylinder. They will be used as intermediaries to determine the position of points S and T. The reconstruction will aim at matching points I and J with specific points of the cylinder, and to use them to recover the position of S and T in the laboratory frame. This is performed using Huang et al. [21] geometric transformation, which creates a new frame in which points I and J are easily matchable with points of the cylinder. In order to obtain this new view of the cylinder, called the canonical view, distinctive features of the cylinder, i.e. the projections of its straight sides, will need to be extracted from the cylinder projection in the original image plane in order to determine the rotation to be applied to go from the image plane of the camera tot the canonical plane.

Figure 3.4a shows the perspective projection of a cylinder, with fig. 3.4b showing a detailed top view. Figure 3.4b also presents the top views of the image plane (on camera) and of the canonical image plane, as well as points P and Q, tops views of $P1$ and $Q1$

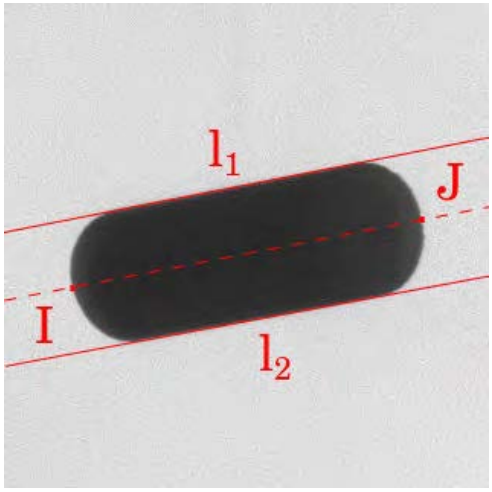

Figure 3.3 – Projected contour, as can be seen by a camera, of a cylinder. Lines l_1 and l_2 are the projection of the straight sides of the cylinder, which need to be detected properly. Points I and J and the two visible points of the end of the cylinder. The reconstruction method will be needed in order to match them uniquely with points of the physical cylinder.

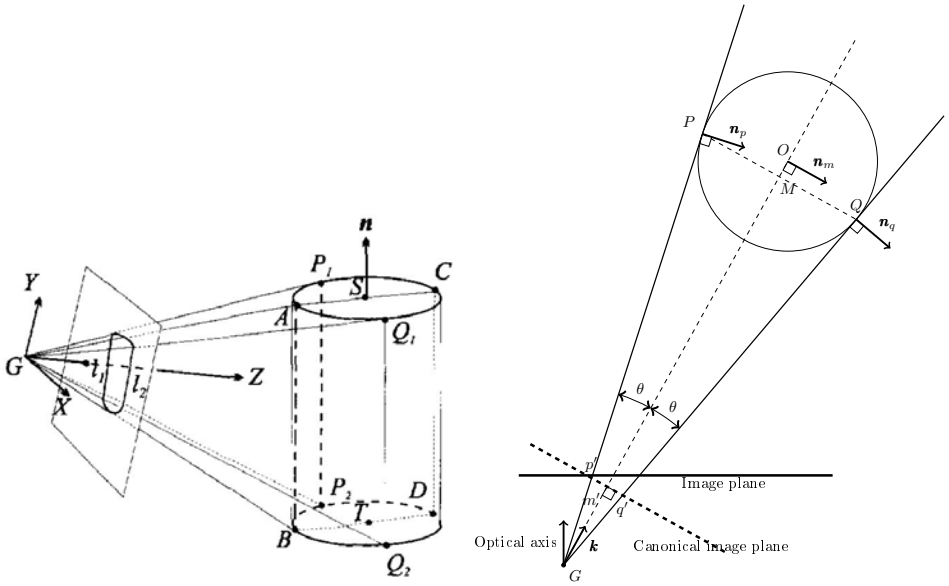

(a) (b)

Figure 3.4 – Top view of a cylinder projection, as can be seen in [21]

in fig. 3.4a. The various steps needed for pose determination are the following (using the notations of fig. 3.4) :

- find the equations of lines $P1P2$ and $Q1Q2$ in the image coordinate system
- find the equation of planes $GP1P2$ and $GQ1Q2$ in the laboratory coordinate system
- using these equations, find $\boldsymbol{n}_p$ and $\boldsymbol{n}_q$, normals to $GP1P2$ and $GQ1Q2$ respectively
- using $\boldsymbol{n}_p$ and $\boldsymbol{n}_q$, find $\boldsymbol{n}_m$, normal to the plane GST and $\boldsymbol{n}$, directed along the cylinder axis
- from the knowledge of these normals, build $\boldsymbol{k}$, pointing from G to the cylinder axis, which is effectively a rotated optical axis
- using $\boldsymbol{k}$ to build an orthonormal basis (i, j, k), canonical basis in which points I and J (fig. 3.3) can be matched to points of the 3D cylinder

We can see that the visible straight lines of the cylinder contour, noted l_1 and l_2, correspond to the straight sides of the cylinder, and to lines P_1P_2 and Q_1Q_2 on fig. 3.4a. However, it must be noted, as showed on fig. 3.4b, that points P and Q are not diametrically opposed. As a result, the apparent diameter observed on the image plane cannot be simply deduced from the cylinder diameter using the scaling law defined in (3.1). From now on, x and y will be the horizontal, respectively vertical coordinates in the image plane, and X, Y and Z will be the coordinates in the camera frame, with Z aligned with the camera axis and X and Y parallel to x and y.

We will use straight lines l_1 and l_2, which are a characteristic feature of the cylinder projection, to perform the 3D reconstruction. Consequently, our first goal will be to find the equation of these lines in the image plane, in the form $ax+by+c = 0$, where a, b, c will need to be determined. MATLAB®, is capable of providing a list of pixel positions corresponding to the cylinder contour. It is also capable, thanks to an ellipse fitting algorithm already implemented, to return the orientation of this contour. However, it is not easy to determine which contour pixels belong to l_1 and l_2. A short preliminary procedure was thus adopted to facilitate their identification. MATLAB® is able to return the orientation of the contour, thanks to an ellipse fitting algorithm. Applying a rotation matrix, of said orientation, to the points of the cylinder contour therefore gives an horizontal contour, with lines l_1 and l_2 being horizontal as well.

The effects of the rotation matrix can be observed on figure 3.5. With this representation, the points belonging to the lines l_1 and l_2 are easily identified : they are located at the top and the bottom of the contour . A degree 1 polynomial is fitted to these points in the image plane, and the equation of lines l_1 and l_2 is known. Let (a_1, b_1, c_1) be the coefficients for lines l_1, projection of GP_1P_2 in the image plane, and (a_2, b_2, c_2) the coefficient of l_2, projection of GQ_1Q_2. These coefficients can now be used to determine the equations of planes GP_1P_2 and GQ_1Q_2, found in fig. 3.4a. In the viewing coordinate system, the image plane is at a distance $Z = f$ from G, where f is the effective focal length of the camera, known after calibration. Therefore, the equations of GP_1P_2 and GQ_1Q_2 are :

$$a_1X + b_1Y + \frac{c_1}{f}Z = 0 \tag{3.4}$$

$$a_2X + b_2Y + \frac{c_2}{f}Z = 0 \tag{3.5}$$

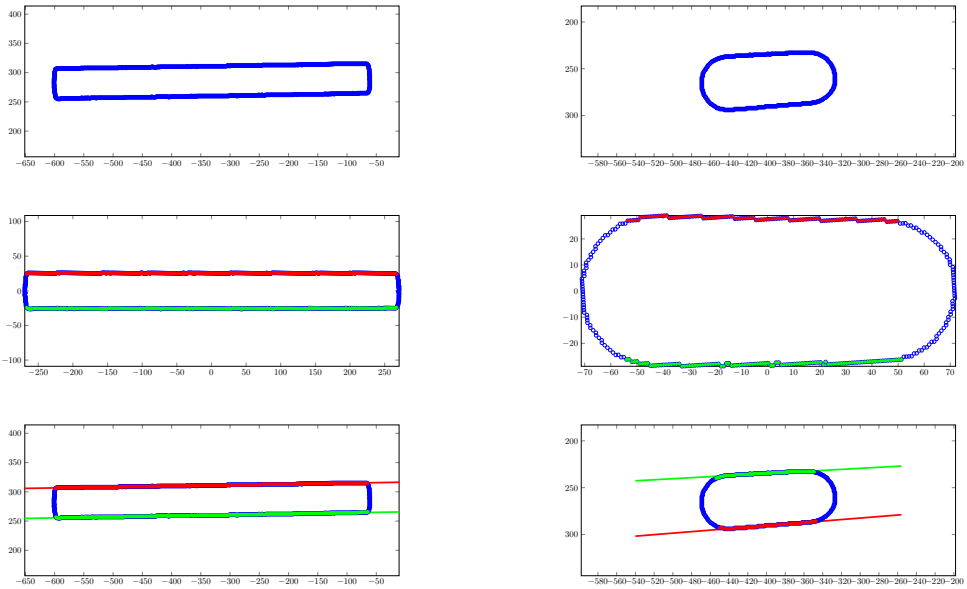

Figure 3.5 – Rotated contour of the cylinder. The two figures on the first row show the projected contour as seen by the two cameras. The middle row shows how rotating the contours allows the easy detection of the straight lines, and the two bottom pictures show the fitted line in the original contour.

We can now deduce the equation of $\boldsymbol{n}_p$ and $\boldsymbol{n}_q$, normals to GP_1P_2 and GQ_1Q_2 respectively. The vector $\boldsymbol{n}$, directed along the cylinder axis as can be seen on fig. 3.4a, and $\boldsymbol{n}_m$, normal to the plane GST, can then be easily deduced :

$$\boldsymbol{n} = \boldsymbol{n}_p \times \boldsymbol{n}_q \tag{3.6}$$

$$\boldsymbol{n}_m = \boldsymbol{n}_p + \boldsymbol{n}_q \tag{3.7}$$

Vector $\boldsymbol{k}$, pointing towards the center of the cylinder from the camera, G, can be written :

$$\boldsymbol{k} = \frac{\boldsymbol{n}_m \times \boldsymbol{n}}{||\boldsymbol{n}_m \times \boldsymbol{n}||} \tag{3.8}$$

The canonical image of the cylinder can now be constructed. The goal of this image is to obtain the cylinder contour, as if it had been aligned with the camera optical axis. Therefore, a new coordinate system (X', Y', Z') is constructed, in which Z' is aligned with the vector $\boldsymbol{k}$, Y' is still vertical, and X' is orthogonal to plane GST Let $\boldsymbol{i}$, $\boldsymbol{j}$, and $\boldsymbol{k}$ be the units vector in the directions X',Y',and Z', expressed in the original viewing coordinates. A new canonical image plane, visible in 3.4b, is then created, with coordinates (x', y').

This new plane created is obtained by a simple rotation :

$$(X', Y', Z') = \boldsymbol{R}(X, Y, Z) \tag{3.9}$$

with

$$\boldsymbol{R} = (\boldsymbol{i}|\boldsymbol{j}|\boldsymbol{k})^T$$

The pixel coordinates (x', y') in the canonical image plane can then be deduced from their laboratory frame counterparts, (X', Y', Z') by the following relationships :

$$x' = X' \frac{f}{Z'}$$
$$y' = Y' \frac{f}{Z'}$$

or

$$x' = f \frac{(x, y, f)^T \boldsymbol{i}}{(x, y, f)^T \boldsymbol{k}} \tag{3.10}$$
$$y' = f \frac{(x, y, f)^T \boldsymbol{j}}{(x, y, f)^T \boldsymbol{k}} \tag{3.11}$$

These reprojected contour points form the canonical image of the cylinder (see fig 3.6a). In this plane, the y' axis is also a symmetrical axis of the canonical cylinder contour. The points of interest I and J in the 3D reconstruction of the cylinder are easily determined in this view.

As can be seen on Figure 3.6b, on the canonical image of a cylinder, 2 points can be seen on the intersection between the cylinder contour and the y' axis. These 2 points are the transforms of points I and J from the original image plane to the canonical plane. The properties of the canonical image will now allow us to match them with specific points of the 3D cylinder. In the configuration described in fig. 3.6b, these 2 points are A and B, but other cases can appear. Indeed, if the whole cylinder is situated above the camera center i.e. if $y_b = y_d > 0$, then the 2 points observed would be A and D. Similarly, if the cylinder is situated below the camera center, i.e. $y_a = y_c < 0$, then the 2 visible points would be C and B.

Using the coordinates of these points, we can easily find the coordinates of S and T, center of the two circular faces of the cylinder. The radius of the cylinder, which needs to be known, is expressed in pixels thanks to (3.1) and called R_c. We can then see on fig. 3.4b that $|\boldsymbol{PM}| = R_c cos\theta$, with $\theta = atan(|\boldsymbol{p'm'}|/f)$ calculated thanks to the measure of $\boldsymbol{p}'m'$ on the canonical image (fig 3.6a). Then, using the similarity between triangles GPM and $Gp'm'$, $|PM|/|p'm'| = |GM|/f$, vector $\overrightarrow{GM}$ can be calculated :

$$\overrightarrow{GM} = (0, 0, f|PM|/|p'm'|) \tag{3.12}$$

From that relationship, the expression of $\overrightarrow{MN}$ and $\overrightarrow{MW}$ (fig. 3.6b) are deduced :

$$\overrightarrow{MN} = (0, 0, R_c(1 - sin\theta)) \tag{3.13}$$
$$\overrightarrow{MW} = (0, 0, R_c(1 + cos\theta)) \tag{3.14}$$

The same similarity technique is used to calculate $\overrightarrow{NA}$, $\overrightarrow{NB}$, $\overrightarrow{WC}$ and $\overrightarrow{WD}$:

$$\overrightarrow{NA} = (0, \pm|GN||m'a'|/f, 0)$$
$$\overrightarrow{NB} = (0, \pm|GN||m'b'|/f, 0)$$
$$\overrightarrow{WC} = (0, \pm|GW||m'c'|/f, 0)$$
$$\overrightarrow{WD} = (0, \pm|GW||m'd'|/f, 0)$$

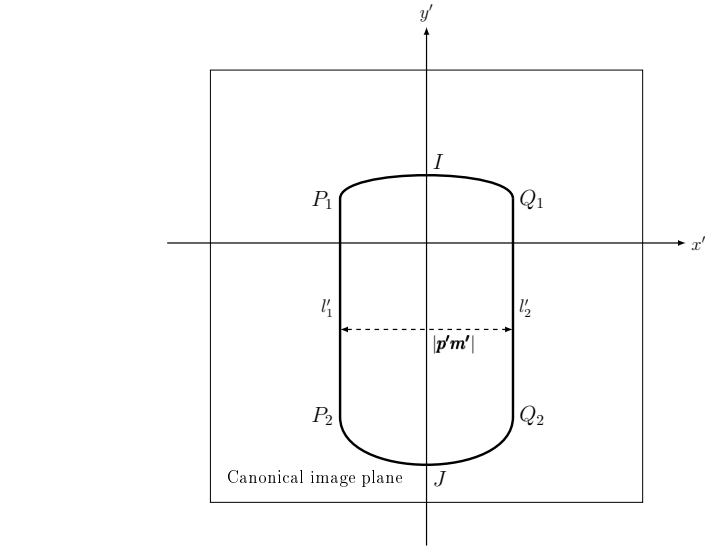

(a)

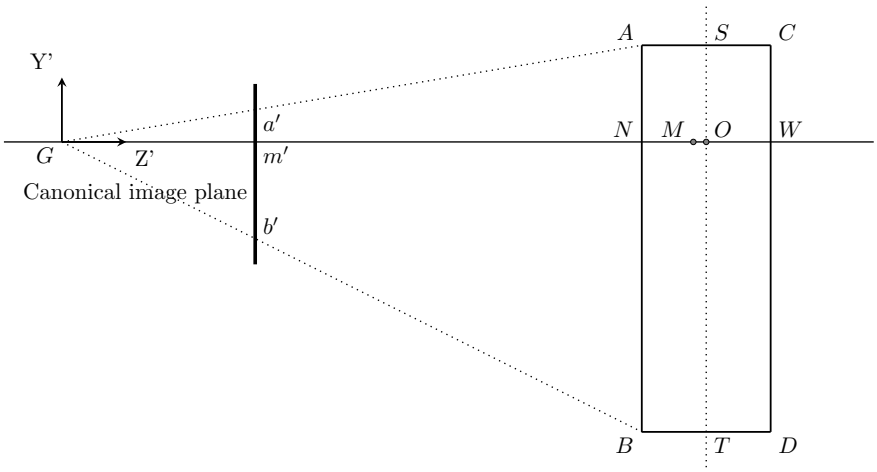

(b)

Figure 3.6 – (a) Canonical view of the cylinder, in the canonical image plane. (b) Side view of the canonical image of a cylinder.

The sign of the Y' coordinate of $\overrightarrow{NA}$, $\overrightarrow{NB}$, $\overrightarrow{WC}$ and $\overrightarrow{WD}$ depends on the sign of the y' coordinate in the canonical image. Then, we need the vectors $\overrightarrow{GA}$, $\overrightarrow{GB}|$, $\overrightarrow{GC}$ and $\overrightarrow{GD}$. As stated above, depending on the position of the cylinder contour compared to the camera axis in the canonical image, only two of these vectors will actually be used :

$$\begin{aligned}
\overrightarrow{GA} &= \overrightarrow{GM} + \overrightarrow{MN} + \overrightarrow{NA} \\
\overrightarrow{GB} &= \overrightarrow{GM} + \overrightarrow{MN} + \overrightarrow{NB} \\
\overrightarrow{GC} &= \overrightarrow{GM} + \overrightarrow{MW} + \overrightarrow{WC} \\
\overrightarrow{GD} &= \overrightarrow{GM} + \overrightarrow{MW} + \overrightarrow{WD}
\end{aligned}$$

And now, to calculate the position of points S and T :

$$\overrightarrow{GS} = \overrightarrow{GA} + (0, 0, R_c) \tag{3.15}$$
$$\overrightarrow{GS} = \overrightarrow{GC} - (0, 0, R_c) \tag{3.16}$$
$$\overrightarrow{GT} = \overrightarrow{GB} + (0, 0, R_c) \tag{3.17}$$
$$\overrightarrow{GT} = \overrightarrow{GD} - (0, 0, R_c) \tag{3.18}$$

Now, the only remaining step is to express these vectors in the original coordinate system, i.e. (X, Y, Z) instead of (X', Y', Z'). This is easily achievable using the rotation matrix $\boldsymbol{R}$ defined in (3.10) :

$$\overrightarrow{GS}^* = \boldsymbol{R}^T \overrightarrow{GS} \tag{3.19}$$
$$\overrightarrow{GT}^* = \boldsymbol{R}^T \overrightarrow{GT} \tag{3.20}$$

With the coordinates of S and T in the original camera frame, and knowing the diameter of the cylinder, a full 3D reconstruction of the cylinder is now easy. Moreover, to check the accuracy of the reconstruction, the computed length of the cylinder, $H = |\overrightarrow{GT} - \overrightarrow{GS}|$ can be compared with its actual length, which is also known. This gives an efficient way of measuring the error induced by the reconstruction. In most cases, the difference between the measured length and the computed one was below 10%. For a difference greater than 10%, the data was rejected.

In our work, this method was fully implemented using MATLAB®. It was, however, necessary to alter it slightly, in order to better suit our needs. These changes will be described in the following sections.

3.2.2 Complementary development

The method developed by Huang et al. [21] allows the accurate reconstruction of a cylinder in 3D using a single image from a single camera. Yet, we need to process two image sequences, coming from 2 cameras with different poses. Hence, the method developed by Huang et al. [21] needs to be adjusted to be made consistent along a time sequence, and to benefits from having 2 cameras instead of a single one.

A camera generate images in a plane, meaning that it measures two coordinates. In the method developed by Huang et al. [21], a 3 dimensional pose estimation is produced out of the image coming from a single camera. Out of the 3 coordinates, two are directly

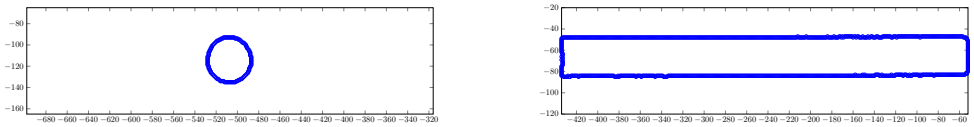

Figure 3.7 – Detected contour of a cylinder, as viewed by the two different cameras. In this case, the left image is the contour seen by Camera 1, whose optical axis is nearly aligned with the cylinder axis, and the right image is the contour seen by Camera 2 whose optical axis is nearly orthogonal to the cylinder axis.

in the image plane, while the other one has to be deduced from the effective focal length. This third coordinate is not as accurate as the other two, because it is dependent on a correct calibration of the camera, and does not come directly from the image plane. Indeed, when the method is applied to an image sequence coming from a single camera, a lot of noise is present on the time evolution of the coordinate corresponding to the depth of the camera. This is by no mean surprising, considering that a camera has no way of measuring distances along its depth. We have seen before that an approximate value of the 3D position of the cylinder could be computed using the method described in 3.1, but without taking into account inaccuracies caused by the perspective projection (see Appendix A of Toupoint et al. (2018)). Thus, applying the method of Huang et al. [21] to compute the two coordinates of the image plane, and using the value computed from 3.1 to compute the remaining coordinate is not satisfactory. New developments in the reprojection transformation method need to be implemented.

The reprojection transformation is applied to each image of the time sequence. We have seen that a single camera can output two coordinates with great precision, but is lacking accuracy with the other one. Indeed, CAM1 is accurate along Y and Z, while CAM2 is along X and Z (see figure 1 of Toupoint et al. (2018)). The orientation of the cylinder can also cause issues with the detection of the straight sides of the cylinder. Indeed, when the cylinder axis is nearly aligned with the camera axis, the projected contour is similar to an ellipse. In this case, straight lines are difficult to identify properly, as can be seen on fig. 3.7. Fortunately, the two cameras used in our set-up are orthogonal, meaning that if the optical axis of one of them is aligned with the cylinder axis, then the optical axis of the other one will be nearly orthogonal to the cylinder axis, creating optimal conditions for detecting straight lines.

In such conditions, for each couple of images, we decided to select the most appropriate one. As the two cameras are roughly equidistant to the cylinder, this means selecting the camera in which the cylinder contour has the more points. This camera will be tagged *Main camera*, and will output the two coordinates corresponding to its image plane, i.e. X and Z for CAM2, or Y and Z for CAM1. The other one, tagged *Other camera*, will output the remaining coordinate, corresponding to the depth of the *Main camera*. When combining the informations of the two cameras, the accuracy of the reconstruction is greater than what it achievable using one camera alone. Moreover, it allows much better 3D placement.

Another problem emerging while using Huang et al's method with image series, instead of single images only, is the consistency throughout the sequence. The routine outputs the 3D position of points S and T, center of the circular faces of the cylinder. Yet, nothing ensures the consistency in the choice of S and T across several images. Even if the reconstruction is accurate, problems can occur when S and T switch places during the sequence. Therefore, we must force the routine to always choose the same location for S and T. Inversion problems typically occur when the apparent angle, measured by MATLAB®, and used in the line detection, as described in 3.2.1 brutally switches sign, or

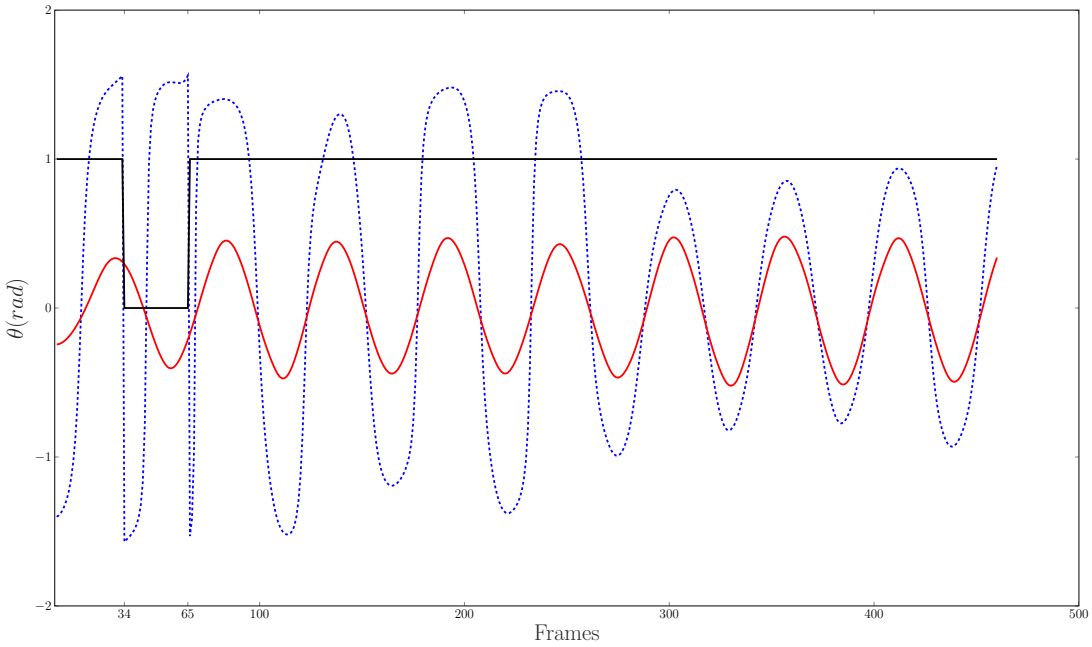

Figure 3.8 – Apparent angle measured by the 2 cameras. The angle θ_1 measured by Camera 1 is plotted in blue, and θ_2 by Camera 2 in red. The dashed lines correspond to indices when the Camera is set as *Other camera*. The black line shows the state of Camera 1, with *true* being 1, and *false*, 0.

when the *Main camera* switches from camera 1 to camera 2. The indices of the inversions must be identified, and dealt with.

Indeed, the apparent angles as measured by MATLAB®are set between $-\pi/2$ and $\pi/2$. When it gets close to either of these limits, it can change sign suddenly. As explained in detail in 3.2.1, this apparent angle is used to rotate the points of the cylinder contour so that it is horizontal, which in turn allows for the detection of the points belonging to the projections of the straight sides of the cylinder. A sign change in the apparent angle means that the contour will be rotated horizontally, but also flipped upside down. Therefore, the lines l_1 and l_2 will be interchanged, and so will the position of points S and T.

This issue becomes even trickier when combining two cameras. We must ensure that the apparent angle measured by the two cameras has the same sign. This issue is especially relevant regarding the Z coordinate, which can be computed from different cameras, depending on the situation. Switching the *Main camera* if the 2 cameras do not measure the same apparent angle effectively means creating an error on the Z coordinate.

Figure 3.8 showcases an example of a run that is relatively easy to process. The *Main camera* is CAM2 for the entire run. In the beginning, θ_1 and θ_2 are in phase, so the state of Camera 1 is set to true. A sudden change of sign is detected at frame 34, and another at frame 65. Indeed, between frames 34 and 65, θ_1 and θ_2 are out of phase. consequently, the state of other other camera, i.e. CAM1, is set to false on this interval, meaning that the coordinates of points S and T, computed by CAM1 will need to be inverted. In some cases, the inversion procedure can be more complex, as sudden sign changes of the apparent angle can be much more frequent, and the *Main camera* can change during the run.

In the example of fig. 3.8, the main in the first images is Camera 2, which will be set to *true* for all the sequence. As there is no discontinuity in θ_2, it remains *true*, meaning that the horizontal coordinate given by Camera 2, X, will never have to be switched. Camera

1 starts as the *Other camera*, but θ_1 and θ_2 are in phase in the beginning, meaning that the starting state of Camera 1 is *true* as well. However, θ_1 displays a discontinuity. The state of the camera is switched at each discontinuity. Once it has been properly computed, the coordinates to be switched can be determined. If the state of Camera 1 is *false*, and Camera 1 is the *Main camera*, then Y and Z are switched. If Camera 1 is*false*, and Camera 1 is the other camera, then only Y is switched.

The routine can accurately apply this procedure to every case with minimal failure. In some rare cases, a discontinuity in the apparent angle is not properly detected automatically, and needs a user intervention to be addressed.

Part II

Free fall of a cylinder in a confined fluid at rest

Chapter 4

Free fall of a cylinder in a confined fluid at rest

4.1 Introduction

In the second part of the thesis, we study the free fall of a cylinder in a confined medium. The goal of this investigation is to serve as a comparison basis for the study of a cylinder falling through a confined bubble swarm (see part III). In addition, an analysis of the motion of the cylinder in a confined environment can give insight on how interaction with multiple other bodies modify the behaviour of a single catalyst particle, in the industrial problem studied by IFPEN. Hence, results from the fall of a cylinder in a confined fluid at rest can also be compared to that of the fall of a cylinder in an unconfined medium. Consequently, we need to build an experimental set-up in which we can study the fall of a cylinder in a confined medium, and compare to results from the two other parts of the thesis. We need to adjust the parameters of the cylinder so that the relevant dimensionless parameters of the problem are similar than in the study in the unconfined medium. Therefore, we select cylinders of elongation ratio $\xi = L/d$ between 3 and 40 (as compared to $2 \leqslant \xi \leqslant 20$ in the unconfined medium). Due to the novel and exploratory nature of our work on the interaction between a falling cylinder and a swarm of rising bubbles, we wish to study a large variety of parameters. In particular, the cylinder density ρ_c will be of particular interest, as it defines not only the density ratio of the cylinder with the fluid, ρ_c/ρ_f, but also that of the cylinder with the gas, ρ_c/ρ_g (with ρ_f density of the liquid and ρ_g density of the gas). For this reason, we will investigate cylinders of three different density, $\rho_c = 1160$ kg.m^{-3}, 2700 kg.m^{-3} and 4500 kg.m^{-3}. The corresponding Archimedes number of these cylinders are thus $60 \leqslant Ar \leqslant 1000$, which matches the range investigated in the unconfined medium ($200 \leqslant Ar \leqslant 1100$).

We thus require a entirely new experimental set-up and image processing algorithm. In this chapter, we give technical details of the experimental set-up. We start by giving a description of the confined cell, details of the building procedure. We discuss the technical challenges that arose during the building of the cell, in particular regarding the gap width. We then describe the cylinders that are going to be released in the cell. Finally, we give details regarding the measurement methods, and the image processing algorithm.

4.2 Experimental device

In order to explore the motion of isolated cylinder falling in a confined fluid at rest, we have built a vertical thin-gap planar cell, filled with a liquid at rest. The cell is 800 mm

in height, 400 mm in width and 1.1 mm in thickness. The cylinder diameter was chosen so that it is very close to the gap width, in order to obtain a 2D motion in the plane of the cell (based on previous observations from D'Angelo et al. [10]). The other dimensions of the cell are large, in order to avoid interaction between the cylinder and the walls of the cell, and to have a sufficient falling height for a complete description of the paths of the cylinders. At the top of the cell, there is a free surface open to the atmosphere. It is also possible to inject bubbles at the bottom of the cell, which will be used in part III to study the interaction between a falling cylinder and a swarm of rising bubbles.

The confined medium allows for an easy visualization of the interaction between a falling cylinder and a swarm of rising bubbles. The building of a confined cell, however, is not trivial, and requires specific care. The width of the gap, in particular, is difficult to control, especially when dealing with small gaps maintained over a large area in (X, Y) plane, such as in the present study (gap width is 1mm, over 800x400mm). In the following, we will detail the building procedure of the confined cell, and provide a general description of the complete experimental setup, and image processing. The same cell is used to study the fall of a cylinder in a bubble swarm and in a fluid at rest. In this section, we will only detail the experimental setup used for the study in the fluid at rest. The additional developments of the setup required in the bubble swarm study will be discussed in 5.2.

4.2.1 Building the confined cell, towards a constant gap

The confined cell was built using 2 borosilicate glass panels of 800 mm in height, 400 mm in width and 13 mm in thickness, encased in an aluminum frame made of two parts, a main frame and a lid, that are screwed together (see figure 4.1c). The cell is horizontal during its building. One of the glass panels is silicone glued to the main aluminum frame. On top of this panel are laid teflon strips of 1 mm of thickness, which control the width of the gap. Then, the second glass panel is laid on top of these strips. The second part of the aluminum frame presses down on the second glass panel as it is screwed on the main frame, which presses the two glass panels on the teflon strips. Once the cell is assembled, it is set vertical and mounted on a supporting frame.

Steel convergent and divergent sections are mounted on top and below the aluminum frame. The top one gives access to the free surface, and allows the release of cylinders in the gap. The bottom one is sealed by an aluminum plate, screwed in place at the bottom of the divergent. The bottom plate can be unscrewed from the divergent to access the inside of the cell, which is needed for cylinder recovery. The plate can be fitted with a series of injectors for creating a bubble swarm in the cell (see 5.2 for additional details on bubble generation).

A schematic top view of the cell is visible in figure 4.1a. The teflon strips are long enough to cover the whole height of the cell. They are located to the sides of the cell (under the aluminum frame, so they are not visible). The aluminum frame presses down the different layers of the cell near the edges of the glass panels, leaving a large area accessible on the front for optical measures.

The gap of the cell is controlled by the teflon strips, of 1 mm in thickness. When the cell is empty, the gap of the cell is exactly 1 mm over the entire area. However, when the cell is filled, the water exerts pressure on the glass panels, causing them to slightly deform and bend towards the outside of the cell. Therefore, the gap is slightly more important in the center of the cell. In order to counterbalance the water pressure, an aluminium reinforcing frame has been added to the cell (visible in figure 4.1), both on the front and back face. A series of nylon screws on this frame are put in contact with the glass panel when the cell is empty. Therefore, when the cell is filled with water, the nylon screws add

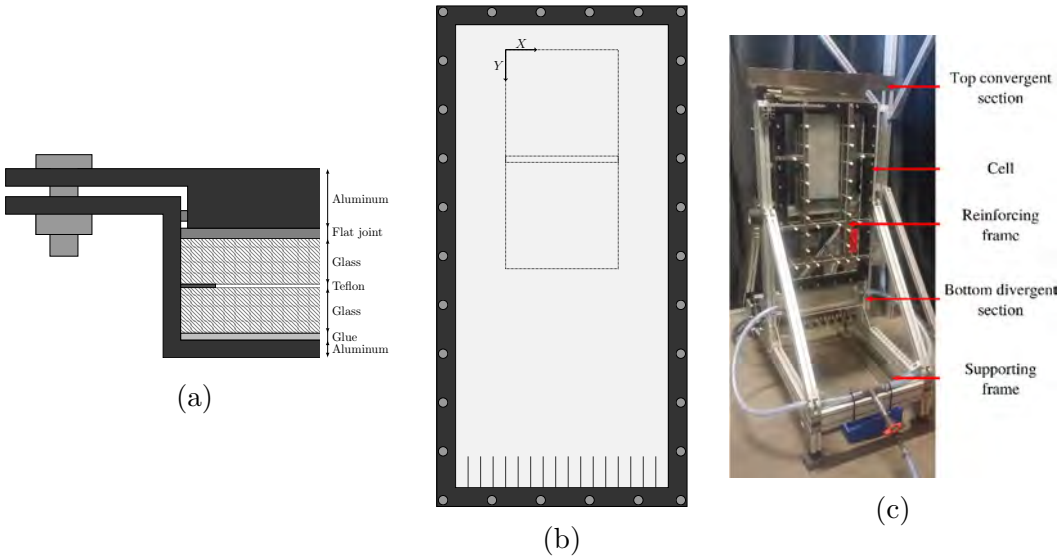

(a) (b) (c)

Figure 4.1 – (a) Schematic Top view of a section of the confined cell, showing the different layers (b) Schematic front view of the cell, with the approximate position of the observation area delimited with dashed lines (c) Photograph of the cell viewed from the front

pressure on the glass, helping contain the glass deformation. In addition to the reinforcing frame, small strips of 3D-printed ABS (of about 5 mm in width and 5 cm in length) were inserted in the bottom of the cell, in-between air injectors, to avoid the bending of the glass panels towards the inside of the cell when the aluminum frame is tightened. On the top of the cell, a 3D printed funnel has been set-up to allow for the easy release of cylinders in the gap. The funnel is fixed in place by two thin strips that go into the gap, which create the additional benefit of preventing glass bending. The use of a funnel was deemed necessary, as releasing the cylinders directly into the 1 mm gap can be difficult. With no funnel, a lot of cylinders (about 40%) would get caught by bubbles and exit the cell, resting on top of the glass panels. With the funnel, nearly all cylinders released in the cell fell to the bottom of it.

The gap of the cell has been measured on a 10×30cm area located in the observation area of the cameras, thanks to a Precitec® confocal sensor CHRocodile 2 SE. The confocal sensor can be used to measure the thickness of transparent materials by illuminating them with a white light, which is split into a continuous spectrum of light with multiple wavelengths. Each wavelength is focused at given distance from the sensor. The wavelength of the reflected light is analyzed by a spectrograph, and can therefore be linked to the distance from the object to the sensor. When the sensor is used on layers of transparent materials of known optical properties, the wavelength of the light reflected by the different interfaces gives us the thickness of the different materials. The thickness measurement is instantaneous, and performed at a single point. In our experiment, the confocal sensor was used to measured the width of the gap of the cell in different configurations (the cell being filled with air or water, and with or without the presence of the reinforcing frame) by mounting the sensor on a 2-axis translation stage. Due to the span and size of the translation stage, the mapping area could not cover the whole observation window (of about 40×40 cm). The gap was measured starting from the bottom of the observation window, and going up 30 cm, which is nearly the entire height of the observation window.

Figure 4.2 shows the map of the gap width with the cell filled with water, with and without the reinforcing frame. Pressure from the water causes a significant increase in gap width over the height of the cell. When the cell is empty, the maximum variation of the

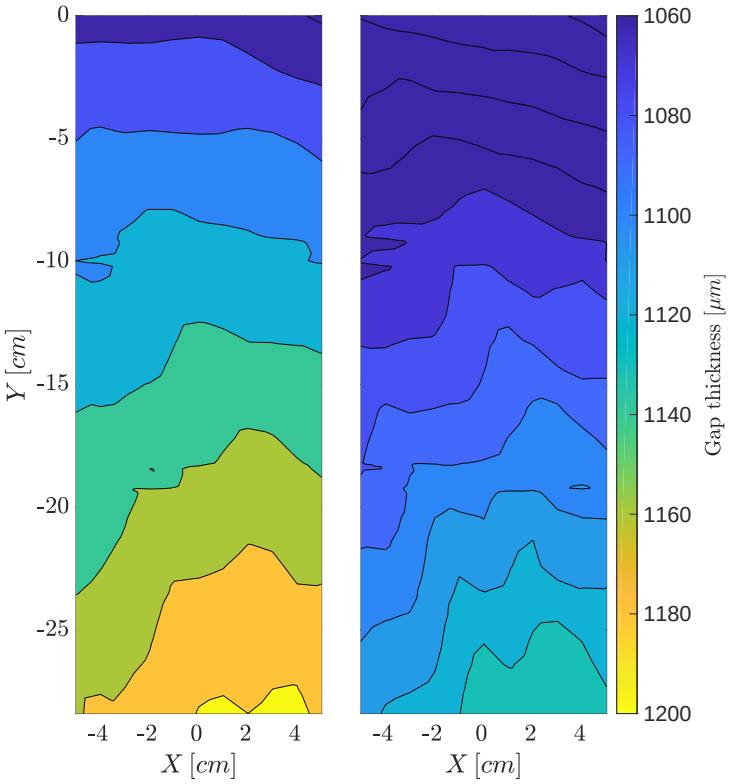

Figure 4.2 – Map of the gap width of the cell without (left) and with (right) the reinforcing frame

gap width is of 35 μm, while it is of 145 μm when the cell is filled with water and of 115 μm with the reinforcing frame. The gap has also been measured after the experimental campaign, showing no variation in time. The gap was also measured with and without the bubble swarm, which showed that air injection has no effect (less than 2 μm) on the deformation of the glass panels.

Building a confined cell with a constant gap is not trivial, especially for thin gaps such as ours. Glass is deceptively easy to deform at such small scales, and even slight deformations can have a big influence on the quality of the gap. In our experiments, we managed to reduce the gap deformations to about 10% of the gap width by adding a reinforcing frame to the cell. We may retain the value of the gap width $H = 1.1$ mm.

4.2.2 Cylinders

Our study aims at comparing the cylinder motion in the confined cell, with the motion of the cylinder in an infinite medium. We study cylinders with diameter d, length L and density ρ_c, falling in a fluid of density ρ_f. We write $\Delta\rho = \rho_c - \rho_f$ and $\Delta\rho/\rho = (\rho_c - \rho_f)/\rho_f$. Therefore, we need to choose cylinders whose motion in the confined cell would be close to the cylinder motion we observed in an infinite medium (that is mainly a periodic oscillation motion, fluttering, and a rectilinear motion). D'Angelo et al. [10] studied the behaviour of a free cylinder in a confined cell, as a function of the ratio of the cylinder diameter, d to the gap width H. They found that the ratio d/H plays a crucial role on the motion of a cylinder in a confined cell. For $d/H < 0.7$, the cylinder rotates about its axis, and oscillates orthogonally to its axis, within the gap. This kind of motion or oscillations was not observed in our study in an infinite medium. Therefore, we need to use cylinders of $d/H > 0.7$, for which D'Angelo et al. [10] observed oscillations of the cylinder orientation and center of gravity which is similar to the fluttering motion we observed in the infinite

medium. We chose to use cylinders of $d = 0.8$ mm for all experiments. Despite slight variations of the gap width, we assume the cylinder diameter to gap width ratio to be of $d/H = 0.72$.

Similarly than in our study of the cylinder motion in an infinite medium, we will study the influence of the cylinder elongation ratio $\xi = L/d$, between 3 and 40. The cylinder elongation ratio influences not only its own dynamics in the cell, but also the interaction with bubbles (studied in III), as longer cylinders have more chances of encountering bubbles. In addition, the cylinder density ρ_c will be a parameter of interest in the confined cell, as it will also be of importance during interactions between the cylinder and bubbles. As a result, cylinders were made out of three different materials, in order to change their density. The lighter ones, of $\rho_c = 1160$ kg.m^{-3}, were 3D printed using a ProJet®3510HD printer, and VisiJet®M3-X as a material. The 3D printer has a resolution of 32.10^{-6} m and an accuracy of $\pm 2‰$. Cylinders were printed vertically, meaning that the ABS layers were deposited along the cylinder length, ensuring a greater accuracy when printing the rounded sides of the cylinder. The cylinders of intermediate densities were made out of aluminum, of density $\rho_c = 2700$ kg.m^{-3}. The aluminum cylinders were hand-made by cutting long aluminum rods with cutting pliers. The pliers left the cylinders extremities heavily bevelled, therefore they were grinded down using very fine grit sandpaper. However, despite the experimenter care, the aluminum cylinders extremities could not be made all identical, especially for the shortest cylinders (2.4 mm). The heaviest cylinders were machined out of titanium by a private company ($\rho_c = 4500$ kg.m^{-3}). The diameter of all the cylinders was measured to be 0.8 ± 0.02 mm. Their length ranged from 2.4 mm to 32.8 mm, which is always at least 10 times smaller than the width of the cell.

We study the free fall of these cylinders in the confined cell filled with distilled water. The choice of distilled water was made to prevent the introduction of impurities in the cell, that could stain the glass, due to the difficulty of cleaning the cell. Cylinders were released in the gap, through the funnel using a pair of thin tweezers.

4.2.3 Measurement tools and image processing

Images of the cylinder falling in the confined cell are acquired using shadowgraphy technique. A backlight is attached on the back of the cell, and two PCO® Dimax cameras, outfitted with 200 mm objectives, record images of the projection of the shadow of the cylinder from the front of the cell. The cameras resolution is 2016×2016 pixels, and the acquisition frequency can go up to 500 Hz. In our experiments on the fall of the cylinder in the confined cell, in a fluid at rest, the acquisition frequency is chosen depending on the cylinder density (i.e. falling velocity). The acquisition frequency is 500 Hz for Titanium cylinders, 250 Hz for aluminum ones and 20 Hz for ABS ones. In presence of the bubble swarm, the acquisition frequency remained 500 Hz for all cylinders, in order to properly describe the motion of the bubbles. The two cameras are installed one above the other in order to extend the area of observation. Their field of view overlap slightly, over approximately 50 pixels, in order to stitch together the images from both cameras during the image processing. Indeed, because of the potentially chaotic nature of the cylinder motion within the bubble swarm, we need a large observation window, in order to reduce the odds of the cylinder exiting the window. Each camera records images over an area of about 18×18 cm of the cell, which gives a total observation area of about 18×36 cm.

Image processing routines are developed to extract the cylinder trajectory from the image sequences. Contrary to the study in the infinite medium, the distortion of the cylinder contour due to the perspective projection is minimal in this case. Indeed, the cylinder remains in the plane of the gap, which means that its axis is always orthogonal

with the camera axis. Furthermore, the cylinder diameter is very small compared to the length of the observation window (about 10 pixels over 2000), which further reduces the effect of the perspective projection. As a result, the cylinder position and orientation are simply given by the MATLAB® function `regionprops`, applied to the binarized image sequence. Techniques used to handle the interactions between the cylinder and the bubble are described in 5.2. In this section, though, we will discuss how to stitch together the images of the two cameras, to obtain the trajectory of the cylinder with no discontinuity over the entire height of the observation window.

A target with a random pattern of circles is inserted in the cell, so that circles are present in the overlap area. An automatic circle detection algorithm (`imfindcircles`) is used in order to locate the position of the circles in the images from the two cameras. This forms a set of matching coordinates, which can be used to compute the transformation matrix that maps the points of an image into the other image coordinate system. In the present case, we use an affine transform, which preserves lines and distance ratios, but can change the orientation, size and position of an object. MATLAB® function `fitgeotrans` takes the set of matching points computed previously as an input, and outputs the transformation matrix allowing to map the image from the bottom camera onto the coordinate system of the top camera. This choice was made to reduce computing time and error margin, as the cylinder is less likely to be present in the image of the bottom camera (because its chaotic motion can bring it out of the observation window before it can enter the bottom region). Images where the cylinder is present in the top camera are processed only using binarization and `regionprops`. However, every image where the cylinder is present either in the overlap area or in the bottom camera field of view are transformed using the affine transformation matrix. This procedure ensures that there is no discontinuity between the stitched image, and the one from the bottom camera.

Figure 4.3 shows the result of the image stitching on both images and trajectory. No distortion of the cylinder contour is visible on the images, and the trajectories show no visible discontinuity despite being zoomed in on a small area. The good quality of the image stitching is assumed to be constant for all runs.

In addition to the shadowgraphy experiments, that provide all the experimental data presented in the following, we also conducted experiments using a tomo-PIV set up. These experiments were conducted much later, and their results are still preliminary. For these reason, they are not discussed in the core of this manuscript. Instead, the interested reader can learn more about the tomo-PIV set up and preliminary results in appendix A.2.

4.3 General description of the cylinder motion in the cell

In the confined cell, the presence of the walls impacts the dynamics of the freely falling object. Lee et al. [26] investigated the motion of a falling sphere through a vertical thin-gap cell, and the fluid perturbations in the liquid using DPIV. They found that the ratio d/H of the sphere diameter d to the width of the gap H plays an important role in the sphere dynamics. For large d/H ($0.7138 < d/H < 0.9091$), the falling behaviour of the falling sphere is closer to that of an unconfined falling sphere, and its wake is three-dimensional. For low d/H ($0.9579 < d/H < 0.9862$), the wake of the falling sphere is two-dimensional, and shares qualitative similarities with that of a fixed unconfined cylinder. Two main regimes of motion exist for Reynolds number ($Re = du_t/\nu$ with u_t terminal velocity of the sphere) going from 26 to 329, and confinement ratio d/H going from 0.9862 to 0.7138, namely, a periodic oscillatory one, and a regime for which no

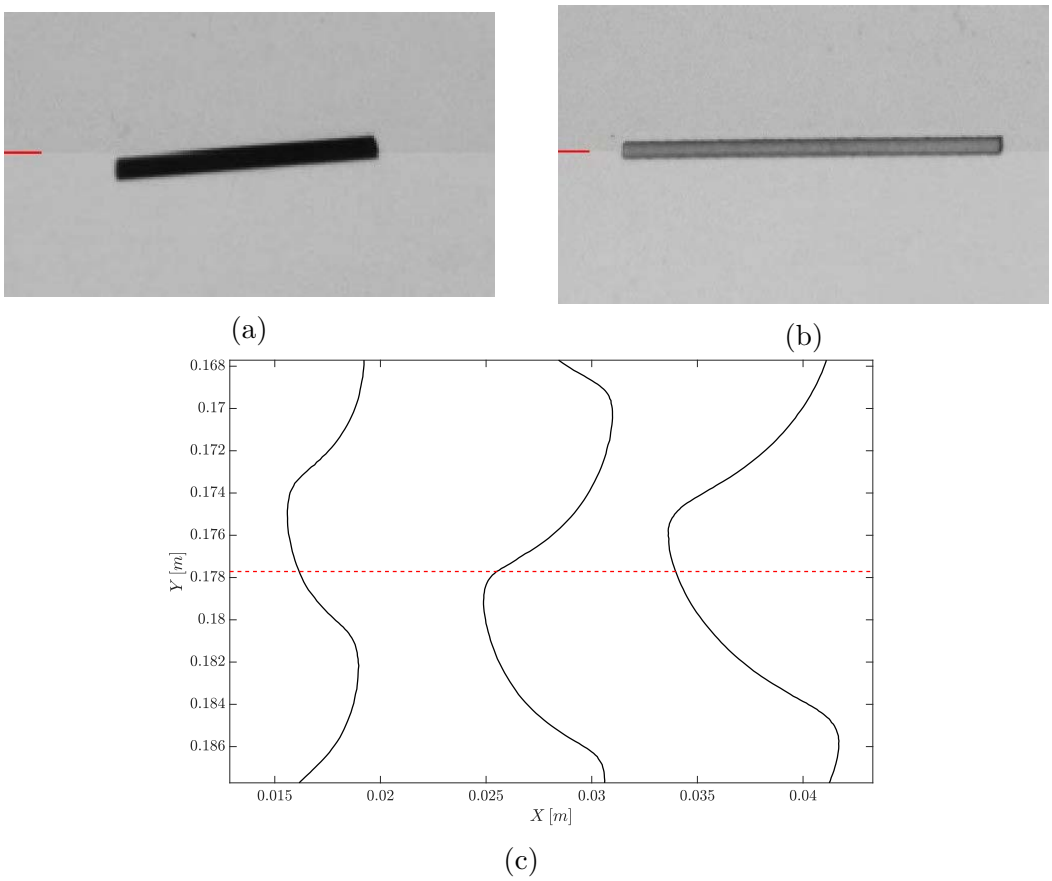

Figure 4.3 – Stitched image of a cylinder at the separation between the two cameras (a) for an aluminum cylinder (b) for an ABS cylinder. The separation between the two cameras fields of view is indicated with a red line on the left side of the image. (c) Example of three different cylinder trajectories, zoomed in at the separation between the two cameras, delimited by a red dashed line.

periodic behaviour is observed. Transition from the latter to the oscillatory regime occurs with rising Reynolds number, at a threshold that increases with the confinement of the sphere (from $Re = 244$ at $d/H = 0.9862$ to $Re = 83$ at $d/H = 0.7138$). D'Angelo et al. [11] studied the fluttering motion of cylinders (length L and diameters 2.2 and 1.9 mm) in a confined cell of width $W = 9\,\text{cm}$ and gap thickness $H = 2.8\,\text{mm}$. They reported the existence of a fluttering motion for Reynolds numbers from 25 to 155, and of a steady rectilinear motion for $15 < Re < 30$. In their study, the ratio L/W goes from 0.05 to 0.5, while it remains smaller than 0.08 for all cases in the present work. The effect of this parameter on the mean vertical motion and on the oscillatory behaviour is expected to be important, and different behaviours are in fact observed in the two studies for cylinders of comparable ρ_c/ρ_f and d/H. Since the panel of varying parameters is already large, comparison with this study will focus on the experiments they performed in water, though they also performed experiments in fluids of various viscosities.

The cylinder motion in the confined cell can vary a lot depending on its density and elongation ratio. The Archimedes number of the cylinder,

$$Ar = \left(\frac{\Delta\rho}{\rho} g d_{eq}\right)^{1/2} \frac{d_{eq}}{\nu} \quad \text{with} \quad d_{eq} = \left(\frac{3}{2} d^2 L\right)^{1/3},$$

varies with both these parameters. In the present study with a confined cell, Ar varies between 60 and 1000, which places it in similar boundaries than in the experiments presented in Part I (between 200 and 1100).

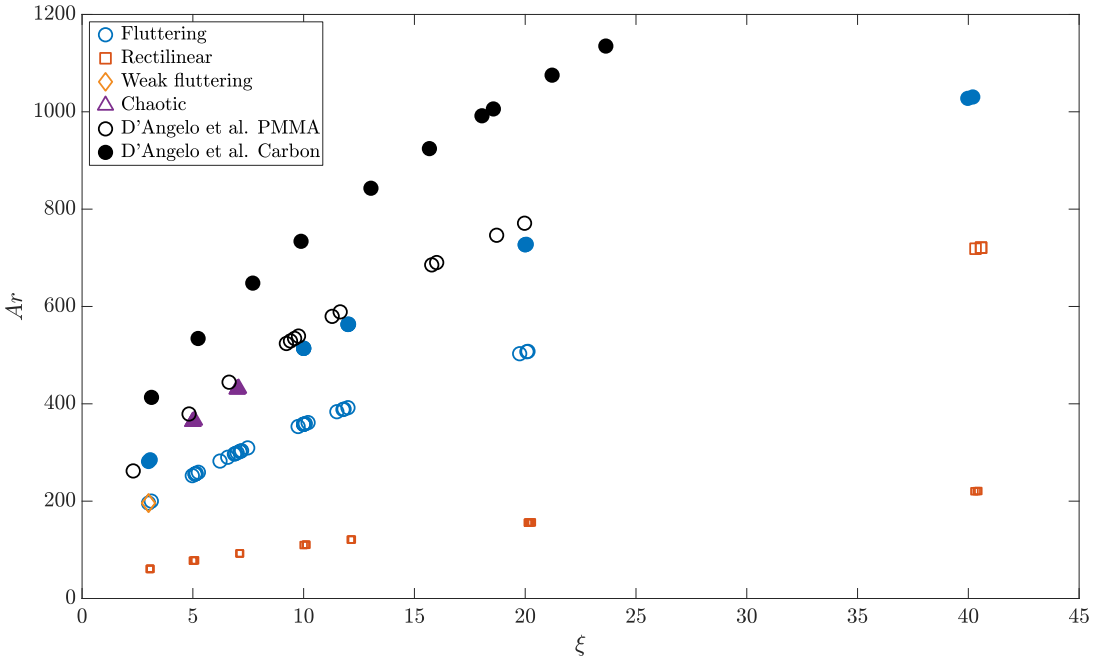

Figure 4.4 – Map of the different types of paths observed in the confined cell as a function of the archimedes number and of the elongation ratio. Titanium cylinders are plotted with filled symbols, Aluminum ones with large empty symbols, and ABS cylinders with small empty symbols. Data from D'Angelo et al. [11] is plotted in empty black circles (for PMMA) and in full black circles (for Carbon).

4.3.1 Different paths observed

Several types of path are observed in the confined cell. Some of them are similar to regimes occurring in a medium considered as unbounded, while others are only seen in the confined case. We used three different cylinders materials, ABS (ρ_c =1160kg.m^{-3}), Aluminum (ρ_c =2700kg.m^{-3}) and Titanium (ρ_c =4500kg.m^{-3}), and varied the elongation ratio ξ of the cylinders between 3 and 40. The diameter of the cylinders is constant at $d = 0.8mm$. The confinement ratio d/H therefore varies between 0.8 and 0.7 around a value of $d/H = 0.72$ due to variations in the gap width (see 4.2). As we do not observe significant changes of the cylinder dynamics in this range, the confinement ratio is considered as constant for all our experiments. In this section, we study the influence of the cylinder elongation ratio $\xi = L/d$ and of the Archimedes number Ar.

Figure 4.4 shows the different types of behaviour observed in the cell. Similarly than in the unconfined medium, the two main types of motion observed are the fluttering one and the rectilinear one. The existence of a fluttering motion for freely falling cylinders in a confined cell has previously been reported by Gianorio et al. [19], and studied in details by D'Angelo et al. [11]. It consists in a periodic oscillating motion of both the cylinder center of gravity and its orientation. It occurs here for all Aluminium cylinders (with the exception of $\xi = 40$), as well as for Titanium cylinders for several ξ. D'Angelo et al. [11] observed a fluttering motion for PMMA cylinders of $\rho_c = 1190kg.m^{-3}$, $2.27 \leqslant L/d \leqslant 20.5$ and $d/H = 0.78$ which is close to our ABS cylinders of $\rho_c = 1160kg.m^{-3}$, $3 \leqslant L/d \leqslant 40$ with $d/H = 0.72$, except with a higher Ar ($260 < Ar < 770$ for PMMA and $60 < Ar < 220$ for ABS). Their PMMA cylinders display a fluttering motion, while our ABS cylinders all have a rectilinear motion. They also observed a fluttering for slightly heavier carbon cylinders ($\rho_c = 1540$kg.m^{-3}). Due to the larger diameter of their cylinders (2.2mm for PMMA and 1.9mm for Carbon), their PMMA cylinders in fact reach similar

Archimedes numbers than our Titanium cylinders. However, they did not observe any kind of apparently chaotic behaviour, as we do for Titanium cylinders with $\xi = 5$ and 7. This difference is likely caused by the high values of L/W in the study of D'Angelo et al. [11], whose cylinder would not have the physical space to perform tumbling phases without hitting the walls of the cell. Belmonte et al. [4] study strips whose width is close to the width of the tank ($w/H = 0.93$ with w strip width) with stabilizing disks. They investigated several strip materials (plastic, brass and steel) and fluids with different viscosities, and found fluttering and tumbling behaviours.

The rectilinear motion is characterized by a steady fall of the cylinder, with the cylinder axis retaining the same horizontal orientation all along its fall. It is observed here for all ABS cylinders, and for Aluminium cylinders with $\xi = 40$. Similarly to the fall of cylinders in an unconfined medium, the fluttering motion is weaker for longer cylinders, up to a point where it totally disappears. Short Aluminum cylinders ($\xi = 3$ only) can also go under a specific type of motion called weak fluttering, where periodic oscillations of the cylinder orientation are seen, but of very weak amplitude (less than 5° peak to peak), with nearly no significant oscillation of the cylinder centre of gravity. This type of motion was seen in 2 out of the 5 runs performed for Aluminum cylinders with $\xi = 3$, while the other three displayed a fluttering motion. Proximity to a change of regime could be an explanation for these two distinct behaviours, as Aluminum cylinders of $\xi = 3$ have the lowest Archimedes number at which fluttering is seen. Inconsistencies in the making of the cylinders could be another explanation, as the fabrication process of Aluminum cylinders makes it difficult to have proper, non-beveled edges, especially for small cylinders.

The last type of motion observed in the cell is an apparently chaotic motion, which is only seen for Titanium cylinders of $\xi = 5$ and 7. During this motion, the cylinder rotates end over end with sharp, unpredictable changes of direction. This type of motion has already been observed for other objects, notably quasi-two-dimensional plates (see in particular [2, 3] in an unconfined geometry and [4] in a confined cell similar to the present one), in a transitional region separating the fluttering and tumbling regimes, during which the plate rotates periodically end over end with no change in motion.

Examples of all these different types of trajectory can be seen in figure 4.5. The fluttering motion depicted in this figure occurs for an elongation ratio and an Archimedes number for which no fluttering is observed in the unconfined medium. Moreover, the amplitude of the oscillations (38°) is much more important than the maximum amplitude seen in the unconfined case ($< 25°$). Similarly, the weak fluttering observed in the confined cell occurs at (Ar, ξ) for which a rectilinear motion is seen in an unconfined fluid. The singular nature of the confined cell is likely to alter the cylinder motion compared to our observations in the unconfined fluid. However, Chow & Adams [9] reported larger fluttering amplitude in a infinite medium than what we found in our own study, for similar parameters ξ and $I^* = \sqrt{\rho_c/(\rho_f \xi)}$, but larger ρ_c. Therefore the difference in cylinder material could also account for a different type of motion. The rectilinear fall of ABS cylinder in the confined cell occurs at couples of values (Ar, ξ) for which a rectilinear motion is also seen in the unconfined case.

4.3.2 Cylinders released vertically

In the unconfined medium, cylinders released vertically very quickly rotate back to a horizontal orientation. The distance over which they recover the horizontal inclination is estimated to be less than $2L$. In the confined cell, however, the recovery time of the cylinders is significantly more important, especially for long cylinders. Cylinders of $\xi = 40$ which enter the observation window vertically exit it with nearly the same orientation.

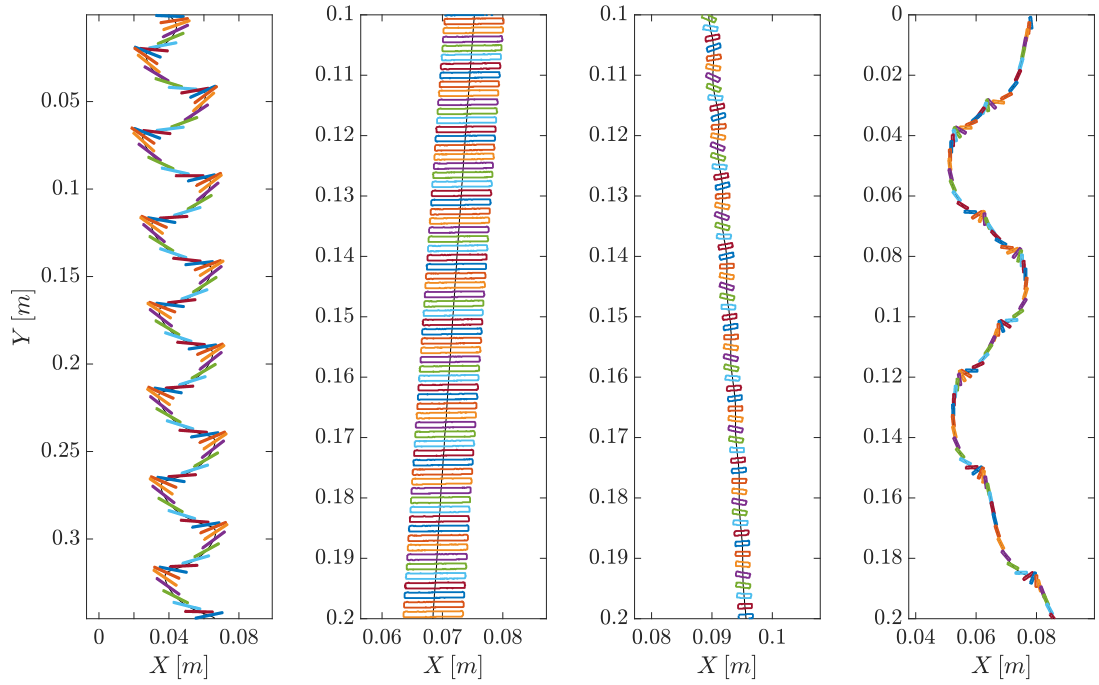

Figure 4.5 – Examples of the different types of behaviour observed in the cell. From left to right : fluttering motion of a titanium cylinder with $(Ar = 725, \xi = 20)$, rectilinear motion of an ABS cylinder with $(Ar = 120, \xi = 12)$, weak fluttering motion of an aluminum cylinder with $(Ar = 200, \xi = 3)$ and apparently chaotic motion of a titanium cylinder with $(Ar = 360, \xi = 5)$.

Cylinders with a nearly vertical orientation have a much higher velocity than the ones with a horizontal orientation.

Recovery time

The recovery time of the cylinders can be estimated from experiments where they are released nearly vertically. As the cylinder release in the cell is not finely controlled and has no optical access, we have no mean of comparing cylinders with the same initial orientation. Instead we define the recovery time as the time it takes for the cylinder to go from a high orientation (arbitrarily defined at $\theta = 80°$) to $\theta = 0°$. We make specific trials of releasing the bodies vertically, but not many cylinders enter the cell at orientations as high as $\theta = 80°$. Therefore, we assume that all cylinders with the same couple of parameters (Ar, ξ) behave similarly. The cylinder recovery time can only be estimated for aluminium cylinders. For titanium cylinders, only cylinders of $\xi = 20$ and 40 were released vertically, and they do not regain a horizontal orientation in the observation window, because their recovery time is too long. For ABS cylinders, we only have data on cylinders of $\xi = 20$. Their recovery time was estimated to be about 5s.

Figure 4.6a shows the superposition of temporal evolutions of θ for cylinders of similar (Ar, ξ). We can estimate the recovery time for cylinders of $\xi = 7$, 10 and 12. Shorter cylinders do not enter the observation window with a high enough angle with respect to the horizontal, even when released vertically. Cylinders of $\xi = 20$ and 40, on the other hand, never recover a horizontal orientation within the camera field of view. Indeed, figure 4.6b shows that the recovery time of cylinders increases steadily with their length. The recovery time is of the same order of magnitude as the fluttering period.

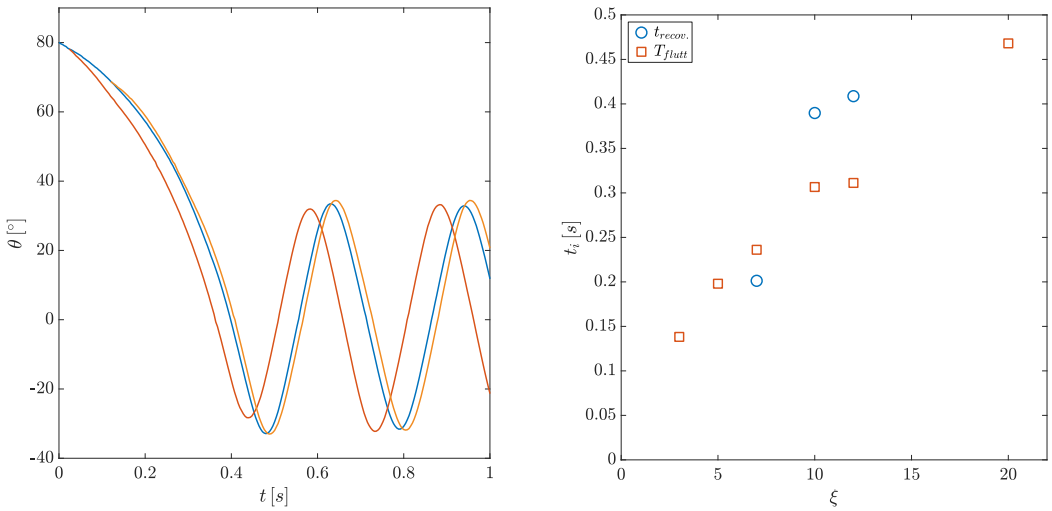

(a) (b)

Figure 4.6 – (a) Temporal signals $\theta = f(t)$ for aluminium cylinders with $Ar = 359$, $\xi = 10.1$ (blue), $Ar = 358$, $\xi = 10.0$ (red) and $Ar = 353$, $\xi = 9.75$ (orange) (b) Plot of the recovery time t_{recov} and of the fluttering period T_{flutt} as a function of ξ for aluminium cylinders

High frequency oscillations during the cylinder vertical motion

During their vertical motion, cylinders oscillate orthogonally to their axis. This oscillation is found to be of high frequency ($\simeq 40Hz$), and happens for aluminium and titanium cylinders and for $\xi \in [12, 20]$. Cylinders with $\xi < 12$ have a recovery time too short to properly see any significant oscillation when they are vertical.

Examples of temporal signals of cylinders of different ξ and material are shown on figure 4.7a. The corresponding oscillation frequency are shown on figure 4.7b. Two things are especially surprising on the oscillations of v (which the the velocity directed orthogonally to the cylinder axis, as defined in (4.6)). The first one is that they occur at the same frequency for cylinders of different elongation ratio and material. The second one is that this oscillation leaves no trace in the wake of the cylinder. Indeed, aluminium cylinders of $\xi = 40$ released vertically do not show any perturbation of their wake (see figure 4.9c). For titanium cylinders of $\xi = 40$, for which vortices are clearly visible in the wake when they are released vertically, the vortex creation frequency is much more important than the one of the oscillations of v (about two time as important).

As for the writing of this thesis, the origin of these oscillations remain unknown. The absence of any visible perturbation of the cylinder wake leads us to believe that a periodic beating of the fluid around the cylinder, in the plane of the cell, could be the mechanism responsible for these oscillations.

4.3.3 Wake comparison and discussion

We performed wake visualization in the confined cell by coating the cylinders with dye before releasing them in the cell. This technique did not yield satisfactory results with ABS cylinders, as because of their low falling velocity, they would have lost nearly all their dye when entering the observation window. Consequently, we only discuss the wake of aluminium and titanium cylinders. When observing these wakes, it has to be borne in mind that due to viscous friction at the walls, liquid flow velocities are exponentially

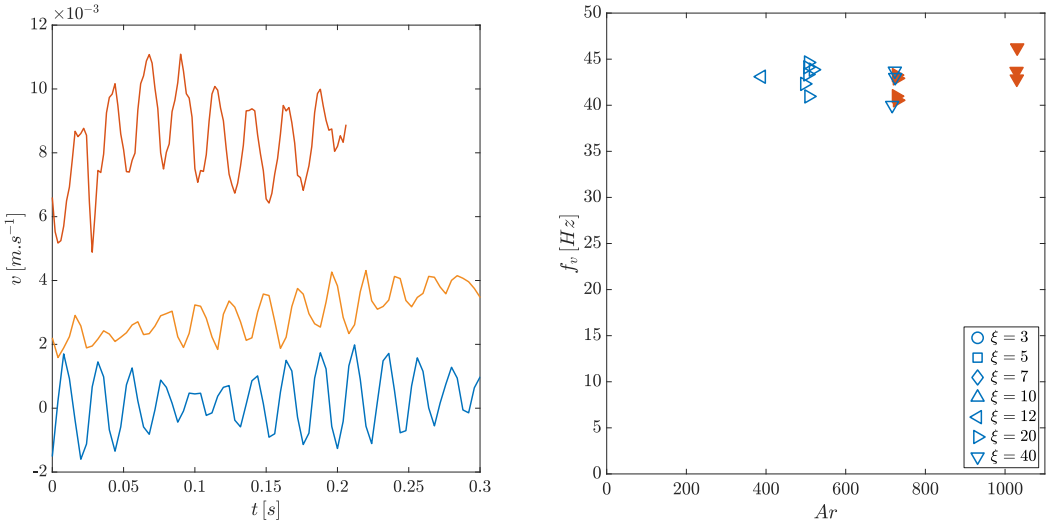

(a) (b)

Figure 4.7 – (a) Temporal signals $\theta = f(t)$ for an aluminium cylinder with $Ar = 723$, $\xi = 40.9$ (blue), a titanium cylinder with $Ar = 727$, $\xi = 20.0$ (red) and an aluminium cylinder with $Ar = 389$, $\xi = 11.8$ (orange) (b) Frequency of the oscillations of v, f_v as a function of ξ. Aluminium cylinders are plotted in blue empty symbols, and titanium cylinders in red full symbols.

attenuated [18]. This occurs on a time scale given by $\frac{H^2}{4\nu} \simeq 0.25$s, of the same order of magnitude than the frequency of vortex shedding associated to the fluttering motion.

In the confined cell, cylinders of different materials and elongation ratios have a fluttering motion. However, different types of cylinders can have different types of wake, despite sharing the same type of motion in the cell.

Figure 4.8 compares the wake of fluttering cylinders of different materials and elongation ratios. For all these cylinders, vortices are shed from the ends of the cylinder when it reaches the extrema of its horizontal motion. The trail of dye released by the $\xi = 5$ aluminium cylinder shows a wave-like pattern, with outgrowths at the peaks of the wave, where the vortices were released. For longer cylinders, such as the aluminium cylinder with $\xi = 20$ featured in figure 4.8b, the trail is nearly straight, instead of being wave-like such as for shorter cylinders. The outgrowths corresponding to the shedding of the vortices are still present.

The wake of the $\xi = 12$ titanium cylinder is more complex. The wave-like trail has much sharper angles, and the outgrowths are bigger in size. Specifically, for this cylinder, a series of smaller vortices are shed by the cylinder when it is moving horizontally. The vortex creation frequency was estimated at about 80Hz. This phenomenon is only observed for titanium cylinder, and therefore probably occurs only at high cylinder velocity. It looks closely similar to the kind of vortex release observed by Andersen et al. [2] for tumbling plates. In their case, the destabilization and break-up of the wake creates these vortices.

The wake of the cylinder is coupled to the cylinder motion. We now consider cylinders whose natural motion in the cell is not fluttering (chaotic or rectilinear motion, for instance) and cylinder released vertically, so that we can focus on their wake during the transient regime.

Figure 4.9 shows an example of a cylinder whose motion in the cell is apparently chaotic. Phases where it rotates end over end are evidenced by the large patches of dye. The quick motion between these phases, however, is difficult to see due to the lack of

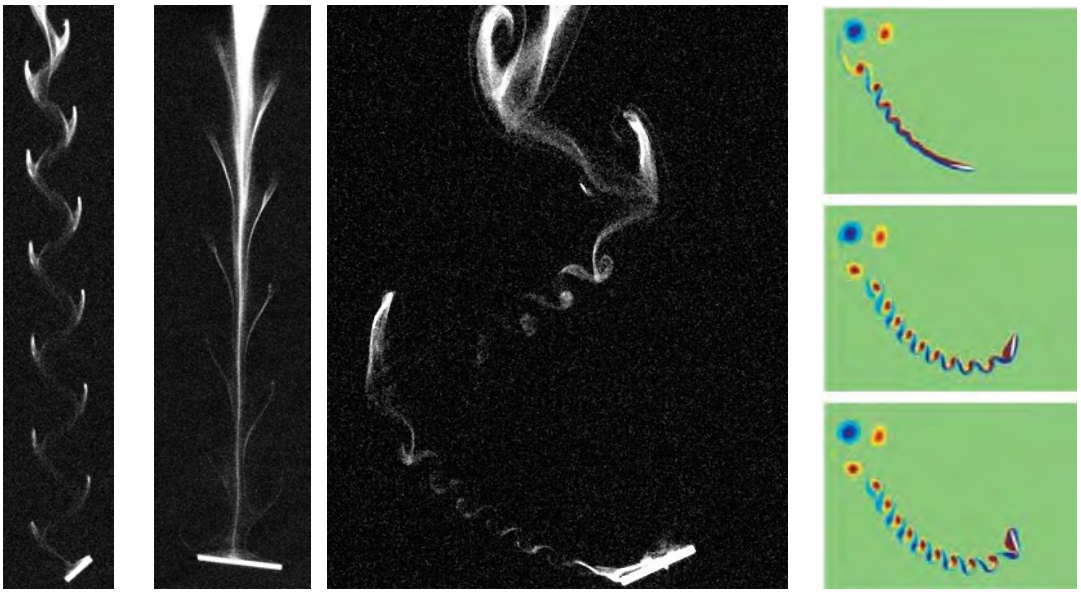

(a) (b) (c) (d)

Figure 4.8 – Wake of (a) an Aluminium cylinder of ($Ar = 257$, $\xi = 5.15$) (b) an Aluminium cylinder of ($Ar = 514$, $\xi = 20.6$) (c) a Titanium cylinder of ($Ar = 563$, $\xi = 12.0$) (d) Vorticity around a tumbling flat plate from Andersen et al. [2].

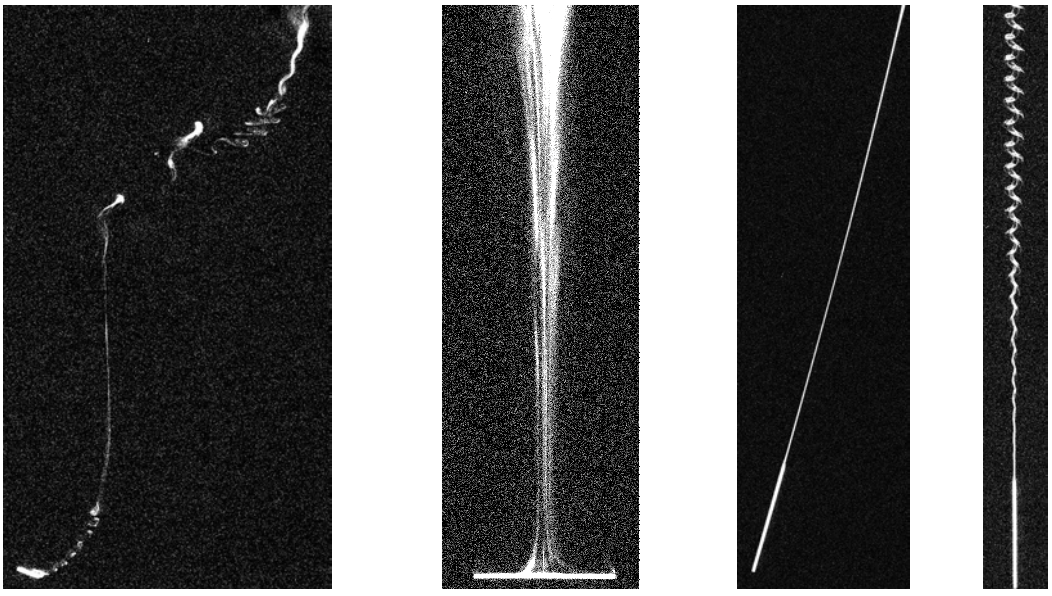

(a) (b) (c) (d)

Figure 4.9 – Wake of (a) a titanium cylinder with ($Ar = 430$, $\xi = 7$) undergoing a seemingly chaotic motion (b) an aluminium cylinder with ($Ar = 715$, $\xi = 39.7$) undergoing a rectilinear motion (c) an aluminium cylinder with ($Ar = 720$, $\xi = 40.3$) released vertically (d) a titanium cylinder with ($Ar = 1028$, $\xi = 40.1$) released vertically.

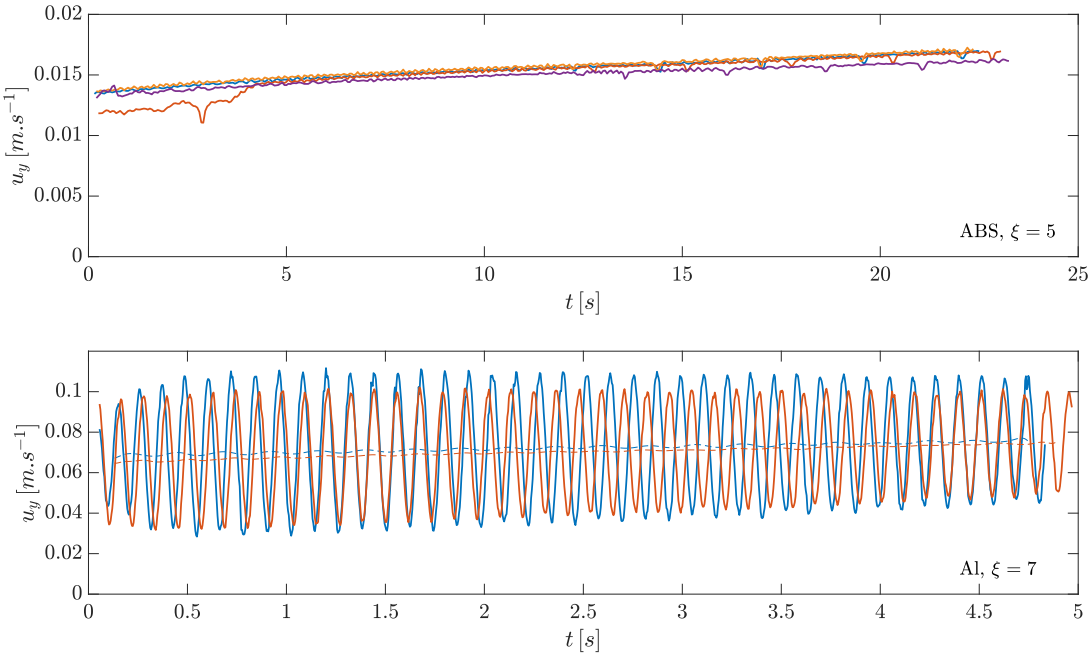

Figure 4.10 – Vertical velocity (top) of 4 ABS cylinders with $\xi = 5$ ($Ar \simeq 80$) (bottom) of 2 aluminium cylinders with ($Ar = 304$, $\xi = 7.2$) and ($Ar = 290$, $\xi = 6.6$), where the vertical velocity u_y is a bold line, and the drift of u_y, obtained by filtering the fluttering frequency out of u_y, is a solid line

dye released. Interestingly, after an especially long vertical motion, vortices similar to the ones of figure 4.8c are created, probably because of the wake break-up. For a cylinder falling rectilinearly, the wake consists in a single trail of dye, coming from the center of the cylinder.

Two very different behaviours are seen on cylinders released vertically. Aluminium cylinders of $\xi = 40$ release a straight rail of dye in their wake, with no perturbation whatsoever. On the contrary, the wake of titanium cylinders dropping vertically destabilizes in a series of pair of vortices.

Additional experiments were performed using a tomo-PIV set-up, which allows to see fluid motion around the cylinder during its passage in the cell. They are very preliminary, and thus not presented here. A first look at the results from these experiments can be seen in Appendix A.2.

4.4 Mean vertical motion of the cylinder in the confined cell

4.4.1 Effect of the gap width on the cylinder motion

Figure 4.10 shows the time evolution of the vertical velocity of ABS cylinders in their rectilinear motion, and of aluminium cylinders in their fluttering motion. In both cases, we see an evolution of the vertical velocity with time. For cylinders whose natural motion is rectilinear, u_y keeps growing at a steady rate. For fluttering cylinders, we observe the same phenomenon, alongside a weak decrease in the amplitude of the fluttering oscillation. In our experiments, we therefore do not observe any steady state. We observe instead a slowly varying state, since the time scale associated to its evolution is much longer than

the characteristic time scales of the body kinematics (inertial timescale, viscous time scale and fluttering period).

A tentative explanation of this behaviour may be found in the vertical evolution of the gap width. The effect of the cylinder diameter to gap width ratio d/H on the settling velocity of the cylinder has been studied numerically for an infinite cylinder by Dvinsky and Popel [12], and experimentally by D'Angelo et al. [10] for a very long cylinder ($L/W \simeq 1$). Both studies found that the settling velocity of the cylinder was dependent on the cylinder diameter to gap width ratio d/H. Dvinsky and Popel [12] computed the falling velocity of a cylinder for $0.3 \leqslant d/H \leqslant 0.90$. They found the falling velocity to increase with d/H up to $d/H = 0.40$, and then to decrease with d/H up to $d/H = 0.90$. In accordance with their results, D'Angelo et al. [10] studied two confinement ratios, $d/H = 0.48$ and $d/H = 0.59$, and found that the confinement indeed reduced the falling velocity.

As detailed in 4.2.1, in our experiments, the gap width is not perfectly constant. The glass panels deform slightly due to the water pressure, and the gap is larger towards the center of the cell than at the top. In our observation window, we observe gap variations of about 10%. We can therefore expect the cylinder motion in the gap to change slightly with its position in the cell. Because the area where the gap was measured and the observation window do not match entirely, it is however difficult to properly link the vertical velocity or our cylinders to the gap width.

The effect of the varying gap width on the vertical velocity of the cylinder can be further investigated by examining the variation in velocity over a certain area of the cell. For fluttering cylinders, the vertical velocity oscillates at twice the fluttering frequency around a mean value, which slowly evolves with the gap width. We consider the evolution of the mean vertical velocity over an area of the cell where the slowly varying state succeeded to the transient period associated to the release of the body from rest and to larger amplitude variations. We choose an area comprised between $Y = 11cm$ and $Y = 26cm$, because it is the longest possible area where a high enough number of cylinders (71 runs) have reached a slowly varying state. We define the velocity difference between the lowest and highest point of this window, $\Delta u_y = u_{y,Y=26cm} - u_{y,Y=11cm}$, and $\overline{u_{y,11-26}}$ the mean vertical velocity in this area. We exclude cylinders with an irregular motion, as their vertical velocity is highly irregular even in this window.

The ratio $\Delta u_y / \overline{u_{y,11-26}}$ is shown in figure 4.11. The effect of the gap width on the vertical velocity depends on several parameters. Regardless of the cylinder material, the increase in velocity is more important for cylinders of high L/d. In addition, cylinders with high ρ_c/ρ_f are less affected by variations of the gap width. Interestingly, titanium cylinders of $\xi = 10$ are slowed down as the gap width increases, contrary to all other cylinders.

4.4.2 Mean fall velocity and drag coefficient

The mean vertical velocity of the cylinders is defined as the average of the vertical velocity over a portion of the slowly varying state. For fluttering cylinders, the amplitudes of the periodic signals are determined over the same portion of the slowly varying state. When the cylinder is released vertically, we remove its recovery motion, and if the cylinder never reaches an horizontal orientation, we do not include the data. For cylinders with an apparently chaotic motion, the mean vertical velocity is defined in this case as the average velocity over the whole trajectory.

Figure 4.12a shows the mean vertical velocity of the cylinder for each run, as a function of its elongation ratio. The effect of the cylinder density is obvious. The vertical velocity of the cylinders heavily depends on ρ_c, as shown by the stratification in cylinder material.

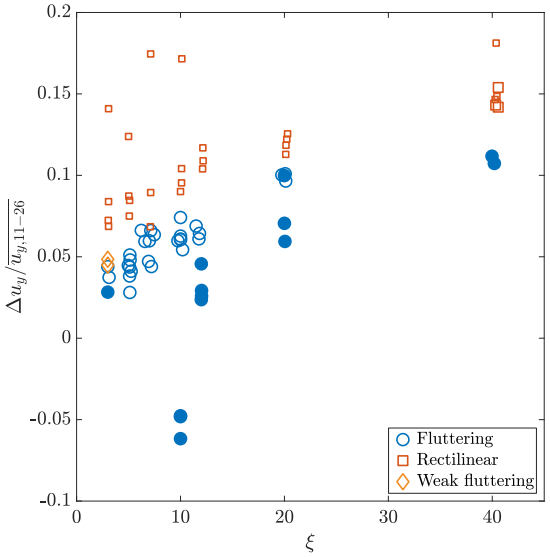

Figure 4.11 – Ratio of the difference in velocity between $Y = 11$cm and $Y = 26$cm, Δu_y with the mean vertical velocity over the same window. ABS cylinders are plotted with small empty symbols, aluminium cylinders with normal-size empty symbols, and titanium cylinders with full symbols.

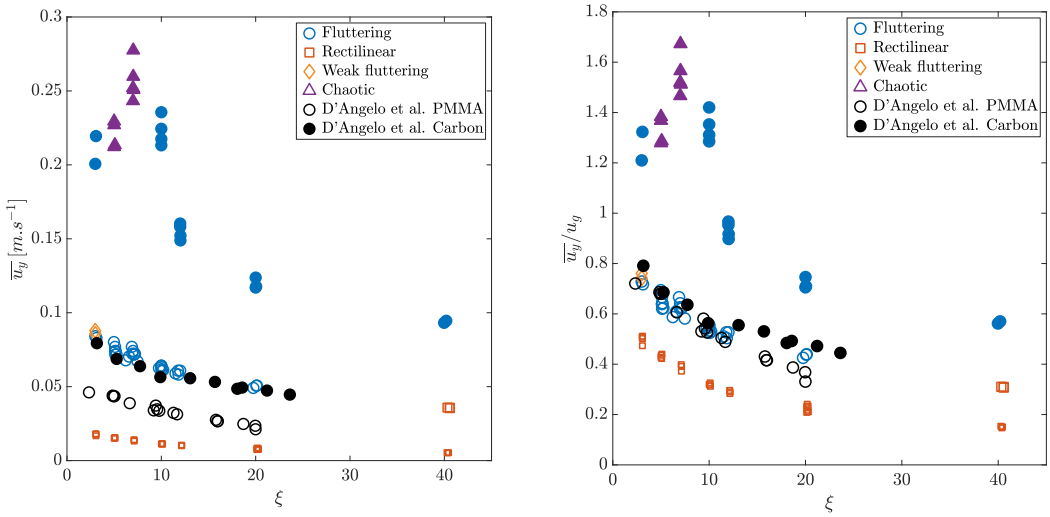

(a) (b)

Figure 4.12 – (a) Mean vertical velocity as a function of the elongation ratio ξ (b) Ratio of the mean vertical velocity $\overline{u_y}$ with the gravitational velocity u_g as a function of ξ. Titanium cylinders are plotted with filled symbols, aluminum ones with large empty symbols, and ABS cylinders with small empty symbols.

For each material, the elongation ratio also plays an important role. Short cylinders consistently have higher falling velocity than longer ones. The type of behaviour on the cell, however, does not appear to have a significant impact on the cylinder falling velocity, with the exception of cylinders with a chaotic-type motion. Yet, for these cylinders, a representative mean vertical velocity is especially difficult to achieve and highly depends on the number of fluttering and tumbling phases in the observation window. Interestingly, titanium cylinders of $\xi = 10$ seem to have a singular behaviour, with abnormally high vertical velocity. Carbon cylinders in the study by D'Angelo et al. [11] have similar falling velocities than our aluminium cylinders, for a lower density ($\rho_c/\rho_f = 1.54$ instead of $\rho_c/\rho_f = 2.70$), and higher Archimedes number ($415 < Ar < 1135$ versus $190 < Ar < 725$). As for the PMMA cylinders, which have a density very close to our ABS cylinders ($\rho_c/\rho_f = 1.19$ for PMMA, and $\rho_c/\rho_f = 1.16$ for ABS), their falling velocity is greater than our ABS cylinders, but lower than that of our aluminium cylinders. As regards the data points of the present experiments, since the cylinders diameter ($d = 0.8$mm) and the kinematic viscosity are constant in all the experiments, figure 4.12a can also be read as a Reynolds number $Re_d = \frac{\overline{u_y}d}{\nu}$ by multiplying all our data values for $\overline{u_y}$ by 800.

The ratio of $\overline{u_y}$ with the gravitational velocity

$$u_g = \sqrt{\frac{\Delta\rho}{\rho} g d}$$

is plotted on figure 4.12b. We can observe that $\overline{u_y}$ stays below u_g for all cylinders but titanium ones of $\xi = 3$, 5 and 7. The role of the cylinder density ρ_c is obvious, with heavier cylinder having larger $\overline{u_y}/u_g$. Also, the ratio $\overline{u_y}/u_g$ decreases steadily with ξ for all materials. All these observations contrast with the fall of a cylinder in an unconfined medium, for which $\overline{u_y}/u_g$ was constant for most cylinders, albeit of a single material. Interestingly, PMMA and Carbon cylinders from D'Angelo et al. [11] have very close $\overline{u_y}/u_g$ to that of our aluminium cylinders, and to each other. In particular, for $\xi < 10$, PMMA and Carbon cylinders have nearly equal $\overline{u_y}/u_g$. For higher ξ (and, in their case, for higher L/W), Carbon cylinders have more important $\overline{u_y}/u_g$ than PMMA ones. Overall, comparison with the study of D'Angelo et al. [11] has to be carried out with caution because of the difference in L/W and Ar. Finally, it can be pointed out that using L as a characteristic length scale to build the gravitational velocity $u_{g,L} = \sqrt{\frac{\Delta\rho}{\rho} g L}$ does not help in collapsing the data across varying density ratio, neither with gathering our data points with the ones of D'Angelo et al. [11].

Following a classical approach, the mean vertical velocity can be used to compute a drag coefficient C_d. Balancing buoyancy with a drag force, we get

$$\frac{1}{2}\rho d L C_d \overline{u_y}^2 = \Delta\rho \frac{\pi}{4} d^2 L g, \tag{4.1}$$

$$\text{so that } C_d = \frac{\pi}{2}\frac{\Delta\rho}{\rho} g d \frac{1}{\overline{u_y}^2}. \tag{4.2}$$

Figure 4.13a shows the evolution of the drag coefficient C_d with the Reynolds number $Re_d = \frac{\overline{u_y}d}{\nu}$. For each material, C_d decreases linearly with Re_d on separated curves (from left to right, ABS, aluminium, and titanium). This definition of the drag coefficient is clearly not satisfying. For ABS cylinders moving at lower Re_d ($4 < Re_d < 15$), the definition of a C_d through a viscous law would be more appropriate. Writing the drag force, as classically done, $\mu C_{d,v} L \overline{u_y}$, we get $C_{d,v} = \frac{\pi d^2}{4\nu}\frac{\Delta\rho}{\rho} g \overline{u_y}^{-1}$, plotted in figure 4.13b. $C_{d,v}$ is found to increase nearly linearly with ξ. In the case of fluttering bodies, we have $35 < Re_d < 250$. However, in this case, the simple balance between buoyancy and drag

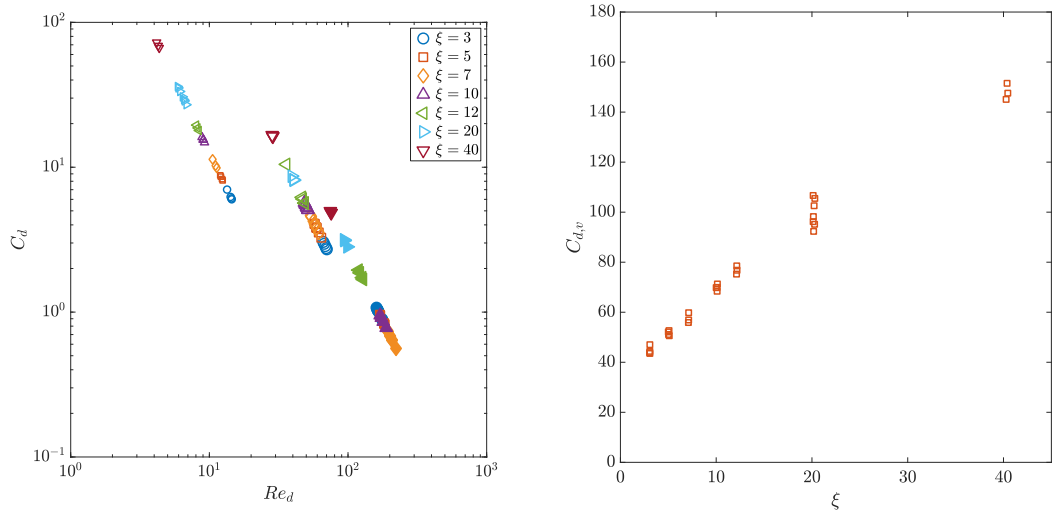

(a) (b)

Figure 4.13 – (a) Drag coefficient C_d as a function of the Reynolds number Re_d (b) Drag coefficient $C_{d,v}$ for ABS cylinders.

force given by equation (4.1) may be questioned considering the high amplitude of the oscillatory components of the translational and rotational velocities of the body. At variance with the investigation performed in the three-dimensional environment, the vertical velocity of the cylinder in the confined cell displays significant oscillations, comparable in amplitude to the mean fall velocity. The drag component along the vertical direction resulting from these oscillatory components can hardly be neglected. Therefore, before considering in more detail the force balance acting on the body, we turn now our attention to the characteristics of the oscillatory motion of the cylinder.

4.5 Oscillatory motion of the cylinder

The fluttering motion we observed in the confined cell shares some similarities with that observed in the unconfined case, as it consists in an oscillatory motion of both the cylinder orientation θ and the position of its center of gravity. It however displays significant differences with its counterpart investigated in Part I. A crucial difference is encountered in the existence of large amplitude oscillations of the vertical velocity of the cylinder. These are displayed in figure 4.14, and can reach 50% and 80% of the mean vertical velocity for aluminium and titanium cylinders, respectively. This type of fluttering is similar to that observed for quasi two-dimensional plates by Andersen et al. [2, 3].

Figure 4.15 presents the temporal signals of the inclination angle of the cylinder θ for two fluttering cylinders of different materials in the cell. In the unconfined medium, the evolution of θ with time could be modeled by a harmonic function $\theta(t) = \tilde{\theta} sin\,(\omega t + \phi)$. In the confined cell, the aluminium cylinder fluttering is close to an harmonic function. Its amplitude decreases slightly with the vertical position of the cylinder (see § 4.4.1 for more details). In addition, as can be seen in the figure, the frequency of the signal also changes slightly. Titanium cylinders of $\xi = 3$ have a similarly-shaped temporal signal of θ. At higher ξ, however, the signal shape changes and becomes closer to a triangular signal, a signature of the presence of non-linearities, as expected from the high-amplitude values of oscillatory components, in particular along the vertical.

The fluttering frequency f is determined by a Fourier transform of $\theta(t)$, which despite the slight evolution described previously presents a sharp peak at f. Figure 4.16a shows

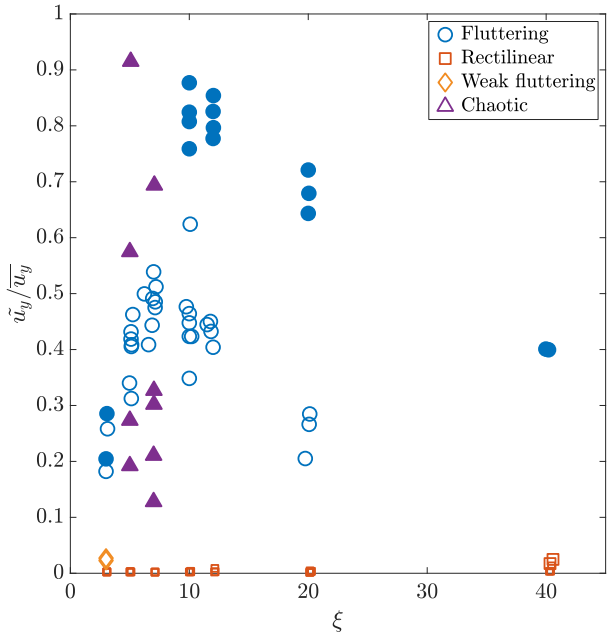

Figure 4.14 – (a) Ratio of the amplitude of oscillation of the vertical velocity with the mean vertical velocity $\overline{u_y}$ as a function of the elongation ratio ξ. Same symbols for the materials as in figure 4.12.

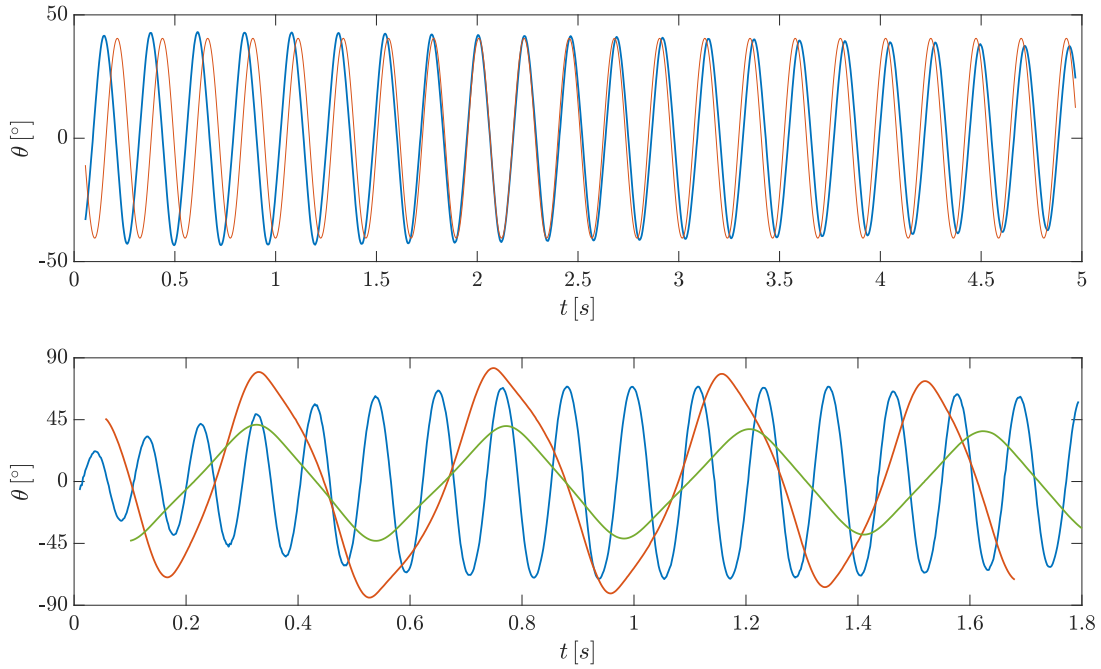

Figure 4.15 – Temporal evolution of the orientation θ of Top : an aluminium cylinder with ($Ar = 290$, $\xi = 6.6$) (thick blue line) and model signal $\theta(t) = \tilde{\theta} sin\omega t + \phi$ (red line) where $\tilde{\theta}$ is the amplitude of the signal, ω its pulsation and ϕ its phase; Bottom : titanium cylinders with ($Ar = 282$, $\xi = 3.0$) (blue), ($Ar = 514$, $\xi = 10$) (red), ($Ar = 728$, $\xi = 20.1$) (green)

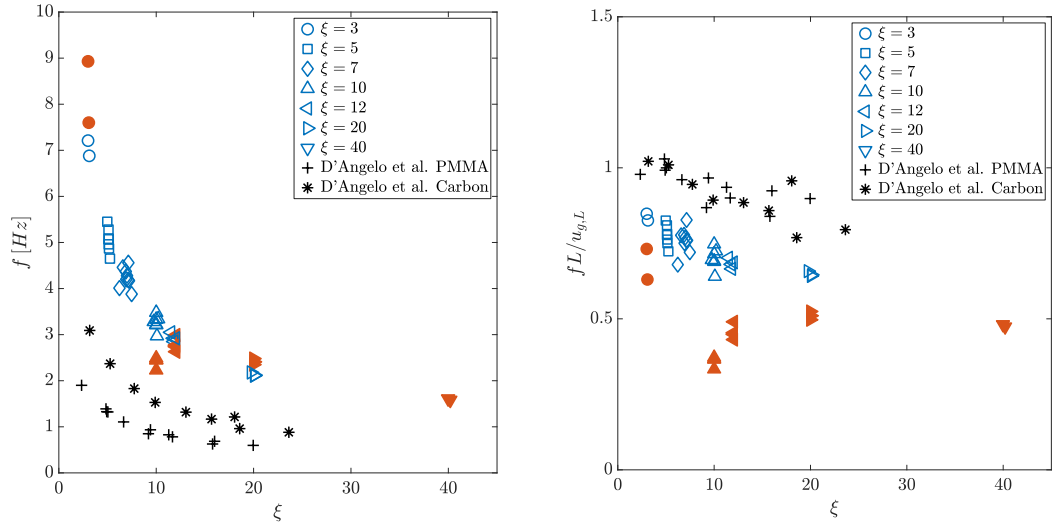

(a) (b)

Figure 4.16 – (a) Frequency of the fluttering motion f as a function of ξ. (b) Strouhal number $\frac{fL}{u_{g,L}}$ versus ξ. Titanium cylinders are plotted with red filled symbols and aluminum ones with blue empty symbols.

the fluttering frequency f as a function of ξ. Surprisingly, without any scaling, all the frequencies lie on a single curve, independently from the material. Only titanium cylinders of $\xi = 10$ deviate from the curve by having a slightly lower fluttering frequency. Ironically, the natural gathering of the fluttering frequency on a single curve makes the building of a proper Strouhal number especially difficult. The classical definition of a Strouhal number $St = fd/\overline{u_y}$ leads to stratified values of St according to the evolution of $\overline{u_y}$. In the study of D'Angelo et al. [11], the fluttering frequency goes from about 0.5Hz to about 3Hz, which is lower than in our study for the same ξ. Their values of f do not collapse for different materials of closer densities, as it does in the present study. To gather their results, they propose a Strouhal number based on the length L and on the characteristic velocity $u_{g,L} = \sqrt{\frac{\Delta\rho}{\rho} gL}$, such that

$$f = 0.102 \frac{u_{g,L}}{L}. \tag{4.3}$$

As can be seen in figure 4.16b, the scaling works well with their results but does not embrace the present data. In their experiments on falling flat strips (with lateral stabilizing disks) in a confined cell, Belmonte et al. [4] propose that the fluttering frequency can be modeled by the frequency of a buoyant pendulum. This can be written

$$f_p = \left(\frac{\rho_c L}{(\rho_c - \rho_f) g} \right)^{-1/2}. \tag{4.4}$$

The ratio of the fluttering frequency with f_p is shown as a function of ξ on figure 4.17a for the present data and the data of D'Angelo et al. [11]. Aluminium and titanium cylinders as well as cylinders from [11] are gathered together quite nicely, despite all the differences observed between the two studies. Surprisingly, no frequency measurement is available from Belmonte et al. [4]. Despite the very nice collapse of the data, the theoretical foundation for the success of the scaling is not clear to understand, as will be discussed in the concluding section 4.7. Finally, in line with the analysis carried out in Part I (figure 11a of Toupoint et al. 2018), we also plot in figure 4.17b the Strouhal number $\omega\delta/u_g$

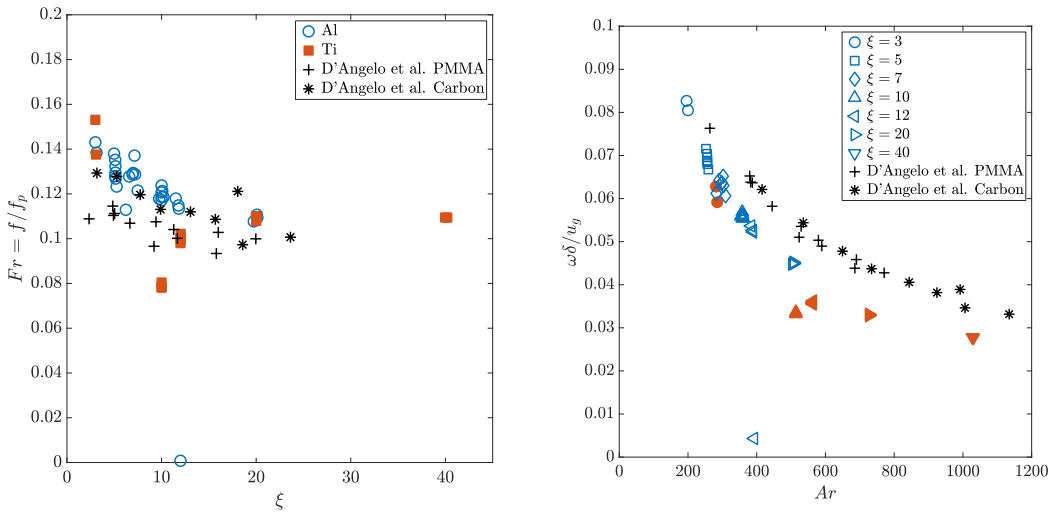

(a) (b)

Figure 4.17 – (a) Ratio of the fluttering frequency f with the frequency of a buoyant pendulum f_p, as a function of ξ proposed by Belmonte et al. [4]. (b) Strouhal number $\omega\delta/u_g$ as a function of the Archimedes number Ar.

based on the Stokes layer thickness,

$$\delta = \sqrt{2\,\nu/\omega} \quad \text{with} \quad \omega = 2\pi f. \tag{4.5}$$

The data for the two studies group well together, though in two separate sets. The grouping is particularly interesting for the data from D'Angelo et al. [11], since they correspond to different ρ_c, d and f (only ρ_c and f change in our data).

Assuming that the evolutions observed for the amplitude of oscillations are related to the vertical evolution of the gap width discussed in section 4.4.1, we determine these quantities by an average in the same portion of the signals used to determine the mean vertical velocities. The oscillation amplitude of the inclination angle of the cylinder axis relative to the horizontal is shown on figure 4.18a as a function of ξ. Similarly to our observations in the unconfined medium, shorter cylinders present higher-amplitude oscillations. For the same elongation ratio, cylinders with higher Archimedes number (i.e. higher mass) also have higher-amplitude oscillations. The amplitude of the oscillations are much larger in the confined cell than in the unconfined medium, for the same range of Archimedes number. Cylinder density is probably the main factor in this increase in $\tilde{\theta}$, which would be concordant with Chow & Adams [9] observations regarding the oscillatory motion of heavy cylinders (with ρ_c/ρ_f going as high as 8) in an unconfined fluid. In addition, the fluttering motion was found to be three-dimensional in the unconfined medium for shorter cylinders ($\xi \leqslant 5$). In the cell, the confinement restricts the cylinder oscillations to be strictly in-plane, which might increase their amplitude. For comparison, D'Angelo et al. [11] observe oscillations of similar amplitudes than the aluminium cylinders with PMMA and Carbon cylinders of larger diameter. It must however be borne in mind in this comparison that the additional lateral confinement (i.e. high L/W) in [11] possibly creates interactions between the fluid displace by the body and the lateral walls of the cell, having in turn an effect on the body motion and its oscillation amplitude.

To analyze the amplitude of fluttering, Belmonte et al. [4] define a Froude number Fr as the ratio between the time scale L/u_g and that of a buoyant pendulum f_p, such that $Fr = u_g/(Lf_p)$. By plotting the maximum angular amplitude of their oscillations versus this Froude number, they predict the onset of tumbling with a critical Froude number

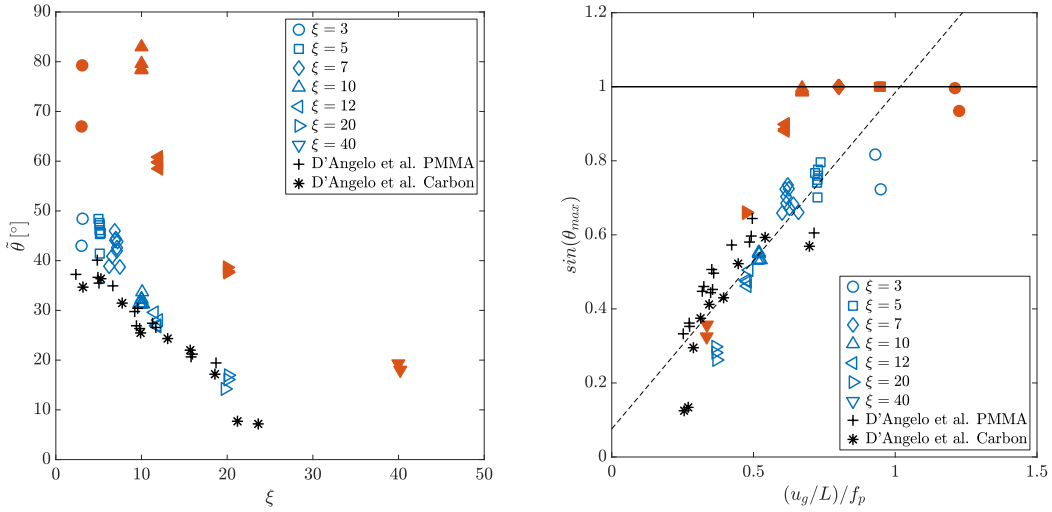

(a) (b)

Figure 4.18 – (a) Plot of the amplitude of the inclination angle $\tilde{\theta}$ versus ξ. (b) $\sin(\tilde{\theta})$ as a function of the Froude number $Fr = u_g/(f_p\, L)$. Titanium cylinders are plotted with red filled symbols and aluminum ones with blue empty symbols.

$Fr \simeq 0.67$ at which $\theta_{max} = 90°$. In their work, Belmonte et al. [4] study strips whose width being close to the width of the tank ($w/H = 0.93$ with w strip width). They gather data from several strip material and fluids of different viscosity on a single curve (figure 3a of [4]). In their study, the Froude number varies between 0.02 and 1.0, which is of the same order of magnitude as our values and the ones of [11]. We replicate the plot with our data and the one of [11] in figure 4.18b. Our aluminium cylinders collapse well on a single curve with both PMMA and Carbon cylinders from [11] and a linear fit of the data crosses $sin(\theta_{max})$ at $Fr = 1.03$, which corresponds to the prediction of Belmonte et al. [4] for the transition to tumbling (the pendulum driven at resonance). Data from titanium cylinders has a less satisfactory collapse with the rest of the points. In particular, titanium cylinders of $\xi = 5$ and 7, which undergo a motion alternating fluttering and tumbling phases, are spread on several values of Fr.

4.6 Kinematics in a rotating frame related to the body

In the study of the cylinder in a unconfined medium, we defined the body frame as having a fixed origin, but axes that rotate to follow the cylinder motion. This frame was found to be better suited to describe the cylinder kinematics, and allowed the use of Kelvin-Kirchhoff equations to obtain a determination of the hydrodynamical forces and torques governing the body motion (ongoing work, not presented in the manuscript). In the confined medium, such a model cannot be envisioned simply, as the Kelvin-Kirchhoff equations are not directly applicable. Despite this, the description of the body motion in the body frame can still provide additional insight on the cylinder kinematics.

By considering that the cylinder motion in the cell is purely two-dimensional, we can define the body frame in the confined medium as

$$\begin{bmatrix} u \\ v \end{bmatrix} = \begin{pmatrix} \cos(\theta) & \sin(\theta) \\ -\sin(\theta) & \cos(\theta) \end{pmatrix} \begin{bmatrix} u_x \\ u_y \end{bmatrix} \tag{4.6}$$

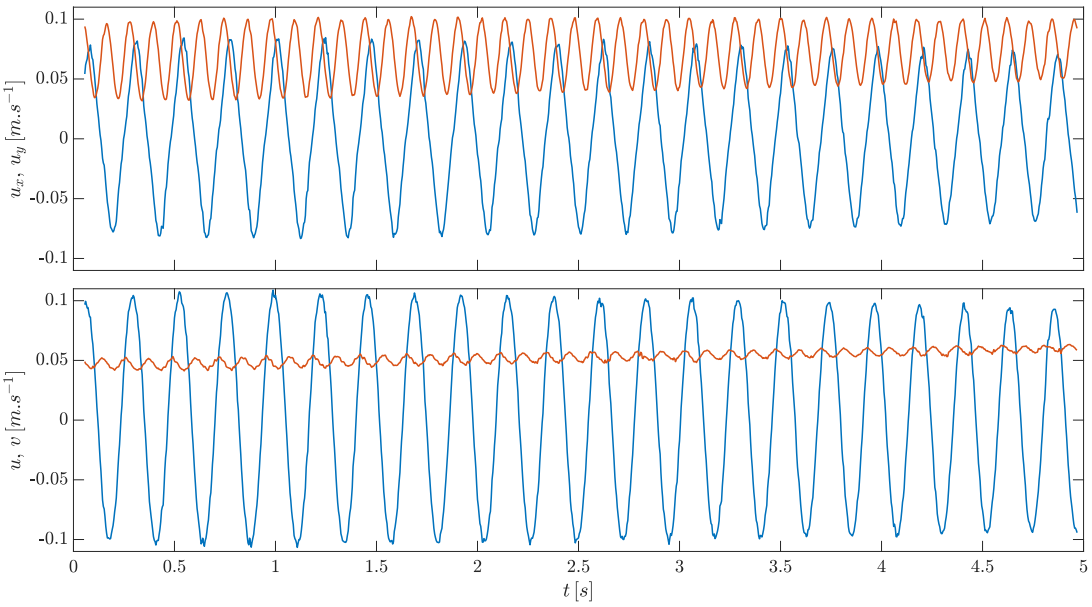

Figure 4.19 – Top : temporal evolution of u_x (blue) and u_y (red), respectively horizontal and vertical velocity of an aluminium cylinder with ($Ar = 290$, $\xi = 6.6$). Bottom : temporal evolution of u (top) and v (bottom) of the same cylinder

In this frame, u is the velocity directed along the cylinder axis, and v, orthogonally to it. Both velocity components u and v are oscillating, at ω and 2ω respectively (where ω is the pulsation of the fluttering). Oscillations of u are centered around 0, while v is oscillating around a mean value, which is obviously different from $\overline{u_y}$.

The temporal evolution of u and v are compared to the ones of u_x and u_y on figure 4.19. u and v differ significantly, both in shape and in amplitude, from u_x and u_y. While u_x and u_y exhibit a nearly triangular shape, u and v are closer to a sinus shape. This observation is even more prominent with titanium cylinders (see appendix A.1), which have a very complex motion in the laboratory frame. The amplitude of the oscillations of v is very small, while u oscillates with an even greater amplitude than u_x. In the body frame, it appears clearly that oscillations directed along the cylinder axis are much more prominent than the ones orthogonal to it. Furthermore, the mean orthogonal velocity $\overline{v}$ is smaller than $\overline{u_y}$, as will be discussed later.

The amplitude of the oscillations of u and v are denoted respectively $\tilde{u}$ and $\tilde{v}$. Their ratio with the mean vertical velocity of the cylinder $\overline{u_y}$ are plotted on figure 4.20a. The oscillation amplitude $\tilde{u}$ is 1 to 2.4 times larger than the mean vertical velocity of the cylinder. This contrasts with the motion of the cylinder in the unconfined medium, where the amplitude of the oscillations of u are smaller than the mean vertical velocity of the cylinder for all investigated cases ($\tilde{u}/\overline{u_y} < 0.80$). With the exception of $\xi = 3$, titanium cylinders all have more important $\tilde{u}/\overline{u_y}$ than aluminium ones. The fact that cylinders have velocity oscillations along their axis of the same order of magnitude as their falling velocity explains the complexity of their motion, as the problem is strongly non-linear.

Additionally, the oscillations of v are comparatively very weak. They never exceed $0.3\overline{u_y}$, and most of them are below $0.1\overline{u_y}$. It should be noted that due to their very low amplitude, oscillations of v are difficult to measure accurately. The comparison of $\tilde{u}$ with $\tilde{v}$ can be seen on figure 4.20b. $\tilde{u}$ is by an order of magnitude more important than $\tilde{v}$, about 5 times as large to about 35 times as large as $\tilde{v}$.

Furthermore, a phase difference between the oscillations of the longitudinal velocity u and of the inclination angle θ of the body can be calculated by fitting the periodic signal of u and θ over the same time period. The choice of this time period does not affect the

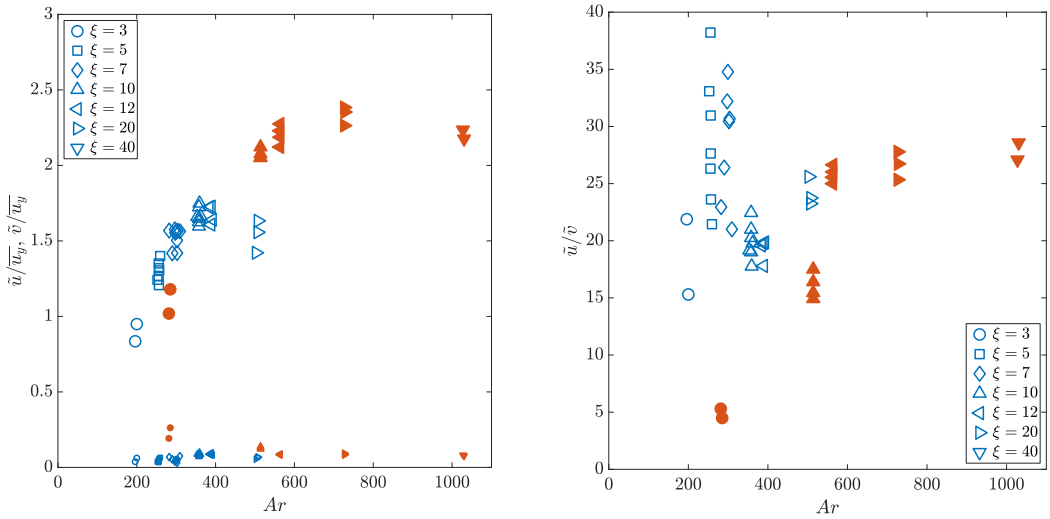

(a) (b)

Figure 4.20 – (a) Ratios $\tilde{u}/\overline{u_y}$ (large symbols) and $\tilde{v}/\overline{u_y}$ (small symbols) as a function of Ar (b) Ratio $\tilde{u}/\tilde{v}$ as a function of Ar. Titanium cylinders are plotted with red filled symbols and aluminum ones with blue empty symbols.

results obtained for phase difference. It turns out that, for all Ar, ξ and $\frac{\rho_c}{\rho_f}$ investigated, the phase difference between u and θ is very close to constant, u being about $\frac{3\pi}{4}$ in advance of phase relative to θ. This result shows a striking similarity with that in the unconfined medium. A very slight increase in the phase difference with Ar is observed, as in the unconfined configuration.

We have seen that the oscillations of the body alongside its axis, u, are very significant compared to the mean vertical motion of the cylinder, $\overline{u_y}$, and to oscillations along the orthogonal direction, v. This velocity component, v, directed orthogonally to the cylinder axis, oscillates around a mean value, denoted $\overline{v}$. The evolution of $|\overline{v}|$ with the cylinder material and elongation ratio is shown on figure 4.21a. We chose to plot $|\overline{v}|$ instead of $\overline{v}$ because of change of sign that occurs to v when the cylinder tumbles end-over-end. On figure 4.21b, we show the ratio between $\overline{v}$ and $\overline{u_y}$ as a function of ξ and for different cylinder behaviours. Cylinders falling rectilinearly have $\overline{v} \simeq \overline{u_y}$, while fluttering cylinders have $\overline{v} < \overline{u_y}$, the mean orthogonal velocity reaching values three times lower than the mean vertical velocity for titanium cylinders. For a single material the largest difference between $\overline{u_y}$ and $\overline{v}$ is found at intermediate elongation ratios, about $\xi = 7$. Thanks to their higher inclination angle θ, heavier cylinders experience therefore a lower velocity component along the direction perpendicular to their axis. Building a Reynolds number on this mean orthogonal velocity and on the cylinder length, $Re_v = |\overline{v}|L/\nu$, changes significantly the perspective, compared to others definitions of Reynolds numbers. As shown in figure 4.22, the plot of Re_v versus Ar gathers all points in continuity on a single curve, independently from the cylinder material, except for cylinders whose motion is of chaotic-type, which has a large impact on v. The remarkable scaling of Re_v with Ar induces us to think that model laws for a drag coefficient have to be sought along the axes associated to the body geometry, and we are working currently in this direction. In doing so, it is clear that a simple balance such as that given by (4.2) will not be sufficient, as non-linearities also contribute significantly. An example of such a non-linearity is provided by the inertial term in the rotating frame coupling translational and rotational velocities. For instance, along the direction orthogonal to the cylinder axis, this term has a mean component (resulting from the phase difference between u and θ) proportional to $m_c\omega\tilde{\theta}\tilde{u}$,

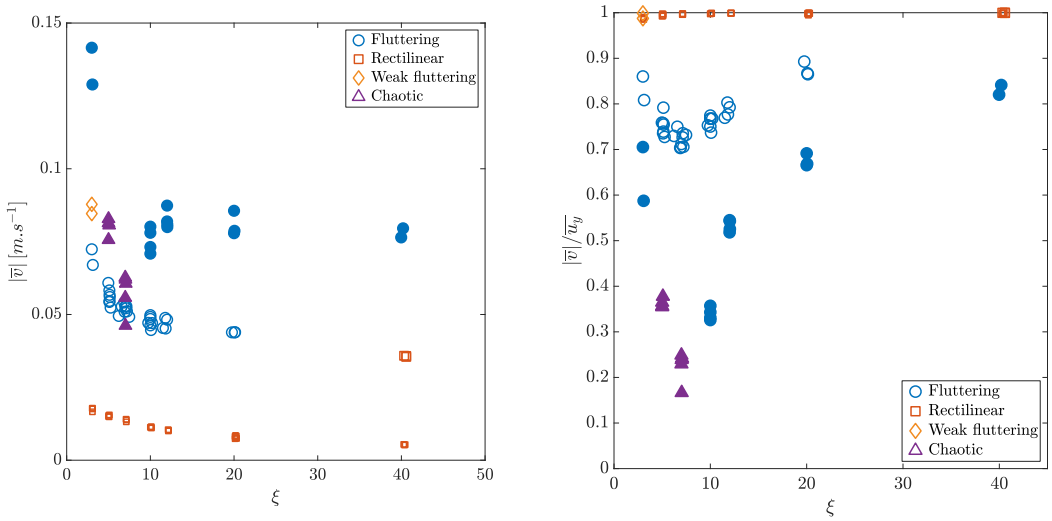

(a) (b)

Figure 4.21 – (a) Mean orthogonal velocity $\overline{v}$ as a function of the elongation ratio ξ. (b) Ratio of the mean orthogonal velocity $\overline{v}$ with the mean vertical velocity $\overline{u_y}$ as a function of ξ.

which is significant as both $\tilde{\theta}$ and $\tilde{u}$ are large.

4.7 Conclusion and discussion

This chapter has shown that different types of behaviour can be observed in the present confined cell for cylinders with different length-to-diameter ratios ξ, Archimedes numbers Ar and density ratios relative to the surrounding fluid. These are the rectilinear motion, the fluttering motion, and an apparently chaotic motion combining phases of fluttering and tumbling. We have also shown that cylinders released with their axis nearly vertical may keep this orientation over distances much longer (several times the length L) than the transient phases observed in an unconfined environment. This is especially the case for longer cylinders. The diversity of paths observed over the investigated range of parameters, and the importance of transient phases depending on release conditions provide a large base for the exploration of the impact of a swarm of bubbles on the free fall of inertial cylinders. This question is the subject of the following chapters.

One of the key elements of the proper dynamics of the cylinders, that will condition its interaction with a bubble swarm is the characteristic time scales of their motion. Two were identified here: a recovery time, which can be very long in the presence of confinement, and a characteristic time of fluttering motion. Different scalings are proposed here for the latter, though their theoretical foundations are still open to reflexion. On the one hand, the proposal by Belmonte et al. [4] based on the frequency of the buoyant pendulum is obtained by considering that

$$m_c R \frac{d^2\theta}{dt^2} = m^* g V_{ol} \sin\theta,$$

where m_c is the mass of the cylinder, m^* is the buoyant mass, and R the length of the pendulum. Assuming that $R = L$ and that oscillations are small, we get the buoyant pendulum frequency f_p from equation (4.4). Among strong assumptions, this balance neglects added-mass and friction effects, which are both expected to be important. On the other hand, the introduction of the viscous penetration length (figure 4.17b) also

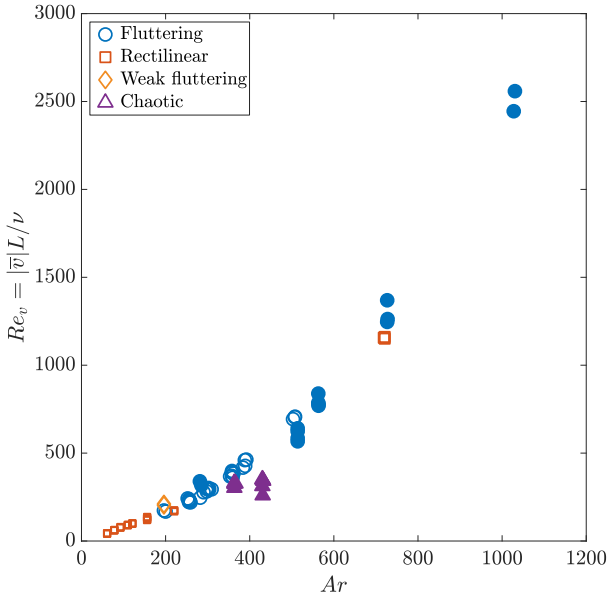

Figure 4.22 – Reynolds number based on the length of the cylinder and on its mean orthogonal velocity, $Re_v = |\overline{v}|\ L\ /\ \nu$ versus the Archimedes number Ar.

seems to work quite well in capturing a common characteristic of the oscillatory motion as the parameters vary. Nevertheless, the reason for this scaling to be still relevant in the presence of advection and of interaction with confining walls is presently an open question. Both however yield reasonable predictions that work with experimental data.

Part III

Fall of a cylinder in a confined bubble swarm

Introduction

In the third part of the thesis, the motion of a cylinder freely falling in a confined homogeneous swarm of monodispersed high-Reynolds number bubbles is studied. The bubbles rise in the planar thin-gap cell previously used in 4.2, in a fluid otherwise at rest. The bubble size is larger than the gap of the cell, so that they are flattened between the walls of the cell, and adopt an in-plane motion. This motion generates fluid perturbations in the liquid phase, that have been described by Bouche et al. [5, 6]. It is a random motion that is always parallel to the plates, except in the vicinity of the bubbles. Despite the randomness of the fluid agitation, it is different from turbulence. Note that in our experimental conditions, the bubbles never dewet the walls of the cell, and that a thin liquid film always exists between the gas interface and the wall of the cell.

As both the Reynolds number of the relative motion, $Re_b = \frac{u_b d_b}{\nu}$, and the modified Reynolds number $Re_b \left(\frac{H}{d_b}\right)^2$ are large, inertial effects are predominant, and instable bubble wakes with vortex shedding that develop for isolated bubbles also contribute to the bubble-induced agitation generated in the liquid phase in the bubble swarm.

The motion of the cylinder in this bubble-induced agitation will thus depend on several dimensionless parameters. Similarly to Part II, $\xi = L/d$, ρ_c/ρ_f and Ar_c will characterize the cylinder own dynamics. The bubble swarm introduces a new set of dimensionless parameters, α_g the gas volume fraction, $Ar_b = \frac{\sqrt{(\rho_g - \rho_f)/\rho_f g} d_b^{3/2}}{\nu}$ the bubble Archimedes number, $Bo_b = \frac{(\rho_g - \rho_f) g d_b^2}{\sigma}$ the Bond number of the bubbles, comparing the effects of the gravitation to the surface tension, and d_b/H the confinement parameter.

In the present study, the bubble diameter will remain nearly constant, giving $Ar_b \simeq 1000$, $Bo_b \simeq 3.2$, showing deformed bubbles, and $d_b/H \simeq 4.9$ for all experiments. The gas volume fraction will vary between 2% and 5%. The mean distance between two bubbles can then be estimated by $L_{12} \simeq \sqrt{\frac{\pi/4}{\alpha_g}} d_b$ (see section 5.3.3), giving 1.5cm$\leqslant L_{12} \leqslant$ 2.5cm. The cylinder lengths chosen will thus cover a large range of relevant scales, from $L \leqslant d_b$ to $L \geqslant L_{12}$.

Experiments were conducted so that cylinders of various elongation ratio were observed for different α_g. Due to time and digital storage constraints, however, some elongation ratio could not be studied as extensively as others. A choice was made to focus on cylinders of $\xi = 7$, 12 and 20, as they were expected to present different and interesting behaviours in the bubble swarm. These three elongation ratios were investigated at more α_g than others. Similarly, we decided to focus on one of the three cylinder materials available (ABS at $\rho_c = 1160 kg.m^3$, aluminum at $\rho_c = 2700 kg.m^3$ and titanium at $\rho_c = 4506 kg.m^3$). Out of 662 cylinder released in the bubble swarm, 547 were aluminum cylinders, 89 were titanium cylinders and 27 were ABS cylinders. The intermediate density of aluminum cylinders lead us to believe their dynamics in the bubble swarm would be richer and more diverse than for the other materials. Additionally, aluminum cylinders were easy to manufacture in large quantities. On top of that, their density ratio with the surrounding fluid is similar to the one of IFPEN catalysts in the industrial problem (see section 1.2.2). As described

in 5.2 cylinders were released in the cell throughout the experiment days, and recovered each evening, meaning that having a larger number of available cylinders allowed for a larger number of experiments. The amount of experiments with ABS cylinders was even lower because of digital storage constraints. Despite their low falling velocity, the camera acquisition frequency could not be lowered without risking to have an unsatisfactory description of the bubble motion (which remained at high velocity). Consequently, recordings performed with ABS cylinders feature an extremely large amount of images (up to about 6000 images), which was deemed too costly in terms of memory (up to 50Go for 6000 images). Time constraints and the requirement for massive storage solutions for the experimental campaign did not allow more experiments to be carried out, the present data reaching a total of 11.6To. In the following, we will discuss in particular aluminum cylinders, as their statistics are the most converged. ABS and titanium cylinders will be used as a comparison to discuss the effect of the cylinder density on its dynamics.

Chapter 5

Bubble swarm characterization

5.1 Introduction

We perform an analysis of the characteristics of the bubble swarm itself. In this chapter, we present a study of the bubble swarm in our experimental setup. First, we describe the experimental means used to generate the bubble swarm, as well as the additional developments in image processing needed to obtain the trajectory of the bubbles and cylinder in the cell. Then, we check the spatial and temporal homogeneity of the bubble swarm. This first characterization allows us to compare to previous studies on the dynamics of confined bubbles swarm, notably to Bouche et al. [5, 6]. We measure the bubble size and velocity in our experiments, and compare them to the results of [5]. After having checked the good agreement between the two studies, we can use the results of [6] to obtain a general description of the fluid motion induced by the bubble swarm inside the confined cell in our configuration.

5.2 Generation of a bubble swarm in the confined cell: experimental tools and image processing

The experiments on the fall of a cylinder in a confined bubble swarm took place in the same cell and with the same cameras as for the study in the confined fluid at rest (see 4.2). However, the addition of a gas phase required to adapt the experimental setup and the image processing routines. This section describes how the bubble swarm was generated in the confined cell, and which image processing techniques were developed to properly characterize it.

5.2.1 Bubble generation

The generation of the bubble swarm in the cell is performed with capillary tubes. A series of 16 air injectors is inserted in the thin gap at the bottom of the cell, allowing the generation of a swarm of bubbles. The injectors external diameter is 0.9mm and their internal diameter, 0.6mm. The air injectors used by [5] have the same internal diameter, but a slightly smaller external diameter of 0.8mm. The injectors are regularly distributed across the entire width of the cell, so that the bubble swarm fills it entirely. They protrude of about 5cm from the bottom of the cell, which is needed for maintenance operations (see figure 4.1b). Indeed, cylinder dropped into the cell can only be recovered by opening up the bottom plate sealing the cell. The injectors, which are fixed to the bottom plate, need to protrude long enough in the cell to avoid slipping out of the gap when lowering

the bottom plate. Each injector has its own individual adjustable valve that can be used to change the air flow going through it. All the injectors are linked to a single feeder tank to equalize the pressure in each of them. The feeder tank, in turn, is linked to a pressure reducer connected to the laboratory pressure outlet (7bar). The pressure reducer is equipped with a manometer which is used to measure the global air pressure in the system (between 0.10 to 0.15mbar in our experiments) and with an oil filter.

In the present work, we wish to generate a swarm of bubbles whose size distribution is monodisperse. In order to do that, we need to inhibit bubble coalescence, which would otherwise create a wide variety of bubble sizes. Several studies have investigated the effect of electrolyte in solution to reduce the coalescence rate of a bubbly flow ([5, 39]). We therefore use magnesium sulfate ($MgSo_4$), similarly to Bouche et al. [5], in order to inhibit coalescence. A concentration of 0.05mol/l^{-1} is used, in accordance to the experimental procedure of Bouche et al. [5], which allowed the generation of a monodisperse bubble swarm up to a gas volume fraction $\alpha_g = 13\%$ in their case. It was shown in Jones and Ray [22] that magnesium sulfate has little effect on surface tension in this range of concentration (less than 2‰). However, in our case the $MgSO_4$ did not inhibit coalescence as much as in the work of Bouche et al. [5] for reasons yet unknown to us and despite the use of high purity magnesium sulfate, and attempts of increasing the concentration of $MgSO_4$. This limited the range of α_g we could explore, as for $\alpha_g > 5\%$, coalescence was too important to be considered negligible. As a result, the range of α_g investigated is in-between 2% and 5%. More details will be given regarding bubble coalescence in 5.4.

In order to generate a homogeneous bubble swarm, the physical spacing of the injectors and their bubble emission frequency need to be made equal across all injectors. The air flow in each individual injector is adjusted so that they all emit bubbles at the same frequency. This is achieved using a stroboscopic light projector in front of the injectors, and adjusting the air pressure of all individual injectors so that their bubble train appears to remain static to the naked eye. This method proved to be quick and efficient. The spacing of the injectors is adjusted by hand after each opening of the bottom of the cell, i.e. at the beginning of each day of experiment.

In a confined cell filled with distilled water, the generated bubbles have a velocity of about 10cm.s^{-1} and a diameter of about 4.5mm, giving a Reynolds number of about 450. A more precise description of the bubbles dynamics will be given in 5.3.

5.2.2 Image processing

New image processing techniques are introduced to handle the new issues that arise with the introduction of the bubble swarm. The first one is the individual tracking of the bubbles, which allows the measure of bubble velocities. The second one the distinction between the bubbles and the cylinder. This will be especially difficult when the bubbles and the cylinder are in contact, and form one single group of connected pixels. Specific techniques have been developed in order to properly separate the pixels belonging to the cylinder from the ones belonging to the bubble it is in contact with.

Bubble tracking is implemented using simply the distance between each consecutive bubble position. The high acquisition frequency of the camera (500Hz) allows the bubble displacement between two frames to be significantly smaller than the distance between two bubbles. As a result, the bubble trajectory can be computed easily by selecting the closest object to the bubble position in the previous frame. For each new frame, the position of each bubble is compared to the ones in the previous frame. The bubble trajectory is reconstructed iteratively, giving access to bubble velocities. Each bubble entering the field of view is counted as a new one, even when it is a bubble that had

Figure 5.1 – Left : image of a cylinder close to a bubble. Right : image of a cylinder in contact with a bubble

been previously identified, and had left the observation window (through the left or right border, for example). Coalesced bubbles are counted as new bubbles as well.

Distinguishing the bubbles from the cylinders when they are not in contact is straightforward. MATLAB© function `regionprops`, which is used after thresholding to determine the properties of detected objects, can output the Euler number. For a region of a binary image, the Euler number is defined as the number of objects in this region minus the number of holes in these objects. Applied to a single object, it is equivalent to counting the holes in this object. Bubbles naturally have holes in them, as only their interface is detected as an object (i.e. appears black on the image) leaving their centre as an open area (i.e. a hole), as illustrated in figure 5.1. The white area in the bubbles is useful, on that it gives the centroid position of the bubble regardless of any object it might be in contact with. All bubbles therefore have an Euler number of 0 (one object minus one hole), and the cylinder of 1. This criterion works well when the cylinder is not in contact with any bubble and was used without error to identify the cylinder in all experiments. The situation is different when the cylinder is in contact with the bubbles, as one single object is then formed by the combination of the cylinder and the bubble. This combined object has an Euler number of 0, because the bubble hole is detected.

The image processing algorithm processes the image series iteratively. When a cylinder is detected, its characteristics are recorded, and the next image is processed. There are two different scenarii in which no cylinder can be found. The first one is when the cylinder exits the observation window. The other one is when the cylinder gets in contact with a bubble. For each frame where no cylinder is detected, the algorithm first assumes that the cylinder is in contact with a bubble, and looks for an object formed by the combination of the cylinder and a bubble by temporal tracking.

When the algorithm finds a proper match for this object, it needs to separate the pixels belonging to the cylinder from the ones belonging to the bubble. Four different techniques are tested for each contact frame, and only one of them is selected (selection is done automatically by the algorithm). The best method is chosen according to a criterion which compares the perimeter, area and eccentricity of the outputs of different methods to the value of these variables for the cylinder when it is not in contact with any bubble. Additionally, the centroid position of the four different outputs are compared to a spline extrapolation of the known cylinder trajectory, i.e. the whole trajectory before the investigated contact. This ensures that the best method is used for each contact frame. If no match can be found, then the cylinder is assumed to be absent from the observation window.

The two first methods make use of a *watershed transform*. The different steps in the process are shown in figure 5.2. The first step is to compute the *distance transform* of the object, which assigns a value to each pixel of the object, which depends on the distance between this pixel and the closest one belonging to the same object. The *distance*

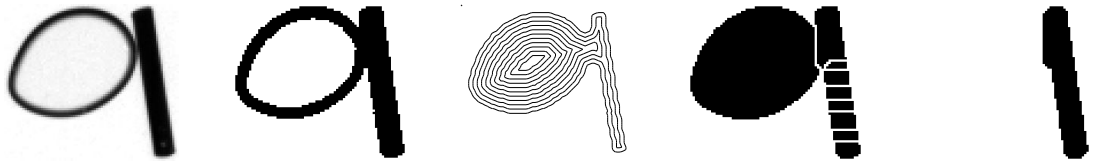

Figure 5.2 – Different steps in the segmentation process with the *simple watershed transform*. From left to right, raw image with background subtraction, binarized image, contour view of the distance transform of the object, watershed transform and finally the cylinder properly separated from the bubble.

transform can be seen as an elevation map, where dark pixels (i.e. with a low value, and therefore few neighbours belonging to the object) are of low elevation, and light pixels (i.e. with a high value, and therefore lots of neighbours belonging to the object) of high elevation (see frame 3 of figure 5.2, where the bubble is of high elevation, and a ridge is formed between the two objects and along the cylinder). The *watershed transform* makes use of this map to determine the separations between the objects, by looking for basins or ridges in the *distance transform*. Indeed, for each individual object, the pixels close to the object center have a high value because they are surrounded by a lot of other pixels belonging to the object, and pixels close to the border of the object have low values. When two different objects are touching each other, it creates a contact area where pixels otherwise belonging to the border of the objects have a high value. On the distance transform, this area forms a ridge between the two objects. Such a marker can be detected by the *watershed transform*, which will then attempt to separate both objects along a line orthogonal to the ridge. More information can be found in the documentation of MATLAB© function `watershed`. This method works best when the cylinder and the bubble have a short contact length (for example, when the cylinder impacts the bubble with its end), as that creates an obvious basin to be found by the *watershed transform*. When that is the case, the segmentation is extremely good, and the output of the contact handling function is very close to the cylinder when it is not in contact with any bubble. However, when the contact length is longer (for instance, when the cylinder falls flat on the bubble), the performance tends to be poor as the watershed transform cannot find any ridge or basin to work on. Contacts during which the cylinder pierces a bubble (see 6.2.1) are also especially difficult, as the contact length encompasses a large part of the cylinder. When the cylinder is in contact with more than one bubble at a time, the performance is also poor, as the cylinder elongated body forms a natural ridge between the two bubbles, and it is nearly always cut in half by the segmentation. In the distance transform of the object, ridges are clearly seen. The watershed transform correctly finds them, and segments the image into multiple parts. The cylinder itself is segmented, but that is not an issue, as the bubble is not. The object closest to the position of the bubble (known thanks to its white area) is removed from the image, leaving only the remaining pixels, belonging to the cylinder. In the cases shown in figure 5.2, the simple watershed transform was chosen as the best method.

Two different variants of the watershed transform have been implemented. The first one is denoted *simple watershed*, and consists in applying the distance transform, then the watershed transform to the object without any additional input, as described above and on figure 5.2. The second one is called the *marker-controlled watershed transform*, and is shown in figure 5.3. In this variant, guesses of the position of the bubble and of the cylinder are given to the watershed algorithm in order to provide better results. The position of the bubble is easily found thanks to its open centre area. For the cylinder, the orientation and centroid displacement are extrapolated, using a spline and the cylinder trajectory prior

Figure 5.3 – Different steps in the segmentation process with the marker-controlled watershed transform. From left to right, raw image with background subtraction, binarized image, mask applied to the object, with the guesses of both the bubble and the cylinder, watershed transform and finally the cylinder properly separated from the bubble.

to the contact. Then, the cylinder contour in the previous time step is rotated and moved accordingly. We cannot rely entirely on this extrapolation, as, especially in contact cases, the cylinder motion can be unpredictable, and the extrapolation is highly susceptible of being erroneous. Consequently, the cylinder guess is taken from the pixels that are found in both the extrapolated contour and the object formed by the combination of the bubble and the cylinder. Once we have a guess for both objects, we can impose local minima (i.e. create a mask) in the *distance transform* of the combined object at the emplacement of these two guesses, meaning that a ridge will naturally be located between the two guesses. This method sometimes yields better results than the simple watershed transform, but is dependent on the accuracy of the extrapolation of the cylinder. Additionally, it retains all the disadvantages of the watershed transform, so that it will perform poorly when the contact length between the two objects is long, of when the cylinder is in contact with several bubbles. In this particular case, the guess for the cylinder is satisfactory, ending up with a proper segmentation of the object.

The third method, whose steps are visible in figure 5.4, makes use of an interesting property of the bubbles, which is their central area. In the objects formed by the combination of the bubble and the cylinder, this gives an interesting starting point to separate the two objects. More specifically, in this method, we aim at cropping out the pixels belonging to the bubble from the combined object. The bubble interface thickness is nearly constant for a bubble. It also follows the same shape as the bubble open area. Therefore, by "extending out" the central area, it should be possible to recreate the shape of the bubble with a certain degree of accuracy. Practically, the outer boundary of the bubble central area is found, and divided into four quadrants, corresponding to four directions, top, bottom, left and right. Pixels are assigned to one of this quadrant depending on their angular position compared to the bubble centre. Pixels whose angular position lies in the range $]\pi/4, 3\pi/4[$ belong to the top quadrant, in the range $]3\pi/4, 5\pi/4[$ to the left one, in the range $]5\pi/4, 7\pi/4[$ to the bottom one, and $]7\pi/4, \pi/4[$ to the right one. These quadrants are visible in the third frame of figure 5.4. The next step is to extend the bubble contour. The pixels belonging to each quadrant are moved away from the bubble centre iteratively one pixel at a time, depending on which quadrant they belong to. Pixels belonging to the top quadrant are moved upwards, those belonging to the left quadrant are moved to the left and so on. As the starting position of these pixels is the bubble open area, this motion makes them cross the bubble interface, belonging to the combined object. When one of the quadrant has moved far enough to lie outside the bubble interface, the extension is stopped, and the area delimited by the four quadrants is cropped out of the combined object. This method works better than the two *watershed* ones when the contact length between the cylinder and the bubble is long. It comes with the additional benefit of working when the cylinder is in contact with several bubbles at once. However, the performance is still poor for bubble piercing, and this methods has a general tendency on cropping out a part of the cylinder alongside the bubble. Regrouping

Figure 5.4 – Different steps in the segmentation process with the *bubble cropping segmentation method*. From left to right, raw image with background subtraction, binarized image, area which is going to be cropped and cylinder properly separated from the bubble.

Figure 5.5 – Different steps in the segmentation process with the *morphological* method. From left to right, raw image with background subtraction, binarized image, eroded object dilated object and cylinder properly separated from the bubble.

the pixels in quadrants was found to work better than to extend the bubble contour by taking the pixels individually, as it retains a bigger part of the bubble original shape. Two different quadrant orientations were tried out, the current one, and a diagonal one (where the criterion on the angular position was $]0\,\pi/2[$ and so on), and the current one was more accurate. The downside of the bubble cropping method is that its performance is tied to the bubble shape. Small, quasi-circular bubbles offer good results, but large coalesced bubbles, or bubbles that are heavily deformed by the contact with the cylinder are more difficult to process. In the case featured in figure 5.4, the cropping methods works almost perfectly, cropping only the bubble contour without removing any cylinder pixel. The four quadrants are clearly visible on the third frame.

The final segmentation method used is *morphological*. The combined object is eroded and dilated in order to erase the bubble from the combined object. Indeed, the bubble interface is typically thinner than the cylinder diameter. Therefore, eroding the combined object by a value which is larger than the typical bubble interface, but smaller than the cylinder diameter will erase the bubble entirely, while keeping a small part of the cylinder. The cylinder is then reconstructed during the dilatation step. This segmentation method works reasonably well in a lot of cases, since this bubble property is independent on the bubble shape. However, cylinders falling flat on top of bubbles are still a problem, as they are badly reconstructed during the dilatation step. Figure 5.5 shows an example of a morphological image transform. The bubble is entirely erased from the object during the erosion, and the cylinder is properly reconstructed afterwards. A small error is visible near the contact point between the two objects, where several bubble pixels are attributed to the cylinder.

The simple watershed method is used in about 14.5% of the contact cases handled, the marker-controlled watershed is used in about 19.5%, the bubble cropping in 50% and the morphological method in about 16% of all cases studied. Having several segmentation methods allows us to handle a wide variety of contact situations. Each one of the methods used has different specificities, being each capable of dealing with certain situations better. Additionally, being relatively light on computation time, they can all be executed at once when dealing with a contact case. Their results are compared afterwards, and the output of only one of them is selected.

Figure 5.6 shows a comparison of the outputs from the different segmentation methods

Figure 5.6 – Comparison of the different contact handling methods. From left to right, raw image with background subtraction, output of the *simple watershed method*, from the *marker-controlled watershed method*, from the *bubble cropping method* and from the *morphological method*.

for a single case. Some situations are poorly handled by all four methods, namely bubble piercing, contact with multiple bubbles or when the cylinder is in contact with a bubble, which is itself touching another bubble. The perimeter and area of the output of the contact handling function are compared to their known values for the cylinder not in contact with any bubble. Should their values differ too much, the output of the contact handling function is cleared and the various properties of the cylinder filled with NaN, resulting in blanks in the trajectory. Even when the output of the contact handling function was deemed satisfactory, errors remain, which depend a lot on the contact situation. The error on the cylinder separation during contact can be estimated using the cylinder area. For each run, we can compute $\Delta A/A$, where ΔA is the difference between the mean area during the contact events and with no contact, and A is the mean area with no contact. By averaging the values of all the runs, we find $\Delta A/A \simeq 1.17\%$. Yet, during contacts, small errors on the position of the cylinder centroid prove to be detrimental to the accurate computation of the cylinder velocity. As a result, the cylinder centroid position is smoothed over the duration of the contacts only, using a moving average over a span of 5 points.

5.3 Gas volume fraction and bubble spatial distribution

In this section, we shall provide a detailed description of the bubble swarm, checking its homogeneity and introducing a statistical description of the bubble motion. This will allow to compare our swarm with one already explored ([5, 6]), and possibly use the knowledge of the agitation of the liquid phase that has already been obtained ([6]). We will see that generating a homogeneous bubble swarm it not a trivial matter due to coalescence. We thus present the operating limits where homogeneity is achievable.

5.3.1 Temporal and spatial bubble swarm homogeneity

For several gas injection conditions, a map of α_g averaged over time and for about 20 different runs is used to visualize the bubble swarm homogeneity over the observation window (figure 5.7). A run consists in the record of the whole trajectory of a given cylinder observed in the observation window. The bubble statistics presented in this section are the result of a bubble swarm analysis performed over 19 to 21 runs for each of the mean values of α_g investigated, totaling 100 runs. The maps are created by superposing bubbles images, where the inside of a bubble is counted as a 1, and the outside as a 0. All values in the resulting images are divided by the number of images taken, ending up with the gas volume fraction in the field of view. The images are then over-segmented into regions of about 1cm^2, corresponding to about 220px. The value of the gas volume fraction is

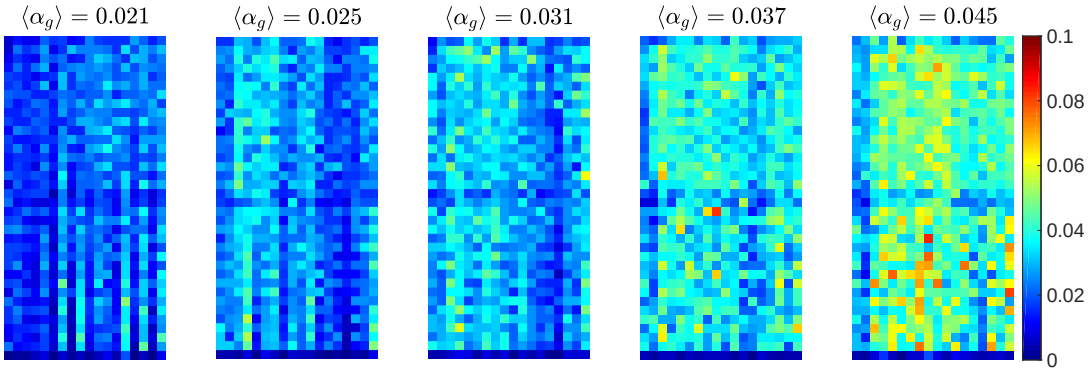

Figure 5.7 – Map of the gas volume fraction α_g over the observation window for each range of α_g. α_g is averaged over regions of $1cm^2$. Values of α_g are inferior to what they should be near the borders of the field of view, and along the line separating the fields of view of the two cameras in the middle of the window. This is caused by the image processing routines, as all bubbles touching any border of the field of view are removed from the images to avoid incomplete objects

averaged over these pixels. Images separated by at least $0.2s$ were taken to combine independent events, as this time interval is superior to the correlation time calculated by Bouche et al. [5] over the same range of α_g.

For the lowest α_g range investigated, $\langle\alpha_g\rangle = 2.1\%$, bubble injectors induce a noticeable modulation in the spatial repartition of α_g in the lower half of the observation window. The bubble dispersion is not sufficient to completely remove the memory effect of the injectors. In the upper half of the observation window, however, the effect of the injectors can hardly be seen. For $\langle\alpha_g\rangle = 2.5\%$, the mark of the injectors is barely visible in the lower half of the observation window. There seems to be an elongated region in the right half of the window where bubbles are scarcer. The probable reason for this is the difficulty of evenly spacing air injectors. Except in this zone, for all $\alpha_g \geqslant 2.5\%$, the gas volume fraction is quite homogeneous in the observation window. This minor lack of bubble spatial homogeneity has little impact on the bubble dynamics in the swarm.

After having discussed the spatial homogeneity of the bubble swarm, we will characterize the temporal homogeneity as well. A proper temporal homogeneity is needed to perform measurement of the cylinder motion for a given gas volume fraction. Stationarity does not mean constant gas volume fractions, and temporal fluctuations of the gas volume fraction may occur. The temporal evolution of α_g has been plotted on figure 5.8 for two examples featuring extreme behaviours. In blue, we can see a case where the gas volume fraction is nearly constant for the entire length of the run. In red, on the other hand, we feature a case where more important variations of the gas volume fraction are observed during one run. This is normal for high gas volume fraction, where spontaneous gas volume fraction variations may appear in the swarm dynamics.

A coefficient that characterize the variation of α_g over time can be calculated simply as the following : $\langle\alpha_g(t)^2\rangle^{1/2}/\overline{\alpha_g(t)}$. It is found to range from 1.4% to 15%, and superior to 10% in only 31 out of 662 runs (or all 546 aluminum cylinders runs but 28). This ensures that the time variation of the gas volume fraction is not significant, and does not affect our results.

The bubble swarm temporal and spatial homogeneity has been checked to be satisfactory over all cases studied. The ranges $\alpha_g = 2.1\%$ and $\alpha_g = 2.6\%$ show some spatial inhomogeneity, but they are minimal, and we will show that they have little impact on the bubble motion, and on the cylinder trajectory.

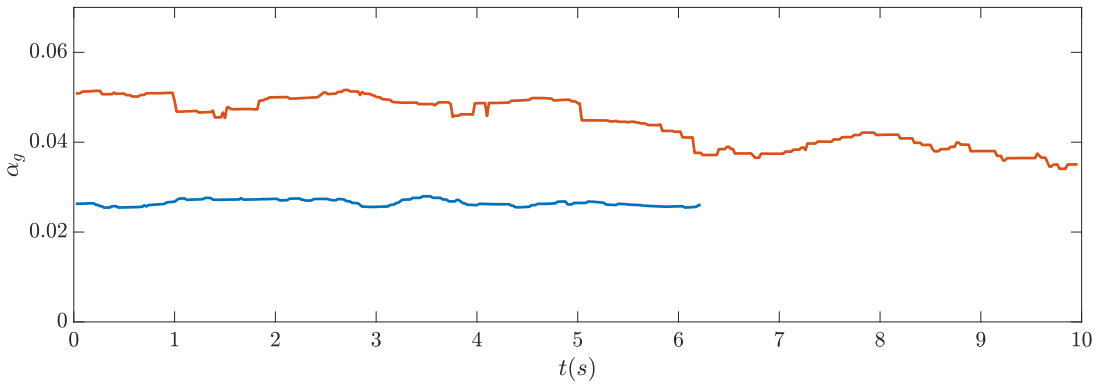

Figure 5.8 – Plot of the time variation go α_g for two different runs

5.3.2 Investigated gas volume fractions

The experiments were conducted for gas volume fractions ranging from 1.4% to 6.6%. No direct measurement of the gas volume fraction was performed during the experiments, as it would have required additional time devoted to image processing for each run. Instead, α_g was assumed to be proportional to the input air pressure. This assumption was checked to be reasonable afterwards. As described in section 5.2, an adjustable pressure reducer was inserted in the air circuit. The air pressure was read using a manometer mounted directly on the pressure reducer, and ranged from 0.10 to 0.15mbar. This method allowed for a quick adjustment of the gas volume fraction inside the cell, but did not allow to set accurately α_g for a long period of time, as the input air pressure could vary at long time. The actual measure of α_g was done *a posteriori* when the images were processed. The image processing routines use binarized images, which made the computation of the ratio between the bubble area and the total measurement area easy. For each single experiment, α_g could be measured as a function of time, and an average value was computed for the experiment. Figure 5.9 shows example of camera views for the different investigated gas volume fractions. The bubble density varies with the gas flow rate, and at large gas volume fraction, large bubbles appear due to coalescence. Ideally, a bubble swarm without coalescence would have been more homogeneous and thus easier to study. Experimental constraints forced us to tolerate a certain amount of coalescence in order to reach higher gas volume fractions. The higher limit of the gas volume fraction was the bubble flow where the maximum tolerable coalescence rate was observed. The lower limit of the gas volume fraction was fixed at the point where the bubble swarm was no longer homogeneous due to gas inlet injection. At low gas volume fraction, bubbles rise in lines at the vertical of the air injectors and do not mix enough to create a homogeneous swarm.

In order to check if our experiments allow us to reach satisfactory statistical convergence, and similar conditions for each type of cylinder, we examine the gas volume fraction generated during our runs. The histogram of investigated α_g for aluminum cylinders at different elongation ratios is displayed on figure 5.10. The instantaneous values of α_g measured for each frame of the image sequences are used. As mentioned before, it shows that not all elongation ratio were investigated over the exact same range of α_g. A larger amount of experiments was performed for $\xi = 7$, 12 and 20 (with a an additionnal emphasis on $\xi = 7$). The investigated α_g for these cylinders covers all different ranges of gas volume fractions, with slightly more data in the range $\alpha_g \in [2.8\%\, 4.1\%]$. The other elongation ratios were not studied as extensively, and the distribution of α_g for cylinders of $\xi = 3$, 5 and 10 features two peaks at around 2.5% and 4.1%, with less experiments around $\alpha_g = 3.3\%$. Obviously, the number of runs performed for both categories of elongation ratio also differs.

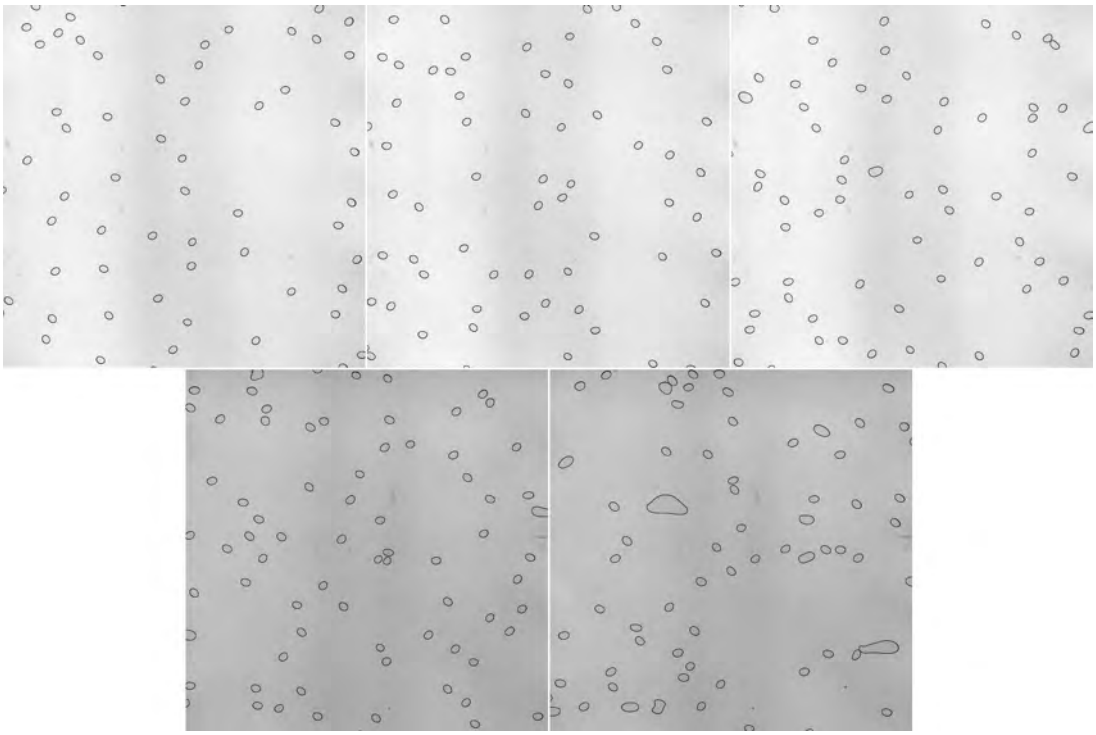

Figure 5.9 – Examples of several images of the bubble swarm for various gas volume fractions. They correspond, from left to right, to the five ranges of gas volume fractions described in this section. A difference in contrast is observed due to the last two images not coming from the same camera than the other three.

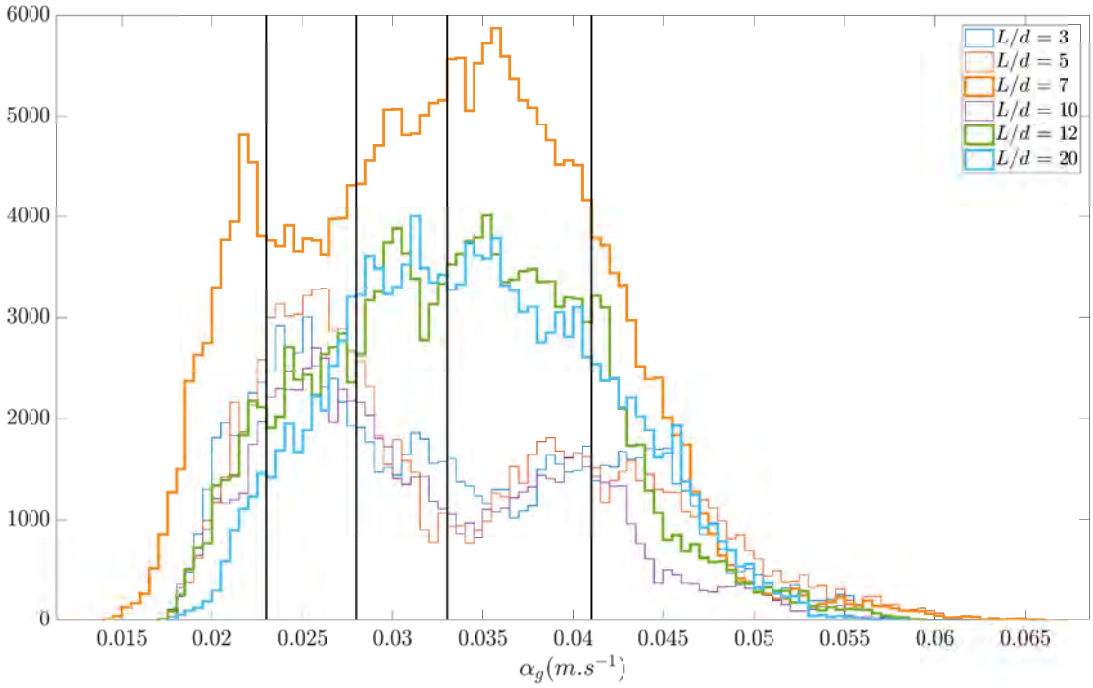

Figure 5.10 – Histogram of the instantaneous gas volume fractions investigated for different ξ. The vertical lines show the different ranges of α_g that we defined.

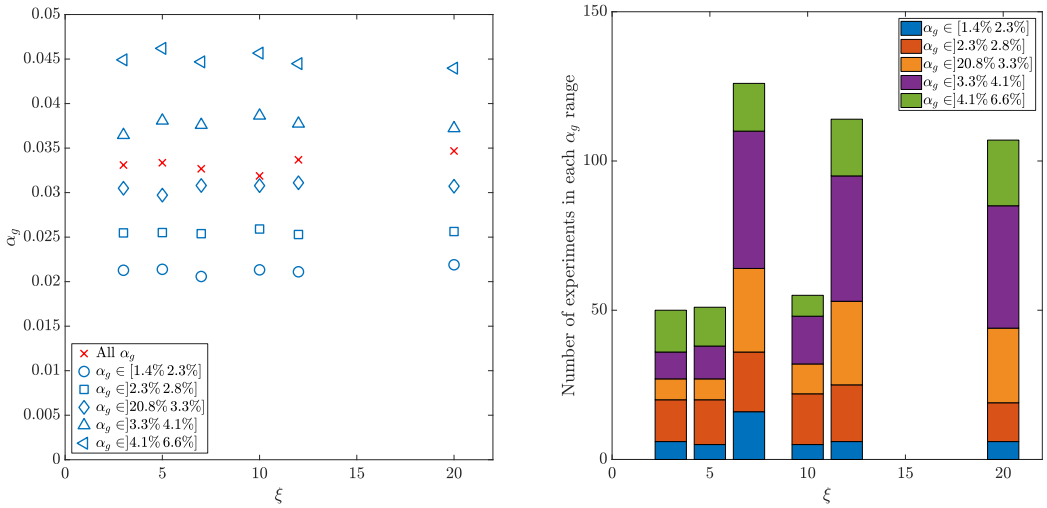

(a)

(b) Number of experiments performed in each α_g range and for all ξ

Figure 5.11 – (a) Values of the mean α_g for all ξ, for aluminum cylinders, (b) Number of experiments performed in each α_g range and for all ξ

Several ranges of α_g are defined to investigate the influence of the gas volume fraction. They are delimited with vertical black lines on figure 5.10. Runs belonging to each of these ranges, are considered to be performed at the mean value of α_g in each of these ranges, 2.1%, 2.5%, 3.1%, 3.7% and 4.5%. For the first range of gas volume fractions, all elongation ratios but $\xi = 7$ have roughly the same number of data points. This is also the case for the second range of α_g, with still more data for $\xi = 7$. Over the third and fourth range, we see a significant decrease in data for $\xi = 3$, 5 and 10. In the final range of α_g, there is slightly more data for $\xi = 7$, 12 and 20, even though the difference is lower at very high gas volume fraction. The distribution shows that cylinders of $\xi = 10$ have even less data in this range than the other ξ.

Figure 5.11a shows the mean values of α_g per range, for all ξ. Although not all ξ were investigated in the exact same conditions, the mean gas volume fractions for all ξ is rather independent of ξ over each defined range. That proves that despite a slightly uneven repartition of α_g in each range, the definition of these ranges is adequate to properly describe the average gas volume fraction. Moreover, the gas volume fraction averaged across all ranges (red crosses) is also close to being constant. All elongation ratios can therefore be compared at different α_g without bias. It should however be noted that the number of experiments performed differs for the various elongation ratios and α_g ranges, as shown in figure 5.11b, which should be kept in mind for a statistical study of the cylinder kinematics. For all ξ, the lowest range of gas volume fraction, $\alpha_g \in]1.4\%\ 2.3\%]$ has fewer experiments than the other ones. In this figure, the values of the gas volume fraction used are averaged for each run, instead of being the instantaneous gas volume fraction in a run, such as in figure 5.10. The two descriptions share common features, such as the predominance of the second and last range of α_g for ξ =3, 5 and 10, and of the third and fourth for the remaining ξ.

Even though the investigated gas volume fraction vary depending on ξ, all elongation ratios can be compared over all ranges of α_g, as shown in figure 5.11a. Vigilance is required, however, when comparing statistics at different α_g, as the size of the sample studied varies with α_g (figure 5.11b).

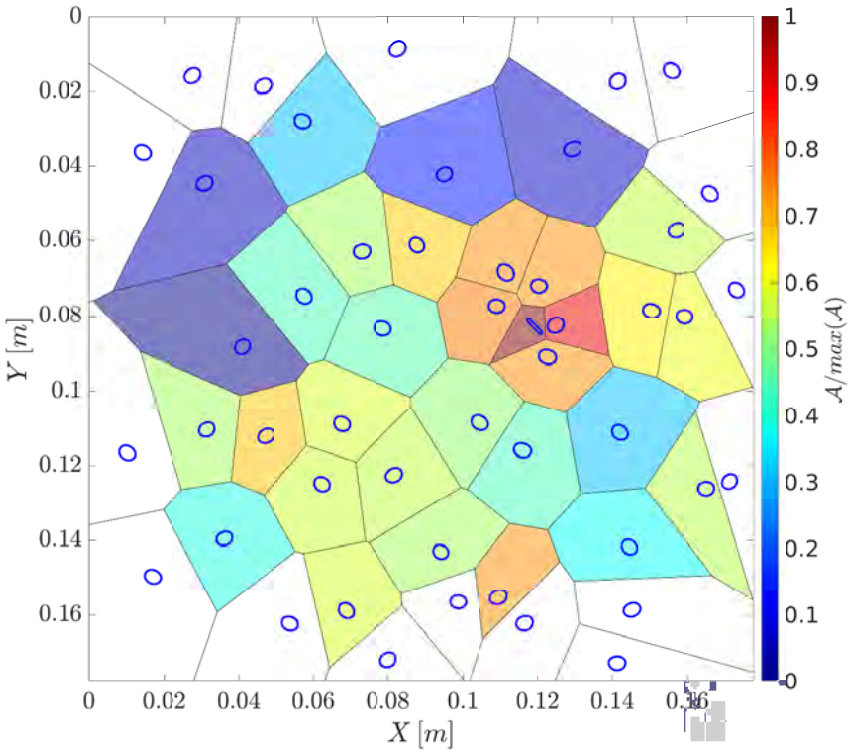

Figure 5.12 – Example of a Voronoi tessellation in the bubble swarm. The colors are dependent on the area of the Voronoi cell, normalized by the area of the biggest cell in the frame, then reversed. As a result, smaller cells and big concentrations of objects appear in hotter colours.

5.3.3 Bubble spatial distribution

The bubble spatial distribution in the confined cell is studied using a Voronoi tessellation. Our goal is to know if, on statistical average, the bubble swarms adopts a random spatial distribution, a random distribution with underlying macroscopic order, or if clusters and voids are present. An accurate description of the bubble spatial distribution will allow us to know if the cylinder tends to go through peculiar regions of the swarm, such as clusters or voids. Two-dimensional Voronoi diagram creates regions based on a set of points, and defined as the space of points which are the closest to a specific point. An example of this tessellation applied to our configuration, using the bubbles and cylinder centres of mass as our set of points, can be seen in figure 5.12. Properties of the Voronoi tessellation have been used in previous works on point particle clusters (see [17, 25, 29]) to characterize particles spatial distribution. In this work, we will use the area of the Voronoi cells to describe the bubble swarm.

MATLAB© functions `voronoi` and `voronoin` are used to perform the Voronoi tessellation. The area of each Voronoi cell is then simply measured based on the vertices of the cell. The cylinder has its own cell, and is treated exactly like a bubble during the tessellation. The area of the Voronoi cells intersecting the limits of the observation window is not computed, as it has no physical meaning. As a result, there is less available Voronoi data, which can cause statistical convergence issues for the Voronoi area including the cylinder. This is not really a problem for the bubble data because of the great amount of bubbles in the cell. It should also be noted that the tessellation is done by taking center of the objects as inputs, not their entire contour. Consequently, it is possible that an object contour lies outside the boundaries of the Voronoi cell associated with said object. This is especially the case with large objects such as long cylinders or coalesced bubbles.

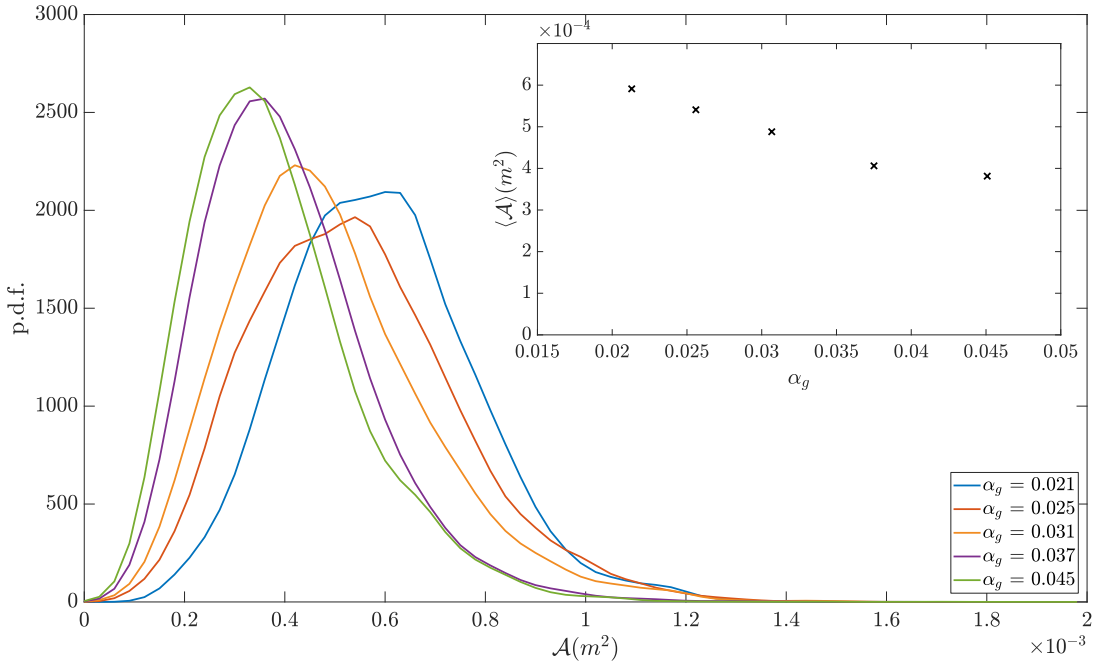

Figure 5.13 – Probability density function of the bubbles Voronoi area, denoted $\mathcal{A}$, as a function of α_g. The inset shows the mean value of $\mathcal{A}$.

The area of the Voronoi cells is shown on figure 5.12 with a color code. All the white cells do not have their area computed as some of their vertices lie outside the boundaries of the observation window. We write $\mathcal{A}$ the area of the Voronoi cells of the cylinder, and $\langle \mathcal{A} \rangle$ the mean area of the Voronoi cells of a frame.

Figure 5.13 shows the p.d.f. estimated by the normalized histograms of the bubble Voronoi areas in the cell for the different ranges of α_g that were studied. The mean area for each range is shown in the inset. The Voronoi area tends to decrease with increasing α_g, with mean Voronoi cell area going from 6.10^{-4}m^{-2} for $\langle \alpha_g \rangle = 2.1\%$ to 4.10^{-4}m^{-2} for $\langle \alpha_g \rangle = 4.5\%$. The bubbles are more tightly packed together at high gas volume fraction. Additionally, the distribution also gets narrower and more left-skewed with α_g, meaning that there is an increasing number of small cells at high gas volume fraction. Large cells are still observed, although both the biggest observed cell and the number of big cells decreases with α_g.

The normalized Voronoi cell area of perfectly randomly and uncorrelated distributed points follows a predictable distribution, called a Poisson Voronoi Diagram (see [15, 29]). Comparison with this ideal distribution allows to characterize the spatial bubble distribution. Indeed, a distribution which is narrower than the Poisson Voronoi Diagram (P.V.D.) indicates a more organized distribution than a perfectly random one. The standard deviation of the distribution, noted σ_ν can be used an an indicator of this tendency, with $\sigma_\nu = 0$ being the limit of a perfect crystal, and $\sigma_\nu \simeq 0.53$ being the value attained for a Poisson Voronoi Diagram.

Figure 5.14 shows the distribution of normalized Voronoi area for the different ranges of α_g. The inset shows the standard deviations of these distributions. The distribution of the normalized Voronoi areas for the bubbles in the bubble swarm is narrower than the one of the Poisson Voronoi Diagram for all α_g. The amount of small cells ($\mathcal{A}/\langle \mathcal{A} \rangle < 0.5$) is significantly lower than for a perfectly random distribution. In addition, there is nearly no extremely small cell ($\mathcal{A}/\langle \mathcal{A} \rangle < 0.1$). In our case, the particle size isn't negligible, meaning that there is a lower limit attainable for $\mathcal{A}/\langle \mathcal{A} \rangle$, as no Voronoi cell can be smaller than a bubble. The minimum normalized Voronoi area is simply given by the ratio of

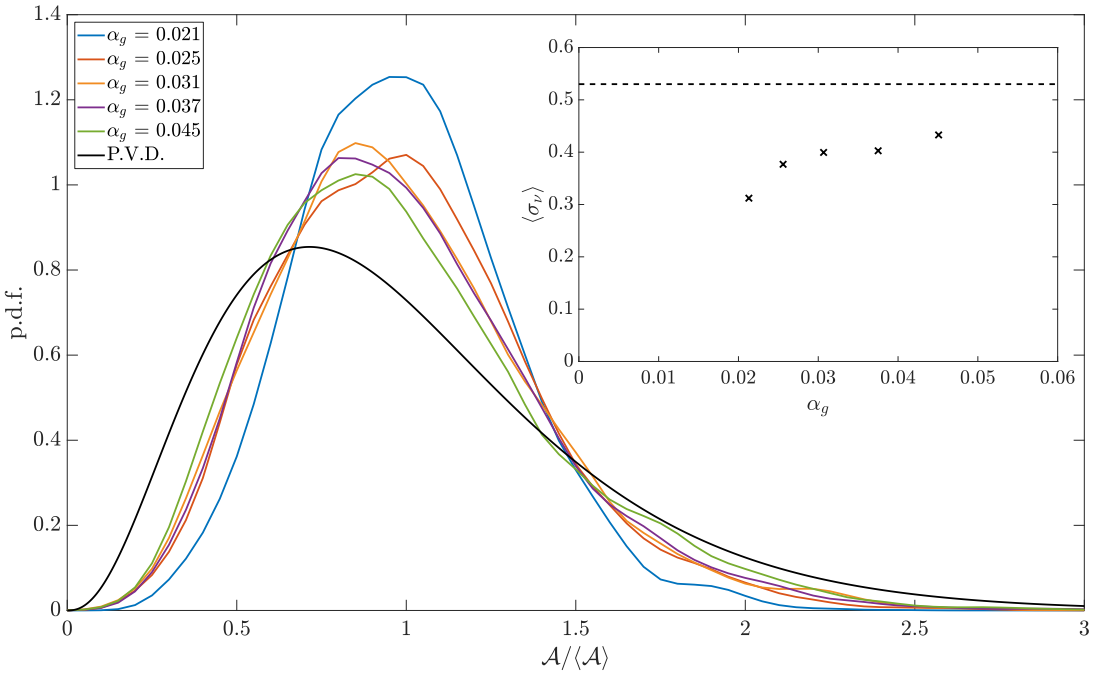

Figure 5.14 – Probability density function of the normalized bubbles Voronoi area, denoted $\mathcal{A}$, as a function of α_g. The inset shows the standard deviation of these normalized areas σ_ν, with the dashed line being the value for a Poisson Voronoi Diagram.

the bubble area to the Voronoi cell area, which corresponds to α_g. For all gas volume fractions, we also find significantly less big Voronoi cells ($\mathcal{A}/\langle\mathcal{A}\rangle > 1.5$). The distribution of $\alpha_g = 2.1\%$ is also noticeably narrower than the other ones, which is characteristic of a particle distribution that is more organized than a perfectly random one. This is confirmed by looking at the standard deviations of the distributions, $\langle\sigma_\nu\rangle$, which are lower than the standard deviation of the Poisson Voronoi Diagram. We also see an increase of the standard deviation with α_g, with $\sigma_\nu = 0.32$ at $\alpha_g = 2.1\%$, $\sigma_\nu = 0.38$ at $\alpha_g = 2.6\%$, and a constant value of about $\sigma_\nu \simeq 0.42$ for $\alpha_g = 3.0.\%$ and 3.7%, and a slight rise for $\alpha_g = 4.3\%$. This observation is consistent with the maps of α_g in the cell (see 5.3.1), which show that the bubble swarm is less homogeneous at these two lower gas volume fractions, as the injectors leave a noticeable trace in the swarm, and there are slightly less bubbles on the right side of the cell.

The distance between the bubbles is not easy to estimate directly. The simple computation of the distance between each pair of bubbles in the observation window is time-consuming, and give results which are dependent on the size of the window. Voronoi cells being defined as the space which is the closest to a certain bubble, it seems natural to use it as a tool to determine the average distance between 2 bubbles. As long as the entire bubble is comprised in its Voronoi cell, the local gas volume fraction inside a Voronoi cell can simply be defined as the ratio between the bubble area and the cell area.

$$\begin{aligned} \alpha_g &\simeq \frac{\pi d_b^2/4}{\mathcal{A}} \\ \mathcal{A}^{1/2} &\simeq \sqrt{\frac{\pi/4}{\alpha_g}} d_b \end{aligned} \tag{5.1}$$

This result can be compared to a simple model, as shown in figure 5.15a. An idealized square section of the cell is taken, of side length L_{12}, with 4 quarters of a bubble whose

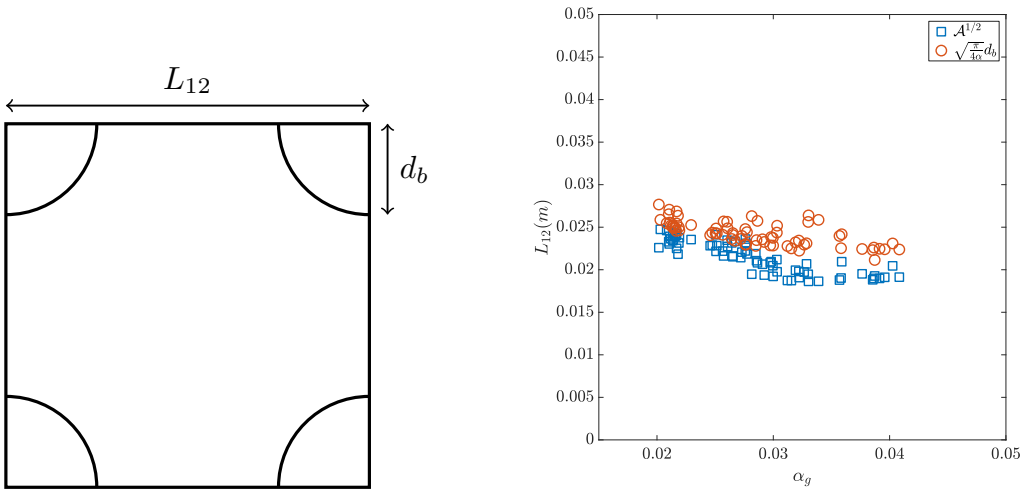

(a) (b)

Figure 5.15 – (a) Schematic view used to estimate the distance between two bubbles as a function of α_g. (b) Comparison of the distance between bubbles L_{12} estimated with the method illustrated in (a) with the square root of the mean Voronoi area of the bubbles in the cell.

centers are located on the corners of the square. In this model, one can very simply express L_{12} as a function of α_g :

$$\alpha_g = \frac{\pi d_b^2/4}{L_{12}^2}$$
$$L_{12} = \sqrt{\frac{\pi/4}{\alpha_g}} d_b \tag{5.2}$$

The concordance between this simple model and the measure of $\mathcal{A}^{1/2}$ (5.1) can be checked on figure 5.15b. There is a very good agreement between the measure of $\mathcal{A}^{1/2}$ and the expression of L_{12} used in (5.2). The values of $\mathcal{A}^{1/2}$ and of L_{12} differ by fewer than 5%.

The estimation of the mean distance between two bubbles can later be compared with the cylinder length as a tool to estimate the probability the cylinder will have to encounter bubbles during its fall in the swarm. Additionally, having a simple model that works well with measured data can prove to be useful when characterizing a confined bubble swarm.

5.4 Bubbles size and velocity

Precise characterization of the bubble swarm is necessary to conduct an in-depth analysis of the cylinder motion in the swarm. The study of Bouche et al. [5] has been done in the same confinement condition than ours, and focused on the study of the bubbles kinematics. If our bubble swarm behaves similarly to the one of Bouche et al. [5], it will justify the use of their analysis, as well as the characterization of the liquid perturbations induced by the bubble swarm that they have explored (see Bouche et al. [6]).

The bubble statistics shown in the present section come from the same set of data than the one investigated in 5.3.1.

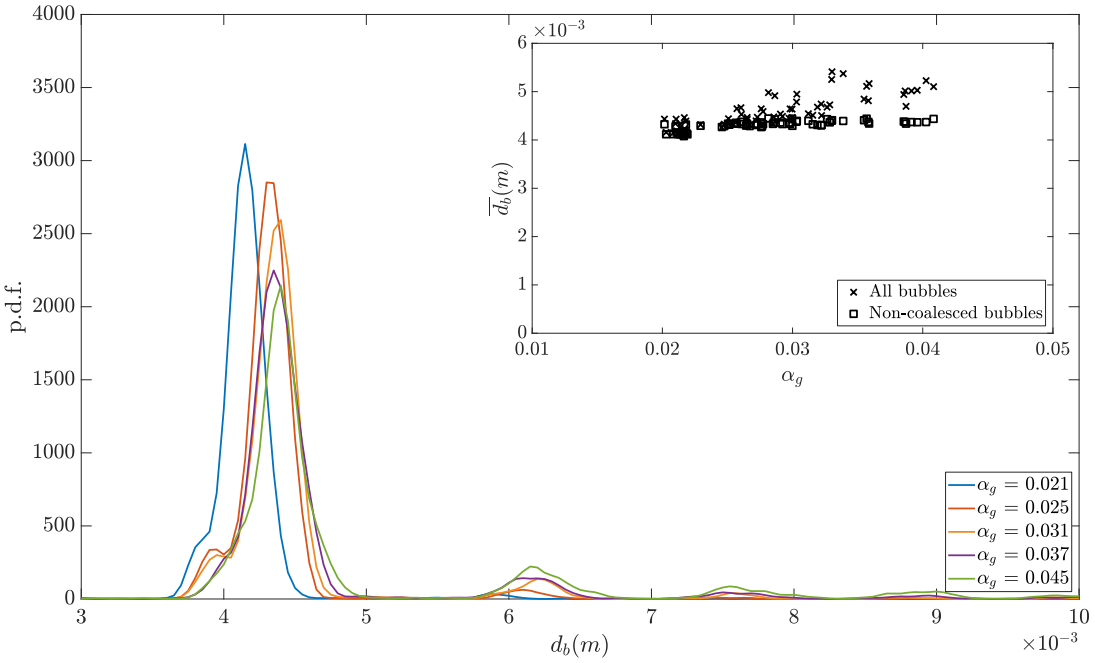

Figure 5.16 – P.d.f. of the the bubble diameter for different ranges of α_g. The inset shows the mean bubble diameter for a run as a function of α_g with black crosses, and the mean diameter of only bubbles within the first peak in the p.d.f. of d_b, corresponding to non-coalesced bubbles, in black squares.

5.4.1 Bubble size

The bubble diameter is defined as the diameter of a disk having the same area as the bubbles $d_b = \sqrt{4A_b}/\pi$ with A_b being the bubble area projected on the plane of the cell. Figure 5.16 shows the distribution of bubble diameters for our experiments, at different α_g. As our image processing techniques allow the tracking of the bubbles, each bubble diameter (involved in the pdf in figure 5.16) is calculated as the average of all diameter measurements for this bubble as it moves through the observation window.

The bubble diameter distribution shows a main peak between 4.1mm and 4.4mm for $\alpha_g = 2.1\%$ and 4.5% respectively. These values are slightly greater than the ones observed by Bouche et al. [5]. This is probably caused by the use of different capillary tubes (see 5.2 for more details). The presence of bubble coalescence is shown with a secondary peak around $d_b = 6$mm, and a tertiary one for $d_b = 7.7$mm. The coalescence was a more predominant phenomenon in our study than in the one of Bouche et al. [5], despite the addition of $MgSO_4$ in the cell. The addition of $MgSO_4$ was not, however, totally without impact, as it decreased significantly the bubble coalescence compared to the case where only pure distilled water was used.

The variation with α_g of the mean bubble diameter for a run, denoted $\overline{d_b}$, is shown in the inset of figure 5.16. Two values are given, the mean diameter of all bubbles, and the mean diameter of only non-coalesced (i.e. whose diameter belongs to the first peak in figure 5.16) bubbles. While the mean bubble diameter goes up significantly with α_g, from about 4.2mm at $\alpha_g = 2.1\%$ to $5.5mm$ at $\alpha_g = 5\%$, the gas volume fraction has a much smaller impact of the diameter of non-coalesced bubbles, with a variation from 4.2mm to 4.5mm for the same range of α_g. There is also a noticeable increase in the difference between overall mean diameter and non-coalesced diameter with α_g. This means that bubbles whose diameter is close to the diameter at injection (i.e. non-coalesced bubbles) are the most numerous, but the coalescence rate rises with α_g. The number of bubble

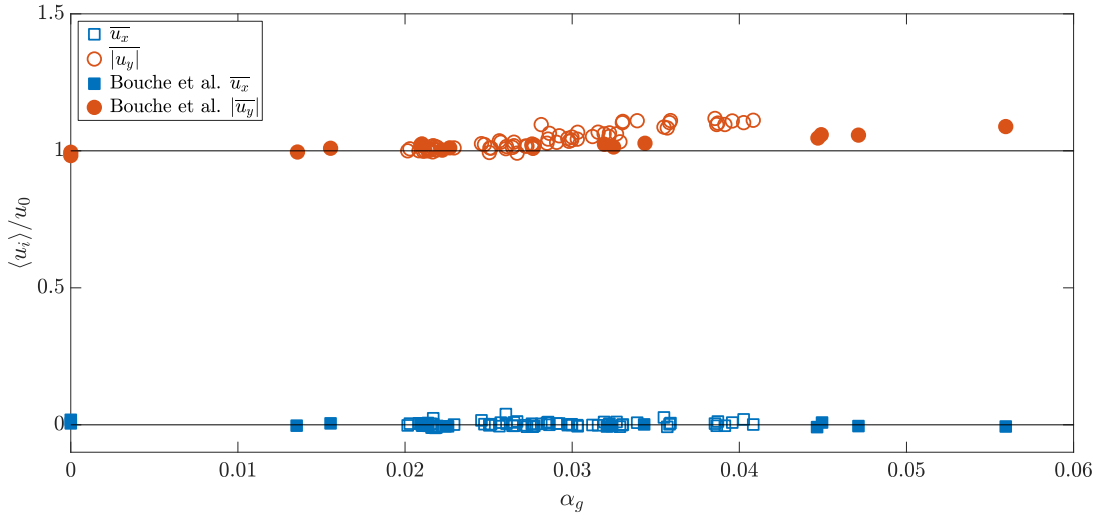

Figure 5.17 – Bubble mean horizontal and vertical velocity as a function of α_g, normalized by the velocity u_0. The horizontal velocity is plotted using squares, and the vertical velocity using circles. The empty symbols are the data of the present study, and the filled ones the ones of Bouche et al. [5].

whose diameters is greater than the ones in the first peak has been found to go from 0% to about 17% of all observed bubbles over the range of α_g investigated.

We have not performed any measurement of the bubble aspect ratio in the present work. It is defined as the ratio between the major and minor axis of an ellipse having the same moments of inertia. We have neither measured the angle between the major axis and the horizontal nor the angle between the vertical velocity and horizontal velocity. The bubble aspect ratio can be important during the interactions between the cylinder and the bubble swarms, as it influences the contact probability between the cylinder and a bubble. Roig et al. [32] give a relationship between the bubble Archimedes number Ar_b and the bubble elongation ratio in a confined cell. In our work, bubble Archimedes number is about $Ar_b \simeq 1000$, meaning their aspect ratio is about 1.3, which is similar to [5].

5.4.2 Bubble velocity

We first define a mean velocity for each bubble of a run. Then the mean velocity for each run is the averaged value of these individual mean bubble velocities. The mean horizontal and vertical velocities are shown in figure 5.17 and compared to the results of Bouche et al. [5]. In our experiments, we have not measured the velocity of a single bubble rising into the gap. Consequently, it was assumed to be close to the mean bubble vertical velocity in the bubble swarm at very low α_g. The bubble vertical velocity was measured in a run of $\alpha_g = 2.02\%$ and noted $u_0 = 10.8\text{cm.s}^{-1}$ in the following figures. Even if it is not exactly the same, it is of the oder of magnitude of the velocity of an isolated bubble, as provided by Filella et al. [18] scaling law (that predicts 11.89cm.s^{-1} for a diameter of 4.1mm). The mean bubble Archimedes number for all bubbles is $\langle Ar \rangle = 960$.

As shown in figure 5.17, the mean horizontal velocity of the present work is close to 0, denoting a satisfactory statistical convergence, as in Bouche et al. [5]. Over the range of α_g investigated, the mean vertical bubble velocity is nearly constant around $\langle u \rangle = u_0$. Similarly to the data of Bouche et al. [5], a slight rise in mean velocity (of less than 0.15%) is observed with rising α_g. This rise is slightly more important in our data, which is likely caused by coalescence, as large bubbles have higher velocities, and have been

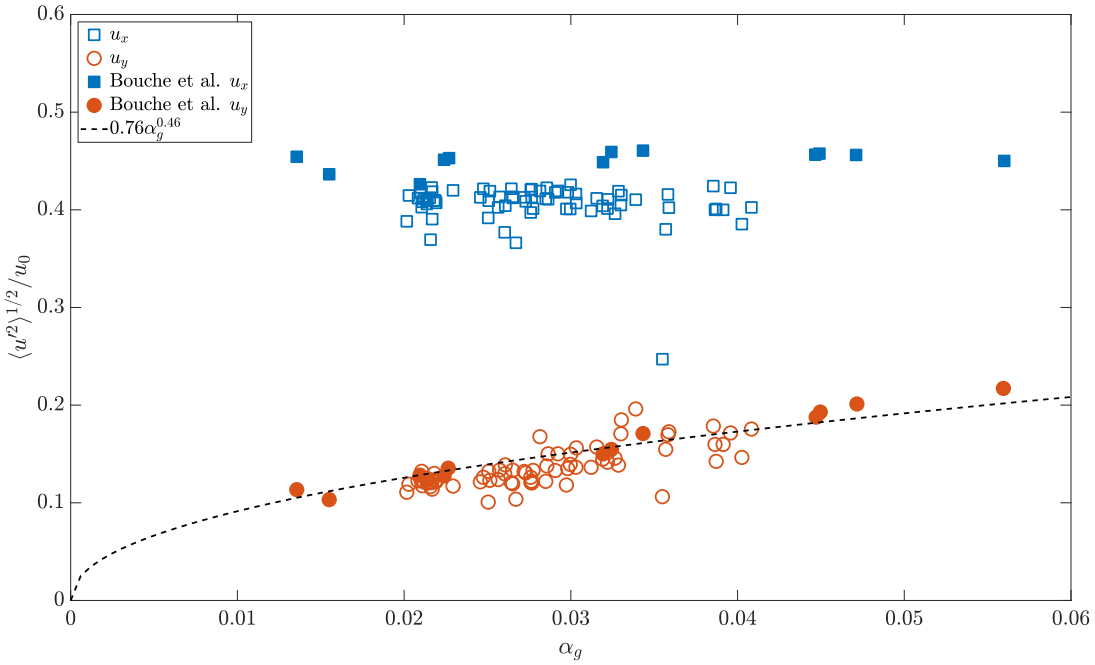

Figure 5.18 – Standard deviation of the bubble horizontal and vertical velocity as a function of α_g, normalized by the velocity u_0. The horizontal velocity is plotted using squares, and the vertical velocity using circles. The empty symbols are the data of the present study, and the filled ones the ones of Bouche et al. [5], with the dashed line being the fit in $0.76\alpha_g^{0.46}$ used in the same reference.

seen to draw smaller ones in their wake, creating surges of vertical velocity. The velocity standard deviation will now be compared.

Figure 5.18 shows the standard deviation of the bubble velocities normalized by u_o. The standard deviation of the bubble vertical and horizontal velocity is slightly lower in the present work than in experimental data from Bouche et al. [5], but they show similar behaviours. Bouche et al. [5] found a constant value of 0.45 for $\langle u_x'^2 \rangle^{1/2}/u_0$, which shows that the main origin of the horizontal fluctuations is the instability of the bubble due to vortex releases. In our experiments, $\langle u_x'^2 \rangle^{1/2}/u_0$ decreases when α_g increases (from 0.42 to 0.38 for α_g going from 2% to 5%) but remains of the same order of magnitude as the one of [5]. The appearance of large bubbles in our swarm may explain this change for a part. Larger bubbles with strong wakes could be able to accelerate smaller ones, contributing to the stabilization of their horizontal fluctuations. It is also possible that a simple dependency of the horizontal fluctuations to the Archimedes number is observed. In the present study, most bubble diameter range between 3.0mm and 5.0mm, which is in the same range of diameters as in the study of Bouche et al. [5] (3.5mm$< d_b <$5.0mm), but coalesced bubbles have a mean diameter of 7.4mm and can account for a maximum of 17% of the bubbles In fact, for larger bubbles (even for isolated ones), the amplitude of the horizontal (or vertical) velocity normalized by the mean velocity decreases in the range of investigated Archimedes numbers (see [32], fig 15.a). In the present study, larger bubbles whose instability is due to their intrinsic instability may have less energy in the horizontal direction than those studied by Bouche et al. [5] .

Similarly than in the swarm explored by Bouche et al. [5], figure 5.18 shows that the standard deviation of the velocity is lower in the vertical direction than in the horizontal one. This is also the case of the amplitudes of the velocity oscillations for a single bubble rising in a fluid at rest when Ar_b increases in the range corresponding to the change of Ar_b between the study of Bouche et al. and the present one (Roig et al. [32]). We

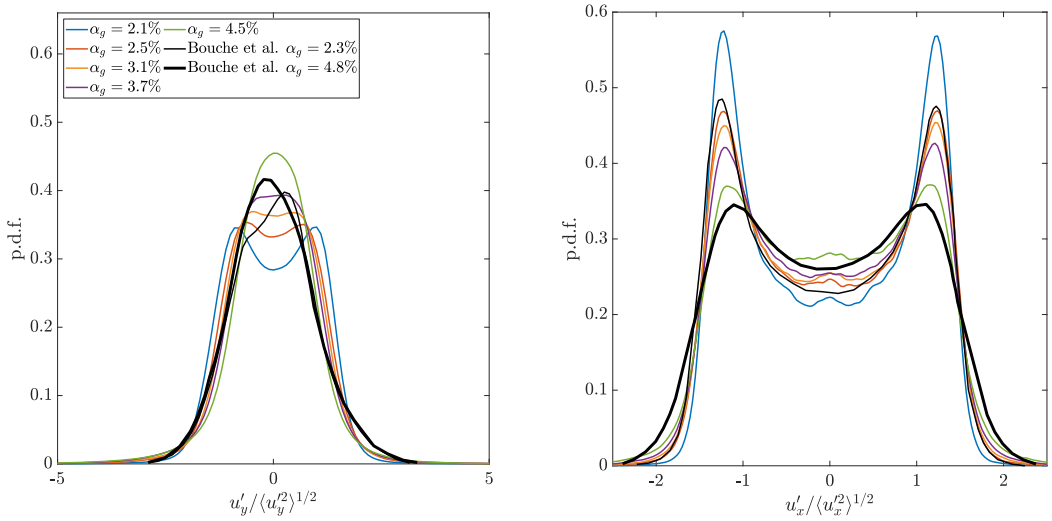

(a) (b)

Figure 5.19 – (a) P.d.f. of the bubble vertical velocity fluctuations u'_y normalized by their standard deviation. (b) P.d.f. histogram of the bubble horizontal velocity fluctuations u'_x normalized by their standard deviation. The thin black line corresponds to the data of [5] for $\alpha_g = 2.3\%$ and the thick black line for 4.8%.

also observe a slight increase of $\langle u'^2_y\rangle^{1/2}/u_0$ when α_g increases, which can be fitted by $\langle u'^2_y\rangle^{1/2}/u_0 = 0.45\alpha_g^{0.35}$ for $\alpha_g \geqslant 1\%$. This fit is different from the one proposed by Bouche et al. [5] ($0.76\alpha_g^{0.46}$). The standard deviation of the vertical velocity in the present work is of the same order of magnitude than in [5], and follows a very similar trend with α_g, despite some technical differences in the generation of both swarms. These differences may be attributed either to small deviations between the bubble spatial distributions or to differences in the bubble size distribution.

Figure 5.19 shows the velocity fluctuations p.d.f., compared with data from Bouche et al. [5] when the gas volume fractions are comparable. Let us examine first the distribution of the vertical velocity fluctuations (5.19a). In our data, for the lowest gas volume fractions, two peaks, typical of a sinusoïdal motion, are visible. Their intensity decreases with α_g, and a single peak is observed for $\alpha_g > 3.0\%$. The distribution of $u'_y/\langle u'^2_y\rangle^{1/2}$ observed for $\alpha_g = 3.8\%$ is very close to the one seen in [5] for $\alpha_g = 4.8\%$. The difference between the present study and the one of Bouche et al. [5] is notable. The observation window in the work of Bouche et al. [5] is farther away from the injectors, which increases the homogeneity of the swarm. In their study, the vertical agitation is less controlled by the release of vortices.

In the horizontal direction (5.19b), two peaks are visible for all gas volume fractions investigated, as well as for $\alpha_g = 2.3\%$ and 4.85% in [5]. The peak height decreases with α_g, while the velocity distribution close to 0 increases. In the present study, a small peak is seen for all gas volume fraction around $u'_x/\langle u'^2_x\rangle^{1/2} = 0$. This may be a trace of the falling cylinders, which slow down bubbles when entering in contact with them. Overall the agreement between our data and the one of Bouche et al. [5] is also satisfactory and even better in the horizontal direction than it is in the vertical direction, because the horizontal agitation is always controlled by vortex shedding.

Comparison of bubble velocity show good agreement between the present work and the one of Bouche et al. [5] for all quantities studied. Despite minor differences in the injection and in the coalescence, both swarms present similar bubble velocity statistics. We can thus consider that the deviation to homogeneity are minor, and take advantage

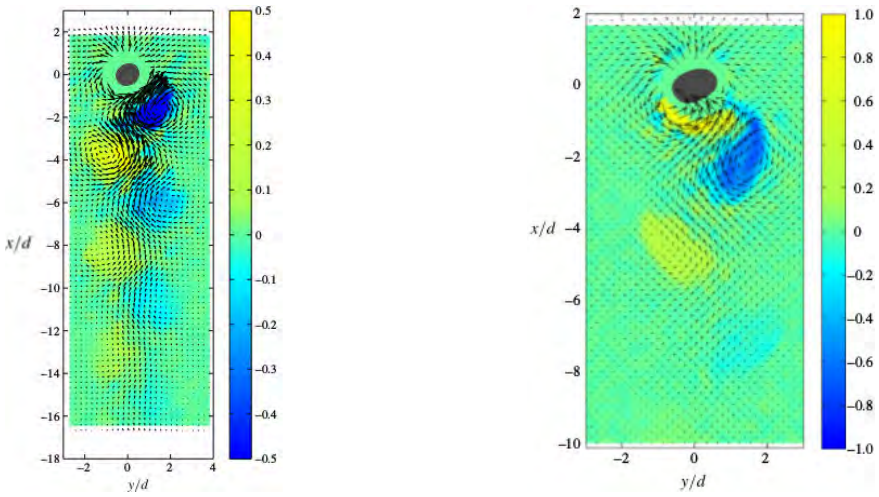

(a) (b)

Figure 5.20 – Velocity (arrows) and vorticity around bubbles at (a) $Ar_b = 700$ (b) $Ar_b = 1500$, from Roig et al. [32]

of the measurements in the liquid phase performed by Bouche et al. [6] to predict the statistics of the liquid agitation in the present bubble swarm.

5.5 Liquid agitation

This section provides a literature review of the liquid agitation in a confined cell with a bubble swarm. Roig et al. [32] performed a study of the dynamics of single bubbles rising in a confined cell, in a range of parameters that is similar to ours. Their use of PIV techniques allowed them to have information of the fluid velocity perturbations induced by the bubbles, which could not be done with our experimental setup. Based on previous comparison in section 5.3, we have checked that the behaviour of their bubbles and ours is similar, and we use their results to describe how a bubble rising in a confined cell affects its surrounding. Filella et al. [18] also studied the motion of a single bubble in a thin-gap cell. They generalized the results observed for a 1mm gap to a 3mm one. We will later use these results to understand how the cylinder dynamics in the cell is affected by the bubbles.

However, in a bubble swarm, the liquid agitation can be expected to be the product of various hydrodynamic interactions between the different bubbles, leading to a complexity which cannot be fully characterized with the wake of a single bubble. Bouche et al. [6] performed PIV experiments in a confined bubble swarm, in conditions close to ours, as we have shown in the previous section (5.4). These two references will allow us to understand how the cylinder falling in the bubble swarm can be affected by the liquid velocity perturbations in the cell.

5.5.1 Liquid flow around a single bubble

The bubble Archimedes number of most bubbles in our experiment are around 960. Coalesced bubbles can appear at high gas volume fraction (see the inset of figure 5.16), and have an Archimedes number of about 1500. Figure 5.20 shows the velocity and vorticity around isolated bubbles of $Ar_b = 700$ and $Ar_b = 1500$ from Roig et al. [32].

Two main areas of velocity perturbations are visible in the liquid. The first and most obvious one is the wake of the bubble, where vortices are shed periodically in a

Von Kármán street. The bubble also pushes fluid above it when it rises, leading to the establishment of a liquid flow in front of the bubble. Roig et al. [32] have shown that this flow could be considered as a potential flow around a cylinder having the same radius as the radius of curvature of the bubble at stagnation point.

Due to the specific confinement of the cell the bubble rises in, the behaviour of the vortices in the wake of the bubble is peculiar, compared to what would be observed in an unconfined medium. Indeed, the confinement reduces drastically the life span of these vortices, compared to an unconfined case. The viscous stress at the walls is very high, causing a very quick attenuation of the vortices. The decay of the vorticity has been shown to be essentially dependent on the diffusive time scale $\tau = H^2/\nu = 1$s when H = 1mm, as the shear caused by the confinement is the dominant effect causing the vorticity attenuation. In the larger gap studied by Filella et al. [18], high-frequency PIV experiments have shown that the vorticity primarily decreases first at short time due to the immersion of the released vortices in the Von Kàrmàn array, and then, at longer times, due to the shear stress of the walls. For a gap of 1mm, Roig et al. [32] show that the vorticity behind the bubble disappears in typically less than $\tau = 1$s for Archimedes numbers between 700 and 1950.

The vortex size is dependent on the bubble diameter and evolves after the vortice release. Vortices grow in size for a time delay of about $0.3H^2/\nu$, then remain of a constant size. Roig et al. [32] have shown that for $Ar_b = 700$, the vortices size stabilizes at about $3d_b$, which corresponds to about 12mm. The final vortice size decreases with increasing Ar_b, up to $2.4d_b$ for $Ar_b = 1250$ and $2.0d_b$ for $Ar_b = 1950$. The vortices released by coalesced bubbles can then be expected to be of about 15mm in diameter. The velocity fluctuations in both the near wake of the bubble and in front of it are of the order of magnitude of the bubble velocity close to the bubble.

The data from Roig et al. [32] thus allows us to characterize the area around the bubbles in which they are able to have a direct effect on the cylinder. We can expect the cylinder to be affected by the liquid perturbations either when they are directly in front of the bubble, or in its wake. As the velocity fluctuations induced by the bubble are localized close to it, it is likely that the cylinder will spend a lot of time outside of the area of a peculiar bubble direct influence. However, this does not mean that the bubble swarm will only affect the cylinder dynamics when it is in close proximity to a bubble, as a global liquid agitation also develops in the swarm due to wake interactions.

5.5.2 Liquid agitation in the bubble swarm

In the bubble swarm, several bubbles can come close together, and the disturbances they induce in the flow then interact. Figure 5.21 shows the effect of the gas volume fraction on the liquid velocity in the cell. Interactions between the liquid perturbations induced by the bubbles becomes more prominent at higher gas volume fractions. At low gas volume fractions, the wake of a single bubble, described in 5.5.1, is still visible in the cell for a bubble far from any other one. As the gas volume fraction α_g rises, this type of wake cannot be identified anymore and the resulting agitation is more complex.

In the swarm, the fluid perturbation above the bubble is a potential flow which is slightly dependent on α_g (see [6]). It is shown to be independent of α_g, and to be negligible for a distance greater than $2d_b$. In the wake of the bubble, the perturbation was found to be negligible for a distance of $5d_b$ from the bubble for $\alpha_g > 2\%$. No values of the gas volume fraction greater than 9 % were investigated. This indicates that the wake entrainment plays a large part in influencing the dynamics of the bubbles within the swarm. For all gas volume fractions investigated in the present study, we can retain the

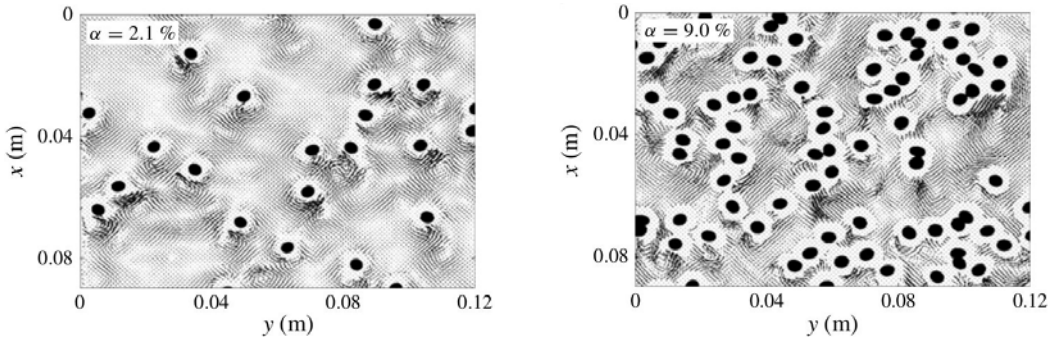

(a) (b)

Figure 5.21 – Velocity fields in a bubble swarm at (a) $\alpha_g = 2.1\%$ and (b) $\alpha_g = 9\%$ from Bouche et al. [6]

idea that the fluid perturbations induced by the bubbles do not extend by more than $2d_b$ above the bubble and $5d_b$ below (see figure 4 of Bouche et al. [6]).

The velocity fluctuations in the liquid were found by Bouche et al. [6] to be a function of α_g. The velocity fluctuation in the horizontal direction, $\langle u_x^2 \rangle^{1/2}$, were found to increase as $0.74\alpha_g^{0.38}u_0$, and the fluctuations in the vertical direction, $\langle u_y^2 \rangle^{1/2}/u_0 \simeq 1.07\alpha_g^{0.46}$. The difference between the two power fits shows an anisotropy in the dynamics of the interaction. Vertical velocity fluctuations have more energy than the horizontal ones, which is coherent with the predominance of the wake in the fluid perturbations caused by a single bubble. The vertical velocity fluctuations in the fluid follow the same trend as the velocity fluctuations for the bubble. This is not the case of horizontal fluctuations, which are independent of α_g for the bubbles, but not for the fluid. The liquid in the bubble swarm is more agitated with increasing gas volume fractions, vertical fluctuations being of greater magnitude. Due to the strong correlation between vertical velocity fluctuations of the bubbles and of the fluid, the physical mechanism at the origin of these perturbations can be supposed to be the same, whereas the horizontal velocity fluctuations in the fluid are probably the result of interacting released vortices.

Spectral analysis of the velocity fluctuations in the fluid show no difference of the scaling law of the power spectra $E(k) \sim k^{-3}$ in the horizontal or vertical direction. Moreover, the length scale of the velocity fluctuations shows no dependence in α_g. The spectra of the liquid velocity in the confined bubble swarm exhibits this k^{-3} subrange, which is also observed for unconfined bubble swarms (see Amoura et al. [1]). A theoretical model developed by Risso [31] showed that the spectrum of spatial fluid agitation in a bubble swarm evolves as k^{-3} under several assumptions, which are that the fluid perturbations induced by the bubbles have a smooth and regular pattern, are uniformly distributed over space, have their strength and size statistically independent, and their size comprised between two finite limits. The evolution of the spectrum of liquid agitation is then $\simeq k^{-3}$ and is valid between these same limits. These assumptions are all coherent with the confined bubble swarm, which indicates that the theoretical model explains the existence of a k^{-3} subrange in this flow configuration.

5.6 Influence of the gas volume fraction on the cylinder

We have seen previously that the bubble swarm is not perfectly homogeneous for all ranges of α_g, and also that there is a significant amount of coalescence at gas volume fraction of

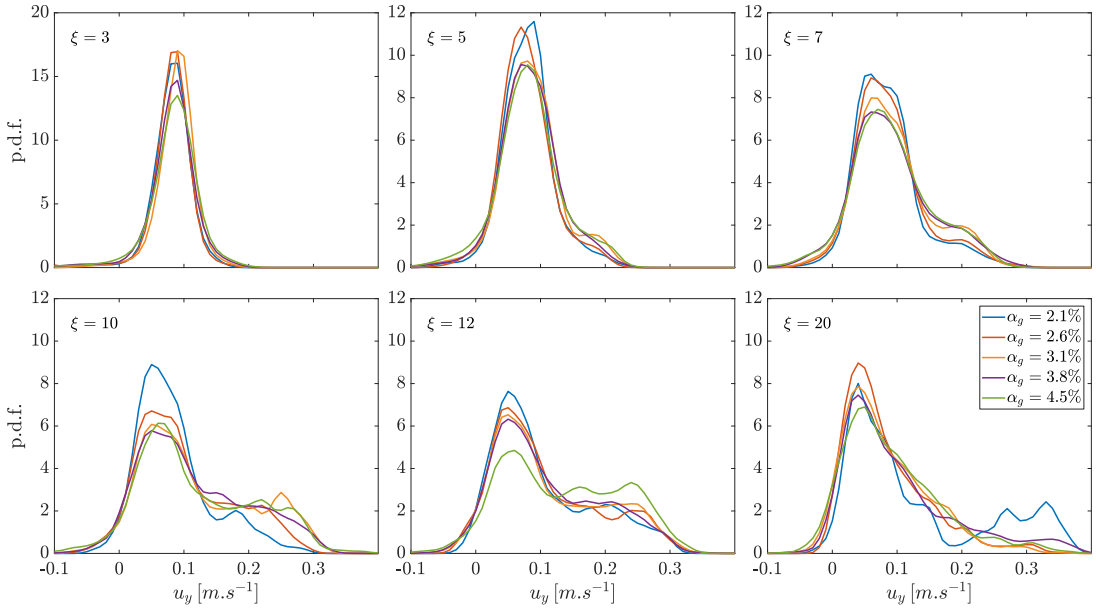

Figure 5.22 – P.d.f. of the cylinder vertical velocity u_y, for all ξ and all α_g, for aluminum cylinders. The horizontal scale is the same of the bottom and top rows of graphs.

about $\alpha_g = 4\%$. However in this study, we consider reasonable to use the present bubble swarm to investigate the motion of freely falling cylinders in a homogeneous confined bubble swarm. In this section, we will discuss the effect of the gas volume fraction on the cylinder motion. We will check that the imperfections of our bubble swarm have no significant impact on the cylinder behaviour. Furthermore, we will also examine if there is or not a significant impact of the various ranges of gas volume fraction we defined in the present experiment.

The cylinder behaviour in the swarm is described using its vertical falling velocity. Figure 5.22 shows the influence of α_g on the vertical velocity u_y of aluminum cylinders. In this section, we want to prove that the effect of the gas volume fraction is minor and we will provide a more complete description of the statistics of u_y later on. For each elongation ratio, the p.d.f. of the different ranges of α_g are very similar. For $\xi = 3$, 5 and 7, a very slight coherent effect of α_g can be seen, with the height of main peak of the u_y p.d.f. decreasing slightly with α_g. We can retain that changes are nevertheless minor. For $\xi = 10$, 12 and 20, some ranges of α_g ($\alpha_g = 2.1\%$ for $\xi = 10$ and 20, and $\alpha_g = 4.5\%$ for $\xi = 12$) depart significantly from the p.d.f. of all the other gas volume fractions with slightly lower (respectively higher) vertical velocity, but most of the p.d.f. obtained at different α_g are similar. The number of runs is different in each range of α_g, meaning that the singular behaviours can be explained by a lack of statistical convergence, which can be checked by looking at individual run data. Cumulating all the runs whatever α_g will thus provide a meaningful p.d.f., representative of the cylinder velocity at low gas volume fraction $2.1\% \leqslant \alpha_g \leqslant 4.5\%$.

Figure 5.23 shows the average cylinder velocity for each run, $\langle u_y \rangle$, for different ξ as a function of α_g. The dispersion appears to be heavily dependent on the elongation ratio. For $\xi = 3$, 5 or 7, there is very little dispersion, and only a very slight increase in velocity with α_g, which is similar for these three elongation ratios. There is an outlier for $\xi = 3$ whose mean vertical velocity is nearly 0, because it is actually the only case of cylinder being transported upward by a bubble (see 6.2.1) that occurred for an aluminum cylinder. For $\xi > 7$, the dispersion becomes much greater, but does not depend on α_g. At $\xi = 20$, two different stacks of points are even observed. As seen qualitatively before, the

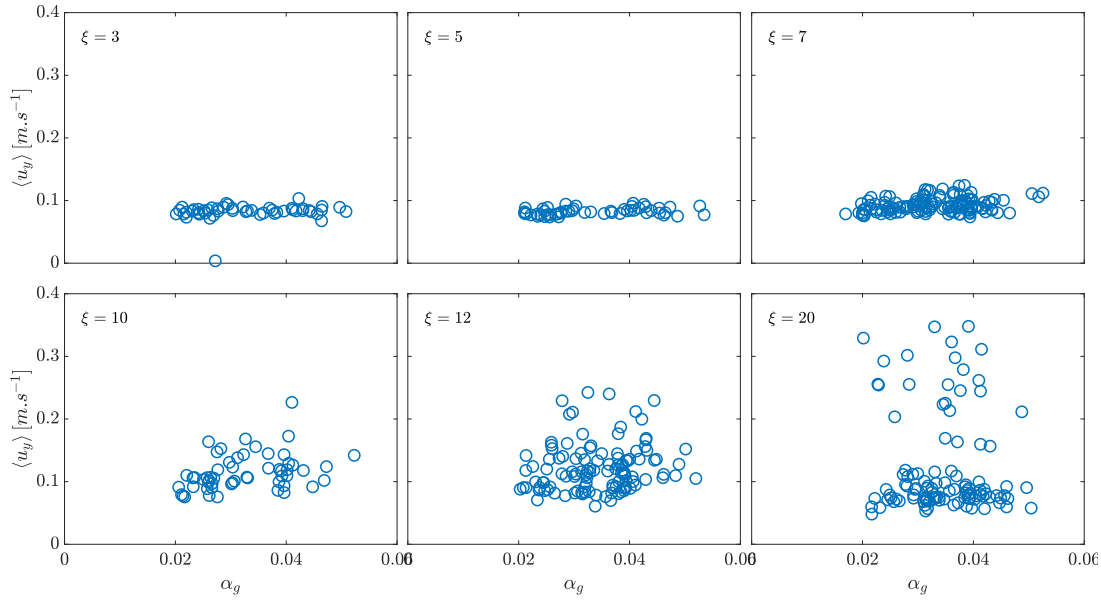

Figure 5.23 – Mean vertical (empty symbols) velocity of the cylinder in the bubble swarm for different α_g. The values have here been computed for each individual run, as opposed to averaged over a range of α_g

orientation of the cylinder plays a large part in its vertical velocity, with cylinders close to the vertical having large velocity. Additionally, in the confined cell, the duration of the transient regime during which the cylinder goes from a vertical orientation to a horizontal one is very dependent on its elongation ratio, with longer cylinders having longer transient times. It is therefore expected to see contrasted behaviour at high ξ between cylinders spending a long time vertical (i.e. with high velocity), and cylinders staying mostly horizontal, creating the dispersion observed on figure 5.23, and ultimately the two different stacks of points for $\xi = 20$. The dispersion of the data can be characterized with the coefficient of variation, defined as $\langle u_y^2 \rangle^{1/2} / \langle u_y \rangle$ (see figure 5.24). Indeed, the dispersion grows greater with ξ (visible on figure 5.24) , but not with α_g (visible on figure 5.23). Yet, $\langle u_y^2 \rangle^{1/2} / \langle u_y \rangle$ shows no significant variation with α_g. Therefore, it appears that the singular behaviours observed for some ranges of α_g in figure 5.22 are caused solely by the lack of statistical convergence for each range.

The effect of the gas volume fraction on the p.d.f. of u_y remains overall very small, and much less significant than the effect of ξ. Even though significant outliers have been noticed when looking at individual α_g, they have been shown to be caused by a lack of statistical convergence over certain ranges of gas volume fraction. In fact, the effect of α_g is small enough to be considered negligible compared to the one of ξ, which allows us to study all runs with no distinction of α_g, increasing the statistical convergence.

5.7 Summary

Our analysis of the bubble swarm, and comparison with results from Bouche et al. [5, 6] gives us the means to characterize the fall of a cylinder in a confined bubble swarm. First, we have checked that the spatial and temporal homogeneity of the bubble swarm were satisfactory. This first point is important, as it allows us a direct comparison with the work of Bouche et al. [5] on the bubble dynamics in a homogeneous confined bubble swarm. We also compared the bubble size and velocity in our swarm with that of [5], and found similar results. In turn, this allows us to use the results from Bouche et al.

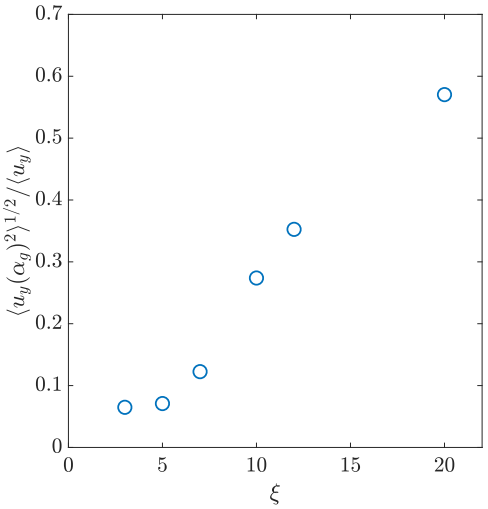

Figure 5.24 – $\langle u_y^2\rangle^{1/2}/\langle u_y\rangle$ as a function of ξ

[6], who performed PIV measurements of the fluid flow in a confined bubble swarm. These measurements give us valuable information on the perturbations of the fluid in the bubble swarm, which we need in order to characterize the cylinder motion in the swarm. In addition, we have determined that the gas volume fraction, in the range we explored, had a limited impact on the cylinder motion. Therefore, in the following, we will consider all investigated gas volume fractions to be equal.

Chapter 6

Fall of a cylinder in a bubble swarm

6.1 Introduction

In this chapter, we study the motion of the cylinder in the confined bubble swarm. The cylinder motion is very complex, unpredictable, and sometimes counter-intuitive. For this reason, we introduce this chapter with a thorough qualitative description of the cylinder motion, paying particular attention to specific features of the problem. We start by showing the main types of interactions between the cylinder and the swarm, which highlight the diversity of the cylinder behaviours in the swarm. Then, we show the qualitative effect of the cylinder elongation ratio and density ratio on its motion.

This qualitative description serves as a preamble for a statistical description of the cylinder of the motion in the swarm. Statistics allow us to characterize the cylinder motion despite its complexity. Throughout this section, we compare the motion of the cylinder in the bubble swarm with its motion in the fluid at rest. We show that the bubble swarm has a large impact on the motion of the cylinder, which we characterize in detail. Then, in order to better isolate the mechanisms responsible for this change in behaviour, we introduce conditional statistics of the cylinder motion, based on the contact with bubbles, and the cylinder orientation. Finally, we discuss the dispersion of the cylinder motion in the swarm.

6.2 Qualitative description of the cylinder motion

The cylinder motion in the bubble swarm is first described qualitatively, and several typical interactions between a cylinder and the bubble swarm are presented. During its fall, the cylinder interacts directly with bubbles, with the liquid perturbations they induce in their near neighborhood, or with the liquid agitation far from the bubbles. This section will provide an overview of the different types of interactions that have been encountered, alongside a qualitative description of the involved mechanisms.

6.2.1 Key direct interactions between a cylinder and a bubble

Contact

The most distinguishable interaction between the cylinder and a bubble is the direct contact, during which the cylinder touches the bubble interface. Note that the possible dewetting of the cylinder by the bubble cannot be characterized through the image processing. We suspect that leaving the cylinders submerged in water at all times prevented their dewetting.

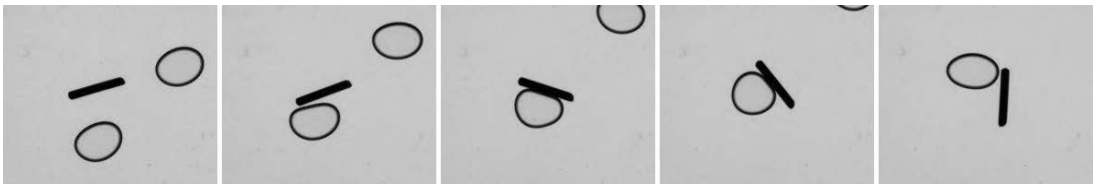

Figure 6.1 – Several steps in a contact interaction between a bubble and an aluminium cylinder of $\xi = 7$ and $Ar = 300$. The time step between each image is $0.02s$.

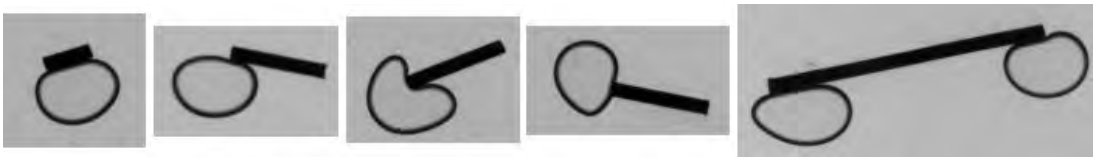

Figure 6.2 – Several examples of different contact cases between a bubble and a aluminium cylinder with, from left to right, $\xi = 3.45$, $Ar = 210$, $\xi = 6.9$, $Ar = 300$, $\xi = 7.2$, $Ar = 300$, $\xi = 6.75$, $Ar = 300$ and $\xi = 20$, $Ar = 500$

Figure 6.1 illustrates several steps in a contact interaction between a cylinder and a bubble. In the first image, the cylinder is still too far away from the bubble for any visible interaction to take place. In the second one, the bubble starts deforming even though there is no contact yet between the two objects. The actual contact can be seen on the third frame, where the bubble deformation appears even more obviously. The cylinder then glides on the bubble, and rotates in the process. Finally, on the fifth frame, the two objects separate. During the contact, the velocity of both the bubble and the cylinder decreases significantly, as the bubble remains nearly immobile.

Based on this example, we can easily imagine that the contact interaction can take multiple other forms depending on the cylinder parameters and the conditions of contact. Obviously, the point of contact between the two objects and the orientation of the cylinder prior to the interaction have a significant impact on the interaction. Indeed, a great variety of behaviours is observed. Contacts toward the ends of the cylinder have different consequences than the ones closer to its center. The size ratio between the cylinder and the bubble also has a big impact on the resulting motion. With the bubbles having mostly all the same diameter, the cylinder elongation ratio solely defines the bubble to cylinder size ratio. It affects deeply the contact interaction, as longer cylinders also have a higher chance of being in contact with several bubbles. It should also be noted that the cylinder weight influences the bubble deformation during contact.

Due to the large number of parameters influencing the nature of contact interactions, it is expected that a lot of different behaviours can appear. Figure 6.2 illustrates this variety.

The first frame shows a small cylinder ($\xi = 3.45$, $L = 2.76$mm) falling flat on top of a bubble. Cylinders with $\xi \simeq 3$ are the only ones having their length significantly smaller than the bubble diameter. With all cylinders having the same diameter, this also means they are the lightest for the same material. This has consequences for both the bubble and the cylinder. A lighter cylinder does not deform the bubble as much as a heavier one, and will not slow down the bubble as much. In contrast, its own velocity is more perturbed by the bubble. The loss of falling velocity for the cylinder, however, is greater for the lighter ones. Contact cases for which the cylinder falls flat on the bubbles such as this one are also the type of contacts that has the greater impact on the velocity of both objects.

Cylinders impacting the bubble near their ends have a tendency to rotate and separate

Figure 6.3 – Several steps in a bubble piercing interaction between a bubble and an aluminium cylinder with $\xi = 11.75$ and $Ar = 388$. The time step between each image is $0.006s$.

faster from the bubble. On the second frame of figure 6.2, the point of contact between the cylinder and the bubble is close to the ends of the cylinder. This type of contact usually has two possible outcomes, which depend on the cylinder motion before and during the contact. If the cylinder horizontal velocity is important, it quickly glides over the bubble, which has a small impact on both objects. It is slightly tilted by the bubble, and loses some of its horizontal velocity, but these effects remain of low amplitude, and the general cylinder trajectory is not drastically changed. However, when the mean cylinder velocity is small, a contact near its ends can cause it to tilt significantly. In this case, we observe an important increase in the vertical velocity of the cylinder, as its new rather vertical orientation drastically reduces its drag coefficient.

On the third frame of figure 6.2, we see a case where the cylinder ends come in contact with a bubble with great velocity. This type of contact is scarce, and happens only after the cylinder has been tilted enough to have an important vertical velocity. The bubble is heavily deformed by the contact, and acts first like a dampener, slowing down the cylinder to a near stop. Then, it regains its original shape, pushing the cylinder away. The bubble deformation combined with its upward motion generally tilts the cylinder again, so that it resumes its fall with a nearly vertical orientation. During this kind of interaction, it happens that the cylinder breaks the bubble, leading to a new type of interaction described later in the current section.

On the fourth frame of the same figure, the contact conditions are close to the previous case, except that the cylinder velocity is much less important. The end of the cylinder glides along a bubble, causing it to deform slightly. The cylinder horizontal motion is slowed by the contact. Often seen when the cylinder is going under periodic oscillation, this interaction inhibits some of the oscillations, and reduces the cylinder velocity.

Long cylinders, as illustrated on the fifth frame of figure 6.2, can easily come in contact with several bubbles. Obviously this happens much more often when the cylinder is long enough, and close to being horizontal. In this case, bubbles can come under the cylinder and glide alongside it. Meanwhile, the cylinder keeps its orientation close to constant. This type of contact induces long horizontal motions of the cylinder.

The great variety of contact types makes it difficult to issue a proper classification. Contact interactions are dependent on both the cylinder motion before the contact and on the cylinder parameters $\left(\xi, \frac{\Delta\rho}{\rho}\right)$.

Bubble piercing

Another type of interaction that occurs is the piercing of bubbles by the cylinders. Figure 6.3 shows several steps of a bubble piercing interaction.

This kind of interaction only takes place when the cylinder impacts the bubble with its end and at a large enough velocity. As a result, bubble piercing occurs mostly for titanium cylinders. For aluminium cylinders, only cylinders of long elongation ratio ($\xi > 12$) are

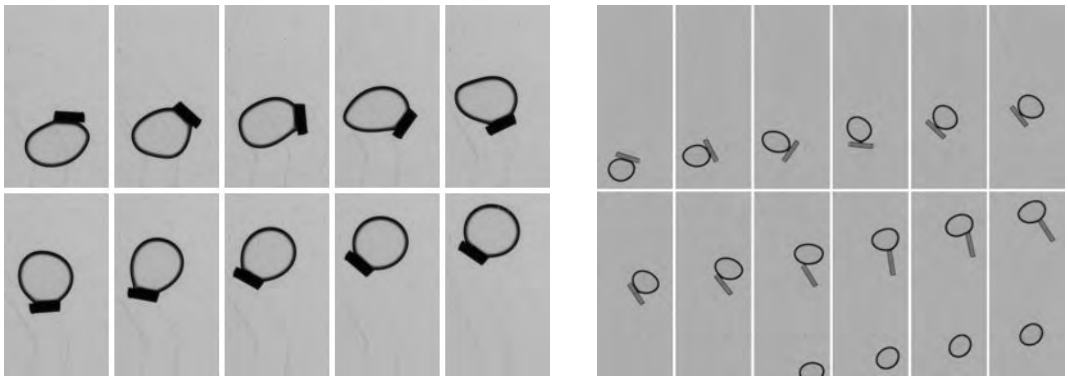

(a) (b)

Figure 6.4 – Several steps in a bubble interaction where a cylinder is caught by the bubble and dragged to the surface of (a) an aluminium cylinder with $\xi = 3.13$ and $Ar = 200$ and (b) an ABS cylinder with $\xi = 3.02$ and $Ar = 60.4$. The time step between each image is $0.01s$.

observed having enough velocity to pierce bubbles. The cylinder impact heavily deforms the bubble, as seen in the third frame of figure 6.3, up to a point where it splits into two smaller bubbles, as seen on the fourth frame. The cylinder is slowed down by this interaction, but its orientation remains nearly constant. This loss of velocity is however less significant for heavier cylinders. The impact of bubble piercing interactions on the cylinder trajectory is minimal, as the cylinder orientation is not affected. As a result, even when the cylinder loses velocity, it accelerates again quickly after the interaction.

Bubble piercing creates bubbles smaller than the ones created by air injection in the cell. They remain scarce, as they can only be created through interaction with the cylinder.

Ascension

In some cases, a cylinder can adhere to a bubble and be carried away to the liquid free surface. This is seen to occur for small ($\xi = 3$ or 5) cylinders of ABS and aluminum. However it remains scarce for aluminium cylinders, with only 1 out of 50 aluminum cylinders of $\xi = 3$ behaving in such a way. It appears to happen more frequently for ABS cylinders, with 1 out of 5 ABS cylinders of $\xi = 3$, and 1 out of 4 ABS cylinders of $\xi = 5$ being seen to have such a behaviour. Yet, the total number of experiments carried out with ABS cylinders is too low to properly characterize the frequency of this phenomenon for this material, even though it is likely to happen much more often than for aluminum cylinders.

Figure 6.4 shows several steps in the ascension of a cylinder carried by a bubble. The cylinder starts by falling flat on top of a bubble, and then glides on its side in a similar way as figure 6.1. Instead of separating from the bubble when it is vertical, though, the cylinder stays attached to the bubble. The physical cause of this adherence remains unknown, even if capillary effects are strongly suspected. The adherence causes the bubble to deform (frame 7 of figure 6.4a). In this case, the point of adherence between the cylinder and the bubble seems to be the entire length of the cylinder. The contact covers a much smaller area on figure 6.4b, while it also moves along the cylinder body, from its side on frames 1 to 8, to the edge of one of its faces on frames 9 to 12.

Once the cylinder has adhered to the bubble, it gets carried to the surface. On the cases where it is attached by one of its edges (figure 6.4b), it moves in the wake of the

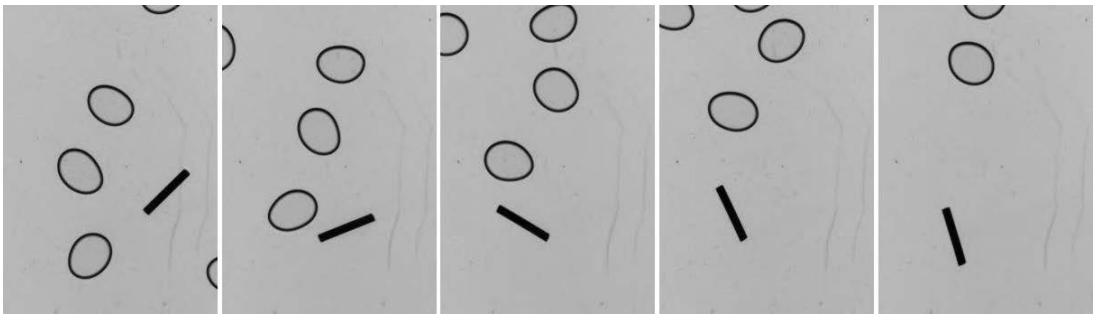

Figure 6.5 – Several steps in a bubble interaction where an aluminium cylinder with $\xi = 11.75$ and $Ar = 388$ is caught in a vortex shed in the wake of the bubble. The time step between each image is $0.03s$.

bubble, swinging from left to right at the same frequency than the bubble oscillatory motion. In the other case, the cylinder also oscillates horizontally, following the bubble deformations. Because its contact area with the bubble is more important, however, it does not swing independently from the bubble motion.

6.2.2 Cylinder interaction with the fluid perturbation

In the confined cells, the fluid perturbations induced by the bubbles are stronger close to the bubbles, due to the very short life span of the vortices shed by the bubbles. Therefore, we discuss separately the effect of the fluid perturbations on the cylinder in the vicinity of the bubbles, and far from them.

In the vicinity of the bubbles

Interaction between a cylinder and a bubble can also occur without any contact between the two objects, when they are close to each other. As seen in 5.5, bubbles create agitation in the liquid everywhere in the cell, but with a higher intensity in the vicinity of the bubbles. In front of the bubble, a potential flow is created up to $2d_b$ away from the bubble (see [7]). Behind it, vortices periodically shed by the bubble exist in the cell for distances of $5d_b$ and less than $1s$ (see [6]). Both these liquid perturbations of the liquid phase can have a significant impact on the cylinder motion. In the present study, the bubble velocity magnitude is similar to the falling velocity of the cylinder. Therefore, the fluid perturbations induced by the bubble in their vicinity is strong enough to generate a noticeable response of the cylinders. Fluid perturbations are the strongest in the potential flow or in the near wake of the bubble.

Figure 6.5 shows an example of an interaction between an aluminum cylinder and the near wake of a bubble. The cylinder comes under the bubble shortly after its passage. In this example, the cylinder is oscillating before going through the wake of the bubble. Its horizontal velocity is low, and it is in the process of tilting. The wake of the bubble propels it upwards, while increasing its change of orientation. Indeed, as can be seen on the fourth and fifth frame, the orientation of the cylinder is greater that what can be observed in a fluid at rest. As a result, the cylinder gains a lot more acceleration than what it would have had without the vortex interaction, creating a rapid vertical motion.

In this particular example, the effect of the wake interaction and the natural motion of the cylinder both tend to rotate the cylinder in the same direction. However, this is not often the case, and most interactions between the cylinder and the liquid agitation created by the bubbles are more subtle. This is especially true with the liquid flow taking place

in front of the bubbles. Firstly, it covers a smaller area, meaning that the interactions are less frequent. Secondly it is weaker than the liquid perturbation in the bubble wake.

Far from the bubbles

In the liquid far away from any bubbles, there is an interstitial agitation resulting from the bubble wakes interaction. During its fall, a cylinder is thus affected by this bubble-induced agitation. Its effect on the cylinder is much harder to identify directly, as there is liquid agitation everywhere in the cell, its effect is of low magnitude. Moreover, it occurs at moments when the cylinder is likely to be under the influence of one or more bubbles, making it harder to dissociate the effect of the liquid agitation from the effect of the possible contacts.

It should be noted that the effect of the liquid agitation on a cylinder is heavily dependent on the cylinder density. ABS cylinder ($\rho_c = 1160\text{kg.m}^{-3}$) are greatly affected by all liquid agitation in the cell. Titanium cylinders ($\rho_c = 4506\text{kg.m}^{-3}$), on the other hand, are barely affected by any form of liquid agitation.

6.2.3 Qualitative description of the influence of the different parameters

The type and nature of the interaction between the bubble swarm and the cylinders depends heavily on the cylinder elongation ratio and density. The gas volume faction also has an impact, although smaller in the range we could explore. The effect of these parameters are discussed and illustrated, compared to the fall of a cylinder in a fluid at rest. Several trajectories are described in detail over a vertical distance of 10cm, which is much less than the total observable falling height (of about 36cm), allowing for a more in-depth description of the various mechanisms involved.

Detailed description of a trajectory in the bubble swarm

To introduce the diversity of cylinder behaviours in the bubble swarm, we describe a specific trajectory in detail in order to highlight the role of the different types of interaction with the bubble swarm seen in section 6.2.1. The cylinder discussed in this example is an aluminium cylinder of $\xi = 7$, which is the more represented type of cylinder in our study. Furthermore, its intermediate elongation ratio and density make it a case where a lot of different interactions can be observed. The effects of both ξ and ρ_c will be discussed further in this section.

Figure 6.6 shows an example of its fall both in a fluid at rest and in the bubble swarm. In the beginning of the trajectory, from $Y = 0$ to 3.0cm, the cylinder falls in an oscillatory motion that looks closely to its behaviour in the fluid at rest, despite a contact with a bubble at about $Y = 0.015$m. Then from Y going from 3.0 to 5.0cm, the cylinder motion changes radically to a horizontal wave-like motion. This sudden change is caused by the combined interactions of the cylinder with a vortex shed by a bubble and a bubble contact. The cylinder is caught by a vortex shed by a bubble while its θ was increasing. The vortex increases this effect and causes the cylinder to start surging downwards and to the left. The cylinder then encounters several bubbles in a quick succession, resulting in short contacts which slow it down and keep its orientation horizontal. Then, at about $Y = 5.5$cm, another vortex interaction occurs, except this time, no bubble contact intervenes and the cylinder is able to freely accelerate downwards. The situation is similar to the one pictured in figure 6.5). Similarly to what happens in a fluid at rest when the cylinder is released vertically, the cylinder tends to go back to

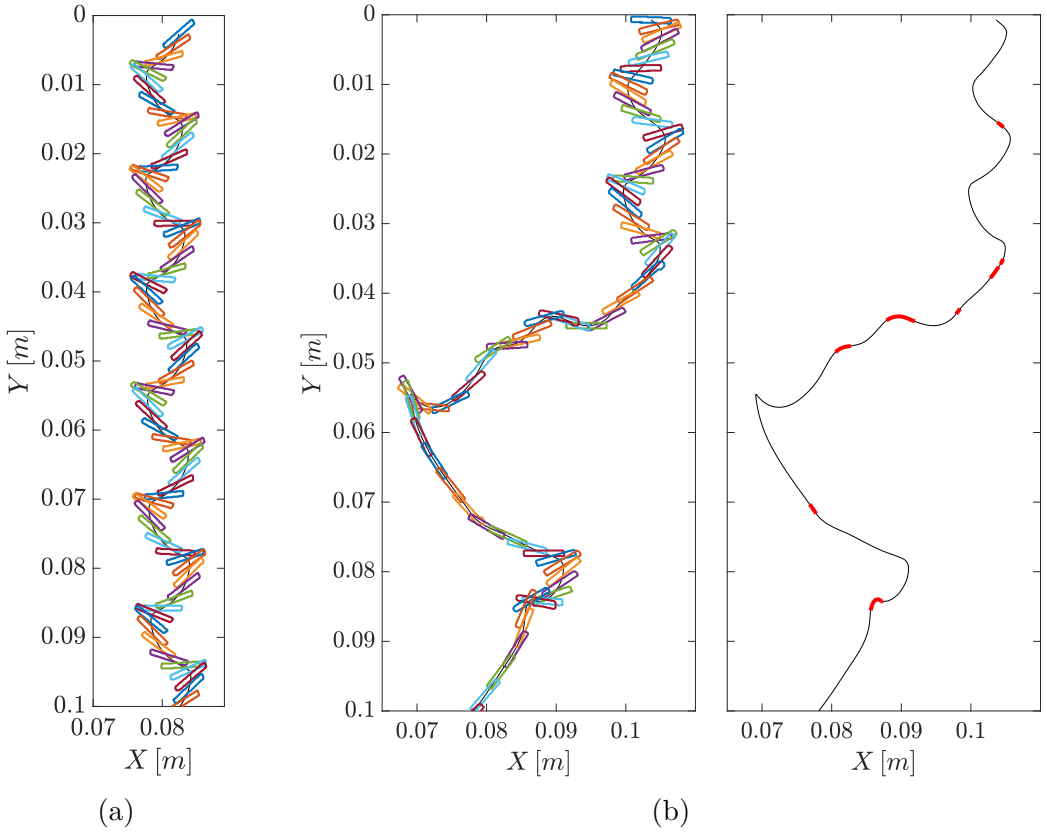

Figure 6.6 – Comparison of the trajectory of an aluminium cylinder with (a) $\xi = 7.13$, $Ar = 300$ in a fluid at rest and (b) $\xi = 7.17$, $Ar = 300$ in the bubble swarm for the same range of Y, with and without contours. The time step between shown cylinder contours is 0.02s. Trajectory points when the cylinder is in contact with a bubble are highlighted with a thick red line.

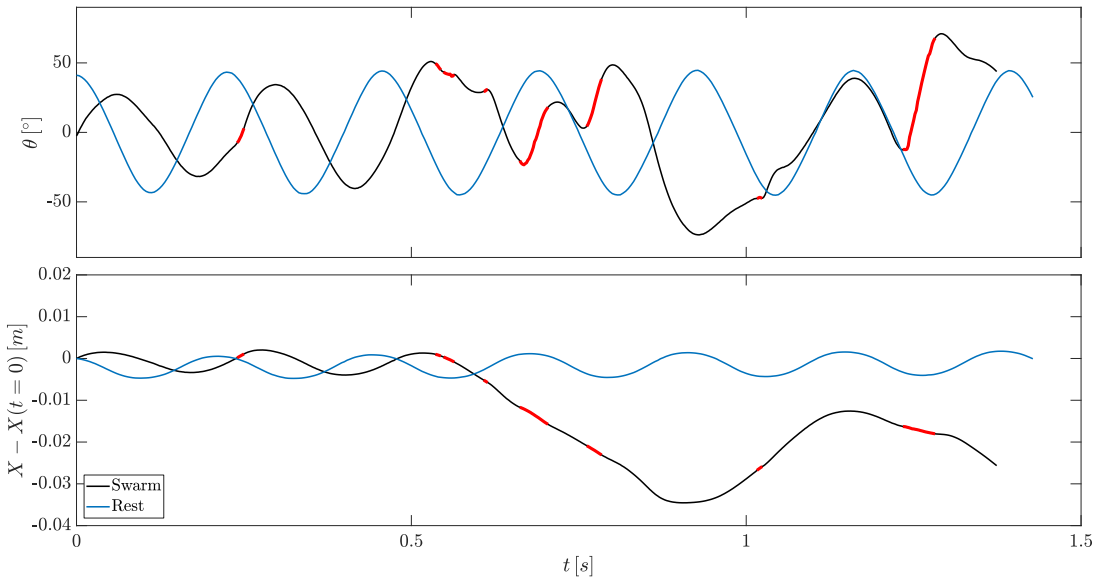

Figure 6.7 – Temporal evolution of the orientation θ and horizontal position X of an aluminium cylinder, over a time span corresponding to the first 10cm of fall, in a fluid at rest with ($\xi = 7.13$, $Ar = 300$) in blue, and in the bubble swarm with ($\xi = 7.17$, $Ar = 300$) in black. Thick red lines correspond to instants where the cylinder is in contact with a bubble.

a horizontal orientation. The downward acceleration ends at about $Y = 8.0$cm, where the cylinder is nearly horizontal, and starts an oscillating motion again. Shortly after, a bubble comes in contact with its end and tilts it downwards once more.

In this sequence, neither bubble piercing nor cylinder ascension are featured, as they are not typically observed for the aluminum cylinders. However, it shows the variety of cylinder behaviours that can be caused by the other 2 types of interaction, bubble contact and vortex interaction. It should be noted that bubble contacts are much easier to observe as they happen more commonly and have effects of a greater magnitude. Based on this example, we can identify several general behaviours of the aluminium cylinder in the bubble swarm. When the cylinder is far from any bubble, it tends to move in the same way it does in the fluid at rest, as the liquid agitation induced by the bubble is low.

Figure 6.7 shows the temporal evolution of the cylinder orientation and horizontal position corresponding to the two trajectories featured on figure 6.6. The similarity between the cylinder motion in the fluid at rest, and in the bubble swarm when it is not strongly influenced directly by the bubbles is obvious up to 0.5s, despite a short contact happening. The cylinder oscillates with the same frequency, and comparable amplitude to the oscillations in the fluid at rest (albeit the amplitude in the swarm is slightly smaller). Strong interaction with bubbles can generate two types of large amplitude motion, oblique motion, and vertical motion. In this example, the oblique motion is a wave-like motion caused by a series of contact with bubbles. Downward motion is initiated when strong interaction with a bubble drastically increases the cylinder orientation. The first downward motion (at about $t = 0.85$s) is created by a relatively weak interaction with the vortex behind a bubble, but with the cylinder at an already high orientation. The second downward motion (at about $t = 1.25$s), on the other hand, is created by a very strong contact interaction with a bubble. These two events, despite these differences, produce similar effects on the cylinder motion.

In the following sections, the effect of the two cylinder parameters of control, ξ and ρ_c will be discussed regarding their effect on bubble interaction.

Cylinder density

As we have seen in part II, the cylinder density influences its falling behaviour in a fluid at rest. In the bubble swarm, additional physical mechanisms come into play and the density of the cylinder also influences how sensitive it is to these mechanisms. We will describe here how the various cylinder densities studied in the present work influence the cylinder response to interaction with the bubble swarm.

Figure 6.8 shows a comparison between an ABS cylinder of $\xi = 7$ in a fluid at rest and in the bubble swarm. It is obvious that the falling behaviour of the ABS cylinder in the bubble swarm changes drastically from the case in the fluid at rest and from the aluminum cylinder discussed previously. At about $Y = 0.11$m, the cylinder motion is extremely chaotic, with significant upward motion. This is due to a contact with a bubble, which carries the cylinder over a large distance, while causing it to rotate significantly. Compared to an aluminum cylinder, the low density of the ABS cylinder makes it much more sensitive to bubble interactions, and direct contact are longer and have more impact than for heavier cylinders. During the contact between the two objects, the cylinder is more easily forced to follow the bubble motion. In this case, the bubbles velocity is much more important than the cylinder one. As a result, bubble contacts are events during which the cylinder velocity and rotation speed increase a lot. From Y = 0.11 to 0.15m, the cylinder axis remains close to the horizontal, and its falling behaviour seems quite similar to the fluid at rest case. Yet, slight perturbations of the path are visible, caused

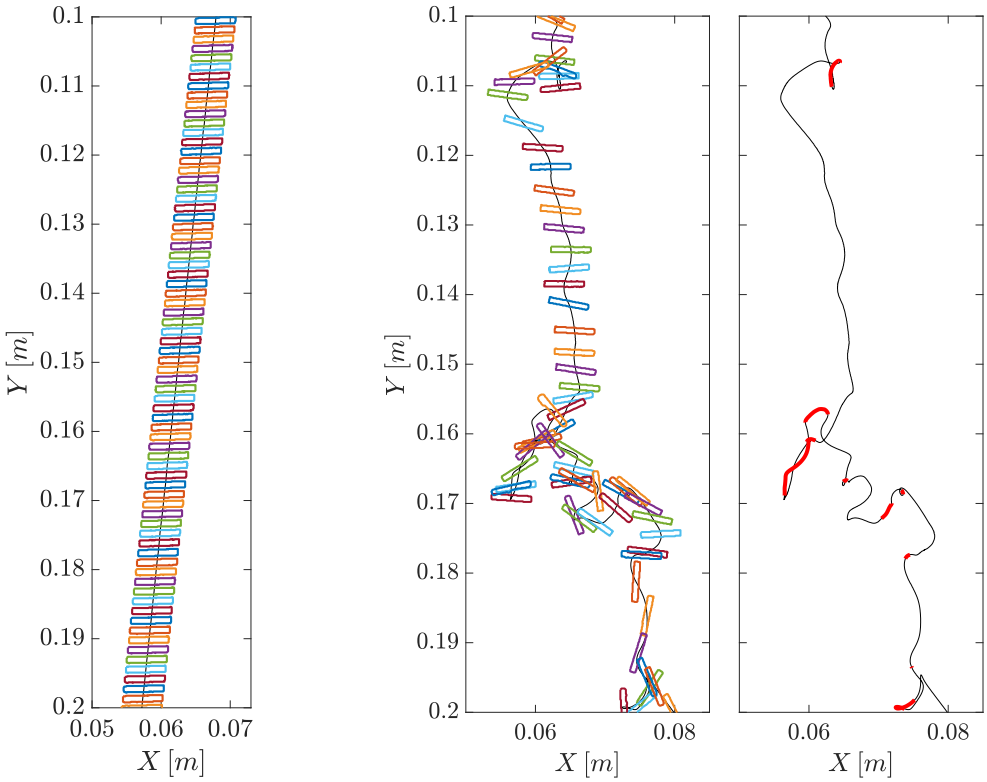

Figure 6.8 – Comparison of the trajectory of an ABS cylinder with $\xi = 7.12$, $Ar = 90$ (a) in a fluid at rest and (b) in the bubble swarm for the same range of Y, with and without contours. The time step between shown cylinder contours is 0.1s. Trajectory points when the cylinder is in contact with a bubble are highlighted with a thick red line.

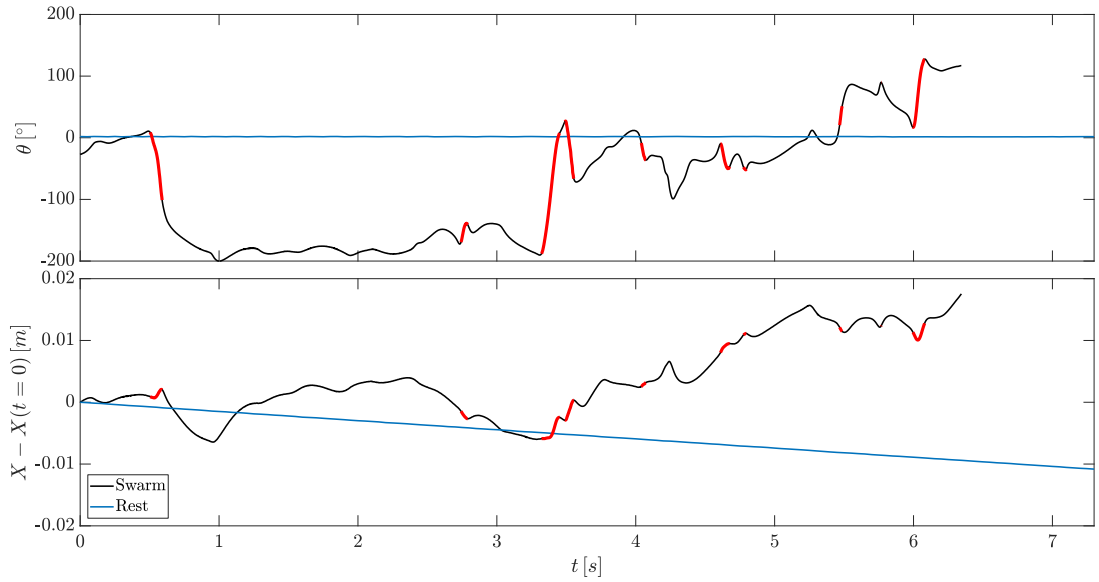

Figure 6.9 – Temporal evolution of the orientation θ and horizontal position X of an ABS cylinder with ($\xi = 7.12$, $Ar = 90$), over a time span corresponding to trajectory shown in figure 6.8, in a fluid at rest in blue, and in the bubble swarm in black

by fluid motion induced by the bubble swarm, and the downward velocity of the cylinder is increased compared to what it is in the fluid at rest. Then, for Y = 0.155 to 0.18m, we observe another chaotic contact phase. The cylinder hits several bubbles in a row, resulting in large-amplitude upwards and sideway motions. At the end of this contact phase, the cylinder axis is vertical, and remains so for the following of the showcased trajectory.

The type of interaction with the bubble swarm does not change with the cylinder density (see figure 6.6 for comparison). The two main kinds of interactions occurring are still contact with a bubble and interaction with fluid perturbations. Similarly, we observe phases where the cylinder is slowed down by the bubble swarm, phases where it is sped up, and phases where its behaviour is similar to the one it has in the fluid at rest. However, the magnitude of the effect of the cylinder interactions with the bubbles is very different from the aluminium cylinder. The contacts between the cylinder and the bubble induce sharp changes in both velocity and orientation, and last a lot longer than for heavier cylinders. The fluid perturbations caused by the bubble also cause a much greater effect on the light ABS cylinders. We also observe that the cylinder motion is more impacted even in phases where its behaviour resembles the one it has in the fluid at rest.

The temporal evolution of the cylinder orientation and horizontal position are shown in figure 6.9. The difference in behaviour between the cylinder in the bubble swarm and in the fluid at rest are obvious on both signals. While the very large changes in cylinder orientation are mainly caused by direct contact with bubbles, the effect of the fluid perturbations is nonetheless very significant, sometimes even stronger than some contact events. The cylinder undergoes several full revolutions during the time span examined, in stark contrast with its behaviour in the fluid at rest. Similarly, its horizontal motion is strongly agitated.

On figure 6.10 and figure 6.11 we can see the effect of the bubble swarm on a titanium cylinder. The trajectories in the liquid at rest and in the bubble swarm look very similar, with a chaotic motion of the cylinder, alternating wavelike oscillations similar to the fluttering motion and full revolutions. Despite this resemblance, in the swarm the titanium cylinder comes in contact with bubbles several times. The first revolution performed by the cylinder at Y = 0.008m is entirely caused by a bubble contact. The second contact, however (at Y = 0.03m), has nearly no impact on its trajectory, as does the third one at Y = 0.053m. The last contact of the sequence (Y = 0.085m) is indeed a bubble piercing event, but there again, the cylinder motion seems hardly impacted.

The cylinder motion in the bubble swarm is controlled both by its intrinsic dynamics and by bubble swarm influence. The cylinder density changes the relative weight of these two contributions on the final cylinder behaviour. Light cylinders are heavily impacted by interactions with the bubble swarm, while heavy ones retain a trajectory similar to their one in fluid at rest. Some kinds of bubble interactions are more prevalent at certain densities. The bubble piercing, for example, occurs much more at higher density (titanium), while bubble-induced ascension is observed more often for lighter (ABS) cylinders. Both aluminium and ABS cylinders can be either greatly accelerated or decelerated by the bubble swarm. The intrinsic dynamics of the ABS cylinders has very little contribution to the motion in the swarm, and even when their trajectory look similar to their one in the fluid at rest, substantial differences are observed. This balance is reversed for titanium cylinders, which are barely affected by the bubble swarm. Aluminum cylinders, finally, feel the influence of the bubbles when they are in direct contact with them, or with a vortex shed in their neighbourhood, but could regain for a part their natural falling behaviour when they are far from any bubble.

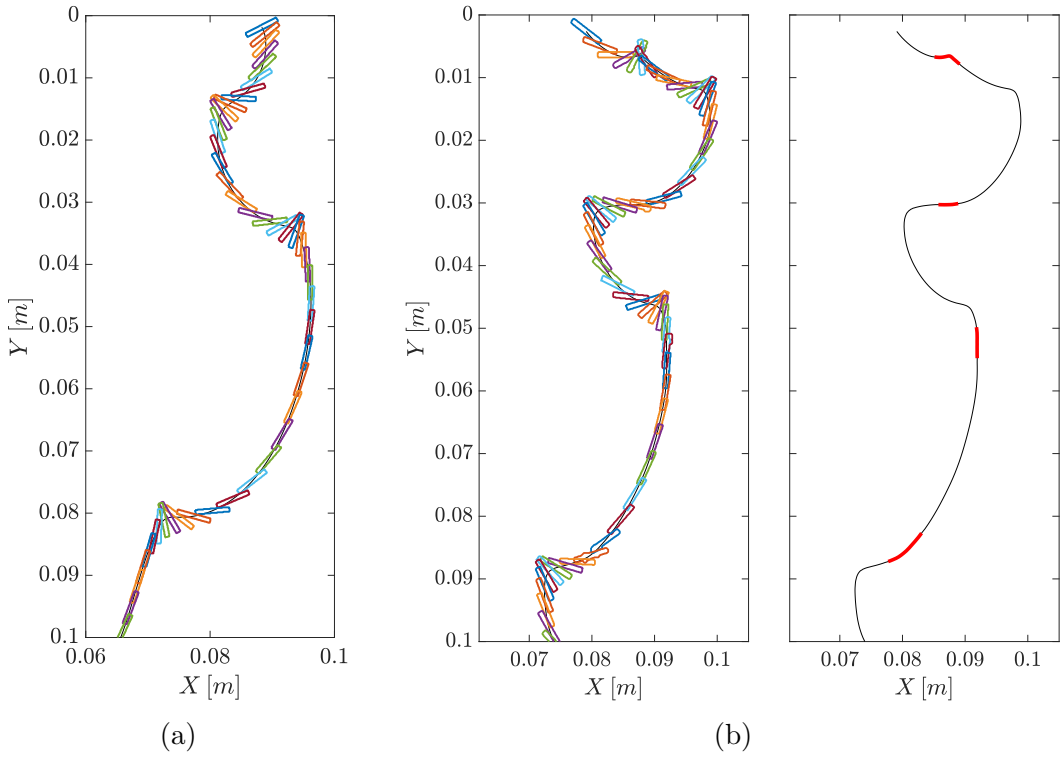

Figure 6.10 – Comparison of the trajectory of a titanium cylinder with (a) $\xi = 7.12$, $Ar = 430$ in a fluid at rest and (b) $\xi = 7.0$, $Ar = 430$ in the bubble swarm for the same range of Y, with and without contours. The time step between cylinder contours is 0.01 s. Trajectory points when the cylinder is in contact with a bubble are highlighted with a thick red line.

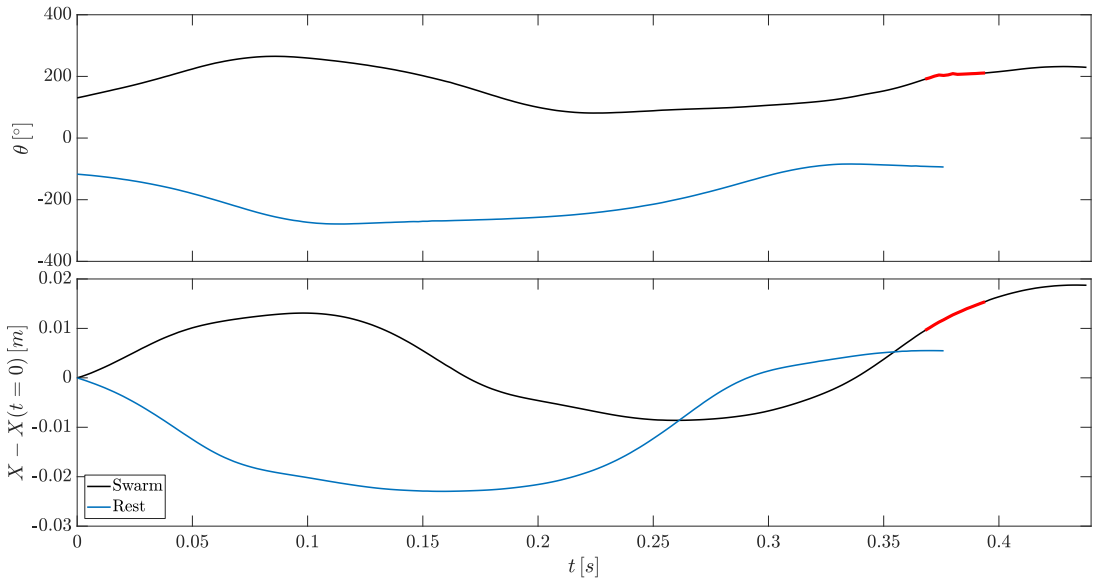

Figure 6.11 – Temporal evolution of the orientation θ and horizontal position X of a titanium cylinder, over a time span corresponding to trajectory shown in figure 6.10, in a fluid at rest with ($\xi = 7.12$, $Ar = 430$) in blue, and in the bubble swarm with ($\xi = 7.0$, $Ar = 430$) in black

Cylinder elongation ratio

The other control parameter of the cylinders is their elongation ratio, defined as $\xi = L/d$, which is varied between 3 and 40. The $\xi = 40$ cylinders are nearly as long as the release funnel. As a result, they tended to get stuck inside of it. It was possible to unstuck them by pushing them through the funnel but that often resulted in the cylinder falling vertically. At this point, we cannot be sure that this vertical falling behaviour is not caused entirely by the inlet condition due to the funnel, and we will only show the results for $\xi = [2, 20]$ in the bubble swarm.

Even more than in the fluid at rest, the elongation ratio plays a critical role in the fall of the cylinders in the bubble swarm. Indeed, as hinted in 6.2.1 the cylinder length impacts its chance of encountering one or possibly more bubbles. Moreover, as discussed in part II, the cylinder elongation ratio directly influences the time it takes to regain its average horizontal orientation after being released vertically. As we have seen previously, bubble interaction can, directly or not, modify heavily the cylinder orientation, which in turn is going to produce very different effects depending on the cylinder elongation ratio. Additionally, as seen in 6.2.3, the cylinder density, and therefore its weight, also changes the effect of the interactions with the bubbles. As all the cylinders studied here have the same diameter, changing the elongation ratio also changes the cylinder weight. We can therefore expect that for the same cylinder density, the influence of bubble interactions will be different for different elongation ratios. In addition, the cylinder moment of inertia is of course directly dependent on ξ. In this section we will describe the effect of the cylinder elongation ratio in the bubble swarm for aluminium cylinders.

For $\xi = 3$, the comparison of the trajectories with the fluid at rest case (figure 6.12) shows clear similarities between the two cases. The beginning of the trajectory between Y = 0 and 0.025m shows an oscillating path in the bubble swarm of nearly similar amplitude and length wave than in the fluid at rest case. A bubble contact occurs at Y = 0.025m which turns the cylinder vertical causing it to surge downwards and perform a full revolution in a tumbling-like manner. For Y = 0.045m, the cylinder has recovered a periodic fluttering motion lasting up to Y = 0.06m. At that point, another contact with a bubble sets the cylinder vertical again. The cylinder then accelerates up to Y = 0.08m, and starts another fluttering motion. On this example, the cylinder natural motion is disturbed several times by bubbles. Several things need to be noted regarding the nature of bubble interactions for a $\xi = 3$ cylinder. Firstly, each bubble interaction modifies the cylinder behaviour on a short distance, of about $5L$ vertically and $2L$ horizontally. Secondly, on the current example, the cylinder resumed its natural fluttering motions several times. Indeed, the time during which the cylinder trajectory is disturbed by bubble interaction appears to be inferior to the time between two such interactions. As a result, the cylinder path can be described as an alternation of sections strongly disturbed by the bubbles or sharing some features of the fluttering motion. The overall motion remains mostly vertical for the whole trajectory, as can be seen on figure 6.12c. The short elongation ratio of the $\xi = 3$ cylinders allows it to encounter few bubbles and also to recover a motion similar to its natural motion shortly after an interaction. The dynamics of $\xi = 3$ cylinders in the bubble swarm keeps of strong memory of their intrinsic dynamics.

The case of $\xi = 20$ (figure 6.13) is very different. The natural motion of the cylinder (see far left image of figure 6.13) is never observed in this example. Instead, large-amplitude oblique motions take place for most of the trajectory. They are interrupted by sudden changes of direction, which generally occur due to an interaction with a bubble. The amplitude of the oblique motions is so large that the cylinder sometimes goes out of the observation window (of 18cm in width). Due to its length, the $\xi = 20$ cylinder encounters a lot of bubbles, sometimes even multiple bubbles at a time. Moreover, the time

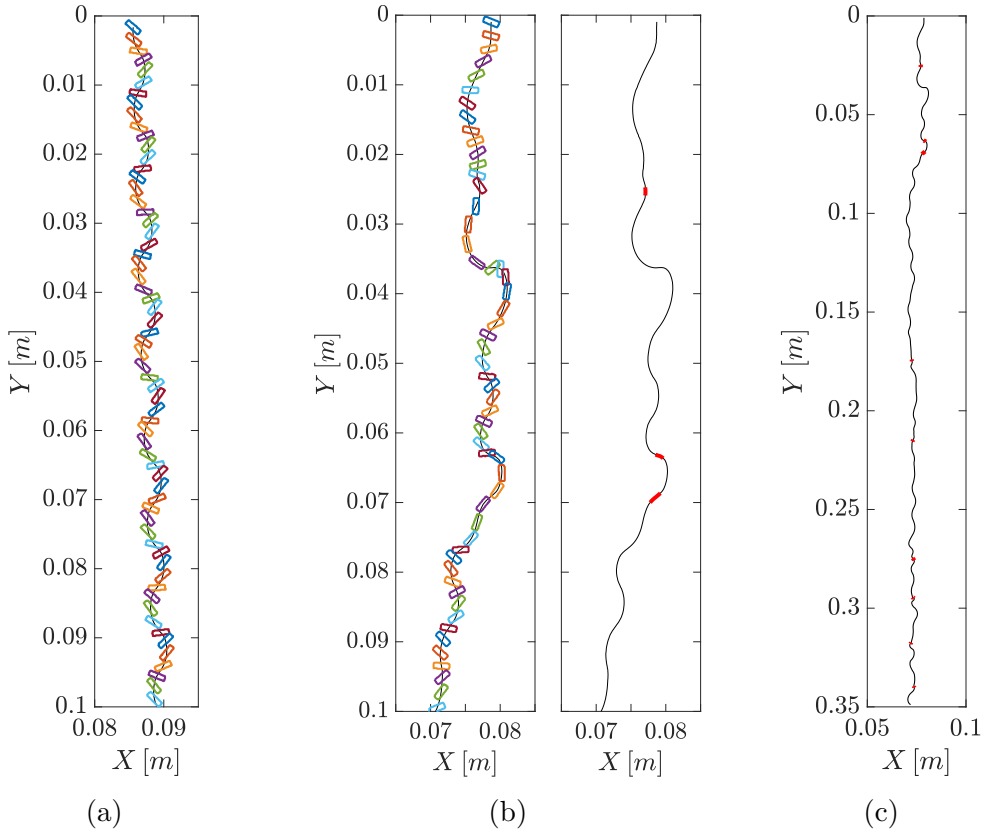

Figure 6.12 – Comparison of the trajectory of an aluminium cylinder with (a) $\xi = 3.12$, $Ar = 200$ in a fluid at rest, (b) $\xi = 3.45$, $Ar = 210$ in the bubble swarm for the same range of Y, with and without contours and (c) of the same cylinder in the bubble swarm for the whole observation window. The time step between shown cylinder contours is 0.02s. Trajectory points when the cylinder is in contact with a bubble are highlighted with a thick red line.

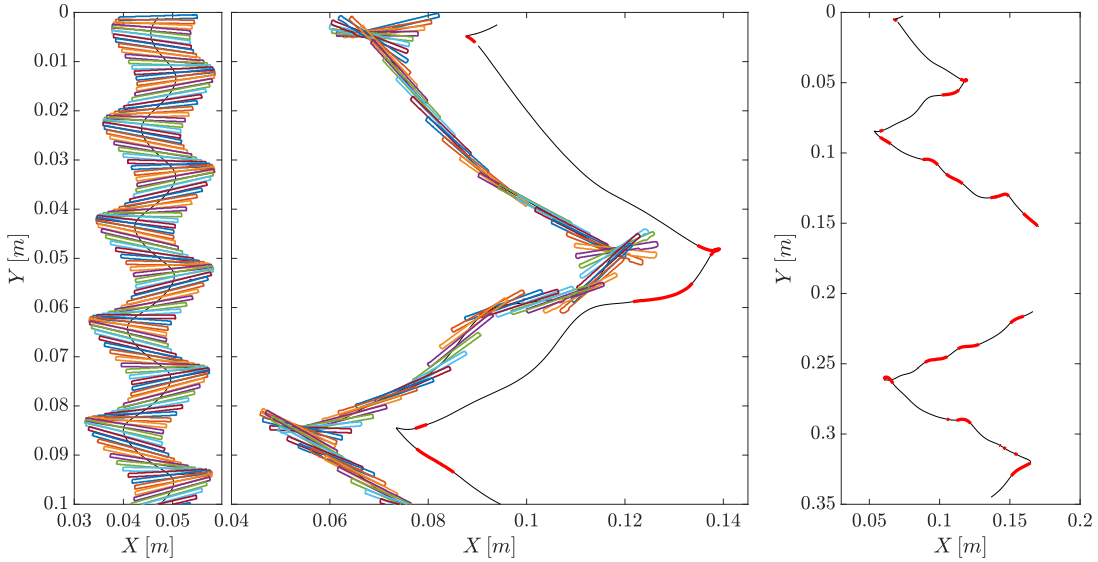

Figure 6.13 – From left to right : trajectory of an alumminium cylinder with $\xi = 20.0$, $Ar = 505$ in the fluid at rest, trajectory of an aluminium cylinder with $\xi = 20.6$, $Ar = 513$ in the bubble swarm zoomed in the first 10cm, with the trajectory with no contour shifted to the right, trajectory of the same cylinder in the bubble swarm for the whole observation window. The time step between shown cylinder contours is 0.02s. Trajectory points when the cylinder is in contact with a bubble are highlighted with a thick red line.

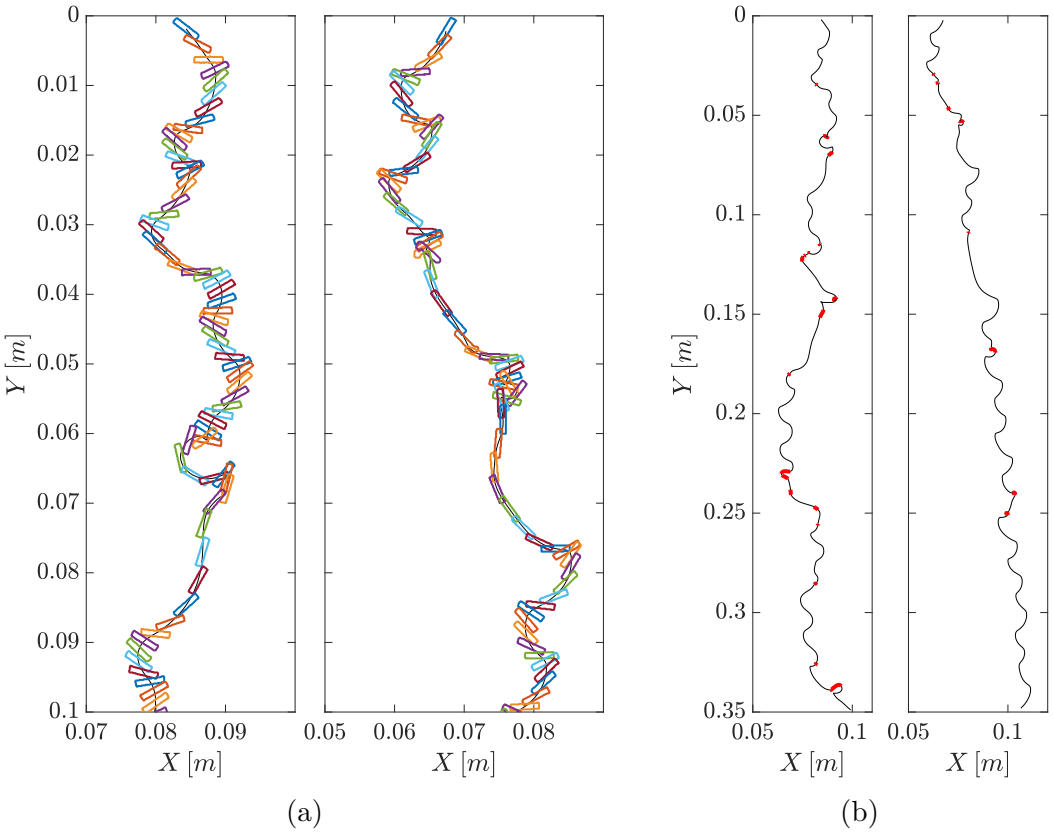

Figure 6.14 – Trajectory of an aluminium cylinder with $\xi = 5.15$, $Ar = 257$ on the left with another one with $\xi = 6.35$, $Ar = 285$ on the right in the bubble swarm (a) zoomed in the first 10cm, (b) for the whole observation window. The time step between shown cylinder contours is 0.02s. Trajectory points when the cylinder is in contact with a bubble are highlighted with a thick red line.

it needs to recover its natural motion after interacting with a bubble is much larger than for the $\xi = 3$ cylinder. The large amplitude oblique motion observed for long cylinders generally starts when the cylinder is tipped by a bubble, giving it its oblique orientation. Large cylinders being also heavy, bubbles are less likely to increase their orientation by the same magnitude as for smaller, lighter cylinders. Indeed, as can be seen on figure 6.13, there seems to be a preferential absolute orientation of the cylinder during its oblique motion. Even consecutive bubble contacts after the initiation of the oblique motion have little impact on the cylinder orientation. The difference between a contact generating radical changes of the cylinder orientation and a bubble contact with little impact lies in several parameters, such as the point of contact between the two objects, or the cylinder velocity before the contact. Due to the cylinder heavy weight for large ξ, such cylinders are not very sensitive to vortices shed by the bubbles. The dynamics of $\xi = 20$ cylinders in the bubble swarm is far more controlled by direct bubbles interactions Such cylinders are gliding on bubbles.

Using two extreme examples ($\xi = 3$ and 20), we have seen how the elongation ratio can affect the cylinder motion in the bubble swarm. We will now describe the other elongation ratios studied ($\xi = 5$, 7, 10, 12) and look for similarities between them. Figure 6.14 shows a direct comparison between a $\xi = 5$ and a $\xi = 7$ cylinder. Similarities between the two trajectories appear obviously on both the total trajectory and the enlargement of the first 10cm of fall. The contact frequency is similar for both cylinders, and consequently, so are the frequency of the phases during which they behave quite similarly to their motion in the fluid at rest. The horizontal displacement of both cylinders during the

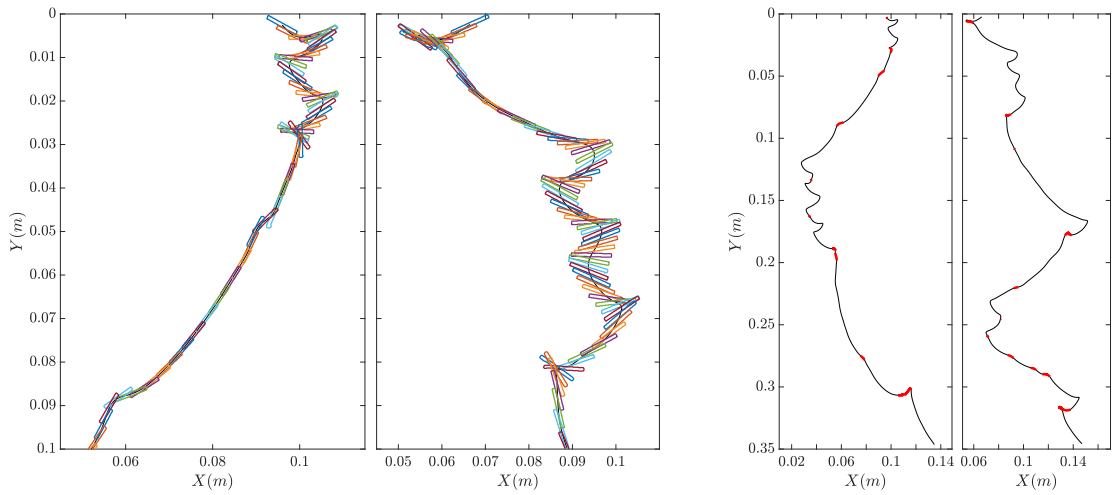

(a) (b)

Figure 6.15 – Trajectory of a cylinder with $\xi = 9.50$, $Ar = 350$ on the left with another one with $\xi = 11.50$, $Ar = 385$ on the right in the bubble swarm (a) zoomed in the first 10cm, (b) for the whole observation window. The time step between shown cylinder contours is 0.02s. Trajectory points when the cylinder is in contact with a bubble are highlighted with a thick red line.

fall is also comparable for both elongation ratios. It is also obvious that these cylinders behave differently from the $\xi = 3$ or $\xi = 20$ cylinders. Cylinders of $\xi = 5$ or $\xi = 7$ are characterized by their rather balanced sensitivity to intrinsic dynamics and to the effect of the bubble swarm.

Similarly, figure 6.15 shows that the paths of cylinders of $\xi = 10$ and $\xi = 12$ are similar. These two elongation ratios feature different behaviour compared to $\xi = 20$, as their intrinsic dynamics plays a larger role. The general behaviour for both these elongation ratio is still dominated by large amplitude downward or oblique motion, and oscillating pseudo-fluttering is scarce. The trajectory is marked by sudden changes of orientation or behaviour, caused by interaction with the bubbles. The overall horizontal displacement of the cylinder is important due to the large oblique motion. Compared to $\xi = 20$ though, the amplitude of these large motions is less important, and pseudo-fluttering occurs more often. For these two elongation ratios, the bubble swarm strongly contributes to the cylinder motion.

The elongation ratios studied in the present work (ξ =3, 5, 7, 10, 12 and 20) can be divided into groups that share similar general behaviours. The two most extreme elongation ratio, $\xi = 3$ and $\xi = 20$ are in categories of their own, as they do not share enough properties with other ξ to be grouped with any. Cylinders of $\xi = 5$ and $\xi = 7$ behave similarly, meaning that the balance between the intrinsic dynamics of the cylinder and the effect of the bubble swarm results in similar paths. A common general behaviour can also be identified for cylinders of $\xi = 10$ and $\xi = 12$. The elongation ratio influences both the intrinsic dynamics of the cylinder and its interactions to the bubbles, and we can therefore expect different sensitivity to the bubble swarm depending on the elongation ratio.

6.3 Statistical description of the cylinder kinematics

In the previous section, we have described numerous types of behaviours observable in the bubble swarm. The types of interactions between the cylinder and the bubble swarm are

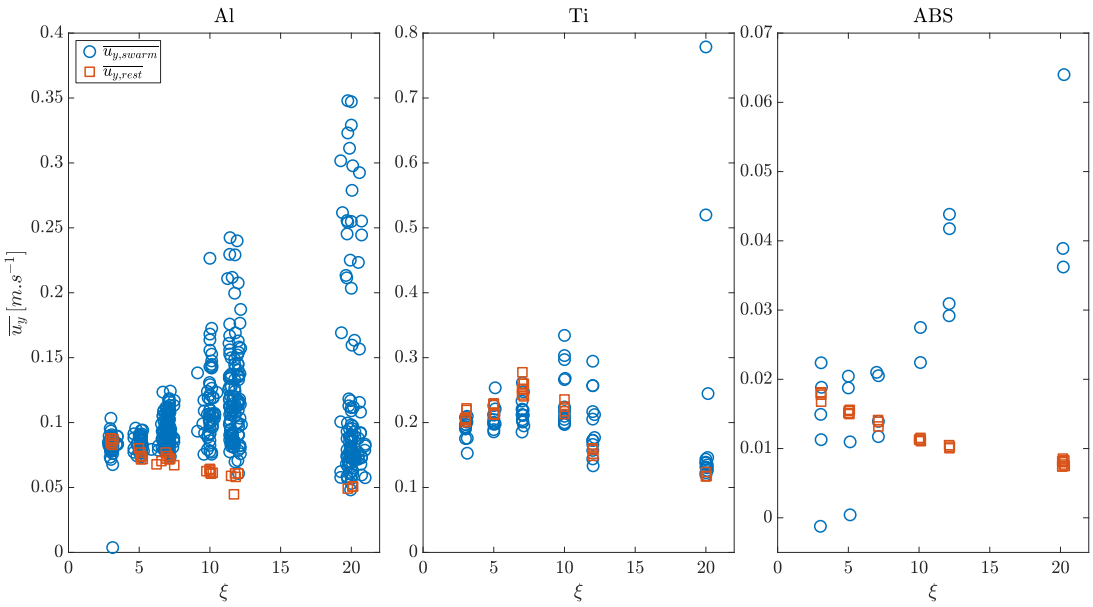

Figure 6.16 – Mean vertical velocity for each run for aluminium cylinders (left), for Titanium cylinders (middle) and ABS cylinders (right), in the bubble swarm (blue ◯) and in the fluid at rest (red □)

numerous, and depend heavily on the two studied parameters : ξ and ρ_c. The influence of each of these parameters on the cylinder motion has been qualitatively described. We will now push our analysis further by taking a look at the motion statistics for all the cylinders. Indeed, due to the chaotic motion of the cylinder in the bubble swarm, statistics are necessary to describe the cylinder motion. They will allow us to more completely characterize the differences that exist between the cylinder motion in the bubble swarm and in the fluid at rest, which have been highlighted in previous sections. We will first focus on the statistical description of some key variables, the orientation of the cylinder to the horizontal θ, its horizontal velocity u_x and its vertical velocity u_y. The amount of data available for each type of cylinder (material, elongation ratio) varies a lot. For a summary of the number of data points in each case, see Appendix B.1. We provide statistical description when convergence has been checked.

6.3.1 Mean motion of the cylinder

The mean motion of the cylinder in the bubble swarm is heavily modified compared to its behaviour in the fluid at rest. Even though there is very little variation in the cylinder motion with α_g (see figure 5.22), the bubble interactions are sufficiently strong to create a big impact on the cylinder dynamics, regardless of the gas volume fraction in the range we investigated.

Figure 6.16 shows the mean vertical velocity $\overline{u_y}$ for each run, in the bubble swarm and in the fluid at rest. There is a significant dispersion of the mean velocities in the bubble swarm, especially at high elongation ratios. In particular, there are two different groups of vertical velocities at $\xi = 20$, for all materials, with one group featuring very high vertical velocity. The likely cause for this increase in velocity is a nearly vertical orientation of long cylinders. The high velocity of nearly vertical cylinders causes them to exit the observation windows very quickly. As the cylinder elongation ratio decreases, the mean vertical velocities are less dispersed, and the velocity in the swarm is closer to the velocity in the fluid at rest. For some runs, the vertical velocity is nearly zero (one

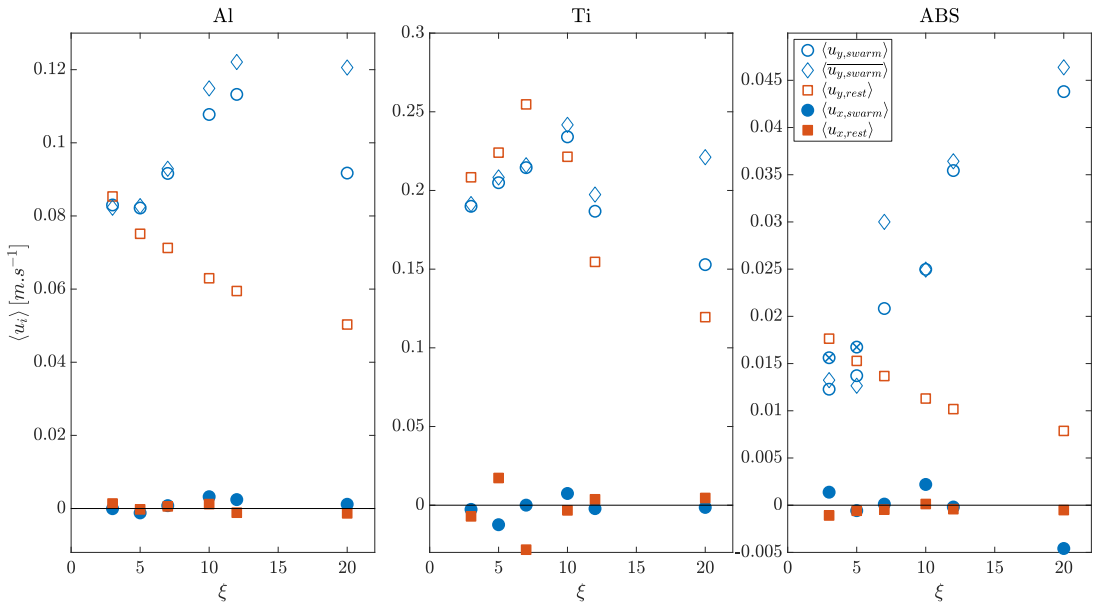

Figure 6.17 – Mean vertical and horizontal velocity of the aluminium (left), titanium (middle) and ABS (right) cylinder in the bubble swarm (blue ◯) and in the fluid at rest (red □). The vertical velocity computed by averaging the average vertical velocities for each run is plotted in thin (◊). The vertical velocity is plotted with empty symbols, and the horizontal velocity with filled ones. For ABS cylinders, (⊗) show the mean vertical velocity for all runs excluding the ones where the cylinders are carried up to the free surface by bubbles. These runs have a very significant weight in the mean due to the low amount of runs with ABS cylinders.

run of an aluminium cylinder of $\xi = 3$, two ABS cylinders of $\xi = 3$ and 5) because of cylinders being dragged to the free surface of the experiment by bubbles.

For a given ξ, there are several ways of computing the average vertical velocity. The first one is to average all the instantaneous velocities values for all the runs at a given ξ. The second one is to average instead the average velocity for each run. These two methods are compared for the vertical velocity in figure 6.17 (the first method is plotted with circles, and the second one with lozenges). The mean vertical velocity computed with the two methods are very close at $\xi \leqslant 7$ for all materials. For longer cylinders, the second method (i.e. $\langle \overline{u_y} \rangle$) gives higher mean vertical velocities. Indeed, with the first method, runs with a high average velocities shown in figure 6.16 weigh less in the mean value due to their small duration. As seen in figure 6.16, large variations of the mean vertical velocity occur especially at high elongation ratio. Despite this difference, the outputs from the two methods remain close to each other. In the following, we select the first method, as it increases the statistical convergence. The mean horizontal velocities in the swarm and in the fluid at rest are both close to zero for aluminium cylinders, which shows a good statistical convergence. For Titanium and ABS cylinders, the statistical convergence is less satisfactory, due to the smaller amount of data. In the fluid at rest, the cylinder falling velocity is averaged over its steady state. In the bubble swarm, no such state can be defined, and the falling velocities are averaged over the entire falling height.

The effect of the bubble swarm is most important for ABS cylinders. While their velocity in the fluid at rest decreases steadily with ξ, it follows the opposite evolution in the swarm. The increase in velocity is especially important for long cylinders ($\xi \geqslant 10$). The same observations also stand for the aluminium cylinders, whose falling velocity in the bubble swarm rises steadily with ξ up to $\xi = 12$. For $\xi = 20$, however, it decreases, despite

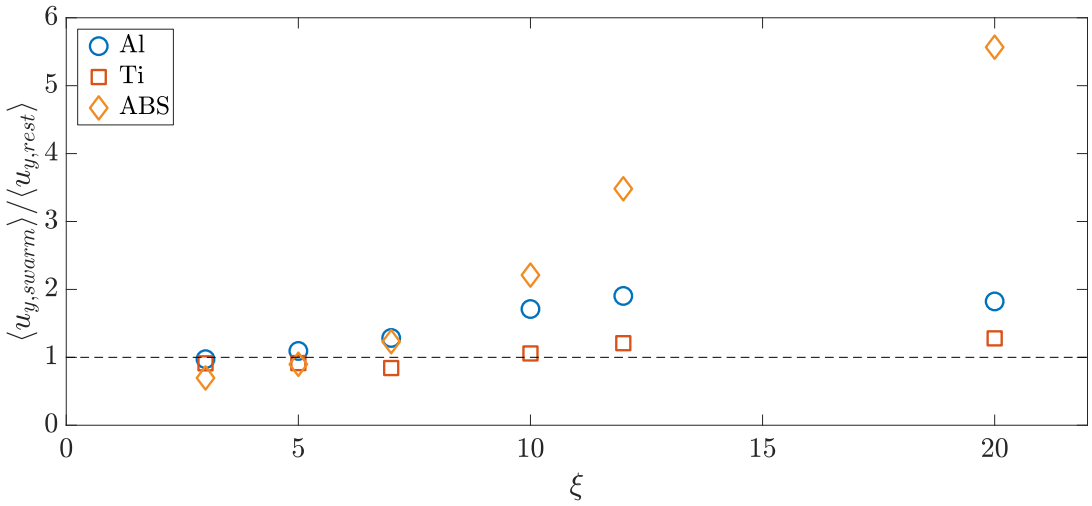

Figure 6.18 – Ratio of the mean velocity in the swarm $\langle u_{y,swarm} \rangle$ with the mean velocity in the fluid at rest $\langle u_{y,swarm} \rangle$ for different ξ and all materials. Aluminium cylinders are plotted with (◯), titanium ones with (□) and ABS ones with (◊).

some runs with very high vertical velocity. The effect of the bubble swarm is different for titanium cylinders. Their velocity in the swarm remains close to their velocity in the fluid at rest for all ξ. In addition, for cylinders of $\xi \leqslant 7$, the falling velocity in the swarm is actually less important than in the fluid at rest.

The ratio between the velocity in the fluid at rest and the one in the bubble swarm is seen figure 6.18. The effect of the bubble swarm is strongly dependent on ξ for all materials. The vertical velocity in the swarm is nearly the same than in the fluid at rest for short cylinders ($\xi \leqslant 7$) of all materials. For $\xi \geqslant 10$, however, all cylinders are accelerated by the bubble swarm, with heavy cylinders being least affected. The acceleration of long cylinders is probably caused by changes in their orientation after interaction with a bubble, because they take a long time to recover a horizontal orientation after an increase in θ. Heavy cylinders being least affected by interactions with bubbles, they are less likely to go under such acceleration phases. Short cylinders ($\xi \leqslant 7$), on the other hand, are less likely to encounter a bubble, and their recovery time is also shorter. As a result, they accelerate less due to interaction with bubbles. In addition, because they are lighter (for the same material) than long cylinders, strong bubble interactions slow them down more.

6.3.2 Discussion of the cylinder energy in the swarm

The cylinder in the bubble swarm is subject to different influences. First, it has its own intrinsic dynamics, for which one can clearly define the kinematic energy. Then, in the bubble swarm, it encounters velocity and pressure fluctuations in the fluid, and may interact directly with bubbles. The energy involved in both these contributions cannot be expressed easily, as the bubble has a negligible mass, and it is impossible to estimate the volume (hence the mass) of fluid randomly displaced. As a result, a direct energetic comparison is not easy to perform. We can however compare the variance of the velocity fluctuations.

The variances of the fluctuations of the horizontal and vertical velocity of the cylinder and of the liquid can be seen in figure 6.19 for the horizontal and vertical directions. The variance of the velocity fluctuations in the fluid, noted u'_y in the vertical direction, and u'_x in the horizontal one, has been calculated using Bouche et al. [6] scaling $\langle u'^2_y \rangle \simeq \left(1.07 u_o \alpha_g^{0.46}\right)^2$ in the vertical direction and $\langle u'^2_x \rangle \simeq \left(0.74 u_o \alpha_g^{0.38}\right)^2$ in the horizon-

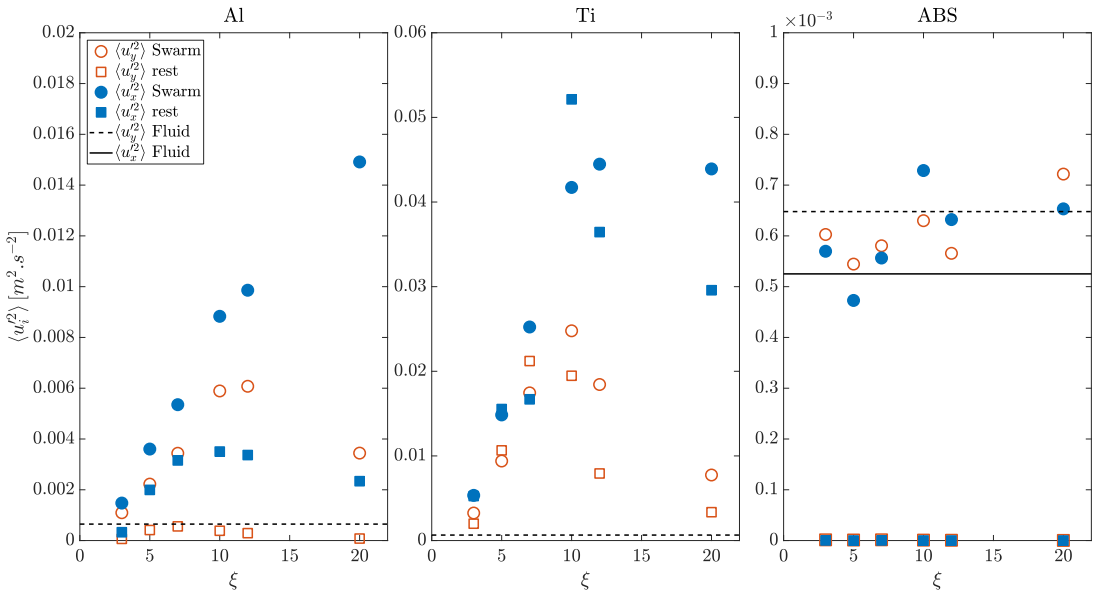

Figure 6.19 – Comparison of the variances of the velocity fluctuations for the aluminium cylinder (left), the titanium cylinders (middle) and the ABS ones (right), in the bubble swarm (◯), in the fluid at rest (□), in the horizontal direction in blue and in the vertical direction in red, and of the vertical velocity fluctuations in the fluid (dashed line), and horizontal velocity fluctuations in the fluid (black line). The vertical scales of the three panels of this figure are very different from each other.

tal direction. In figure 6.19, the highest value of α_g was taken, which gives a meaningful order of magnitude, as there' not much variation from the lowest to the highest α_g. Indeed the variance of the velocity fluctuations goes from $3.93.10^{-4}$ $m^2.s^{-2}$ for $\alpha_g = 2.1\%$ to $6.47.10^{-4} m^2.s^{-2}$ for $\alpha_g = 4.5\%$ in the vertical direction, and from $3.47.10^{-4}$ $m^2.s^{-2}$ to $5.25.10^{-4}$ $m^2.s^{-2}$ in the horizontal direction. For all materials, we see an increase in the velocity variance in the bubble swarm compared to in the fluid at rest. For aluminium cylinders, $\langle u_y''^2 \rangle$ can be 10 times as high in the bubble swarm than in the fluid at rest, and $\langle u_x''^2 \rangle$, 7 times as high. The increase is stronger in the vertical direction, and grows with ξ. For titanium cylinder, we actually see a decrease of both $\langle u_y''^2 \rangle$ and $\langle u_x''^2 \rangle$ in the swarm at $\xi = 3$. However, for all other elongation ratios, the variance of the velocity fluctuation is at least as high in the swarm as it is at rest. Interestingly, for titanium cylinders, the increase in the variance of the velocity fluctuations in the swarm is stronger in the horizontal direction, for $\xi \geqslant 10$. For ABS cylinders, the variance of the velocity fluctuation in the fluid at rest is extremely small, as the body motion is rectilinear.

The velocity variance of titanium cylinders in the fluid at rest is significantly greater than the variance of the fluid agitation in both directions (figure 6.19 in the middle). As a result, the variance of its velocity fluctuations is of the same order of magnitude in the swarm and in the fluid at rest. Indeed, for most elongation ratios, the behaviour of titanium cylinders in the swarm is close to its behaviour in the fluid at rest. Both the mean motion of the cylinder (see 6.3.1) and its velocity variance are dominated by its intrinsic dynamics. Long cylinders ($\xi \geqslant 12$) are the most affected by the bubble swarm, as bubble interaction can sometimes cause them to go under large amplitude vertical motion. The density of titanium cylinder is much greater than the density of the fluid, which explains that the cylinders are not very responsive to fluid perturbations.

The ABS cylinders feature a radically different behaviour (figure 6.19 right). Their velocity variance at rest is negligible and at least significantly lower than the variance of the fluid agitation in any direction (they fall steadily). In the bubble swarm, both

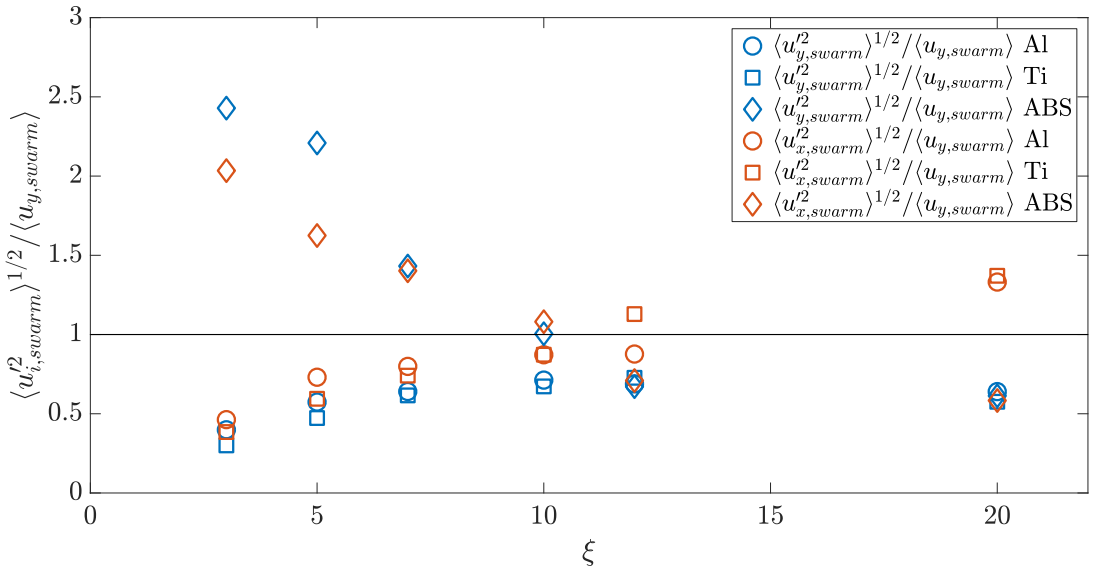

Figure 6.20 – Ratio of the standard deviation of the velocity fluctuation $\langle u'_y\rangle$ and $\langle u'_x\rangle$ to the mean vertical velocity $\langle u_y\rangle$ of the cylinder in the swarm, for all materials and ξ

$\langle u''^2_y\rangle$ and $\langle u''^2_x\rangle$ are of the same order of magnitude as the velocity variance for the fluid, with no significant impact of ξ on the variance of its velocity fluctuations in the swarm. Qualitatively, we have seen that ABS cylinders were, indeed, greatly affected by the velocity fluctuations in the fluid. Contrary to other density ratios, ABS cylinders in the bubble swarm never behave in a way that closely mimics their behaviour in a fluid at rest (see figure 6.8b). They respond strongly to the agitation generated by bubbles of similar size, in a liquid of similar density. Their motion is therefore excited by fluid perturbations in the cell.

The variance of the velocity fluctuations of the aluminium cylinder in the both directions is significantly more important in the bubble swarm than in the fluid at rest figure 6.19 left). Interestingly, its vertical velocity variance in the fluid at rest is of the same order of magnitude as the variance of the fluid velocity in the bubble swarm. Excitation of the cylinder motion by liquid agitation is thus expected to be possible. The increase in velocity variance observed in the swarm cannot be attributed to the fluid agitation in the cell. Indeed, the aluminium cylinders density is much more important than the fluid density, and their motion is expected to be weakly impacted by fluid perturbations. One must deduce that the source of the increase in velocity variance in the swarm is not directly the fluid perturbations in the cell. Instead, interactions of the cylinder with bubbles change its behaviour and result in more variation of its velocity.

Figure 6.20 compares the standard deviation of the velocity fluctuations with the mean falling velocity for all materials and ξ. The ratio $\langle u'^2_y\rangle^{1/2}/\langle u_y\rangle$ is remarkably similar for aluminium and titanium cylinders. Similarly, $\langle u'^2_x\rangle^{1/2}/\langle u_y\rangle$ is also very close for these two materials (except for $\xi = 12$). For $\xi \leqslant 7$, $\langle u'^2_y\rangle^{1/2}/\langle u_y\rangle$ and $\langle u'^2_x\rangle^{1/2}/\langle u_y\rangle$ are also very close to each other. In both directions, the ratio of the standard deviation to the mean velocity rises steadily with ξ, except in-between $\xi = 12$ and 20, where it decreases again in the vertical direction.

ABS cylinders follow an entirely different trend as compared to the two other materials. Both $\langle u'^2_y\rangle^{1/2}/\langle u_y\rangle$ and $\langle u'^2_x\rangle^{1/2}/\langle u_y\rangle$ decrease steadily with ξ. Except for $\xi = 3$ and 5, $\langle u'^2_i\rangle^{1/2}/\langle u_y\rangle$ are very similar in both directions, contrary to the other materials. This confirms that the response of the cylinder agitation to that of the fluid in the swarm are very different for ABS and metal cylinders. ABS cylinders are strongly influenced by both

fluid motion in the cell and interaction with bubbles. The motion of metal cylinders, on the other hand, is only weakly disturbed by the fluid motion in the cell, and the dominant source of agitation is the direct interaction with bubbles.

The comparison of the cylinder velocity variance while in the fluid at rest with the one of the fluid agitation in the bubble swarm seems to be related to the general cylinder behaviour in the bubble swarm when comparing cylinders of different densities. When the fluid velocity variance is significantly greater than the cylinder one, the cylinder dynamics in the bubble swarm is dominated by interactions with the surrounding bubbles and fluid. On the contrary, when the cylinder has a lot more intrinsic energy than the fluid in the bubble swarm, it is much less by the bubbles, and its trajectory in the bubble swarm is closer to its one in the fluid at rest. Finally, when the two variances are of the same order of magnitude, the cylinder dynamics is a complex balance between its natural motion, and the effect of strong interaction with bubbles.

6.3.3 Comparison between the probability density function of the cylinder kinematics in the bubble swarm and that in the fluid at rest

Cylinder orientation

The statistics of the angle of the cylinder with the horizontal, θ, are compared in the bubble swarm and in the fluid at rest. The analysis of the differences is a first way of pointing the specific action of the bubble swarm on the cylinder motion. At first, statistics of the cylinder motion in the fluid at rest are only calculated over the slowly varying regime of the cylinder. This choice was made because the observed transient regimes in the fluid at rest depend a lot on the cylinder elongation ratio. Short cylinders have nearly reached their slowly varying state when entering the observation window, whereas the transient regime of long cylinder takes a substantial place in the field of view.

The p.d.f. of the aluminium cylinder orientation θ (figure 6.21) are symmetrical with respect to the origin for all ξ. This indicates a good statistical convergence, and an independence of the phenomena to the sign of θ. It is therefore possible to study the absolute value of the cylinder orientation to provide additional statistical convergence. Subsequent p.d.f. of θ will be p.d.f. of $|\theta|$ instead (figure 6.21b).

In the fluid at rest, the p.d.f. of $|\theta|$ for all elongation ratios shows a strong signature of the fluttering motion. Two peaks are visible in the p.d.f. at the amplitude of the oscillating motion. This is usual for sinusoidal motions. However, there is a supplementary peak in the p.d.f. at $\xi = 3$ near 0 value. For $\xi = 3$, two types of motion are observed in the fluid at rest, fluttering and weak fluttering, during which the cylinders goes under very small amplitude oscillations, with hardly any motion of the cylinder centre of gravity, which explains the peak near $|\theta| = 0°$. These two types of motion did not occur intermittently for a single run. Instead, the cylinders kept the regime of motion they had at the beginning of their fall throughout their entire fall.

In the bubble swarm, the distribution of the cylinder orientation is reminiscent of the one in the fluid at rest. Indeed, we observe local peaks at the same values than the ones in the fluid at rest. Figure 6.21c shows the p.d.f. of $|\theta|$ normalized by the amplitude of the fluttering motion in the fluid at rest. For all elongation ratios but $\xi = 20$, the peak in the p.d.f. is at a value slightly lower than A_θ, which shows that the agitation of the cylinder in the bubble swarm may present phases similar to oscillations in the fluid at rest, but that it has to develop in a random environment and could have no time to reach steady state before being perturbed again. The oscillating motion of the cylinder in the swarm is

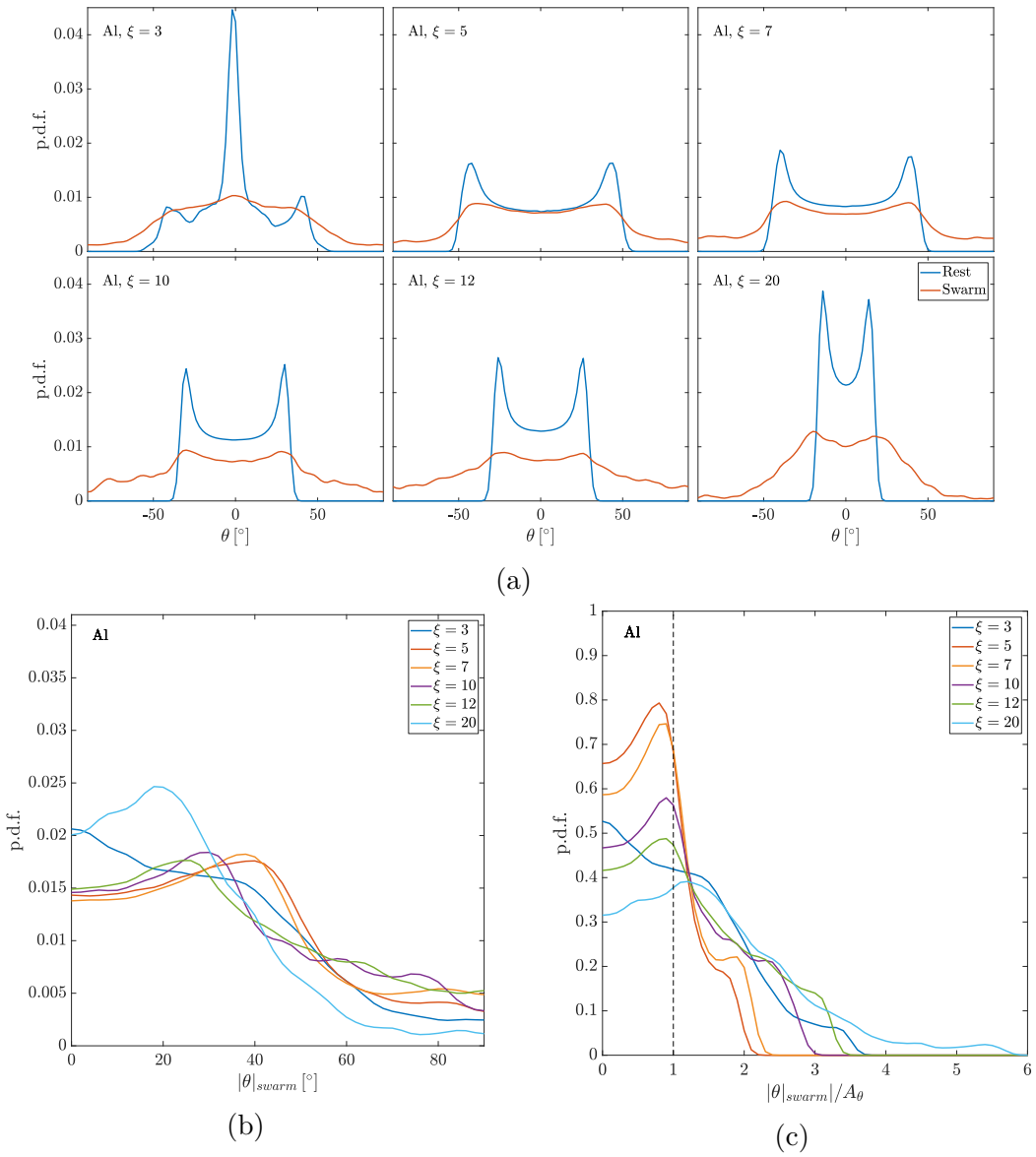

Figure 6.21 – (a) Superposition of the p.d.f. of θ for aluminium cylinders in the fluid at rest and in the bubble swarm for all ξ (b) superposition of the pdf of the absolute of θ, $|\theta|$ in the bubble swarm for different ξ (c) superposition of $|\theta|$ in the bubble swarm, normalized by the fluttering amplitude in the fluid at rest A_θ, for different ξ.

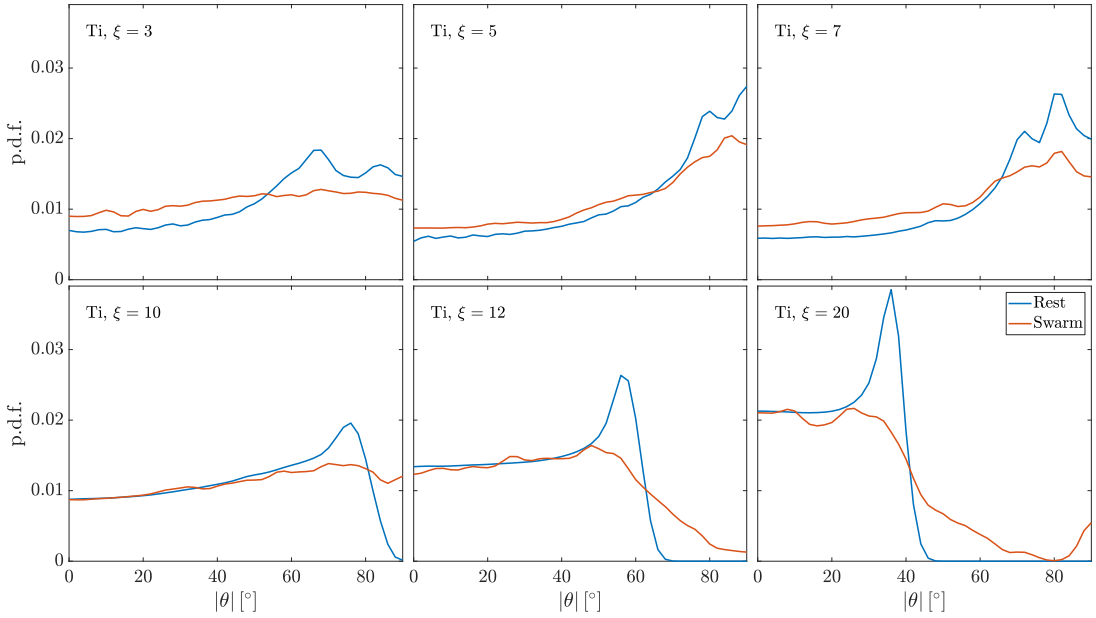

Figure 6.22 – Superposition of the p.d.f. of $|\theta|$ for titanium cylinders in the fluid at rest and in the bubble swarm for all ξ

a succession of transient oscillations interrupted by strong interactions with bubbles. At $\xi = 20$, the oscillating motion is rarely seen in the swarm. The peak in the p.d.f. which appears at a θ value larger than A_θ is likely caused by large amplitude oblique motion, with nearly constant θ, as shown by visual observations.

Cylinder orientations observed in the fluid at rest have a significantly higher probability of being also observed in the swarm. Yet, cylinder orientations larger than any observation in the fluid at rest appear at all ξ. For $\xi = 3$, 5, and 7, the p.d.f. of the cylinder orientation in the swarm shows that these high values of the cylinder orientation ($|\theta| > 70°$) are equiprobable. For cylinders of $\xi = 10$, 12 and 20, the p.d.f. in the swarm decreases for these high orientations. Cylinders of $\xi = 10$ and 12 are more often under large orientations in the swarm than shorter cylinders. Long cylinders encounter more bubbles, and therefore have more chance of being tilted significantly. Their greater mass, however, means that they are less likely to reach very high θ than lighter cylinders, due to the interaction with bubbles. Cylinders of $\xi = 20$, for instance, are very rarely observed at $\theta > 70°$. Figure 6.21b suggests that we can gather cylinders of different elongation ratios in groups based on similarities of the p.d.f. of their orientation in the swarm. Cylinders of $\xi = 5$ and 7 have very close p.d.f. of θ, as do cylinders of $\xi = 10$ and 12. Cylinders of $\xi = 3$ and 20 present different p.d.f. This separation in different groups will be more deeply assessed by further results.

The influence of the cylinder weight on its interactions with bubbles can be further examined by looking at statistics of other materials. The p.d.f. of $|\theta|$ for titanium cylinders are shown in figure 6.22. In the fluid at rest, titanium cylinders of $\xi = 3$ go under a fluttering motion with few seemingly chaotic tumbling phases. The bubble swarm homogenizes the p.d.f. of the orientations. For $\xi = 5$ and 7, whose motion in the fluid at rest is seemingly chaotic, the p.d.f. in both media are close. The maximum angle θ reached in the fluid at rest is 90°, which means that the bubble swarm cannot generate more important cylinder orientations. On the contrary, the cylinder in the swarm is more often under low angles than in the fluid at rest, which is only seen for these cylinders. For $\xi = 10$, 12 and 20, which are fluttering in the fluid at rest, high cylinder orientations appear in the bubble swarm, that were never observed in the fluid at rest, where the

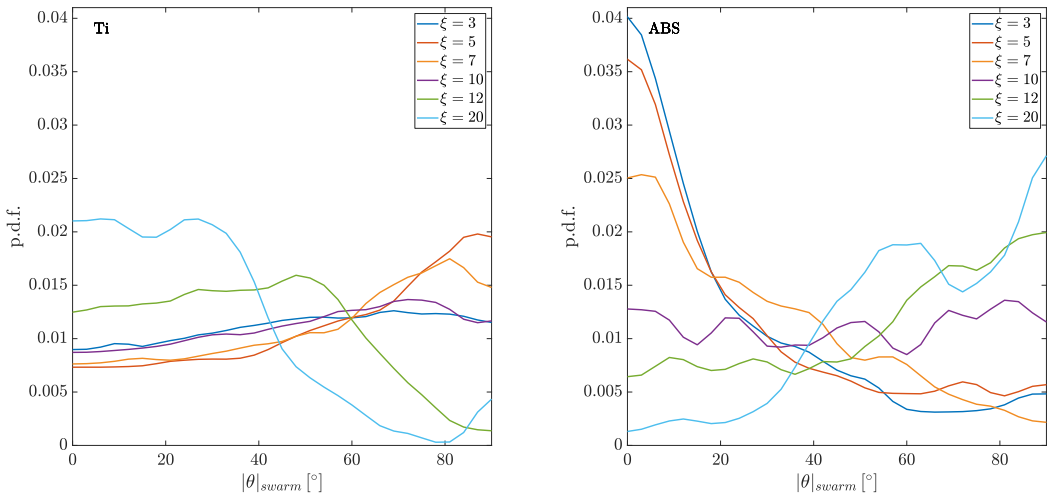

(a) (b)

Figure 6.23 – (a) Superposition of the p.d.f. of $|\theta|$ for titanium cylinders in the bubble swarm (b) Superposition of the p.d.f. of $|\theta|$ for ABS cylinders in the bubble swarm

motion is pure fluttering. This behaviour is closer to the one of aluminium cylinders, but even if the motion of titanium cylinders in the bubble swarm is largely dependent on their motion in the fluid at rest, the peak associated to pure fluttering disappears. On the other hand, fluttering titanium cylinders are affected by the bubble swarm in the same way than fluttering aluminium cylinders are. Interactions with bubble generate higher angles that the maximum θ observed in the fluid at rest. Due to the higher mass of titanium cylinders, for a given ξ larger than 10, the range of angles that are only present in the bubble swarm, and that are assumed to be primarily generated by bubble contacts is less important than for aluminium cylinders (see figures 6.22 and 6.21a). Bubble contacts are less able to turn a titanium cylinder than an aluminium one due to the difference in mass. In addition, the influence of the elongation ratio on the motion of fluttering titanium cylinders is more difficult to evaluate, due to the high maximum θ reached by titanium cylinders in the fluid at rest. Similarly than for aluminium cylinders, we can gather titanium cylinders in different groups depending on the p.d.f. of their orientation in the swarm (shown on figure 6.23a). Cylinders with $\xi = 5$ and 7 share similar behaviour, as do cylinders of $\xi =$ 12 and 20. The p.d.f. of θ for cylinders of $\xi = 3$ and 10 also look similar, but further discussion will show that these two cases cannot be gathered, as the mechanisms leading to this similarity are different for the two ξ.

The comparison of the p.d.f. of $|\theta|$ for various ξ in the bubble swarm for ABS cylinders is shown on figure 6.23b. No comparison was made with the orientation in the fluid at rest, as all ABS cylinders follow a rectilinear motion, with their orientation being close to 0° at all times for all ξ. The elongation ratio plays a major role on the motion of ABS cylinders in the swarm. Indeed, they all have the same natural motion in the fluid at rest, but their orientation in the bubble swarm varies greatly with ξ. For low ξ ($\xi = 3$, 5 and 7), the most probable angles are low ($< 20°$), but there is a significant amount of high angles being observed as well. For $\xi = 10$ in particular, all values of θ are nearly equiprobable. At higher elongation ratios, the most probable angles are the high ones ($> 50°$). Numerous bubble interactions increase their orientation up to the point where they are nearly vertical. At low angles, bubble interactions are numerous and potent enough to make the cylinder nearly stationary. The cylinder can only go down in the cell when it is nearly vertical. The elongation ratio is the prevalent factor in determining how the cylinder interacts with the swarm. The switch in the p.d.f. of $|\theta|$ from a peak at 0°

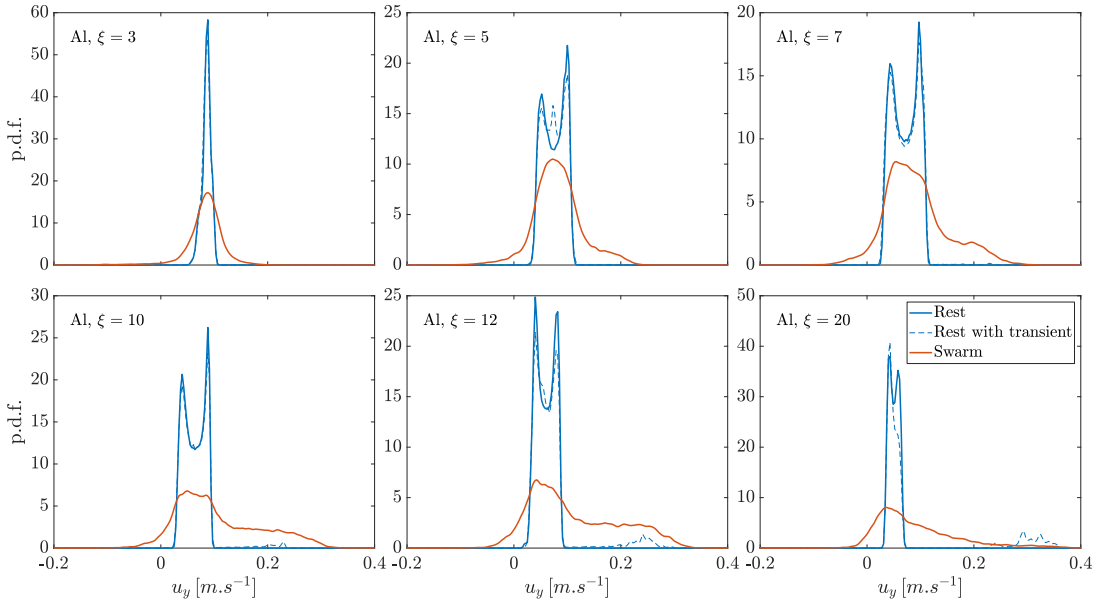

Figure 6.24 – P.d.f. of the aluminium cylinder vertical velocity, u_y, for different ξ , in the fluid at rest, in the fluid at rest including the transient regime, and in the bubble swarm.

for cylinders of $\xi \leqslant 7$ to a peak at 90° for cylinders of $\xi \geqslant 12$ is remarkable.

All of these observations show the competition between the body intrinsic dynamics and the effect of the bubbly flow. Titanium cylinders are too heavy to be completely controlled by the agitation generated by the bubble swarm. Their natural motion is the most important factor in determining their behaviour in the bubble swarm. On the contrary, the light mass of ABS cylinders make them very susceptible to all influences of the bubble swarm. The elongation ratio plays an important role in determining their behaviour in the swam, as it partly dictates the frequency of interactions between the cylinder and the bubbles. For aluminium cylinders, we observe a more complex interplay between their intrinsic motion and their response to the swarm. In the bubbly flow, the predominance of the observations of θ within the same range as the fluid at rest highlights the remanence of the cylinder intrinsic dynamics. Interestingly, this phenomenon is notable even for high elongation ratios, where the natural motion of the cylinder is barely observable qualitatively (see 6.2.3). The bubble swarm tends to increase the cylinder orientation (except when the cylinder already reaches 90° in the fluid at rest) regardless of the cylinder material and elongation ratio. Yet, heavier cylinders are less susceptible to interaction with bubbles. Longer cylinders tend to encounter more bubbles, and therefore are more affected by the swarm. For a single material, longer cylinders are also heavier, and these two effects compete.

Cylinder vertical velocity

The cylinder vertical velocity plays a large part in its dynamics. It is also closely related to the cylinder orientation, especially in the confined cell. In the fluid at rest, aluminium cylinders follow a fluttering motion, which generates vertical oscillations at twice the fluttering frequency.

The p.d.f. of the vertical velocity are displayed on figure 6.24 for the aluminium cylinder, and the superposition of u_y in the swarm can be seen in figure 6.25. The data in the fluid at rest are included with and without the transient regimes, in order to compare the similarities between the transient regime in the fluid at rest, and the motion of the cylinder in the swarm. In a fluid at rest, similarly to the cylinder orientation $|\theta|$, the

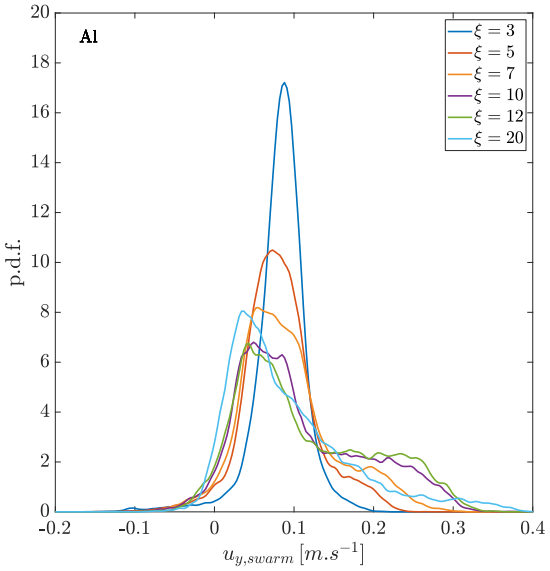

Figure 6.25 – Superposition of the p.d.f. of the aluminium cylinder vertical velocity, u_y, for different ξ in the bubble swarm.

periodic motion of the cylinder induces two peaks in the p.d.f. of the cylinder vertical velocity. Cylinders of $\xi = 3$ feature only a single peak, which is explained by the small amplitude of its oscillations, and by the occurrence of what we have called weak fluttering (see part II).

In the bubble swarm, p.d.f. are strongly modified. At first, negative velocities are present. They correspond to upward motions when the cylinders are pushed by the bubbles, or to what happens shortly after contact with a bubble. Negative velocities are seen for all elongation ratios. In the bubble swarm, high values of the cylinder falling velocities are also observed. A tail of high velocities is seen on the p.d.f. of all elongation ratios, and gets more important with higher ξ. Interestingly, these high velocities are in the range of the vertical velocity of the cylinder in the fluid at rest during their transient motion, when they are released vertically as shown by the p.d.f. in dashed line on figure 6.24. Such transient behaviour leaves a signature on the p.d.f. in the fluid at rest. Yet, for all elongation ratios, the most probable values of u_y in the swarm are the ones that are observable in the fluid at rest. The probability of observing u_y in the same range than in the fluid at rest decreases however significantly with ξ.

The p.d.f. of the cylinder vertical velocity at $\xi = 3$ is nearly symmetrical. For $\xi = 5$ and 7, we start to see larger velocities of the cylinder fall caused by the bubbles. For $\xi = 10$, 12, the increase in the falling velocity becomes stronger, and the p.d.f. of u_y in the swarm is even less strongly marked by the dynamics of the cylinder in the fluid at rest. For $\xi = 20$, the p.d.f. of u_y in the swarm and at rest are also strongly dissimilar, and the bubbles swarm creates lower velocities of the cylinder compared to $\xi = 10$ and 12, as the tail of the p.d.f. of u_y is more contracted. These observations are concordant with the ones for the mean vertical velocity of the cylinder (see figure 6.17). Indeed, the bubble swarm can decrease the cylinder vertical velocity during contact events (even creating negative velocities). On the other hand, increases in velocity are probably caused by high cylinder orientations seen in the bubble swarm (see figure 6.21). For short and light cylinders ($\xi = 3$), the decreases and increases in velocity due to the swarm rather balance, resulting in similar mean vertical velocities in the swarm and in the fluid at rest. For all other cylinders, the increase in mean velocity is more important.

Figure 6.26 shows the p.d.f. of the vertical velocity for titanium cylinders. The motion

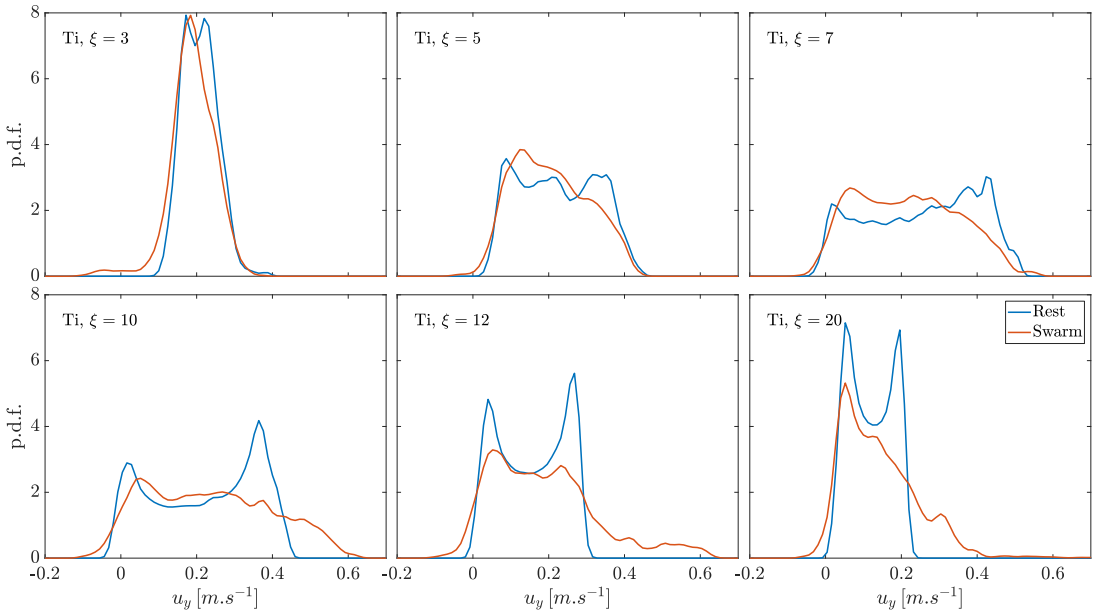

Figure 6.26 – P.d.f. of the titanium cylinder vertical velocity, u_y, for different ξ and all α_g.

of titanium cylinders in the swarm was found to be qualitatively similar to their motion in the fluid at rest. However, differences are observed in the p.d.f. of their vertical velocity in both media, even though the difference is less important than for aluminium cylinders. In the swarm, all elongation ratios feature negative velocities, even though much less than aluminium cylinders. Cylinders of $\xi = 3$ in particular show a tail of negative velocities. Cylinders of $\xi = 5$ and 7, whose motion in the fluid at rest is apparently chaotic, have lower velocities, which is concordant with their lower mean vertical velocity in the swarm (see figure 6.17). In addition, it is interesting to note that titanium cylinders of $\xi = 7$, 10 and 12 feature negative velocities even in the fluid at rest. The p.d.f. for longer cylinders ($\xi \geqslant 10$) all feature a tail of higher velocities. For all fluttering cylinders ($\xi = 3$, 10, 12 and 20) the two-peaked shape of the p.d.f. associated to motion in the fluid at rest is nearly evanescent in the bubble swarm.

Figure 6.27 shows the p.d.f. of the vertical velocity for ABS cylinders in the bubble swarm. As the vertical velocity of these cylinders in the fluid at rest is nearly constant, the p.d.f. in the fluid at rest are not shown. Instead, figure 6.27b shows the p.d.f. of $u_y/\langle u_y \rangle$ to compare the velocity of the cylinders in the swarm and in the fluid at rest. Short cylinders ($\xi = 3$, 5 and 7) share nearly the same vertical velocity, and their p.d.f. features a peak which is very close form their velocity in the fluid at rest. Long cylinders ($\xi = 10$, 12 and 20), on the other hand have increasing vertical velocity with ξ, and depart significantly from their velocity in the fluid at rest. Indeed, long ABS cylinders were seen to fall with their orientation nearly vertical at all times, resulting in a large increase in their velocity. This behaviour is caused by numerous interactions with bubbles.

For all three materials, cylinders of $\xi = 3$, 5 and 7 behave differently from cylinders of $\xi = 10$, 12 and 20. Long cylinders are more likely to encounter bubbles, and therefore to interact with them. The parameter L/L_{12} where L_{12} is the mean distance between two bubbles therefore seems to be of great importance in the cylinder motion in the swarm. In the following, we will come up with a finer classification of the cylinder motion depending on its density.

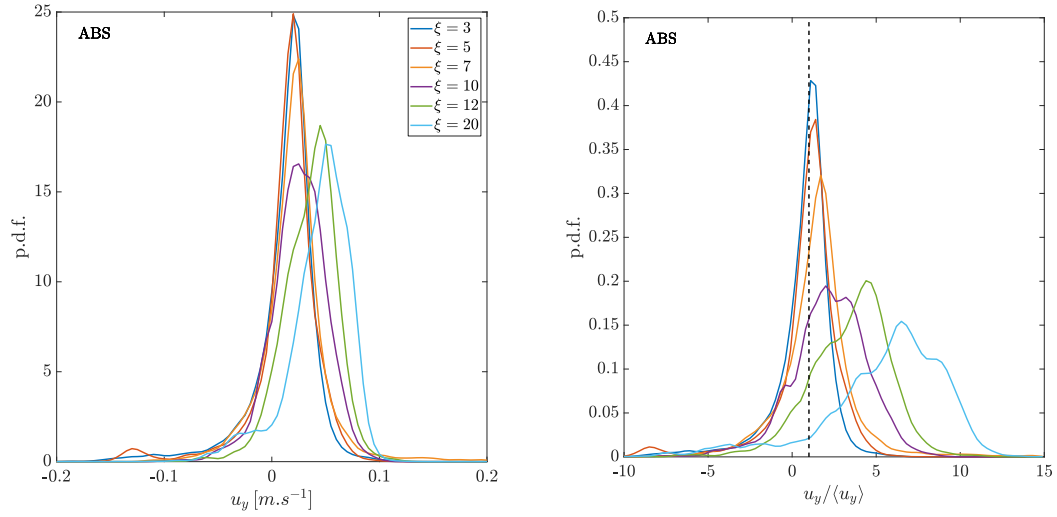

(a) (b)

Figure 6.27 – (a) Superposition of the p.d.f. of u_y for ABS cylinders in the bubble swarm for all ξ (b) Superposition of the p.d.f. of $u_y/\langle u_y \rangle$ for ABS cylinders in the bubble swarm

Cylinder horizontal velocity

We now consider the statistics of the cylinder horizontal velocity, u_x. Similarly to θ, the horizontal velocity of the cylinder is symmetric with respect to 0, as shown on figure 6.28a. Therefore we now study the distribution of $|u_x|$ instead (figure 6.28b).

In the fluid at rest, the p.d.f. of the horizontal velocity shows two peaks characteristic of a periodic motion. Concerning aluminium cylinders, similarly to the p.d.f. of $|\theta|$ and u_y, the distribution of u_x for $\xi = 3$ does not feature these peaks due to the coexistence of fluttering and weak fluttering in the fluid at rest, and the low amplitude of the fluttering for this elongation ratio. The peak of the fluttering motion is barely visible, while weak fluttering creates a single peak centered around 0.

In the bubble swarm, the p.d.f. of the horizontal motion shows no trace of the peaks caused by the periodic motion in the fluid at rest. For $\xi = 3$, 5, and 7, the p.d.f. of u_x in the bubble swarm is marked by a peak centered around 0. Compared to the p.d.f. in the fluid at rest, high horizontal velocities are observed more often. For ξ =10 and 12, the p.d.f. in the swarms shows a plateau of equiprobable horizontal velocities followed by a sharp decrease. At ξ =20, a peak is visible at high velocities, which is characteristic of large amplitude oblique motion.

Statistics of the horizontal velocity for the titanium cylinder (figure 6.29) shows a strong similarity between the p.d.f. of u_x in the swarm and in the fluid at rest for ξ = 3, 5 and 7. The peak seen in both p.d.f. at $\xi = 5$ and 7 is likely a trace of the chaotic motion of the cylinder. For $\xi = 10$ in the fluid at rest, the cylinder is fluttering, but we also observe two peaks in the p.d.f., similarly to the one of the titanium cylinders with a seemingly chaotic motion ($\xi = 5$ and 7). While the peak at low velocities is also seen in the p.d.f. in the swarm, it is not the case for the other peak, which is likely cause by the fluttering motion. Similarly, the peak associated with the fluttering is not present in the p.d.f. in the swarm for $\xi = 12$ and 20. The maximum horizontal velocity is increased in the swarm only for cylinders of $\xi = 12$ and 20, for which large amplitude oblique motions appear. Similarly to u_y, the horizontal velocity of titanium cylinder is less impacted by the bubble swarm than the one of aluminium cylinders.

For the ABS cylinder, the p.d.f. of $|u_x|$ (figure 6.30) shows that larger horizontal velocities appear with increasing ξ. Cylinders of $\xi = 3$ and 5 feature a single narrow peak

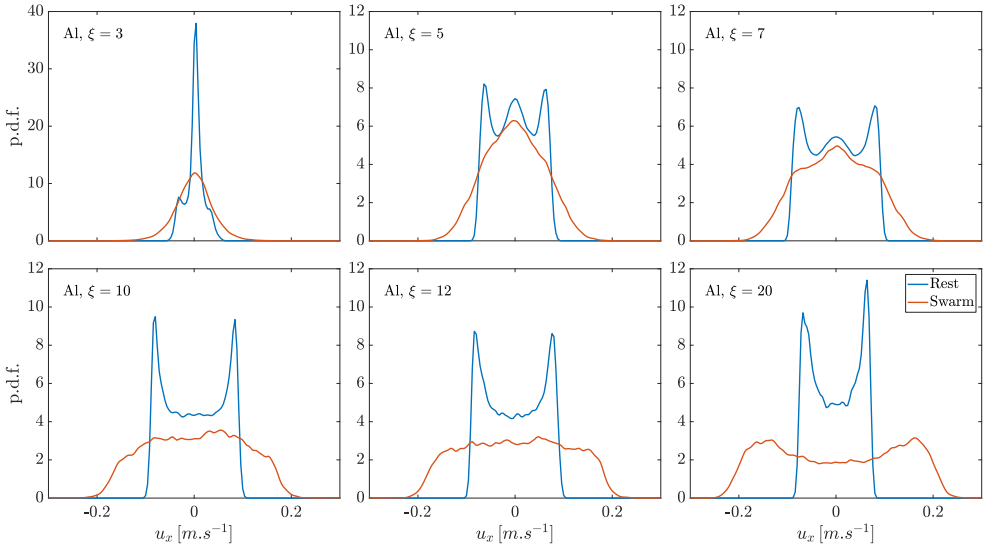

(a)

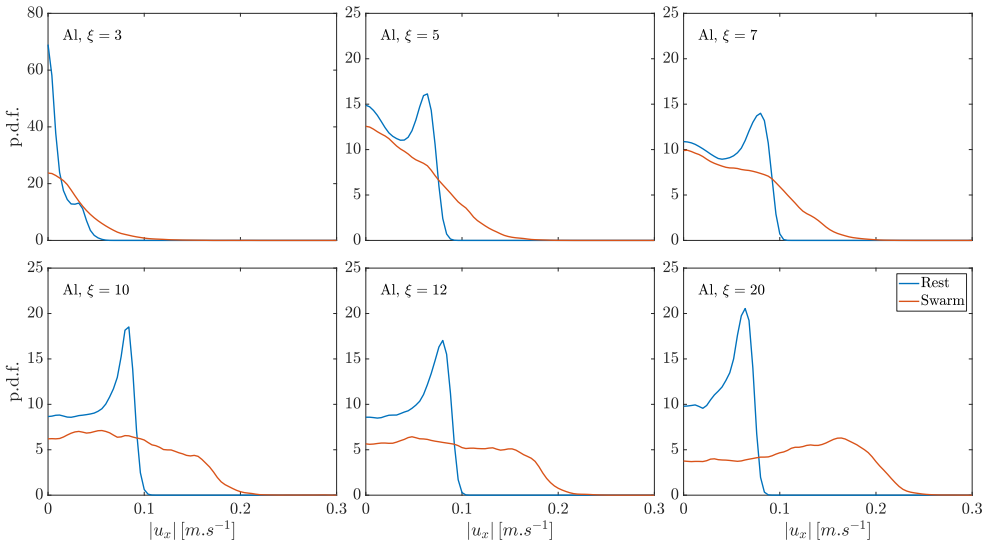

(b)

Figure 6.28 – Normalized histograms of the aluminium cylinder horizontal velocity, u_x in (a) and $|u_x|$ in (b), for different ξ and all α_g. Two different cases are compared, the cylinder in the fluid at rest, and in the bubble swarm

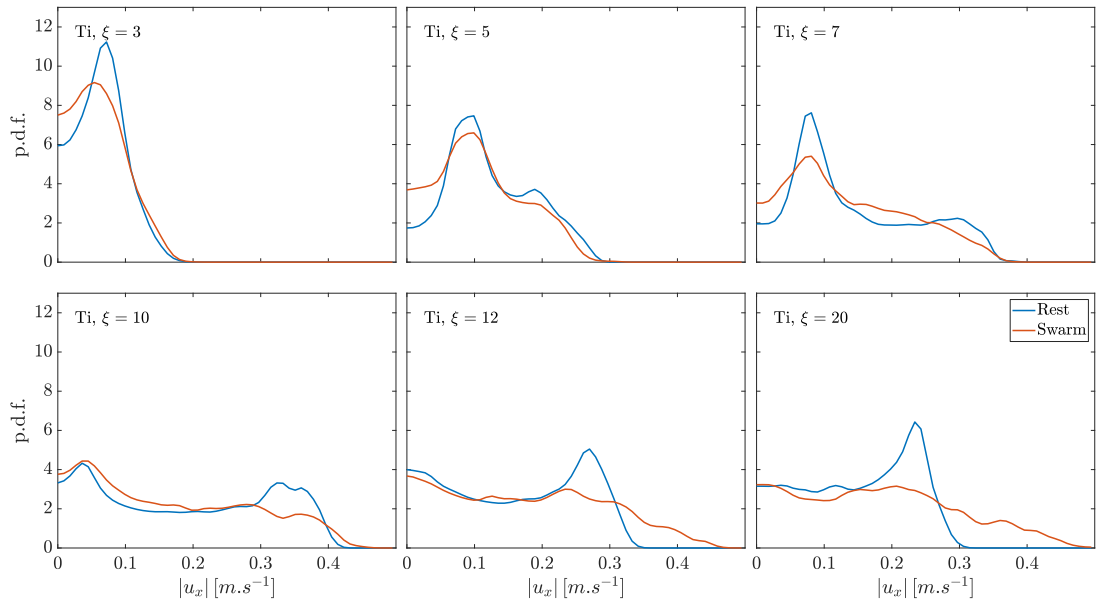

Figure 6.29 – P.d.f. of the titanium cylinder horizontal velocity, $|u_x|$, for different ξ in the bubble swarm

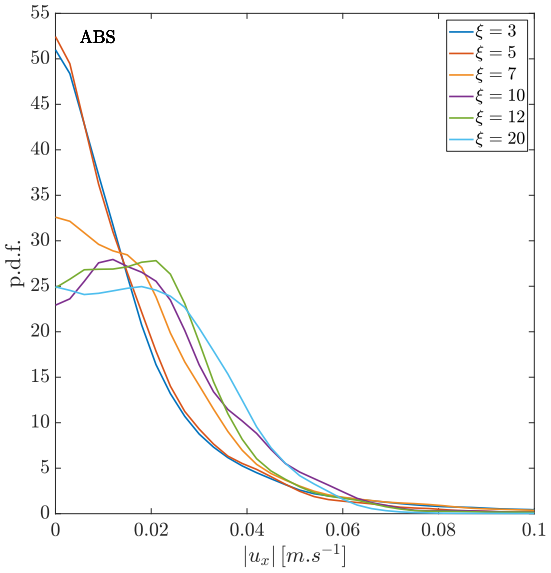

Figure 6.30 – P.d.f. of the ABS cylinder horizontal velocity, $|u_x|$, for different ξ in the bubble swarm

around 0 in the p.d.f. of $|u_x|$, while longer have higher horizontal velocities. The increase in horizontal motion of long cylinders comes from interactions with bubbles created by gliding over several bubbles. We see the same trend for $\xi = 20$, despite the cylinder falling with their orientation nearly vertical.

We can try to provide a synthesis of the statistical results. The density and length of the cylinders strongly affect the characteristics of their motion. The cylinder length, in particular, was found to be of particular importance in the sensitivity of its motion to interaction with the bubble swarm. The p.d.f. of u_y, u_x and θ, along with the mean vertical velocity of the cylinders (see section 6.3.1) show that a first separation of the cylinders in two groups, depending only on their length, can be made. Indeed, for all materials, cylinders with $\xi \leqslant 7$ and with $\xi \geqslant 10$ behave differently.

We also propose a finer classification of the cylinders for each material. Aluminium cylinders can be gathered in 4 groups of behaviour : $\xi = 3$, $\xi = 5$ and 7, $\xi = 10$ and 12 and finally, $\xi = 20$. The p.d.f. of θ, u_x or u_y share similar shape, and we can search for a unique normalized p.d.f. within each group. The groups are different for titanium cylinders. We find $\xi = 3$, $\xi = 5$ and 7, $\xi = 10$, and finally $\xi = 12$ and 20. For $3 \leqslant \xi \leqslant 10$ we find similarities in the shape of the p.d.f. of all variables. For $\xi = 12$ and 20, however, the p.d.f. of u_y show some differences, that may be attributed to a lack of convergence. Based on the shape of the p.d.f. of θ, the classification of ABS cylinders is clear. Three groups appear, the first one for $\xi \leqslant 7$, the second for $\xi = 10$ and the third one for $\xi = 12$ and 20. Nevertheless, because of the strong sensitivity of ABS cylinders to bubble-induced agitation, and of poor statistical convergence, it is not entirely clear if cases with $\xi = 10$, 12 and 20 are all different, despite similarities between them. In fact, the changes of shape of the p.d.f. of u_y and u_x happen at different values of ξ.

6.4 Interaction between the cylinder and the bubbles, introduction of conditional statistics

We have previously seen a statistical description of the cylinder motion in the bubble swarm, and we have qualitatively compared its behaviour with the case in the fluid at rest. The modification of the cylinder behaviour in the swarm comes from different types of interactions between the cylinder and the swarm. For aluminum cylinders, the contact between the cylinders and the bubble is one of the dominant interactions occurring. Additionally, as shown in section 6.3.3, the modification of the cylinder orientation by the swarm is very important in explaining its interaction with the bubbles. Because contact events are still relatively scarce, statistics of titanium and ABS cylinders are not converged enough to provide conditional statistics at contact. As a result, this section will focus on aluminium cylinders, and only present results for titanium and ABS cylinders as a comparison basis.

6.4.1 The contact interaction and its consequences in the cylinder motion

Contact duration and period

A simple way of characterizing the contact interaction is to look at the contact duration, and the time interval between two contacts, shown on figure 6.31a, as a function of ξ for cylinders of all materials. Contact events are defined as events when the cylinder is touching one or more bubbles. As the cylinder occupies a large part of the gap of the

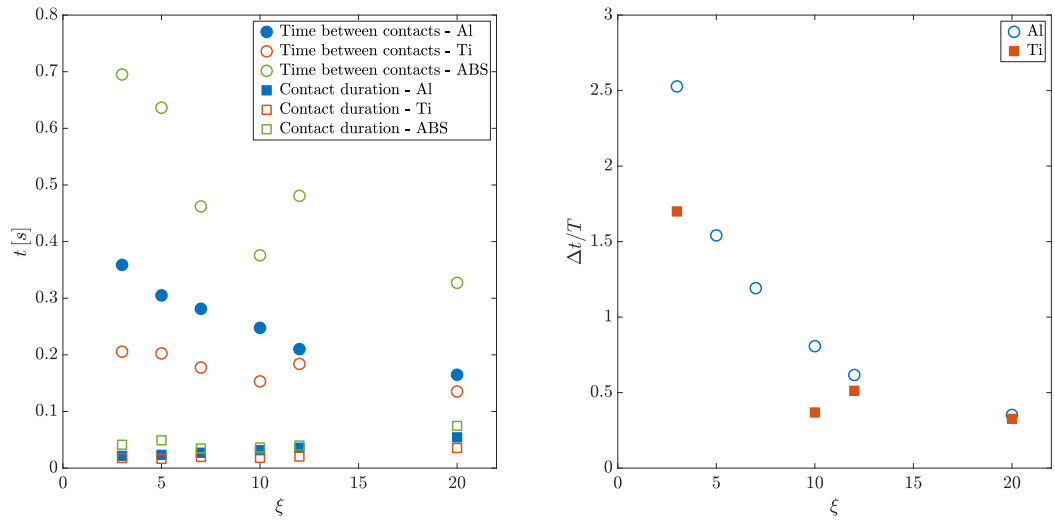

(a) (b)

Figure 6.31 – (a) Mean time between contacts (◯) and contact duration (□) for aluminium (blue), titanium (red) and ABS (green) cylinders (b) Ratio of the mean time between contacts with the fluttering period in the fluid at rest

cell ($d/H = 0.8$), the gas phase cannot go through the space between the cylinder and the walls. During the contact, the bubble and the cylinder are therefore displaced in the plane of the cell. Additionally, the cylinder can rotate, and the bubble can deform during the contact.

The cylinder elongation ratio plays a very important role on the frequency and duration of the contacts. The time interval between two contacts decreases steadily and strongly with ξ, while the contact duration rises slightly. As observed qualitatively (6.2.3), long cylinders ($\xi \geqslant 10$) encounter more bubbles during their fall, which is expected in a homogeneous swarm if they remain close to the horizontal (which was shown to be mostly the case for all elongation ratios for aluminium cylinders on figure 6.21b, and for other materials on figure 6.23). Short cylinders, on the other hand, are less likely to encounter a bubble. Both the contact duration and the time between two contacts increase as the cylinder density decreases. The time between two contacts is of course influenced by the cylinder velocity, which partly explains why the time between two contacts is lower for heavy cylinders. In addition, light cylinders are very sensitive to fluid motion in the cell, and the fluid flow above a bubble can push them away before they can come in contact with the bubble. The evolution of the contact duration with the cylinder density is probably caused by the difference in cylinder velocity.

In the fluid at rest, all aluminium cylinders go under a periodic oscillatory motion called fluttering. Titanium cylinders of $\xi = 3$, 10, 12 and 20 flutter as well. The period T of their oscillations is compared to the time between two contacts Δt on figure 6.31b. For cylinders with $\xi \leqslant 7$, the ratio $\Delta t/T$ is superior to 1 for aluminium and titanium cylinders, which is consistent with observations of phases of periodic motion similar to their motion in the fluid at rest in the bubble swarm. This behaviour is not observed for longer cylinders, whose ratio $\Delta t/T$ is inferior to 1, and whose motion in the swarm is dominated by bubble interactions.

The contact duration increases with the cylinder elongation ratio. Short cylinders are displaced very quickly when they encounter a bubble, which reduces the contact duration. Longer cylinders, on the other hand, require more energy to be significantly displaced or rotated, which leads to longer contacts. Also, simultaneous contacts with different bubbles

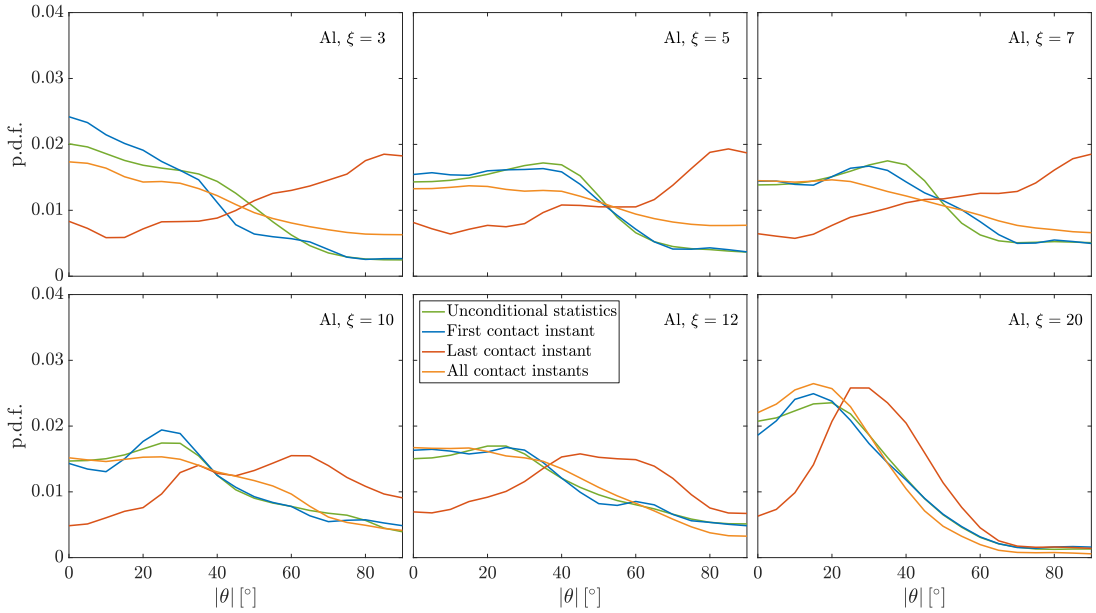

Figure 6.32 – P.d.f. of the cylinder orientation $|\theta|$ in the swarm (green), at the first instant of the contact (blue) at the last one (red), and at all instants during contact(orange) for aluminium cylinders

may increase the duration of contacts. The behaviour of long cylinders of the swarm was shown to be vastly different from the fluid at rest, which is related to the more numerous and longer bubble contacts.

Cylinder behaviour during the contact

The contact with a bubble changes drastically the cylinder behaviour during a short period of time. Large and sudden changes of the cylinder velocity and orientation are observed during such events.

Figure 6.32 compares the cylinder orientation at the first and last detected frames in the contact interactions, and for all frames during this interaction. The unconditional p.d.f. of θ in the swarm (green) is similar to the p.d.f. of θ at the first instant of contact (blue). This shows that, for aluminium cylinders of all ξ, the interaction with the bubble before the contact is not strong enough to create a preferential orientation of the cylinder. In contrast, the p.d.f. of θ at the last instant of contact (red) are very different, and show that the angle at which the cylinder separates from the bubble is significantly more important for all ξ. All cylinders of $\xi \leqslant 7$ also have a high probability of the cylinder being nearly vertical during the last instant of contact. For $\xi \geqslant 12$, the p.d.f. of θ at the end of contact show that they rotate to less important values. The p.d.f. of the cylinder orientation during all instants of contact shows little variation with ξ with the exception of $\xi = 20$.

We present the p.d.f. of the cylinder orientation at first and last instants of contact for titanium cylinder on figure 6.33, and for ABS cylinders on figure 6.34. Because we only select one frame per contact, and the data set is more limited than for aluminium cylinders, the statistical convergence is not ideal. However, we can make general observations that are coherent with the rest of our analysis. For titanium cylinders, the p.d.f. of the cylinder orientation at the first and last instants of contact shows that titanium cylinders are not very sensitive to the contact with bubbles. Indeed, there is very little variation in the p.d.f. of the first and last contact instants, which are also close to the p.d.f. of all contact instants, and of the unconditional p.d.f. in the swarm, for all ξ. For ABS

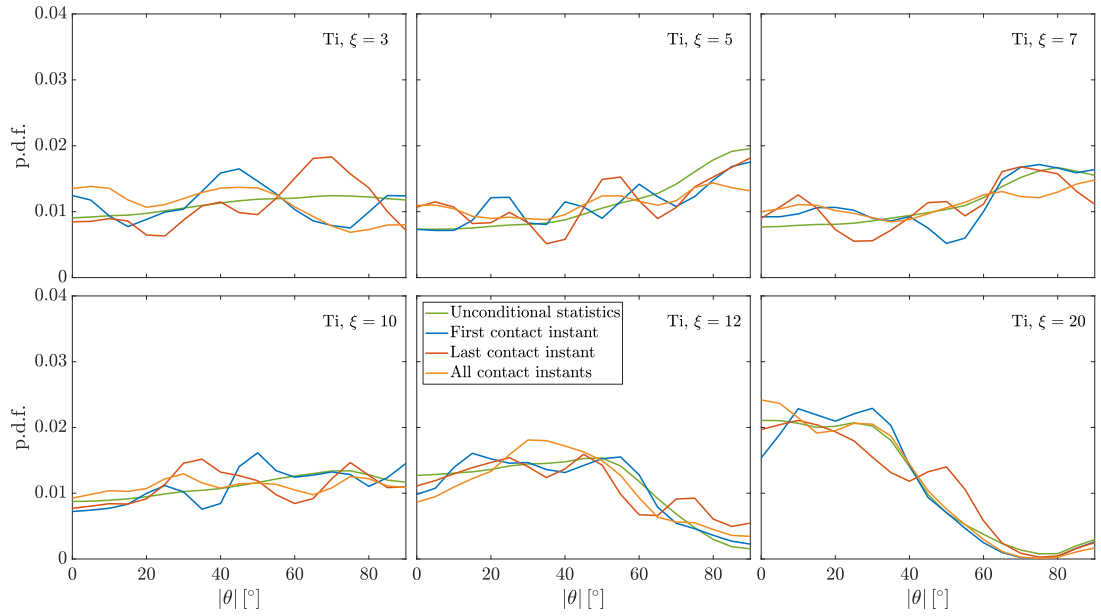

Figure 6.33 – P.d.f. of the cylinder orientation $|\theta|$ in the swarm (green), at the first instant of the contact (blue) at the last one (red), and at all instants during contact(orange) for titanium cylinders

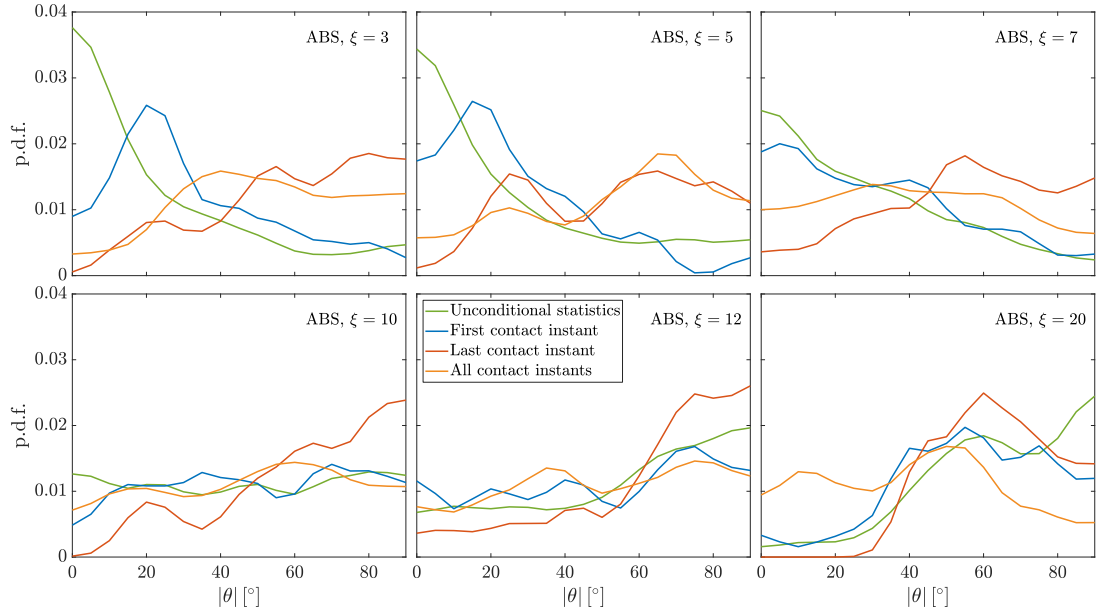

Figure 6.34 – P.d.f. of the cylinder orientation $|\theta|$ in the swarm (green), at the first instant of the contact (blue) at the last one (red), and at all instants during contact(orange) for ABS cylinders

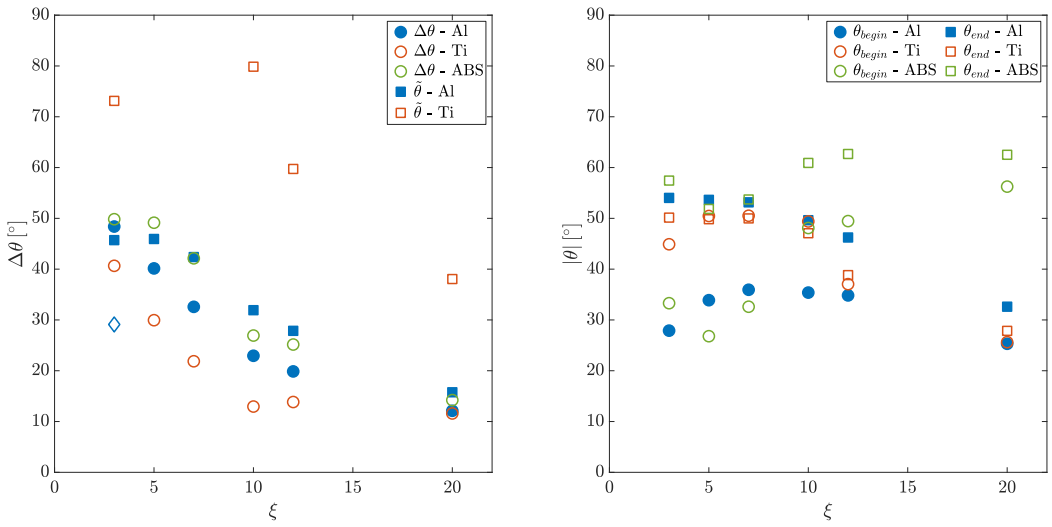

(a) (b)

Figure 6.35 – (a) Average difference between the angle of the cylinder at the first and last instants of contact (◯), amplitude of the fluttering oscillations in the fluid at rest (□) for aluminium (blue), titanium (red) and ABS (green) cylinders. Cylinders of $\xi = 3$ feature two different types of motion in the fluid at rest, fluttering and weak fluttering. The amplitude of their motion taking only fluttering cylinders is denoted with a square, while the mean amplitude of all $\xi = 3$ cylinders, including weakly fluttering ones, is denoted with a diamond (◇) (b) Mean orientation $|\theta|$ of the cylinder and the first (◯) and last (□) instants of the contact events

cylinders, we observe a distinct increase in the cylinder orientation at the end of contact for ξ but $\xi = 20$, similarly than for the aluminium cylinders. For $\xi = 3$ and 5, we also observe an increase in orientation at the first instant of contact (blue) compared to the unconditional p.d.f. (green), which is likely to be caused by the fluid flow above a bubble. Interestingly, for $\xi = 20$, low angles are mostly observed during the contact, but are scarce at the beginning and the end of contacts (at the end in particular, no $|\theta| < 20°$ is never observed). Indeed, these cylinders spend most of their time in the cell with a nearly vertical orientation. If they come to a horizontal orientation, contacts with bubble set them to be nearly vertical again.

The point of contact between the two objects is obviously very important when it comes to changes in the cylinder orientation during contact. The bubbles exert an upward force on the cylinder, which can induce cylinder rotation, especially when the force is applied near the ends of the cylinders. Even when the point of contact between the cylinder and the bubble is not originally close to the cylinder ends, it is very likely to shift during the contact, as the bubble glides underneath it. Therefore, the chances of the cylinder orientation being close to the vertical at the end of the contact are high. When the cylinder has an important orientation, it occupies less space in the cell, which lets the bubble resume its ascension. Additionally, the cylinder also generates a lot of acceleration, hence departing quickly from the bubble.

Figure 6.35a shows the mean difference between the first and last angles of contact for all contact events, $\Delta\theta$, compared to the fluttering amplitude in the fluid at rest. It should be noted that the vast variety of contact interactions leads to large standard deviation of the mean orientation jump, of the same order of magnitude as the mean value. The fluttering amplitude and the θ jump in contact are close, and follow similar evolutions with ξ for aluminium cylinders. For titanium cylinders, however, the angular amplitude

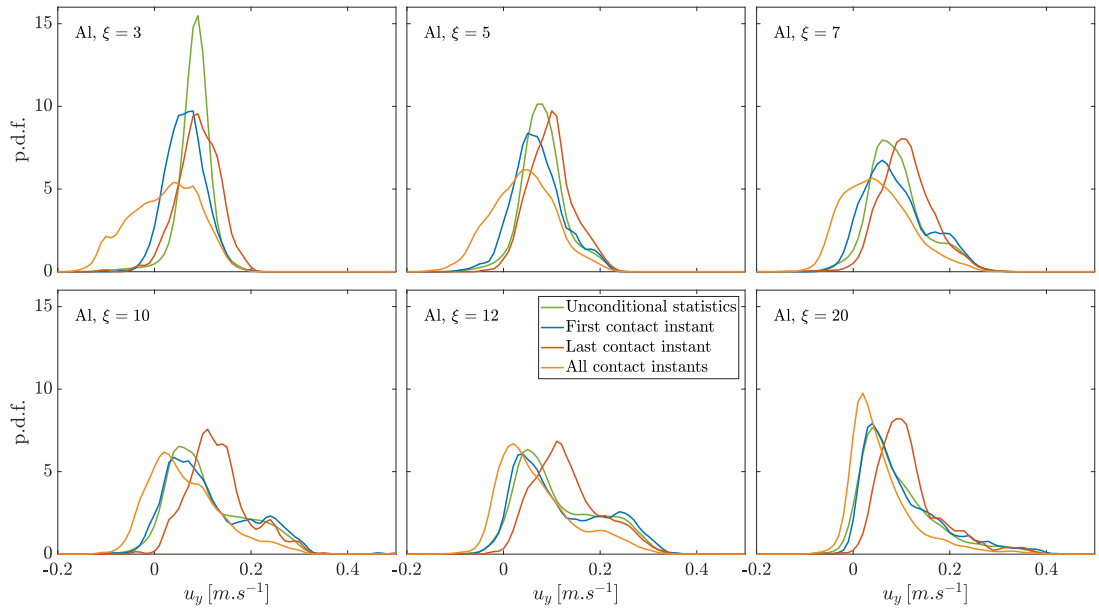

Figure 6.36 – P.d.f. of the cylinder vertical velocity u_y at the first instant of the contact (blue) at the last one (red), and at all instants during contact(orange) for aluminium cylinders

of the fluttering motion is much larger than the jump in $|\theta|$ at contact. For ABS cylinders, $\Delta\theta$ is slightly greater than that of aluminium cylinders. Predictably, the amplitude of the orientation jump at contact decreases for long cylinders of all materials, which have more mass and displace more fluid during their motion. For the same reason, the mean cylinder orientation at the last instants of contact decreases steadily with ξ for aluminium and titanium cylinders (figure 6.35b). In fact, the mean orientation at the first and last contact instants is nearly the same for all ξ for titanium cylinders. The interaction with the bubbles does not change the motion of these cylinders. However, ABS cylinders see their orientation both at the first and last instants of contact increase with ξ, which is concordant with observations on figure 6.34. This confirms that the effect of the bubble contacts increase as the cylinder density decreases.

Vertical velocity at contact is shown on figure 6.36, for the first and last instants of contact as well as for all contact frames. For all elongation ratios, negative vertical velocities, denoting a rising cylinder, are observed at contact. Yet, they are scarce for both the first and last instants of contact. Some negative velocities are also seen at the first instant of contact, and may be caused either by the fluid displacement above the bubble, of by previous bubble interactions which had caused the cylinder to be rising at the first instant of contact. Occurrences of rising cylinders during contact are rare during the first contact frame though, meaning that cylinders are more likely to be lifted up by bubbles during the rest of the contact. At the last instant of contact, the cylinder vertical velocity is higher than for the rest of the contact, which is consistent with the observations in figure 6.36 showing high cylinder orientation at the end of the contacts.

The p.d.f. of the cylinder vertical velocity are shown for titanium and ABS on figures 6.37 and 6.38 respectively. Again, the vertical velocities of titanium cylinders show little variation with the contact. Cylinders of $\xi = 3$ are slightly slowed down during the contact, and, surprisingly, at the last instant of the contact. Cylinders of $\xi = 20$ show a slight increase in u_y at the last instant of contact. It is not possible to conclude definitively for both cases due to poor statistical convergence. For all other elongation ratios, the statistical convergence does not allow us to make any significant difference between all

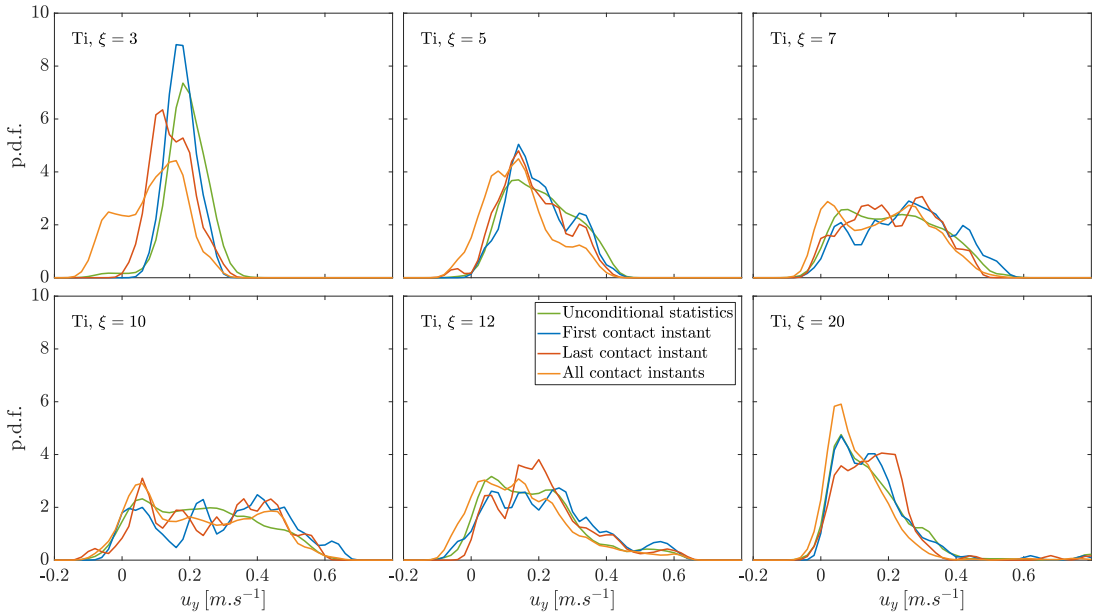

Figure 6.37 – P.d.f. of the cylinder vertical velocity u_y at the first instant of the contact (blue) at the last one (red), and at all instants during contact(orange) for titanium cylinders

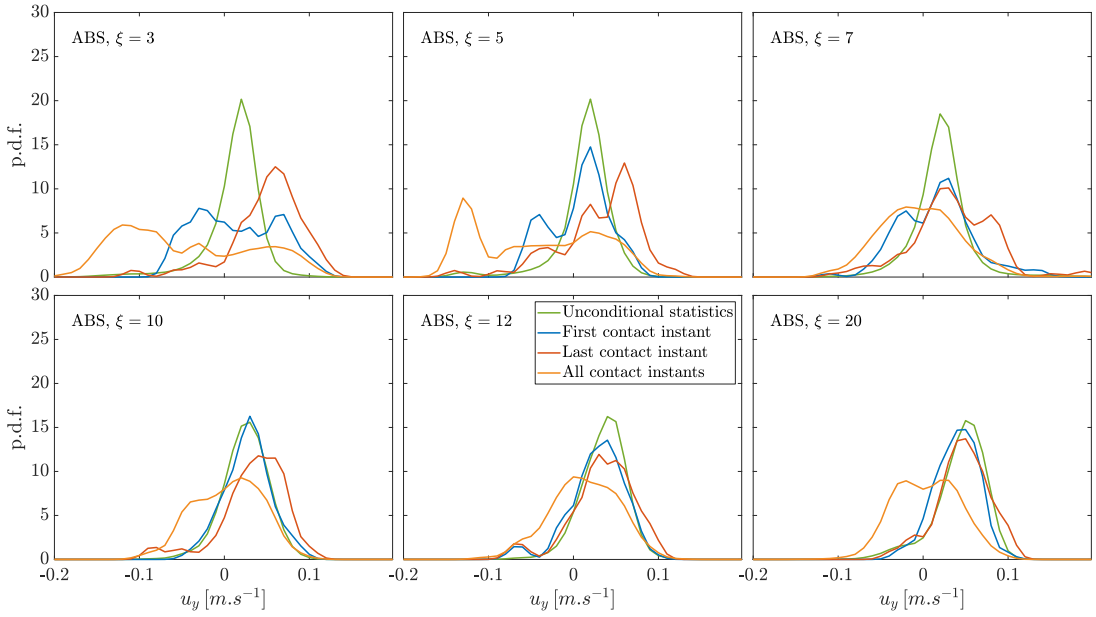

Figure 6.38 – P.d.f. of the cylinder vertical velocity u_y at the first instant of the contact (blue) at the last one (red), and at all instants during contact(orange) for ABS cylinders

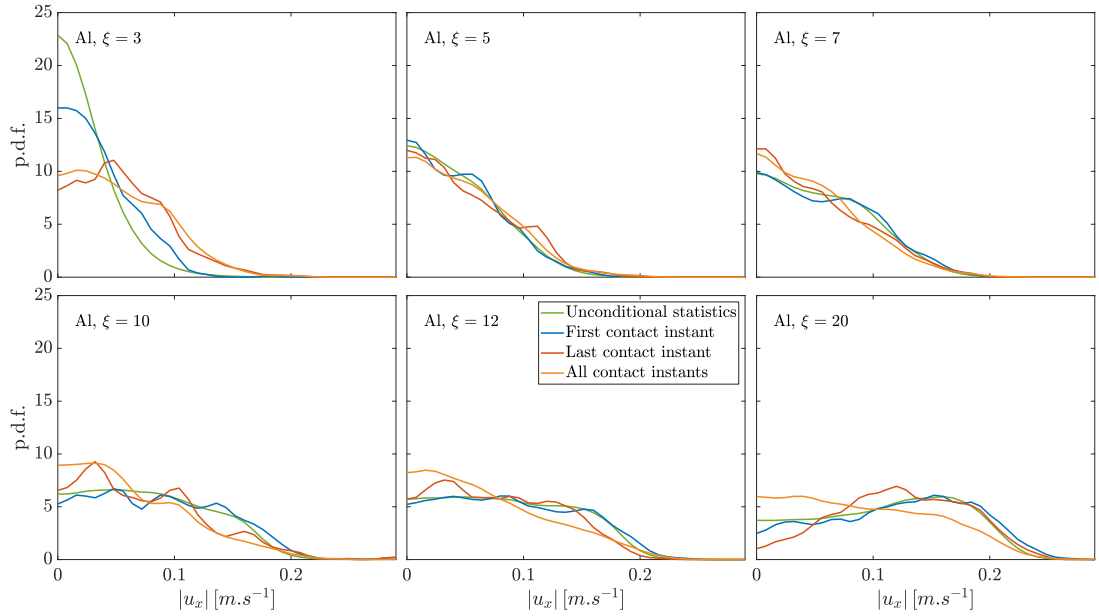

Figure 6.39 – P.d.f. of the cylinder horizontal velocity u_x at the first instant of the contact (blue) at the last one (red), and at all instants during contact(orange) for aluminium cylinders

the p.d.f., even though it could be that contacts have no significant impact on the body motion. ABS cylinders of $\xi = 3$, 5 and 7 show higher vertical velocity at the end of the contact and lower at the beginning, which is another sign of the influence of the fluid flow above the bubble. For higher ξ, the cylinders are slowed down during the contact, but the p.d.f. of u_y ar very similar at the beginning of contact, end of contact, and at all instants in the swarm. This probably comes from the very high orientation of the cylinder in the swarm for these ξ. Bubbles tend to glide on the sides of a vertical cylinders, which does not have a large impact on the cylinder behaviour. This comparison for titanium and ABS cylinders show that the velocity of heavy cylinders is only significantly impacted by contacts with bubbles at very low ($\xi = 3$) or high elongation ratio ($\xi = 20$). Light cylinders that are mostly horizontal during their fall are very impacted by contacts with bubbles, but not so much at high ξ, when their orientation in the swarm is mostly vertical (see figure 6.23b for the superposition of the p.d.f. of $|\theta$ in the swarm for ABS cylinders of different ξ).

The difference in velocity between the beginning and the end of the contact is much less important in the horizontal direction (with the exception of $\xi = 3$), as seen in figure 6.39. For $\xi = 3$, the horizontal velocities at the beginning of the contact are significantly less important than for the other contact frames. The large amplitude oblique motion observed at $\xi = 20$ are visible in the beginning and end of the contact events, whose p.d.f. show a peak at high horizontal velocity. Low velocities are observed on the remaining contact events though.

The p.d.f. of the cylinder horizontal velocity at first and last instants of contacts is shown on figure 6.40 for titanium cylinders, and on figure 6.41 for ABS cylinders. Titanium cylinders of $\xi = 3$ could show an increase of their horizontal velocity at the last instant of contact. For other elongation ratios, the contact seems to have little impact on u_x. ABS cylinders feature a very different behaviour. For $\xi = 3$ and 5, the horizontal velocity is increased significantly at the first, last and for all instants of contact. This effect is still present at $\xi = 7$, even though is magnitude is less important. For $\xi = 10$, 12 and 20 the p.d.f. of the horizontal velocity do not seem to be very affected by the contact,

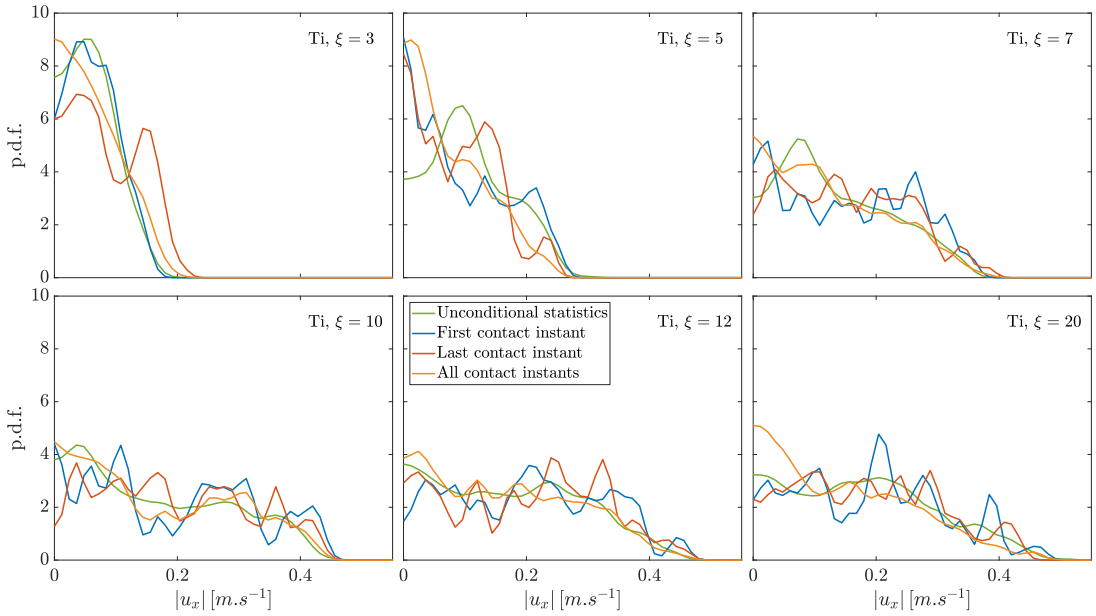

Figure 6.40 – P.d.f. of the cylinder horizontal velocity u_x at the first instant of the contact (blue) at the last one (red), and at all instants during contact(orange) for titanium cylinders

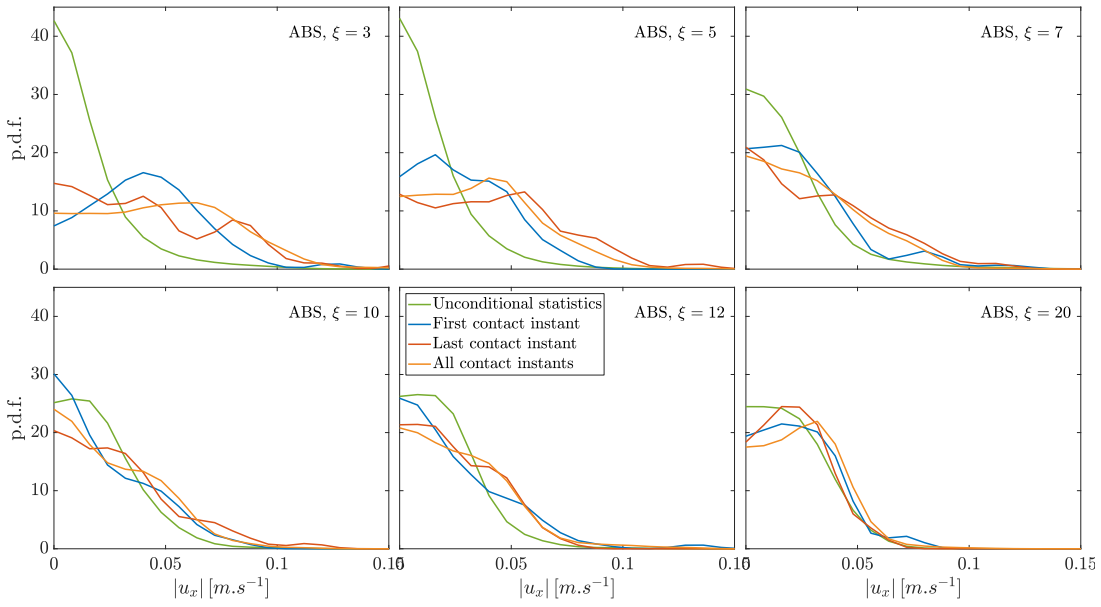

Figure 6.41 – P.d.f. of the cylinder horizontal velocity u_x at the first instant of the contact (blue) at the last one (red), and at all instants during contact(orange) for ABS cylinders

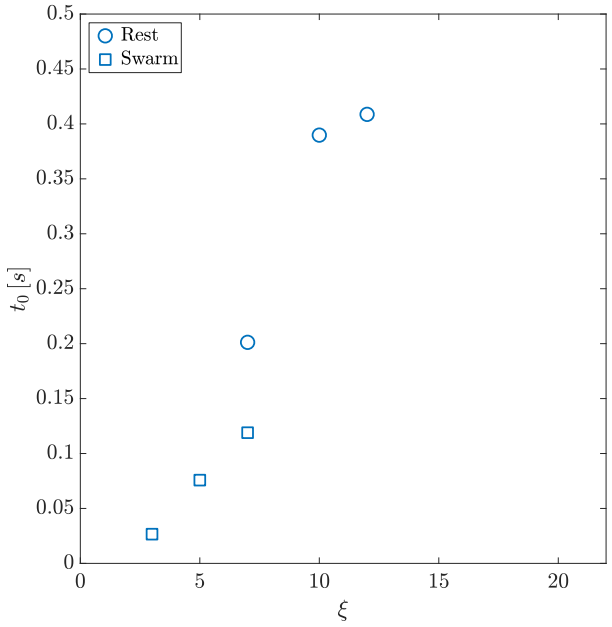

Figure 6.42 – Recovery time of the cylinder, going from an orientation of $|\theta| = 80°$ in the fluid at rest (◯) and in the bubble swarm (□)

and all share the same shape.

The cylinder display a great diversity of behaviours when in contact with a bubble. Yet, some specific behaviours are observed, related to the cylinder elongation ratio. Cylinders are sometimes briefly lifted upwards by the bubbles during contact. The upward motion of the cylinder is stronger for shorter ones. Then, cylinders are rotated up to a point where they can separate from the bubble. Even though the net velocity balance during the contact can be negative, the high cylinder orientation at the end of the contact can increase the cylinder velocity over a large period of time.

We have seen that the cylinder in the confined cell takes a very long time to recover its nearly horizontal orientation after being released vertically. This type of behaviour was not observed in the infinite medium, where the cylinder quickly regained its horizontal orientation. We have previously discussed the cylinder recovery time in the confined cell and in a fluid at rest (see 4.3.2). In the bubble swarm, bubble contacts tend to increase the cylinder orientation, to the point where it is nearly vertical. We can therefore compute the cylinder recovery time in the bubble warm, corresponding to the time needed by the cylinder to go from $|\theta| = 80°$ to $|\theta| = 0°$ after a contact which increases its orientation enough. For each elongation ratio, t_0 is the average of all recovery times after contact. A comparison between the recovery time of the cylinder after contact in the bubble swarm with its recovery time in the fluid at rest is shown in figure 6.42. Data is only available for $\xi = 3$, 5 and 7, as longer cylinder cannot regain their nearly horizontal orientation before encountering another bubble (see figure 6.31b). As a result, the only comparable data point between the two configuration is $\xi = 7$. The cylinder recovery time appears to be shorter in the bubble swarm, but of the same order of magnitude.

These differences may be explained by the nature of contact. The bubbles create perturbations in the fluid around, notably in their wake. The cylinder may go through these perturbations after a contact, modifying its recovery compared to in the fluid at rest.

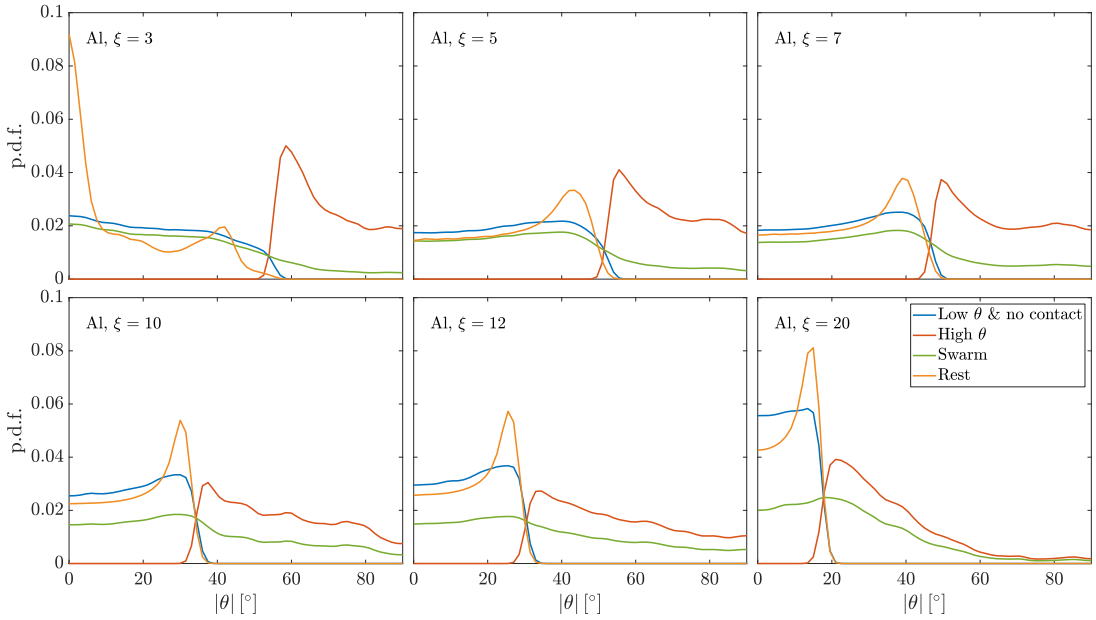

Figure 6.43 – Conditional p.d.f. of $|\theta|$ for the aluminium cylinders, taking only *low* θ when the cylinder is not in contact with any bubble (blue), only *high* θ (red), all the data in the bubble swarm (green), and all the data in the fluid at rest (orange)

6.4.2 Conditional statistics based on the cylinder orientation

The comparison of the statistics of the cylinder orientation in the fluid at rest and in the bubble swarm (see figure 6.21a) has shown that the cylinder in the swarm could take orientations that are not seen in the fluid at rest. It is therefore reasonable to think that these cylinder orientations occur only when the cylinder is strongly under the influence of the bubble swarm. In this section, we introduce conditional statistics of the cylinder. Statistics at *high* θ are taken only when the cylinder orientation is greater than the maximum θ observed in the fluid at rest. Such statistics are thus observed in the swarm, and are a part of the statistics in the swarm. Similarly, statistics at *low* θ & *no contact* are taken only when the cylinder orientation is within the limits of the θ observed in the fluid at rest, and when it is not in contact with any bubble. It should be noted that these two conditions do not account for all the events in the bubble swarm. The goal of selecting only *low* values of θ is to look for moments during which the cylinder is not strongly interacting with the bubble swarm, hence excluding contact events. These statistics will only be studied for the aluminium cylinder, as the statistical convergence is not satisfactory for other materials. In addition, the distinction between *high* and *low* θ cannot be done for ABS cylinders, as their maximum orientation in the fluid at rest is close to 0. Similarly, titanium cylinders of $\xi = 5$ and 7 have a seemingly chaotic motion in the fluid at rest, and their maximum orientation is 90°, which makes the distinction also impossible. Another attempt at isolating the behaviour from the cylinder when it is not strongly under the influence of bubbles can be found in appendix B.4. It uses Voronoi measurements, but is not conclusive.

These conditional statistics are illustrated on figure 6.43 for the p.d.f. of $|\theta|$ for aluminium cylinders. The introduction of these conditional statistics allows us to go in a deeper discussion of the mechanisms that contribute to the p.d.f. in the bubble swarm.

The p.d.f. of $|\theta|$ at *low* θ is different from the one in the fluid at rest, despite sharing the same range of orientations. The p.d.f. of $|\theta|$ at *low* θ features a slight peak at the amplitude of the fluttering oscillations, but it is much less prominent that the one in the fluid at rest p.d.f. Indeed, even when the cylinder presents some phases of periodic motion

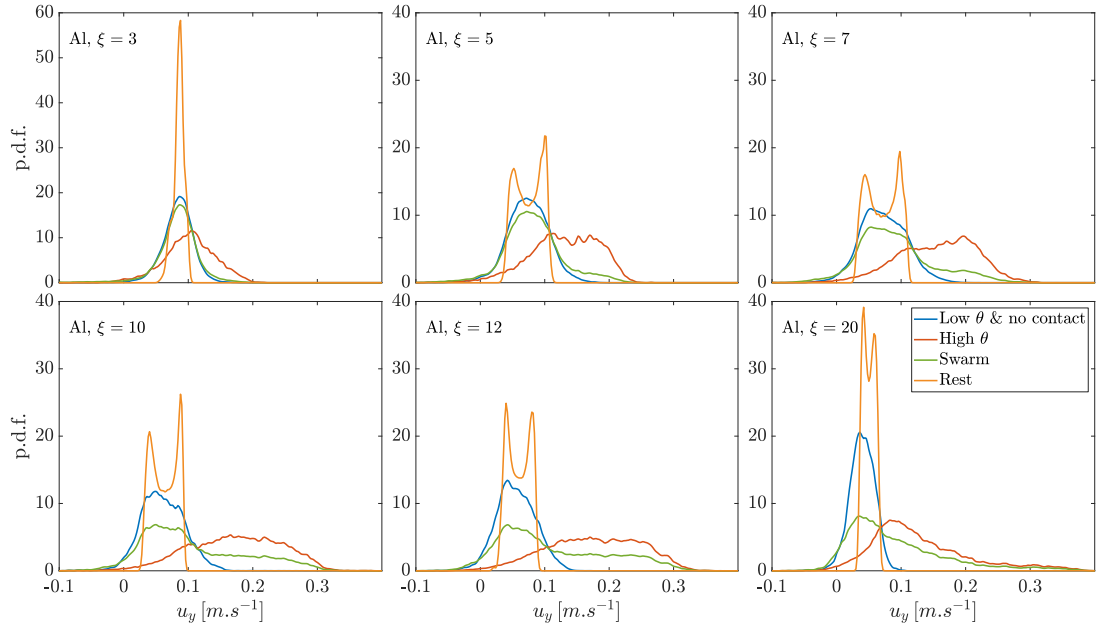

Figure 6.44 – Conditional p.d.f. of u_y for the aluminium cylinders, taking only *low* θ when the cylinder is not in contact with any bubble (blue), only *high* θ (red), all the data in the bubble swarm (green), and all the data in the fluid at rest (orange)

in the swarm, the amplitude of its oscillations is not constant, as the cylinder is likely to be in a transient mode of growing or dampening oscillations. The p.d.f. of *high* θ shows a peak near the maximum orientation observed in the fluid at rest for all ξ. Then, for $\xi \leqslant 7$, we have a plateau of high orientations, while for $\xi \leqslant 10$, we have a decreased of the p.d.f. for θ more important than the maximum orientation observed in the fluid at rest.

Figure 6.44 shows the p.d.f. of u_y for the aluminium cylinder. The role of the cylinder orientation on its vertical velocity is highlighted by the use of conditional statistics. When the cylinder orientation is within the boundaries of the observed θ in the fluid at rest, their vertical velocity has a higher probability of also being within the boundaries of the observed u_y in the fluid at rest. Most of the negative velocities observed in the bubble swarm occur at low cylinder orientation, while all the highest ones are seen only at *high* θ. Even at *low* cylinder orientation, the bubble swarm has a significant impact on the cylinder motion. It is capable of generating low or even negative cylinder velocities, but can also creates velocities higher than in the fluid at rest. Yet, the highest cylinder falling velocities observed in the bubble swarm are only created when the cylinder orientation is significantly increased by interactions with the bubbles. It should be noted that the p.d.f. of u_y at *low* θ features both higher and lower falling velocities than the p.d.f. in the fluid at rest. At *high* θ, the p.d.f. of u_y shows that high velocities are nearly equiprobable for all ξ but 3 and 20. This observation is concordant with the tail of equiprobable high velocities in the p.d.f. of u_y in the swarm.

Figure 6.45 shows the mean vertical velocity of aluminium cylinders for the different elongation ratios. In accordance with the observations on figure 6.44, the mean velocity in the fluid at rest, and in the swarm at *low* θ with no contact are very close to each other, and follow similar evolutions. For long cylinders ($\xi \geqslant 10$), the mean velocity at *low* θ and no contact starts getting lower than the one in the fluid at rest. At *high* θ, the vertical velocity is significantly greater than both the one in the fluid at rest, and the one in the bubble swarm.

Figure 6.46 shows the effect of the cylinder orientation on its horizontal velocity $|u_x|$.

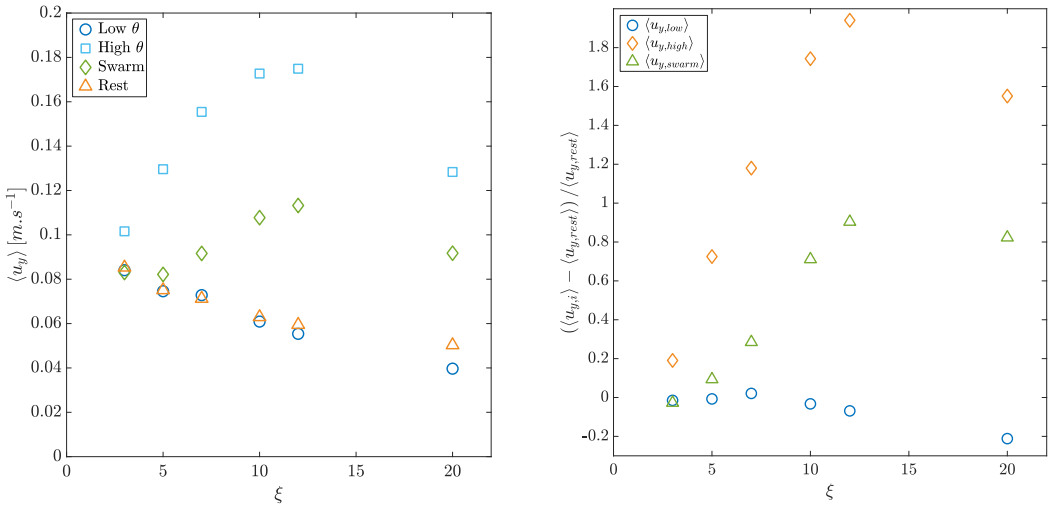

(a) (b)

Figure 6.45 – (a) Mean vertical velocity $\langle u_y \rangle$ at *low* θ, *no contact*, *high* θ, in the bubble swarm and in the fluid at rest (b) Comparison of the mean vertical velocity $(\langle u_{y,i} \rangle - \langle u_{y,rest} \rangle) / \langle u_{y,rest} \rangle$ where $\langle u_{y,i} \rangle$ can be u_y for *low* θ, *no contact*, *high* θ, and for all angles in the bubble swarm with the mean falling velocity in the fluid at rest.

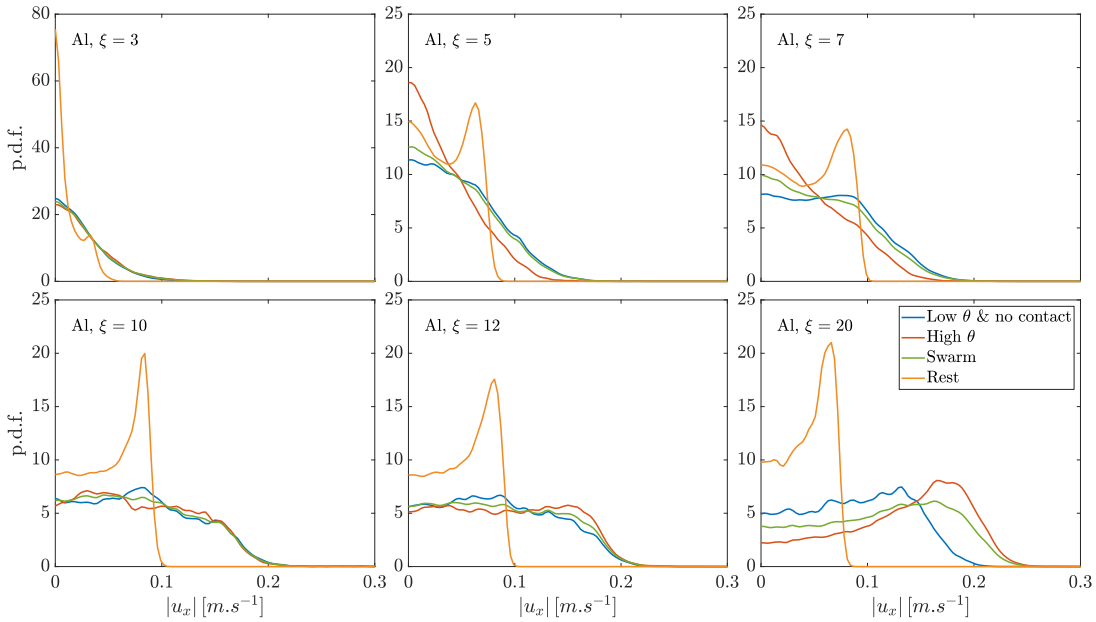

Figure 6.46 – Conditional p.d.f. of $|u_x|$ for the aluminium cylinders, taking only *low* θ when the cylinder is not in contact with any bubble (dark blue), only *high* θ (light blue), all the data in the bubble swarm (orange), and all the data in the fluid at rest (green)

The cylinder orientation has little effect on its horizontal velocity at $\xi = 3$, 10 and 12 as the p.d.f. collapse. For $\xi = 5$ and 7, a high cylinder orientation corresponds to low horizontal velocities. At $\xi = 20$, the existence of a large amplitude oblique motion at *high* θ is visible through the predominance of high horizontal velocities at *high* θ.

At low cylinder orientation, and in the absence of any contact, the cylinder motion in the swarm mimics some of the characteristics of its behaviour in the fluid at rest. Notably, the mean falling velocity in the swarm in such conditions is very close to the mean falling velocity in the fluid at rest. At *low* θ & *no contact*, the falling velocity of short cylinders ($\xi \leqslant 7$) only differs by less than 5% to the one in the fluid at rest. The bubble swarm has a greater impact on longer cylinders, which are slowed down compared to the fluid at rest, probably because of more frequent contacts. On the other hand, the increase in vertical velocity created by high cylinder orientations is much greater for long cylinders. Changes in cylinder orientation caused by strong interaction with bubbles are the leading factor in changing the motion of the cylinder in the swarm. When the cylinder orientation remains close to what it is in the fluid at rest, the bubble swarm has a more moderate impact on the behaviour of aluminium cylinders.

6.4.3 Toward the modelization of the cylinder motion in the bubble swarm

The statistics of the cylinder in the bubble swarm and in a fluid at rest has been extensively described. The creation of a model of its motion in the swarm, based on these observations can be envisioned. The influence of the bubble swarm on aluminum cylinders comes mainly from direct contact with bubbles. The frequency and effect of this interaction on the cylinder dynamics has been analyzed in 6.4.1. When the cylinder is not under the influence of any kind of bubble interaction, its motion in the swarm can be assumed in a first approximation to be similar to the one it has in the fluid at rest. Therefore, the trajectory of the cylinder in the bubble swarm could be decomposed between phases during which its oscillatory motion develops, similarly to the transient regime it has in the fluid at rest, with a series of contact events modifying its behaviour. Such a model has yet to be created.

6.5 Autocorrelation functions and motion dispersion

6.5.1 Autocorrelation functions and characteristic timescales

In general, we think about the idea that the cylinder motion in the swarm alternates between a periodic oscillatory motion, caused by its intrinsic dynamics, and a more random motion caused by bubble interactions. Getting to understand how the cylinder motion is correlated to itself may lead to interesting findings about the relative weights of these two phenomena. Additionally, this analysis will render possible the calculation of the characteristic timescale, which may shed additional light. In the present section, the autocorrelation functions were computed for u'_x and u'_y. Autocorrelation functions and corresponding lagrangian timescales from other variables can be found in Appendix B.6.

The autocorrelation functions of the velocity fluctuations of the cylinder are plotted in figure 6.47 for aluminium cylinders. For the velocity in the vertical direction, even in the swarm, C_{yy} reveals oscillations with the frequency of the fluttering in the vertical direction for $\xi = 3$, 5 and 7. Such oscillations also exist at $\xi = 10$ and 12 but their amplitude is very weak. C_{yy} also attenuates less rapidly for longer cylinders. In the horizontal direction, the autocorrelations C_{xx} shows oscillations at the fluttering frequency for the same elongation

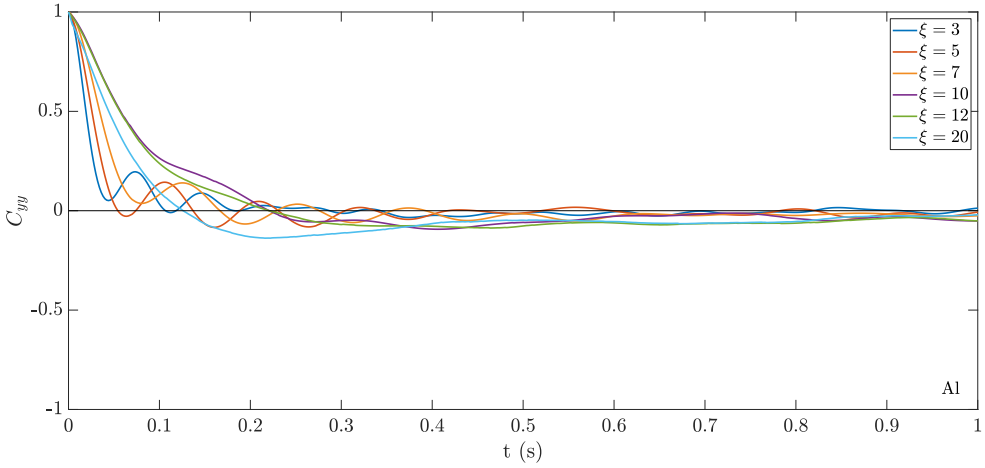

(a)

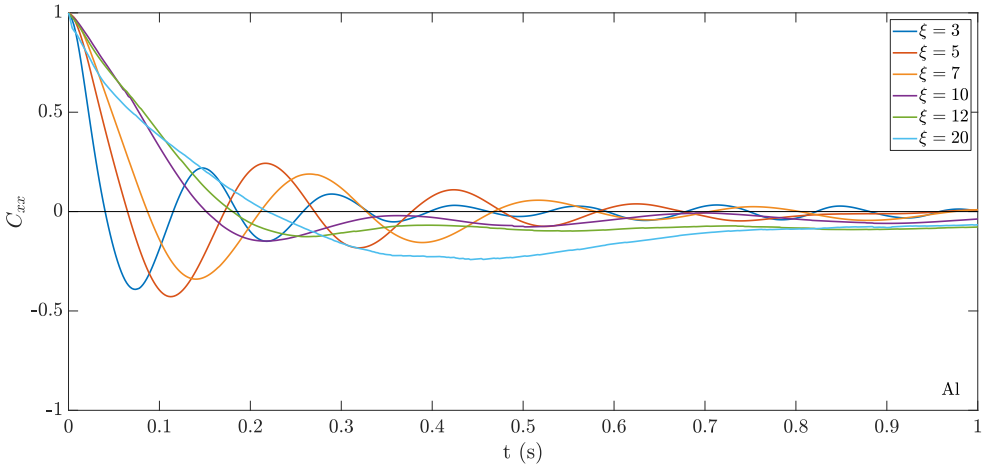

(b)

Figure 6.47 – Autocorrelation coefficients of the aluminium cylinder velocity (a) $C_{yy} = \langle u'_y(t)u'_y(t+\tau)\rangle/\langle u'^2_y\rangle$ (b) $C_{xx} = \langle u'_x(t)u'_x(t+\tau)\rangle/\langle u'^2_x\rangle$

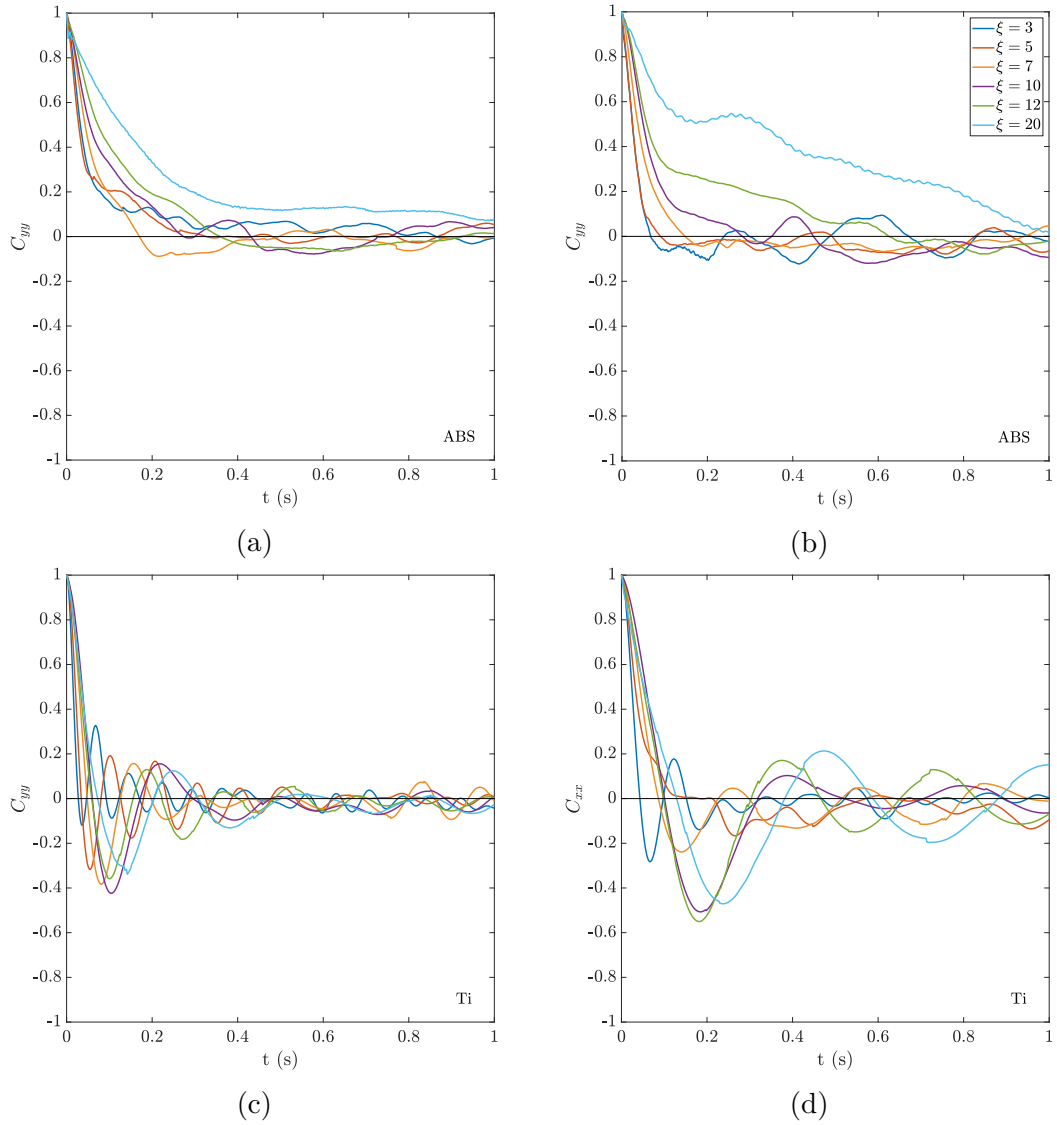

Figure 6.48 – Autocorrelation coefficients of the ABS (top row) and Titanium (bottom row) cylinders velocity (a) $C_{yy} = \langle u'_y(t)u'_y(t+\tau)\rangle / \langle u'^2_y\rangle$ (b) $C_{xx} = \langle u'_x(t)u'_x(t+\tau)\rangle / \langle u'^2_x\rangle$

ratios. The evolution of C_{xx} is often and more or less that of a damped cosine function, with the damping growing stronger with ξ. The autocorrelation functions in the horizontal direction are marked by phases of natural oscillatory path of the cylinder for all ξ but $\xi = 20$. The magnitude of this signature is also dependent on ξ, with the autocorrelations of $\xi = 10$ and 12 barely bearing the mark of the fluttering.

The autocorrelation functions for ABS and Titanium cylinders are plotted on figure 6.48. They are less converged due to the limited number of runs. We can nevertheless see some general tendencies. The autocorrelation functions are not marked by any periodicity for ABS cylinders. Instead, C_{yy} decreases steadily with time, with no clear effect of ξ. The decrease is slow, and the autocorrelation functions for $\xi = 3$, 5 and 20 do not reach 0 before 1s. In the horizontal direction, the autocorrelation function decreases with time, with stronger decreases being seen for lower ξ.

For titanium cylinders, C_{yy} takes the form of a dampened cosine function, for all ξ. In the swarm, they thus spend more time in periodic motion, probably than aluminium cylinders, as the latter have a C_{yy} function looking less like a dampened cosine function. The damping is much stronger for the titanium case. Interestingly, even titanium cylinders of $\xi = 5$ and 7 show oscillations in C_{yy} in the swarm, even though their motion in the fluid

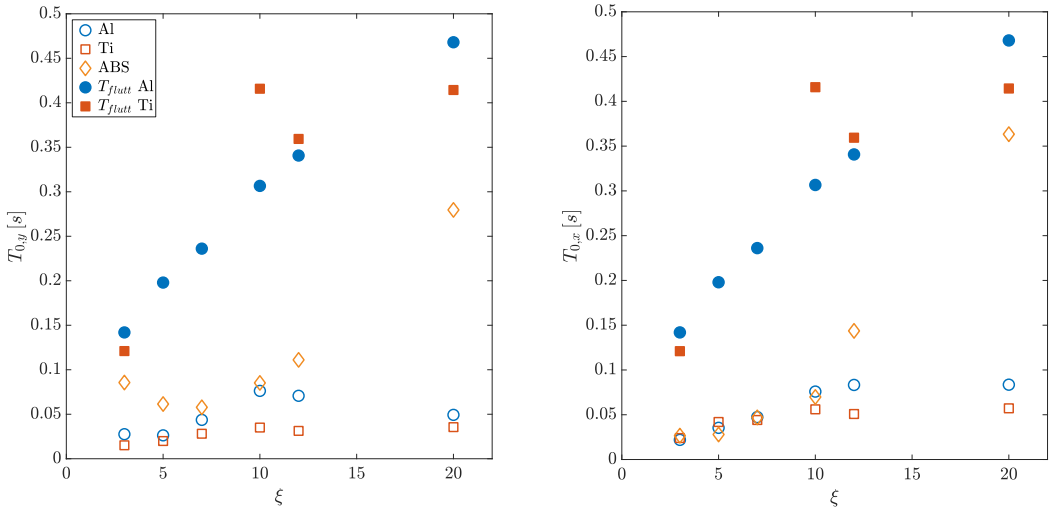

Figure 6.49 – Characteristic timescale T_0 defined as $T_0 = \int_0^{t_0} C(\tau).d\tau$, where t_0 is the time indice of the first zero-crossing of C. Aluminium cylinders are plotted with (circles), ABS ones ($\Diamond$) and Titanium with ($\square$), on (a) the vertical direction and (b) the horizontal direction. The period of the fluttering motion was plotted in filled symbols when available. in the vertical direction, we plotted the period of the oscillations of u_y, which is half the period of the oscillations in the horizontal direction.

at rest is not regularly oscillating. In the horizontal direction, a lot more noise is seen on the autocorrelation functions, but signature of periodic motions is still very present. The lack of convergence of the autocorrelation functions for titanium cylinders is expected. As they are not very affected by the bubbles, hence going under a periodic motion even in the bubble swarm, it is difficult to estimate the dampening as any phase change in otherwise periodic motion can vary a lot the autocorrelation function.

Autocorrelation functions can be used to define a characteristic timescale of the correlation of the cylinder motion. There is no unique way of calculating these timescales for such complex functions. The characteristic integral timescale is usually defined from the autocorrelation function $T = \int_0^{\infty} C(\tau)d(\tau)$. For obvious reason, we cannot integrate the autocorrelation function up to an infinite time. For both examples shown in figure 6.47, we can consider that the convergence of C_{xx} and C_{yy} is satisfactorily reached for $t = 0.7s$, and therefore integrate the autocorrelation function up to 1s. Another commonly used method is to perform the integral up to the first zero crossing of the function, which avoids the integration of a substantial amount of noise into the characteristic timescale (noise being mostly seen at long times).

Figure 6.49 shows the characteristic timescales, computed using the zero-crossing method. Measurements of velocity in the vertical direction provide characteristic timescale growing steadily with ξ for aluminum and titanium cylinders, and for ABS cylinders for $\xi \geqslant 7$. This exception for ABS cylinders at $\xi = 3$ and 5 may be due to large vertical motions when these small and light cylinders are carried upward by the bubbles.

The characteristic timescales of C_{xx} are remarkably similar for all materials at $\xi = 3$, 5, 7 and 10. For longer elongation ratios, lighter materials have more important characteristic timescales, with a significant increase for the ABS cylinders. For $\xi = 12$ and 20, $T_{0,x}$ is nearly constant for aluminum and titanium cylinders. We should also note that $T_{0,x}$ and $T_{0,y}$ are of the same order of magnitude.

Figure 6.50 shows the characteristic timescales integrated over 1.0s. The evolutions of the timescales for the different materials are similar to the ones estimated with the

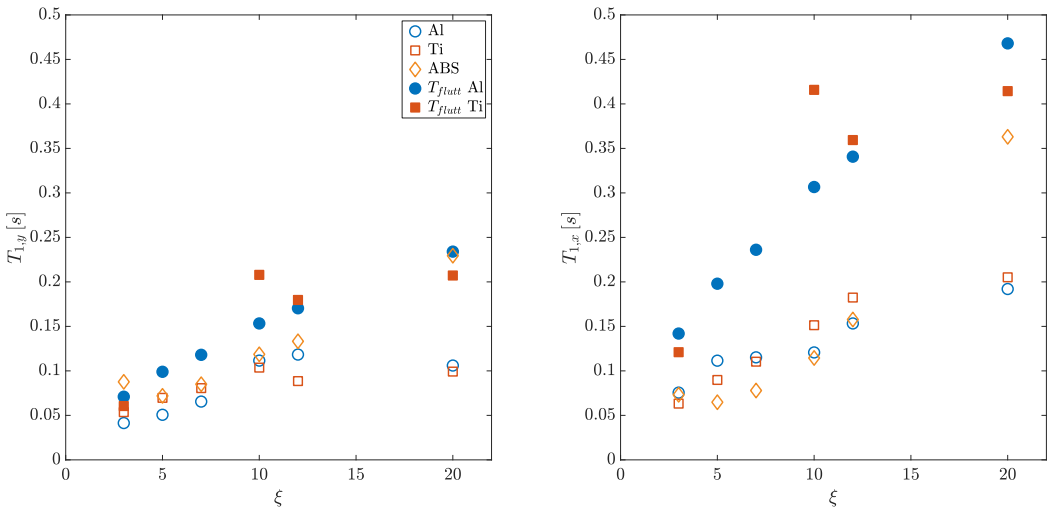

(a) (b)

Figure 6.50 – Characteristic timescale T_1 defined as $T_1 = \int_0^{t_1} |C(\tau)|.d\tau$, where $t_1 = 1.0s$. Aluminum cylinders are plotted with (◯), Titanium ones with (□), and ABS ones with (◇) on (a) the vertical direction and (b) the horizontal direction. The period of the fluttering motion was plotted in filled symbols when available. in the vertical direction, we plotted the period of the oscillations of u_y, which is half the period of the oscillations in the horizontal direction.

other method, except for the aluminum cylinders in the horizontal direction, where the characteristic timescale for $\xi = 5$ and 7 is significantly longer. Overall, the characteristic timescales are longer with the second computation method, which was expected as it includes a larger interval in the measurement.

The characteristic timescales $T_{0,y}$, $T_{0,x}$, $T_{1,y}$ and $T_{1,x}$ are both smaller than the period of the fluttering of the cylinder in the fluid at rest. In particular, for high elongation ratios, the difference between any integral timescale and the fluttering period is very significant.

6.5.2 Dispersion

In this section, only the aluminium cylinders are examined, as the statistical convergence for the other materials is not satisfactory. The interested reader may find the data for other materials in appendix

Trajectories and temporal signals superposition

Previous qualitative and quantitative observations have shown that the aluminium cylinder motion in the swarm is very dependent on its elongation ratio. Therefore, the dispersion is expected to be also impacted by ξ. We start by showing superposition of trajectories and temporal signals to have a qualitative appreciation of the dispersion in the swarm.

Figure 6.51 shows the superposition of 50 trajectories for all ξ, starting from the same point. In reality, the cylinders may enter the observation window at any point of its border. In agreement with the behaviours described in 6.2.3, small cylinders fall nearly at the vertical of their release point, while longer ones have more important sideways motion. The cylinder dispersion is seen to increase with ξ, to the point where cylinders of $\xi \geqslant 10$ are seen to get out of the observation window (of about 18cm in width). As a result, accurate quantitative measurements of the cylinder dispersion will be limited to low ξ

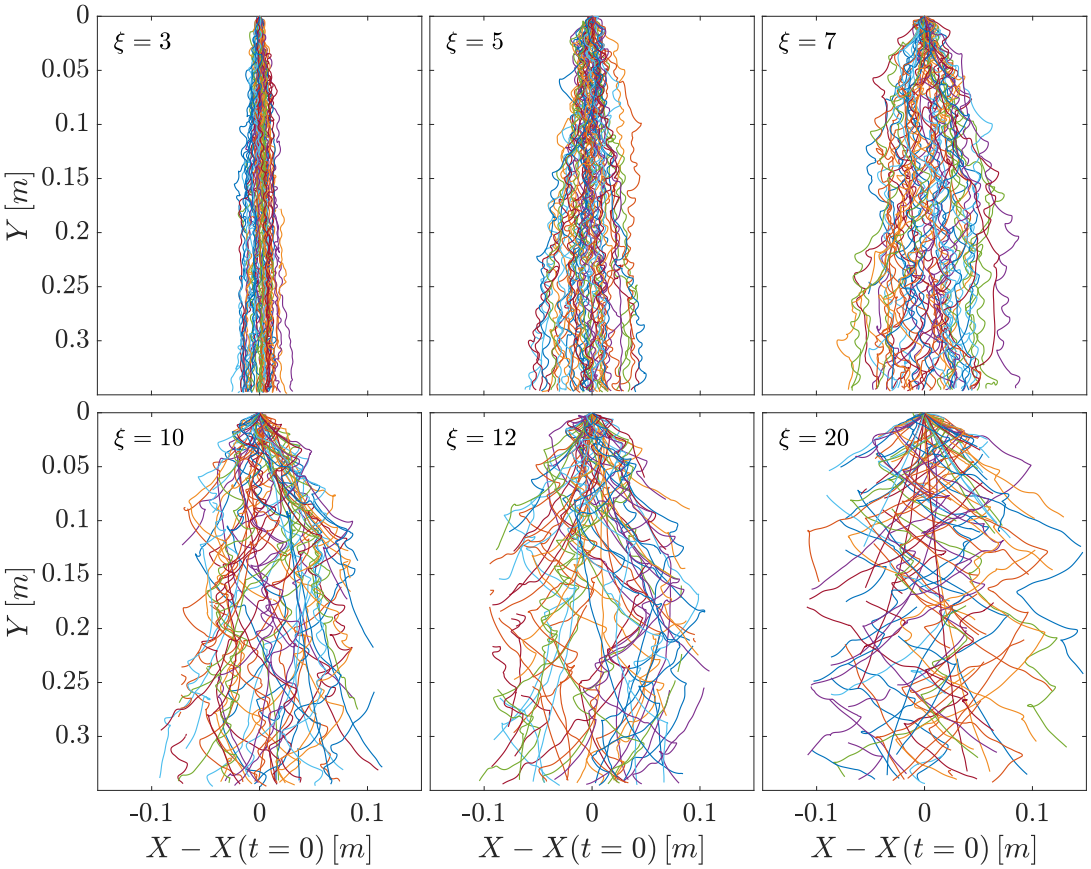

Figure 6.51 – Superposition of 50 aluminium cylinder trajectories for different elongation ratios.

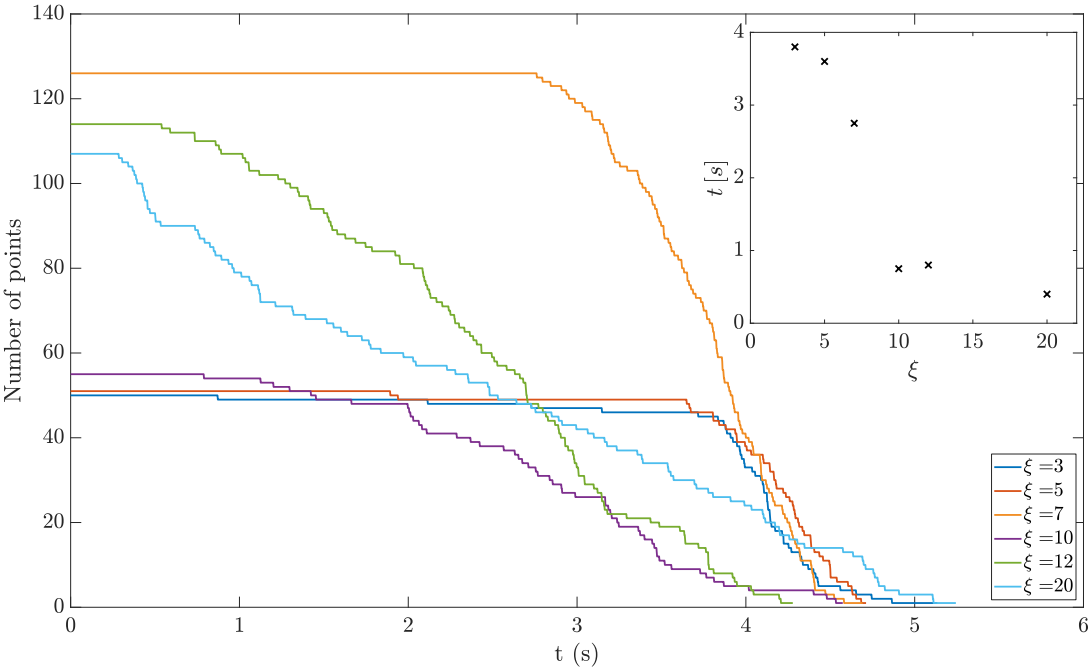

Figure 6.52 – Number of points at each time step for all elongation ratios. Inset : maximum time over which dispersion will be computed for each ξ

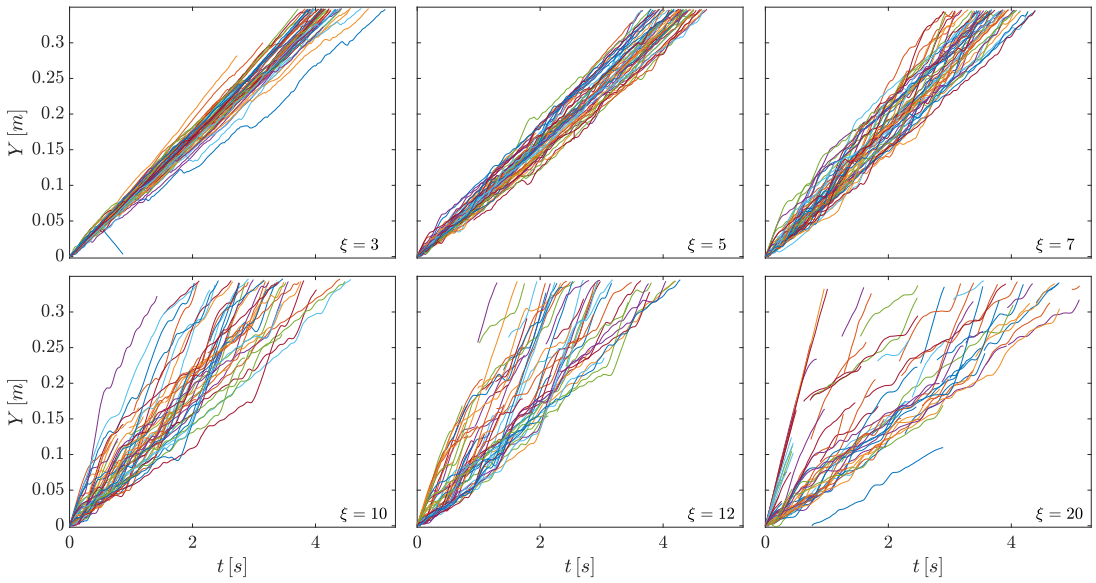

Figure 6.53 – Superposition of 50 aluminium cylinder temporal signals $Y = f(t)$ for different elongation ratios.

as dispersion is artificially limited by the size of the observation window at high ξ. For each elongation ratio, the time over which the measure of dispersion could be accurately computed was estimated based on the number of available data points (see figure 6.52).

The horizontal spread of the cylinder trajectories is caused by their intrinsic oscillation, by small amplitude response to bubble-induced agitation, or by large amplitude oblique motion. Figure 6.51 shows that, as ξ increases, the cylinder motion is more and more dominated by oblique motions, to the point where its amplitude is of the same order of magnitude as the width of the observation window. For $\xi \geqslant 10$, large amplitude vertical motion is also seen, when the cylinder falls with its orientation nearly vertical.

The vertical dispersion of the trajectory is difficult to see in figure 6.51. Figure 6.53 shows instead the superposition of temporal signals of $Y = f(t)$. For $\xi = 3$ and 5, there is little variation in the vertical motion of the cylinder. It starts getting more important at $\xi = 7$, with the notable appearance of surges in vertical velocity caused by high orientation of the cylinder. This behaviour is even more prominent at higher ξ. At $\xi = 20$, there are two distinct groups of trajectories, because cylinders entering the observation window do not recover a horizontal orientation before exiting the observation window. The corresponding temporal evolution of X can be found in appendix B.5 for the interested reader. In this appendix, we also provide superposition of trajectories and temporal signals for titanium and ABS cylinders.

Displacement variance

The temporal evolution of the variances are now studied. For each elongation ratio, the variance is only examined over the time span shown in the inset of figure 6.52.

Figure 6.54 shows the temporal evolution of the variance of the cylinder displacement. Both the horizontal and vertical variances grow nearly linearly for all elongation ratios. The vertical and horizontal variances are very similar for all elongation ratios but $\xi = 3$. For this value of ξ, the variance of the vertical displacement is much more important than that of the horizontal displacement. This is likely because aluminium cylinders of $\xi = 3$ are more substantially carried upwards by the bubbles during contact events. The dispersion of the cylinder motion in the bubble swarm is caused both by the intrinsic motion of the cylinder, and the perturbations caused by the bubbles. In agreement with

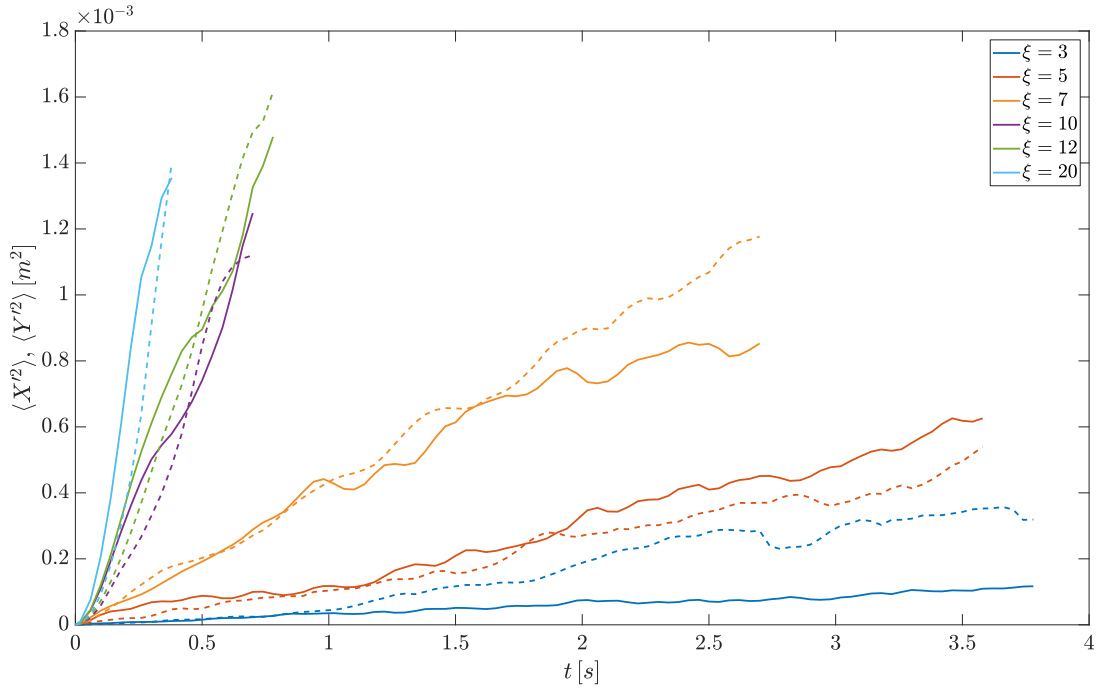

Figure 6.54 – Variance of the aluminium cylinder displacements normalized by the variance of their velocity in the vertical direction (dashes lines) and in the horizontal direction (solid line).

qualitative observations from figure 6.51, the temporal evolution of the variance of the displacements shows obviously two different groups of cylinders. Short ones (ξ =3, 5 and 7) have significantly lower displacement variance than longer ones (ξ =10, 12 and 20).

The nearly linear evolution of both $\langle X'^2 \rangle$ and $\langle Y'^2 \rangle$ observed for t greater than $T_{i,x}$ and $T_{i,y}$ allows us to define constant dispersion coefficients $\mathcal{D}_x$ and $\mathcal{D}_y$, except for $\xi = 20$, for which the limited time of observation does not allow to satisfactorily measure $t \gg T_{i,x}$ or $T_{i,y}$. We thus calculate :

$$\mathcal{D}_y = \frac{1}{2}\frac{d\langle Y'^2 \rangle}{dt} \tag{6.1}$$

$$\mathcal{D}_x = \frac{1}{2}\frac{d\langle X'^2 \rangle}{dt} \tag{6.2}$$

For long time delays, these dispersion coefficients are related to integral timescales and variances by relations $\mathcal{D}_x = \langle u_x'^2 \rangle T_{i,x}$ and $\mathcal{D}_y = \langle u_y'^2 \rangle T_{i,y}$ where $T_{i,x}$ and $T_{i,y}$ are the integral timescales defined in figures 6.50 and 6.49 (see Taylor [38]).

Figure 6.55 shows $\mathcal{D}_x$ and $\mathcal{D}_y$ for aluminium cylinders at all ξ. As expected from figure 6.54, the dispersion coefficients in the two directions are very close to each other for ξ =3, 5 and 7. For $\xi \geqslant 10$ they become significantly larger in both directions. In addition, $\mathcal{D}_y$ is in general slightly more important than $\mathcal{D}_x$.

Figure 6.55b compares the measurements of $\mathcal{D}_x$ and $\mathcal{D}_y$ obtained from (6.2) and (6.1) with Taylor's expression valid for $t \gg T_{i,x}$ or $T_{i,y}$, $\langle u_x'^2 \rangle T_{i,x}$ and $\langle u_y'^2 \rangle T_{i,y}$ respectively. We expect $\mathcal{D}_i / T_{i,j} \langle u_j'^2 \rangle$ to be constant for all ξ, yet it is only roughly the case.

Several issues have risen during our study of the dispersion of the motion of aluminium cylinders. The statistical convergence is not always sufficient. In addition, long cylinders ($\xi \geqslant 10$) often exit the observation window, which limits the time during which we can get a measurement of the dispersion. The study of the dispersion of the motion of the cylinder therefore remains an ongoing work. The characteristic timescales T_0 and T_1 were

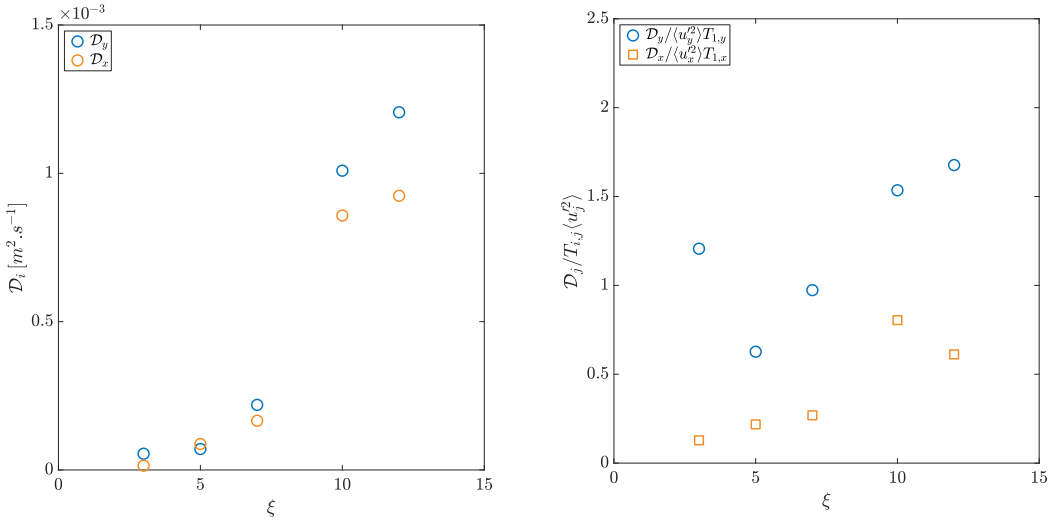

(a) (b)

Figure 6.55 – (a) Dispersion coefficients $\mathcal{D}_x$ and $\mathcal{D}_y$ as a function of ξ (b) Comparison of $\mathcal{D}_x$ and $\mathcal{D}_y$ as computed from (6.2) and (6.1) with $\langle u_j'^2\rangle T_{1,j}$, as a function of ξ

defined using classic definitions, but other definitions could be explored. The changes in the cylinder behaviour with ξ could also lead to choose different time scales for the various elongation ratios.

6.6 Summary

In the confined cell, the two main modes of motion of a freely falling cylinder are the rectilinear fall, and the fluttering motion (as studied in part II). The introduction of a swarm of rising bubble induces large perturbation of the motion of the cylinder, through various interactions between the cylinder and the swarm, such as contact with a bubble, or interaction with fluid perturbations. The resulting cylinder motion shows signs of a competition between the cylinder intrinsic dynamics, and the loads originating from the bubble swarm. Interactions between the cylinder and the bubbles produce very diverse effects, depending on the cylinder density and elongation ratios. Indeed, the cylinder parameters ξ and ρ_c/ρ_f determine both the cylinder intrinsic dynamics, and how the cylinder will react to interactions with the swarm.

We used a statistical analysis of the cylinder motion to determine the effect of these parameters. Short cylinders ($7 \leqslant \xi$) are less affected than long ones. First, their short size decreases the odds of them directly encountering a bubble. Secondly, their recovery time after having been disturbed by a bubble is shorter than for longer cylinders, which means that they are less affected by each interaction with a bubble. The motion of long cylinders ($\xi \geqslant 10$) is therefore marked by numerous interactions with bubbles, with a strong effect on their trajectory. The cylinder density ratios also plays a role in their interaction with the swarm. Heavy cylinders are much less affected by interactions with the bubble swarm than light ones, and their motion in the swarm is closer than their one in the fluid at rest. For all materials and elongation ratios, the bubble swarm primarily affects the cylinder motion through changes of its orientation. Contacts between the cylinder and the bubbles are one of the main interactions producing this change of orientation, especially for aluminium cylinders. The study of the dispersion of the cylinder motion, performed only on aluminium cylinders (for reasons of statistical convergence), revealed that short cylinders had much less important dispersion in the swarm than long ones.

Chapter 7

Conclusion

We performed a threefold study of the motion of a freely falling cylinder in various conditions. In a first part, we conducted an experimental investigation of the free fall of cylinders of various elongation ratio ξ and Archimedes number Ar, but fixed density ratio ($2 \leqslant \xi \leqslant 20$, $200 \leqslant Ar \leqslant 1100$ and $\rho_c/\rho_f \simeq 1.16$) in an unconfined medium. We developed advanced image processing techniques, which allowed us to obtain accurately the body trajectory in three dimensions. In further experiments, we used dye to obtain a qualitative characterization of the wake of the cylinder. In the second part of the thesis, we studied cylinders freely falling in a confined vertical cell. Their trajectory was acquired with shadowgraphy, and their wake visualized with dye, similarly to part I. In addition to the effect of their elongation ratio on their motion, we also investigated that of their density ratio, but we remained within the same span of Archimedes number (in this part , $3 \leqslant \xi \leqslant 40$, $60 \leqslant Ar \leqslant 1000$ and ρ_c/ρ_f ($1160 \leqslant \rho_c/\rho_f \leqslant 4500$). Finally, in a last part, we studied the interaction between the cylinder studied in part II and a swarm of rising bubble, in the same confined cell as in part II. We started by performing an analysis of the bubble dynamics, and comparing it to results from Bouche et al. [5]. After having checked that the bubble swarm is satisfactorily homogeneous and stationary, with limited changes of bubble diameter and nearly constant gap width, we performed investigations of the cylinder motion in this swarm. The satisfactory comparison of the kinematics of the bubbles with that observed in the research of Bouche et al. [5] also allows to use PIV measurements by Bouche et al. [6] to determine the fluid agitation in the bubble swarm. The results allowed us to characterize the different kinds of interactions occurring between the cylinder and the swarm. This approach of increasing complexity was chosen in order to shed light on the motion of cylindrical catalyst particles inside Ebullated Bed Reactors.

Our analysis of the cylinder motion in these different configurations revealed that a cylinder freely falling in a fluid at rest could take a wide variety of trajectories. In the unconfined medium, we highlighted the existence of three main types of path. The first one is the fluttering motion, consisting in simultaneous periodic oscillations of the body centre of gravity and orientation. We also observed the existence of another oscillatory regime of comparatively low-amplitude oscillations of the body centre of gravity and orientation. The last of the main types of path observed is the rectilinear fall, during which the cylinder falls steadily with its axis horizontal at all time. These three types of paths are also known to occur for other geometries, such as spheres and disks. In addition to these, we also observed, in the unconfined medium, an oscillatory motion of the body of modulated amplitude, as well as low-amplitude high-frequency oscillations of the body azimuthal angle. In the confined cell, all ABS cylinders, and very long aluminium ones ($\xi = 40$) fell steadily in a rectilinear motion with their axis horizontal. Titanium cylinders of intermediate elongation ratio ($\xi = 5$ and 7) adopted a seemingly chaotic

motion alternating tumbling phases with unpredictable changes of direction, similar to that observed for plates (see [3]). All other aluminium and titanium cylinders fell with a fluttering motion.

Besides this diversity of trajectories, we also observed a wide variety of cylinder wakes throughout our experiments on isolated cylinders. Interestingly, several distinct kinds of wake were seen to occur for similar body motion. In the unconfined medium, cylinders falling rectilinearly can have either a steady wake, consisting of two pairs of longitudinal vortices, or an unsteady one, with a periodic release of hairpin vortices. Whilst a slight oscillation of the body at the vortex release frequency cannot be entirely excluded, it was not observed experimentally. The nature of the wake in the confined cell is significantly different than in the unconfined medium, at first due to the confinement that may introduce a specific 3D local field close to the cylinder, that is linked to the competition between the in-plane flow around the cylinder and the flows in the thin region between the cylinder and the walls of the cell. Strong viscous effects at the walls of the cell also drastically decrease the life span of the vortices. Despite this difference, the fluttering motion, both in the confined and unconfined medium, is characterized by the periodic release of vortices from the flat faces of the cylinder, at the same frequency than the one of the body motion. In the confined cell, the amplitude of the fluttering motion can be very high. In fact, the cylinders are very close to the vertical at the maximum of their angular oscillations. This modifies substantially the wake of fluttering cylinders in this case. A series of small vortices is created in the cylinder wake during its sideways motion, probably because of the destabilization of the wake. Other cylinder modes of motion have their own associated wake, such as the azimuthal oscillating mode in the unconfined medium, or the seemingly chaotic one in the confined medium.

In the range of parameters we investigated, freely falling cylinders exhibit a wide variety of trajectories and wakes. However, remarkable scalings exist, that gather the data independently from the control parameters. In the unconfined medium, the gravitational velocity, defined as $u_0 = \left((\frac{\rho_c}{\rho_f} - 1)gd\right)^{1/2}$ is a relevant characteristic velocity to gather the vertical velocity, so that $\overline{u_Z} \simeq 1.46u_0$ for all explored values of ξ and Ar. Similarly, using $l_0 = \sqrt{dL}$ as a characteristic length scale allows the scaling of the oscillating frequency f independently from Ar and ξ as $St^* = fl_0/u_0 \simeq 0.115$, which is close to the value of $St^* = 0.10$ obtained for disks by Fernandes et al. [16]. However, these scalings do not allow for a proper gathering of the mean velocity in the confined medium, be it for a single, or for several ρ_c/ρ_f. The influence of the confinement on the motion of the cylinder appears to be difficult to summarize, and scaling laws are not obvious. The large amplitude of the velocity oscillations, that are comparable to the mean velocity, make it difficult to find a scaling law for the average falling velocity. In addition the multiple density ratios investigated in the confined medium increase the difficulty of the problem. Whilst the analysis of the motion of the cylinder in the confined cell is not yet complete, interesting discoveries have been made. In the unconfined medium, an in-depth analysis of the fluttering motion of the cylinder highlighted that the body oscillations were best described in a frame whose axes rotate with the body. The velocities u and v, directed respectively along the cylinder axis and in the direction orthogonal to it, are of interest in the description of the motion of the cylinder in both media. In the confined medium, in particular, the mean value of v, denoted $\overline{v}$ allowed the building of a Reynolds number $Re_{\overline{v}}$ which gathered data from all three density ratios when plotted against the Archimedes number, which was not the case when using other velocity scales. The velocity u was found to oscillate with an amplitude equal up to 2.5 times as high as the mean vertical velocity of the cylinder. In addition, the phase difference between oscillations of u and the body orientation θ are constant across all elongation ratios and Archimedes number

both in the confined and unconfined media.

The next step of this research was to characterize the effect of a swarm of rising bubbles on the falling dynamics of a cylinder in a confined medium. Indeed, the bubble swarm heavily disturbs the motion of cylinders falling through it. The trajectories of the cylinders in the swarm are seemingly random, and cannot be easily described. For this reason, we study the statistics of the motion of the cylinder. A first strong result of this analysis is that the dynamics of a cylinder falling in a confined bubble swarm are marked by a competition between the body intrinsic dynamics, and interaction with the swarm. The two control parameters of the cylinder, its elongation ratio L/d and density ratio ρ_c/ρ_f, determine both the cylinder own dynamics and the effect of interactions with the swarm on its motion. As the cylinder diameter is constant across all of our experiments, the elongation ratio of the cylinders also determines the ratio of the cylinder length over the mean distance between two bubbles, L_{12}. The effect of the bubble swarm on the falling velocity of the cylinders was found to be very dependent on ξ. Cylinders of $7 \leqslant \xi$ have roughly the same falling velocity in the bubble swarm than in the fluid at rest, for all density ratios. On the contrary, cylinders of $\xi \geqslant 10$ show a much higher falling velocity than in the fluid at rest across all ρ_c/ρ_f. This increase is more important for cylinders of low ρ_c/ρ_f, for which interactions with the bubble swarm weigh more than the cylinder intrinsic dynamics for determining the cylinder behaviour in the swarm. We found that the increase in the vertical velocity of the cylinder in the swarm was caused, for all density ratios, by higher cylinder orientations in the bubble swarm compared to in the fluid at rest. The dispersion of the cylinder motion in the bubble swarm was also found to be heavily dependent on the cylinder elongation ratio. Unfortunately, it was only computed for cylinders of $\rho_c/\rho_f = 2.7$, because of a lack of statistical convergence for other density ratios. Again, cylinders for which $7 \leqslant \xi$ were found to have much lower dispersion in the swarm than cylinders with $\xi \geqslant 10$, both horizontally and vertically.

The work done during the course of this thesis opens several interesting perspectives for follow-up studies. Our investigation of the kinematics of a cylinder in an unconfined medium is planned to be followed by a study of the hydrodynamical loads acting on the body. We described the body motion in a frame whose axis rotate alongside the cylinder, which can be used in the generalized Kirchhoff equations to determine the hydrodynamical forces and torques governing the body motion. This is an on-going work, and is scheduled to be submitted for publication shortly after the defense of this thesis.

The study of the motion of the cylinder in a confined fluid at rest has already yielded several interesting results. However, the current scalings do not always allow the proper gathering of the data across all ξ and ρ_c/ρ_f. In a continuation of this work, we expect to find definitive scalings characterizing the motion of the body. Whilst an in-depth analysis of the data currently at hand may provide additional information, the use of other experimental techniques would allow a better understanding of the physics of the problem. In particular, additional measurements using novel Tomo-PIV technique (see appendix A.2) have already been performed. The results are very early, and have not been analyzed, but future in-depth work may yield interesting results on the underlying mechanisms governing the motion of a cylinder in a confined medium. We expect notably to be able to characterize the flow going between the cylinder and the walls of the cell, which may provide an additional velocity scale relevant to the dynamics of the cylinder. In addition, the knowledge of the flow all around the cylinder may bring to light features of the impact of the cylinder on the fluid around it that are not visible through wake visualization using dye. Once proper characterization of the dynamics of a single cylinder in the confined cell has been achieved, it would be interesting to investigate interactions between multiple bodies in the confined cell. Indeed, such a study would bring relevant

elements to the study of the industrial problem motivating this thesis, the Ebullated Bed Reactors, in which a large number of catalyst particles are present. In addition, the confined cell greatly facilitates the experimental observation of multiple bodies, as it prevents optical obstruction.

We have provided a large volume of statistical data on the motion of a cylinder falling through a swarm of rising bubbles. For this exploratory work, we aimed at covering a large span of parameters in order to shed some light on the kind of behaviours to be expected. Because of the large scope of this work, we were not able to focus our attention on a more in-depth analysis. For instance, the data for ABS and titanium cylinders does not show sufficient statistical convergence to conduct a proper analysis of the dispersion of the motion. Furthermore, data on the aluminium cylinders could also be investigated further, with the study of the skewness of kurtosis of the displacements of the cylinder in the horizontal or vertical direction. In addition, our statistical analysis of the motion of cylinders of high ξ was limited by the large amplitude of the cylinder motion compared to the size of the cameras field of view, which led to incomplete data due to the cylinder exiting the observation window. Also, while our initial goal of varying the gas volume fraction could not have been achieved, it remains a parameter of interest in the problem, and would deserve additional attention. Nevertheless, we provide a quite complete description of the statistics of the kinematics of a cylinder freely falling in a bubble swarm, aiming at an identification of the controlling mechanisms. In particular, we show statistics of contacts with the bubbles, which strongly influence most cylinders. We also made an effort to provide conditional p.d.f. of the velocity and orientation of the cylinder, separating contact events, low and high cylinder inclination. We could develop an analysis of the instantaneous cylinder environment, defining an estimation of the distance to the bubble having the most influence on the cylinder motion. A first attempt has been made using Voronoi tessellation (see appendix B.3), and has to be carried on.

Appendices

Appendix A

Free fall of a cylinder in a confined fluid at rest

A.1 Temporal evolution of u and v for other cylinders

We provide the temporal signals of u_x and u_y in the laboratory frame, and u and v in the body frame for different cylinders. Systematically, the shape of u and v is simpler and closer to a sinus than the one of u_x and u_y. this is especially prominent for titanium cylinder of $\xi = 10$; for which the horizontal velocity exhibits an especially complex shape. Even though the temporal signals are complex in both frames, the ones in the body frame are closer to sine waves. For titanium cylinders $\xi = 3$ (figure A.1), u_x and u_y have a saw blade shape, while u and v are more rounded. For titanium cylinders of $\xi = 10$ (figure A.2), u_x has an especially complex time signal, while u is much closer to a sine wave. For titanium cylinders of $\xi = 20$, u_x and u_y have a nearly triangular shape, while u and v are more rounded.

A.2 Preliminary experimental results using tomo-PIV

Due to the peculiar nature of the confined medium, questions arise regarding the nature of the flow around the cylinder. Several studies ([19, 36, 37]) have highlighted the importance of the confinement in the motion of a cylinder in a confined medium. In our own study, we observed significant differences between the behaviour of a cylinder in a confined and in an unconfined medium. Gianorio et al. [19] discussed the relative role of the flow going between the cylinder and the walls of the cell, and of the flow going around the cylinder faces, in the cylinder motion.

Interactions between the body motion, the fluid motion and the walls of the cell create a very complex problem. Semin et al. [36] performed numerical simulation of the flow around an infinite confined cylinder capable of translating in the gap of the cell (i.e. orthogonally to the plane of the cell), up to $Re = 130$. They also conducted experiments for cylinders of very large L/W. To the knowledge of the authors, no in-depth description of the flow around a freely moving cylinder of small L/W and moderate Reynolds number ($Re_d \leqslant 250$) is currently available. Indeed, numerical simulations cannot investigate easily freely moving bodies at moderate Reynolds number. Experimentally, numerous challenges arise for properly visualizing the flow motion in a confined cell. In particular, it is very difficult to obtain a satisfactory spatial resolution inside the gap.

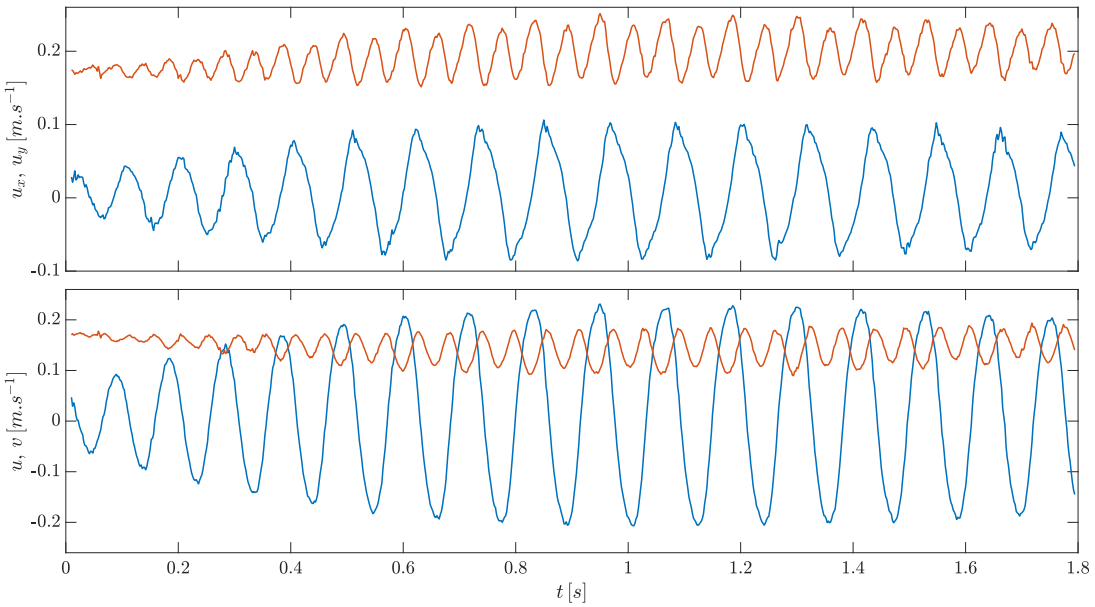

Figure A.1 – Top : temporal evolution of u_x (blue) and u_y (red) horizontal and vertical velocity of a titanium cylinder of ($Ar = 282$, $\xi = 3.0$), respectively. Bottom : temporal evolution of u (top) and v (bottom) of the same cylinder

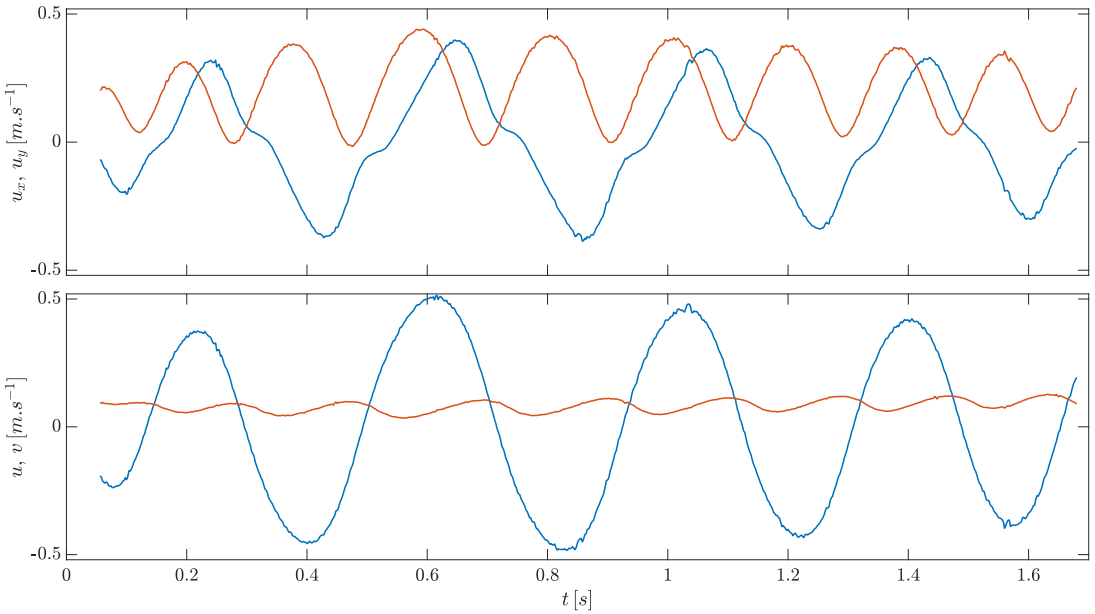

Figure A.2 – Top : temporal evolution of u_x (blue) and u_y (red) horizontal and vertical velocity of a titanium cylinder of ($Ar = 514$, $\xi = 10$), respectively. Bottom : temporal evolution of u (top) and v (bottom) of the same cylinder

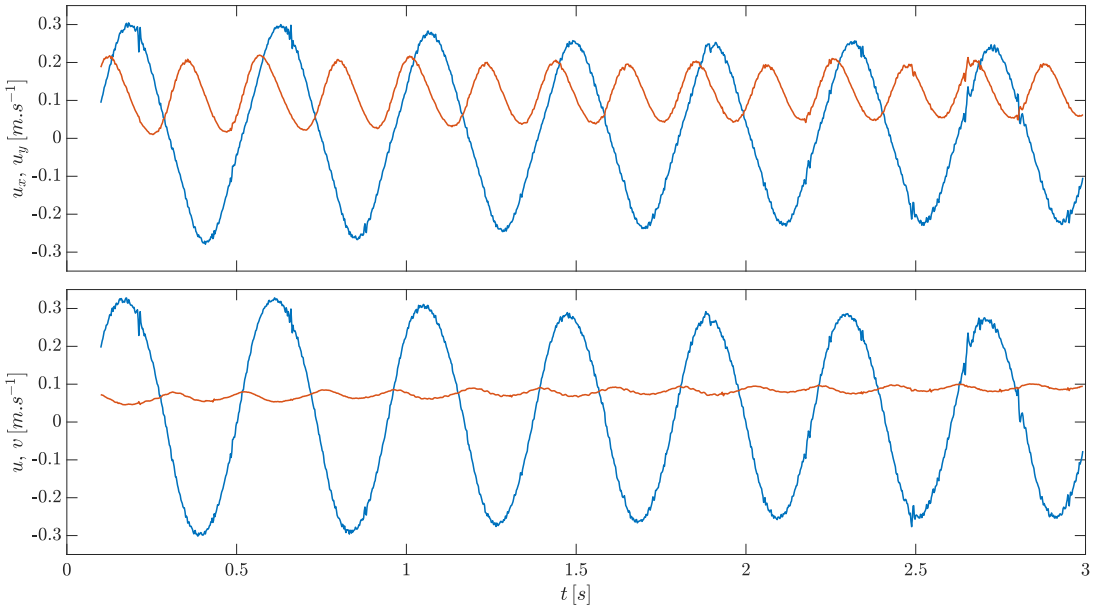

Figure A.3 – Top : temporal evolution of u_x (blue) and u_y (red) horizontal and vertical velocity of a titanium cylinder of ($Ar = 728$, $\xi = 20.1$), respectively. Bottom : temporal evolution of u (top) and v (bottom) of the same cylinder

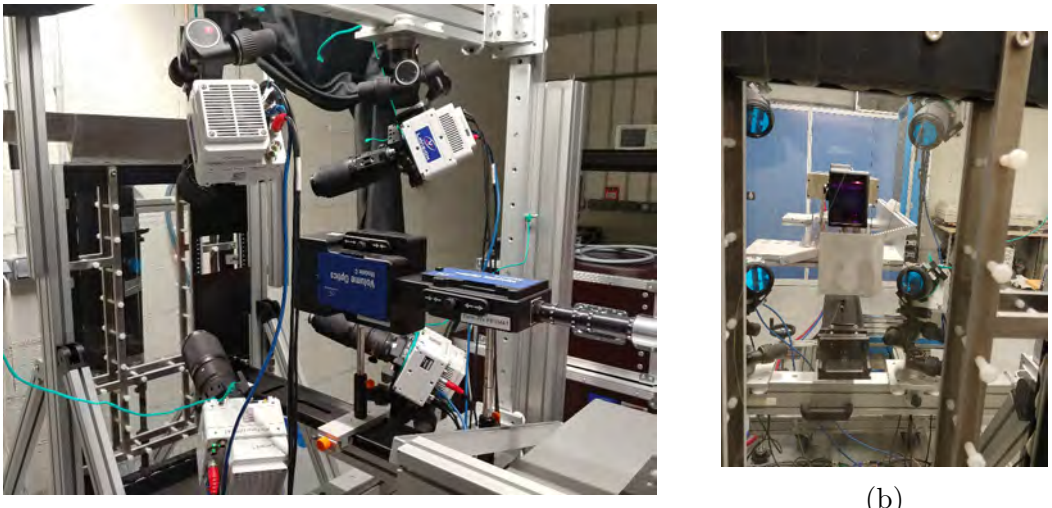

(a) (b)

Figure A.4 – (a) Picture of the experimental set up used for our tomo-PIV experiments (b) Picture of the calibration target inside the cell, viewed from behind the cell

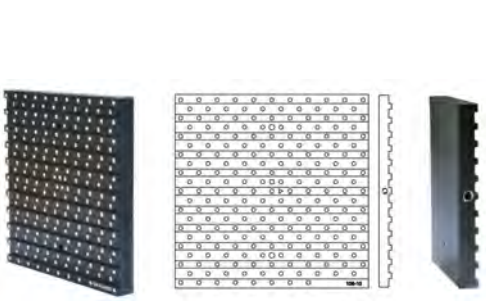

(a)

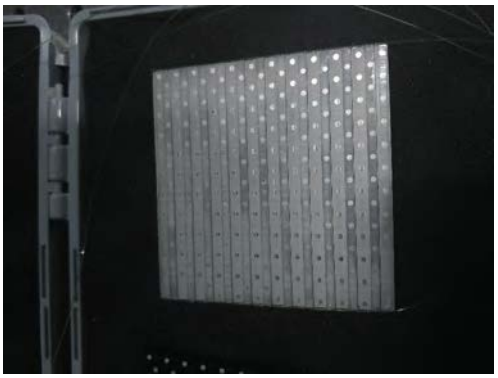

(b)

Figure A.5 – (a) Picture of the commercial calibration target from LaVision®(b) Picture of the calibration target

In order to obtain detailed information in the flow around a freely moving cylinder in the confined cell, preliminary experiments using a tomo-PIV set up were conducted. Because of the complexity of the set-up, we were helped by Sébastien Cazin and Zeinab Rida, who performed the experiments, and processed the data. The cell is the same as the one described in section 4.2. We use four VEO cameras from VisionResearch®(2600 $\times$ 1600 pixels, with a maximum acquisition frequency of 1400 Hz) cameras and a Photonics Industries DM60-527 Dual Head laser (527nm) to perform tomo-PIV measures inside the cell (the experimental setup is visible in figure A.4). In order to perform calibration inside the cell, a specific target is required. We need a two-plane calibration target, where a regular pattern of dots is printed on two different planes (see figure A.5a for a picture of the commercial target by LaVision®), which allows a volume calibration with no need to move the target in the observation volume, as it would have been very difficult in the confined cell. However, commercially available two-plane calibration targets are too thick to fit inside the gap of the cell. As a result, a custom target had to be made specifically for our experiment, as seen in figure A.5b. This custom target, made by Xavier Dollat from the LAAS laboratory, is 0.8mm in thickness at it maximum, and can be slided inside the cell (see figure A.4b) attached to thin fishing lines. On top of this first calibration using the target, the self-calibration capacities of DaVis® are used to further enhance the quality of the calibration. The self-calibration uses recorded particle images to calibrate the setup. In our case, the first calibration using the custom target was not ideal, as the target presented some defects (in particular it was slightly bent), which could be satisfactorily corrected using self calibration, with a reprojection error of less than 0.1 pixel.

We are able to acquire Lagrangian data on the particles trajectory using DaVis® Shake-the-box software (see Schanz et al. [34]). This allows us to have a high degree of accuracy in the gap. For now, we only have very early results. Nevertheless, they are very promising, and show the capacity of the experimental setup. We have performed several wake visualizations using dye in the confined cell (see section 4.3.3). While this technique gives us valuable information on the behaviour on the wake of the cylinders, it is only qualitative, and cannot characterize fluid flow anywhere but in the wake of the cylinder. Tomo-PIV allows us to compare our qualitative wake analysis with PIV measurements of the fluid flow around the cylinder. In the following figures, we show the trajectories of the tracer particles (of 25 μm in diameter) inside the cell, obtained with tomo-PIV set-up. We superpose different time steps of the particle in order to see their trajectory. The color of the particle is function of their instantaneous velocity (see the color bars).

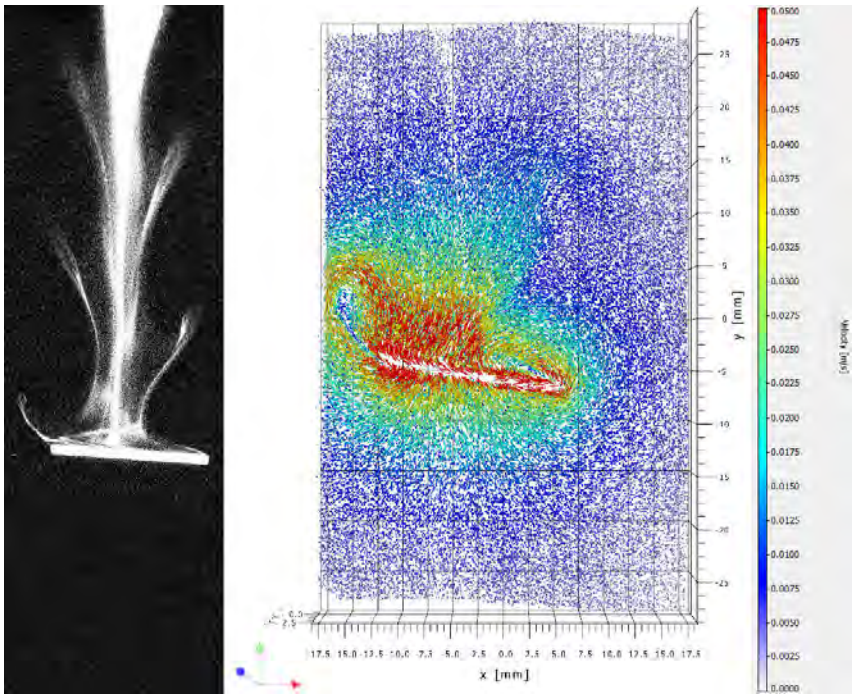

Figure A.6 – Preliminary result of the tracer trajectories in the cell when an aluminium cylinder of $\xi = 20$ ($Ar \simeq 500$) is traveling inside it.

In order to maintain a sufficient accuracy in the gap, we had to select a rather small observation volume, as compared to shadowgraphy experiments presented in part II. The final measurement volume is about $50 \times 30 \times 1.1$mm.

We start by showing comparisons of the wake of fluttering cylinders. Figure A.6 shows the wake obtained through dye visualization and with tomo-PIV for an aluminium cylinder of $\xi = 20$, and figure A.7 for a titanium cylinder of $\xi = 20$. Near the cylinder extremities, we observe in both cases zones of very low fluid velocities, which are probably areas of flow recirculation caused by the vortex release.

On figure A.8, we show images of a titanium cylinder of $\xi = 7$ obtained with dye and the tomo-PIV set-up. The flow recirculation above the cylinder while it is rotating appears clearly.

Figure A.9 shows the flow around an aluminium cylinder of $\xi = 40$ released vertically in the cell. As compared to the dye visualization, we are able to see the fluid being pushed away from the cylinder near its bottom extremity, and being dragged towards it near its top extremity.

Figure A.10 shows the flow around a titanium cylinder of $\xi = 40$ released vertically in the cell. Numerous vortices are created in the wake of the cylinder. The time it takes these vortices to stop evolving due to the viscous stress at the walls of the cell will be estimated in further analysis of the sequence.

While these preliminary results are already very promising, future analysis is expected to yield important results of the fluid flow caused by a cylinder freely falling in a confined cell. In particular, the tomo-PIV set-up can give an accurate measurement of the fluid flow going between the cylinder and the walls of the cell. In addition, the complete picture of the fluid motion with get with this technique mays allow us to characterize more finely some of the phenomena observed, such as the small vortices being created in the wake of titanium cylinders of $\xi = 10$ or 12, or of cylinders with $\xi = 40$ being released vertically.

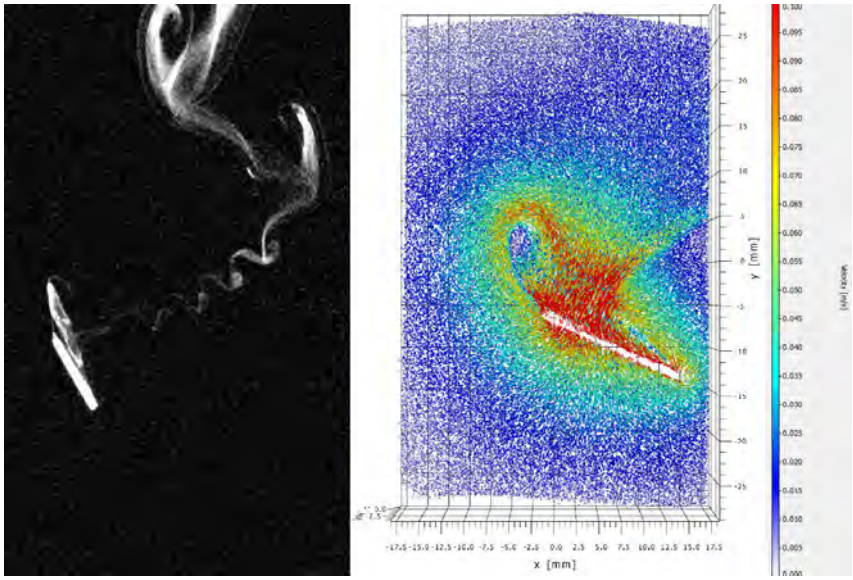

Figure A.7 – Preliminary result of the tracer trajectories in the cell when a titanium cylinder of $\xi = 12$ ($Ar \simeq 560$) is traveling inside it.

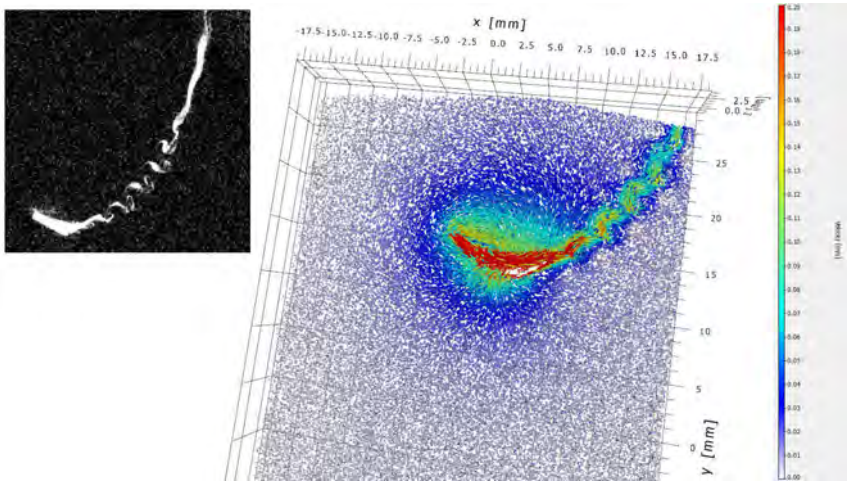

Figure A.8 – Preliminary result of the tracer trajectories in the cell when a titanium cylinder of $\xi = 7$ ($Ar \simeq 430$) is traveling inside it.

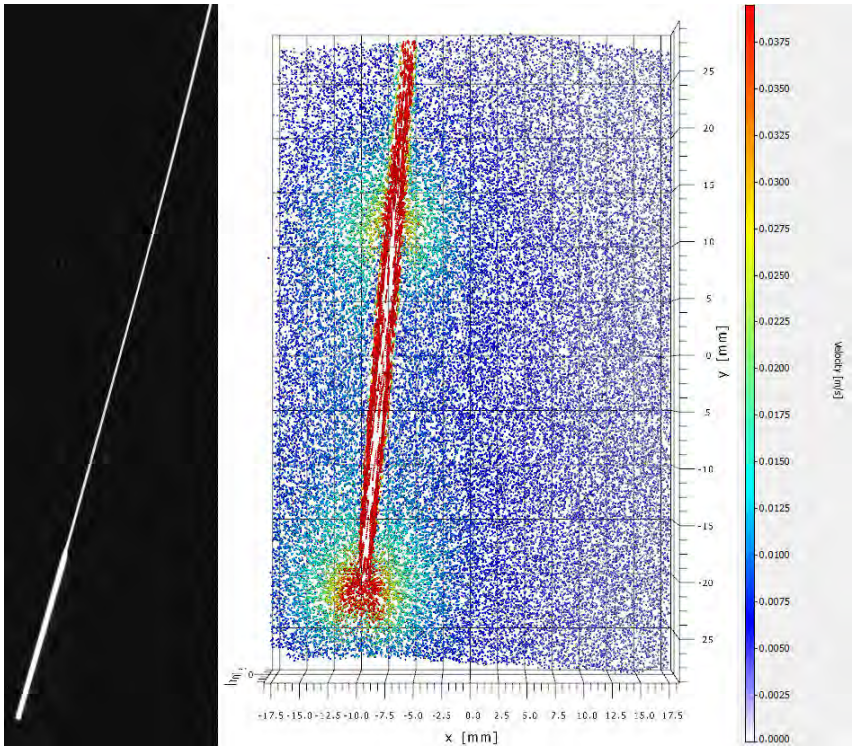

Figure A.9 – Preliminary result of the tracer trajectories in the cell when an aluminium cylinder of $\xi = 40$ ($Ar \simeq 720$) is traveling vertically inside it.

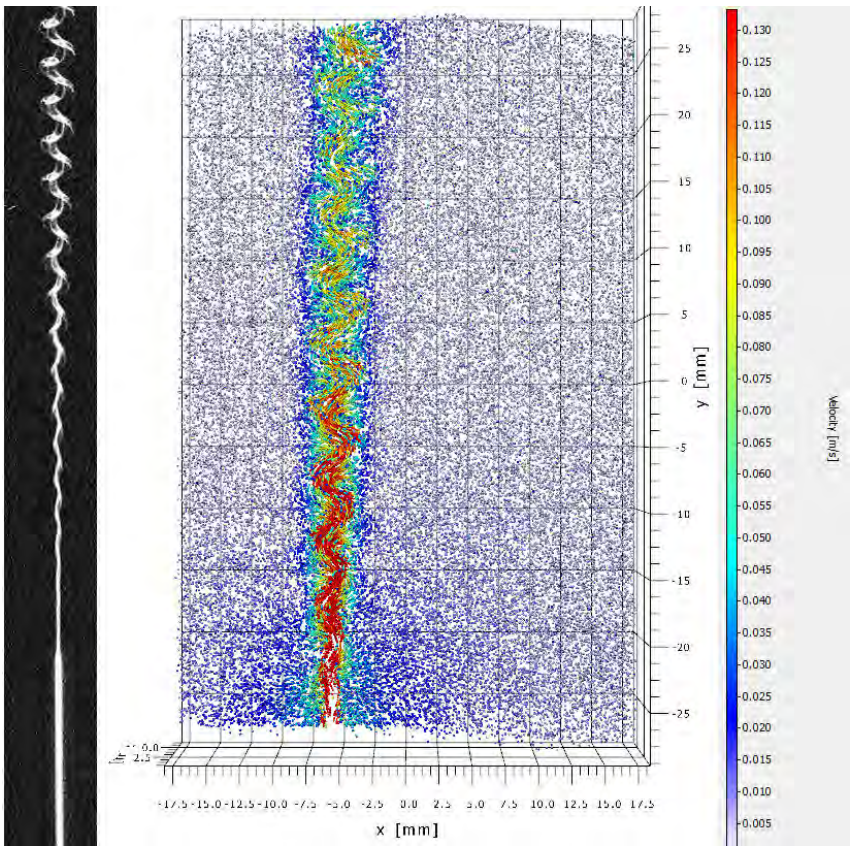

Figure A.10 – Preliminary result of the tracer trajectories in the cell when a titanium cylinder of $\xi = 40$ ($Ar \simeq 1030$) is traveling vertically inside it.

Appendix B

Fall of the cylinder in a bubble swarm

B.1 Amount of data for each material and elongation ratio

Due to the difference of run number and length between the different materials and elongation ratio, statistics of the cylinder motion are calculated on vastly different amount of data. The amount of data points for each material / elongation ratio pair is shown in table B.1.

ξ	3	5	7	10	12	20
Al	100568	105415	238101	76969	135366	111742
Ti	10970	9009	9564	9439	10084	10469
ABS	24651	22458	24161	12182	18742	11056

Table B.1 – Amount of data points for each material / elongation ratio pair

B.2 Other temporal signals

In section 6.2.3, we show temporal signals of the cylinder orientation θ and horizontal position X for certain specific runs. The interested reader can find in this appendix the temporal evolution of the horizontal and vertical velocity, u_x and u_y respectively, for these runs.

We show in figure B.1 the horizontal and vertical velocities of an aluminium cylinder of $\xi = 7$, whose orientation θ and horizontal position of the centre of gravity X have been shown in figure 6.7.

Similarly, figure B.2 temporal signals of u_x and u_y corresponding to the cylinder showcased in figure 6.9.

Finally, figure B.3 shows the velocities of a titanium cylinder of $\xi = 7$, presented in figure 6.11.

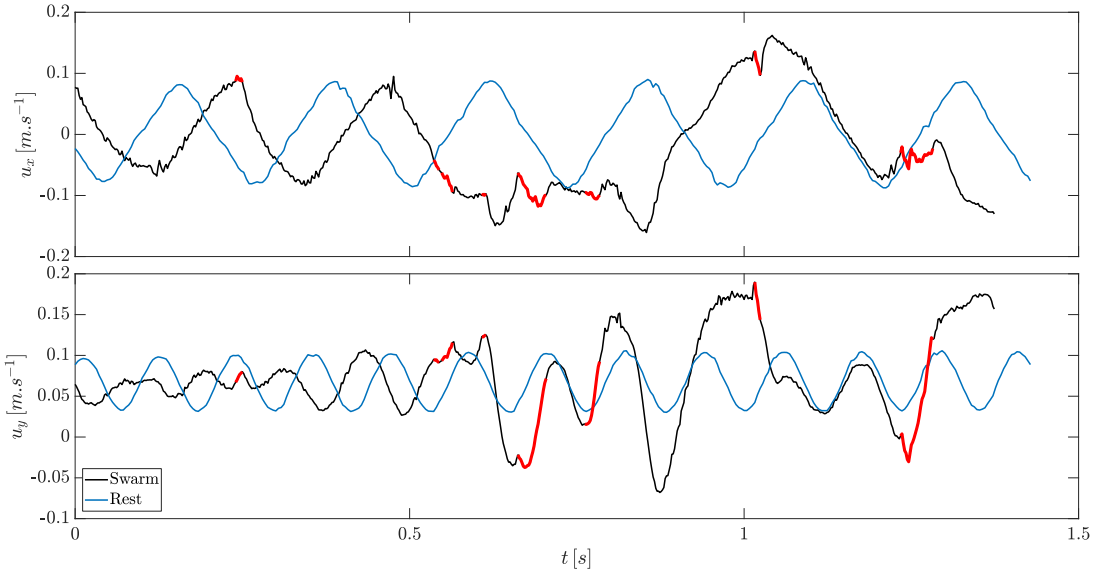

Figure B.1 – Temporal evolution of the horizontal and vertical velocity, respectively u_x and u_y, of an aluminium cylinder, over a time span corresponding to the first 10cm of fall, in a fluid at rest ($\xi = 7.13$, $Ar = 300$) in blue, and in the bubble swarm ($\xi = 7.17$, $Ar = 300$) in black. Thick red lines correspond to instants where the cylinder is in contact with a bubble.

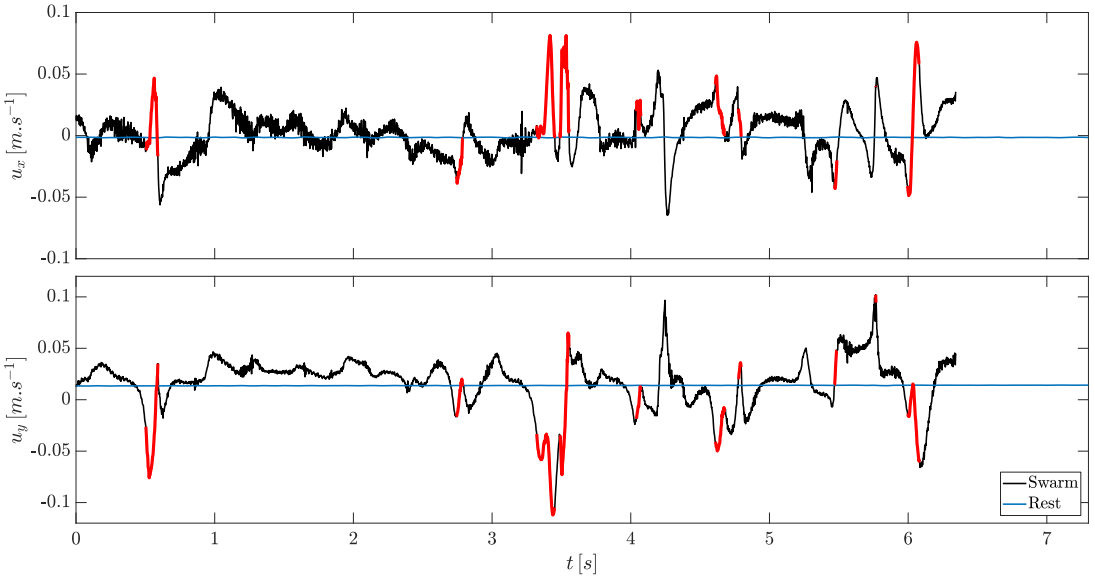

Figure B.2 – Temporal evolution of the horizontal and vertical velocity, respectively u_x and u_y, of an ABS cylinder of ($\xi = 7.12$, $Ar = 90$), over a time span corresponding to trajectory shown in figure 6.8, in a fluid at rest in blue, and in the bubble swarm in black

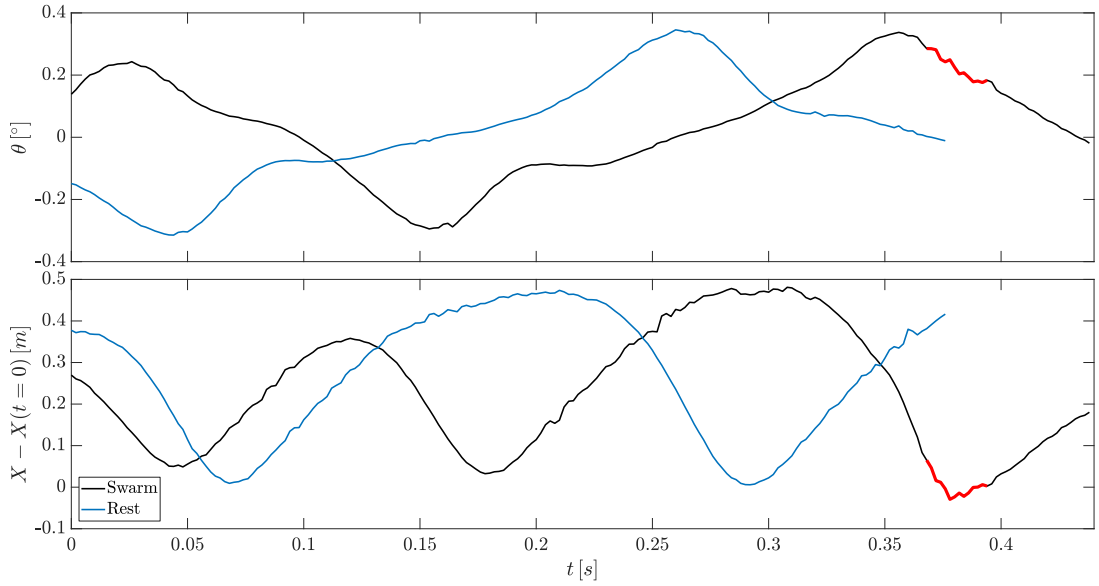

Figure B.3 – Temporal evolution of the horizontal and vertical velocity, respectively u_x and u_y, of a titanium cylinder, over a time span corresponding to trajectory shown in figure 6.10, in a fluid at rest ($\xi = 7.12$, $Ar = 430$) in blue, and in the bubble swarm ($\xi = 7.0$, $Ar = 430$) in black

B.3 Voronoi analysis of the cylinder in the cell

Voronoi analysis has been used to give a description of the bubble spatial distribution in the cell in 5.3.3. In the bubble swarm, the cylinder is a singular body, which behaves differently from all other objects in the cell. Interactions between the bubbles and the cylinder play a critical role in the cylinder dynamics in the swarm. The use of a Voronoi analysis on the cylinder in the bubble swarm allows the direct comparison between the "area of influence" of the cylinder and the one of the bubbles. In this section, we present the results of a Voronoi tessellation performed on the centroids of the bubbles and the cylinder. Therefore, the Voronoi cell based on the cylinder centroid is effectively an area where the local gas volume fraction is zero. The size of this gas-free area can also give an information on the proximity between the cylinder and the bubbles, hence, on the bubbles influence on the cylinder.

Figure B.4 shows a comparison between the area of the Voronoi cell of the cylinder with the one of the bubbles. The p.d.f. of the Voronoi area shows two important results. The first one is that all cylinders have similar distribution of the Voronoi cells area, regardless of their elongation ratio. The second one is that the Voronoi cells of the cylinder are significantly smaller, on average, than the Voronoi cells of the bubbles. This means that the cylinder tends to be closer to the bubbles than other bubbles do. This behaviour also seems to be independent on the cylinder elongation ratio, which was nevertheless shown to significantly influence the interactions between the cylinder and the bubbles. The mean Voronoi area of the cylinder remains nearly constant with ξ. It is significantly lower (of about 25%) when the cylinder is in contact with bubbles, which is expected as the area of influence of the cylinder is limited by the bubble in contact. The Voronoi area of the cylinder when it is in contact is also nearly independent on ξ.

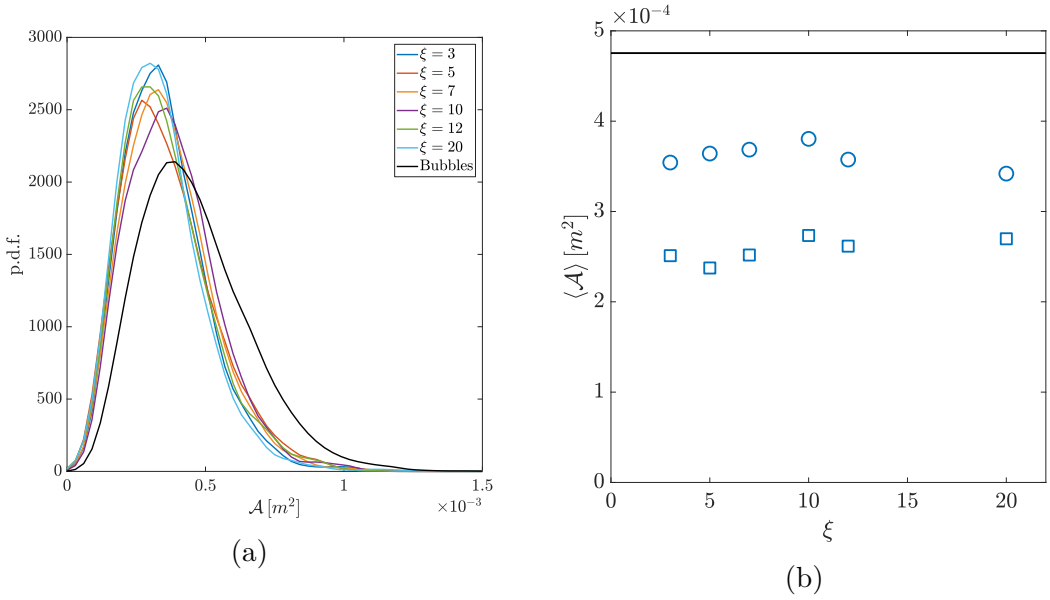

Figure B.4 – (a) p.d.f. of the area of the Voronoi cell of the cylinder for different ξ, compared to the area of the Voronoi cell of the bubbles (b) Mean Voronoi area of the cylinders (◯), of the cylinder at contact (□) and of the bubbles (black line)

B.4 An attempt at describing the cylinder motion far from bubble influence using the Voronoi tessellation

The cylinder trajectory in the bubble swarm comes from a competition between the cylinder own dynamics and the influence of the bubbles. This competition is depending on the cylinder elongation ratio. In the bubble swarm, short cylinders ($\xi < 10$) are seen to go under phases where their motion is similar to what it is in the fluid at rest. We assume that this behaviour exists when the cylinders are far from the influence of any bubble. Our goal in this section is to compare the cylinder behaviour in the bubble swarm far from the bubbles, to the cylinder behaviour in the fluid at rest. It is more difficult to do so than to describe the influence of the bubble contacts on the cylinder dynamics, as there is no simple way of knowing when the cylinder is far from the bubbles influence.

The Voronoi tessellation delimits "areas of influence" for all objects in the bubble swarm. We can attempt to define a criterion based on the size of the Voronoi cell where the cylinder is located to characterize its distance to bubbles. However, the cylinder is not in the center of its Voronoi cell. As a result, even in a large Voronoi cell, the cylinder can be close to bubbles. Furthermore, the main kind of bubble interactions for aluminium cylinders are the bubble contact and the vortex interaction, during which the cylinder paths is disturbed by the wake of a bubble.

Figure B.5 shows the comparison of the p.d.f. of the cylinder orientation only when it is in big Voronoi cells. The size criterion on the Voronoi cells ($>6.24e{-}4m^2$) has been chosen arbitrarily from visual simultaneous observations of signals of $u_y(t)$ and $\mathcal{A}(t)$. For $\xi = 3$ 5 and 7, we see that the distribution of $|\theta|$ is closer to the one in the fluid at rest when the Voronoi cell of the cylinder is large. However, the difference in the distribution is slight. For longer cylinders, no such effect is seen. This is consistent with previous observations that cylinders of these elongation ratios never had a motion similar to their fluid at rest path when in the bubble swarm. The dynamics of these cylinders in the swarm seems to be independent from the area of their Voronoi cell.

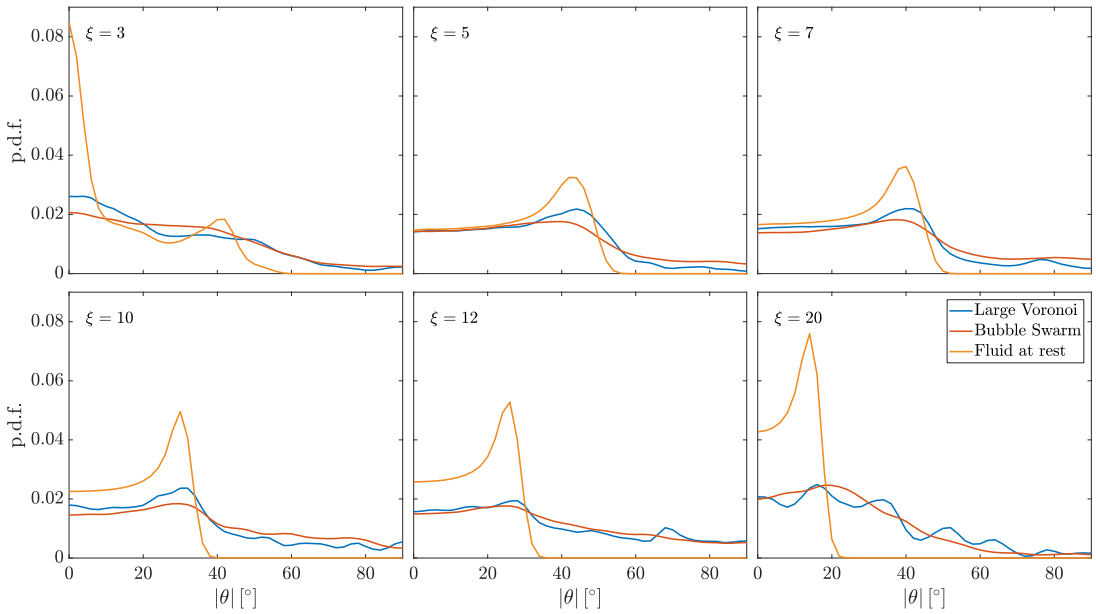

Figure B.5 – P.d.f. of the cylinder orientation $|\theta|$ only for big Voronoi cell ($>6.24e-4m^2$) (blue), for all times in the bubble swarm (red) and in the fluid at rest (orange)

It should be noted that even though the cylinder can be expected to behave in a similar manner as in the fluid at rest if it is far from any bubble, its statistics however, cannot be expected to be directly compared. Indeed, in the statistics in the fluid at rest, the cylinder first gets into a transient motion, during which the amplitude of its oscillatory motion increases, and then reaches a steady state. However, this steady state may not always be reached in the bubble swarm, even if the cylinder motion resembles the oscillations it goes under in the fluid at rest.

B.5 Superposition of the temporal evolution of the horizontal position of aluminium cylindres

In section 6.5.2, we present a series of superposition of temporal signals. We show on figure 6.51 the superposition of 50 aluminium cylinder trajectories, and on figure 6.53 the superposition of the temporal evolution of Y.

We show on figure B.6 the corresponding temporal evolution of X for the same aluminium cylinders.

In addition, we provide the superposition of all available trajectories of titanium and ABS cylinders on figures B.7 and B.8.

B.6 Autocorrelation function on other variables

In search of the correct Lagrangian timescale, we have experimented with autocorrelation functions from other variables than the ones listed in 6.5.1 (that are u'_x and u'_y). Considering the importance of the cylinder orientation on its motion in the cell, we decided to compute $C_{\theta\theta} = \langle\theta'(t)\theta'(t+\tau)\rangle/\langle\theta'^2\rangle$, with $\theta'(t) = \theta(t) - \overline{\theta}$, and $C_{ll} = \langle u_l(t)u_l(t+\tau)\rangle/\langle u_l^2\rangle$ with u_l the longitudinal velocity.

Figure B.9 shows autocorrelation functions $C_{\theta\theta}$ and C_{ll} for the aluminium cylinder. It is notable that these two functions are very close to each other. In addition, they also appear to be very close to C_{xx} (see figure 6.47b).

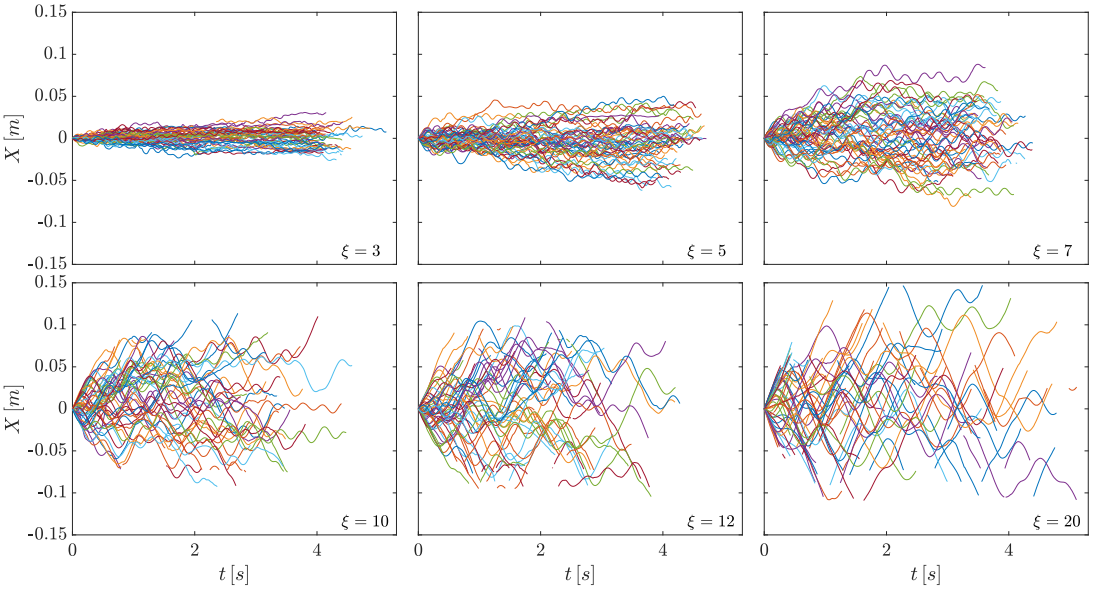

Figure B.6 – Superposition of 50 aluminium cylinder temporal signals $X = f(t)$ for different elongation ratios.

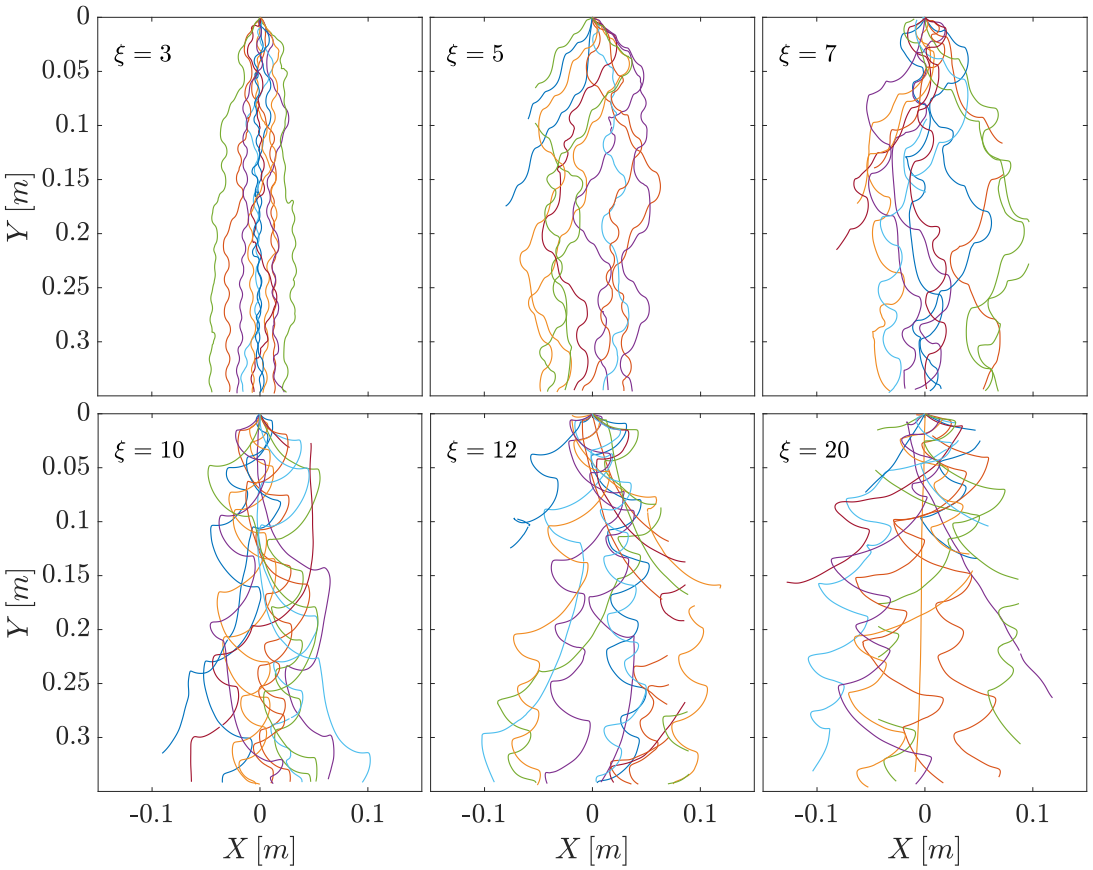

Figure B.7 – Superposition of all available titanium cylinder trajectories for different elongation ratios.

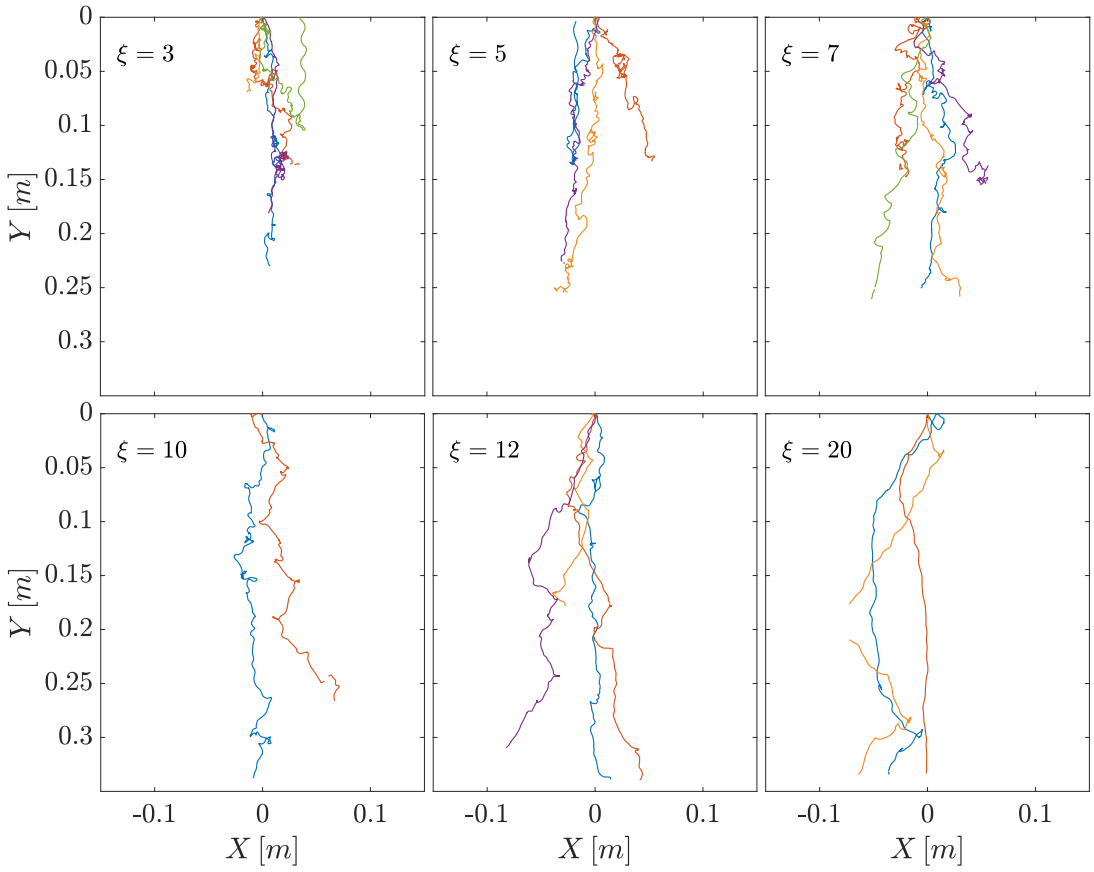

Figure B.8 – Superposition of all available ABS cylinder trajectories for different elongation ratios.

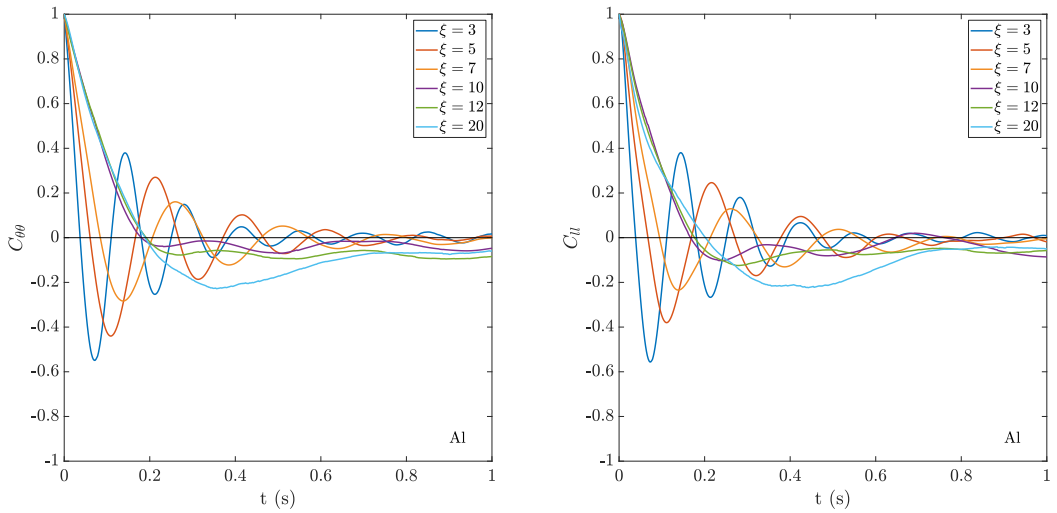

(a) (b)

Figure B.9 – Autocorrelation functions of the aluminium cylinder (a) for θ (b) for u_{longi}

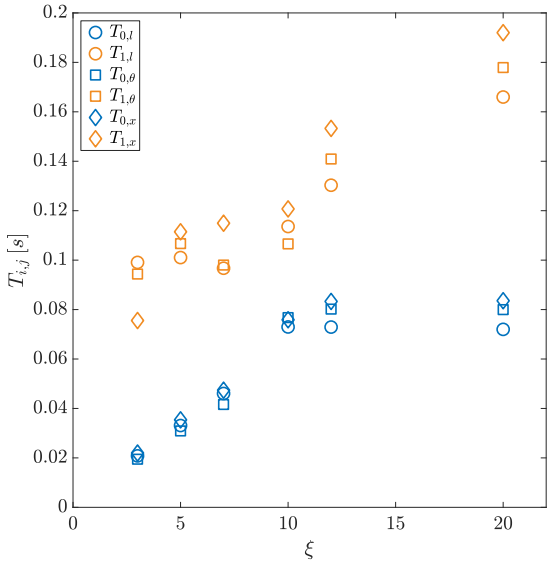

Figure B.10 – Comparison of the Lagrangian timescales from computed from C_l (◯), C_θ (□) and C_x (◊)

FigureB.10 shows the characteristic timescales $T_{0,i}$ and $T_{1,i}$ for $C_{\theta\theta}$, C_{ll} and C_{xx}. Similarly to section 6.5.1, $T_{0,i} = \int_0^{t_0} C_i(\tau).d\tau$, where t_0 is the time indice of the first zero-crossing of C_i, and $T_{0,i} = \int_0^{t_1} C_i(\tau).d\tau$, where $t_1 = 1s$. There is very little difference in $T_{1,i}$ for all three autocorrelation functions. The difference is greatest for long cylinders, but all $T_{0,i}$ remain within 10% of each other. The difference in $T_{1,i}$ is more significant, and occurs at all elongation ratios.

Bibliography

[1] Zouhir Amoura, Cédric Besnaci, Frédéric Risso, and Véronique Roig. Velocity fluctuations generated by the flow through a random array of spheres: a model of bubble-induced agitation. *J. Fluid Mech.*, 823:592–616, 2017.

[2] A Andersen, U Pesavento, and Z Jane Wang. Unsteady aerodynamics of fluttering and tumbling plates. *J. Fluid Mech.*, 541:65–90, 2005.

[3] Anders Andersen, Umberto Pesavento, and Z Jane Wang. Analysis of transitions between fluttering, tumbling and steady descent of falling cards. *J. Fluid Mech.*, 541: 91–104, 2005.

[4] Andrew Belmonte, Hagai Eisenberg, and Elisha Moses. From flutter to tumble: Inertial drag and froude similarity in falling paper. *Phys. Rev. Lett.*, 81:345–348, Jul 1998. doi: 10.1103/PhysRevLett.81.345. URL https://link.aps.org/doi/10.1103/PhysRevLett.81.345.

[5] Emmanuella Bouche, Véronique Roig, Frédéric Risso, and Anne-Marie Billet. Homogeneous swarm of high-Reynolds-number bubbles rising within a thin gap. Part 1. Bubble dynamics. *J. Fluid Mech.*, 704:211–231, 2012.

[6] Emmanuella Bouche, Véronique Roig, Frédéric Risso, and Anne-Marie Billet. Homogeneous swarm of high-Reynolds-number bubbles rising within a thin gap. Part 2. Liquid dynamics. *J. Fluid Mech.*, 758:508–521, 2014.

[7] JWM Bush and I Eames. Fluid displacement by high reynolds number bubble motion in a thin gap. *Int. J. Multiphase Flow*, 24(3):411–430, 1998.

[8] Jinwen Chen, Novica Rados, Muthanna H Al-Dahhan, Milorad P Duduković, Duyen Nguyen, and Krishniah Parimi. Particle motion in packed/ebullated beds by CT and carpt. *AIChE J.*, 47(5):994–1004, 2001.

[9] Aaron C Chow and E Eric Adams. Prediction of drag coefficient and secondary motion of free-falling rigid cylindrical particles with and without curvature at moderate reynolds number. *J. Hydraul. Eng.*, 137(11):1406–1414, 2011.

[10] Maria Veronica D'Angelo, Jean-Pierre Hulin, and Harold Auradou. Oscillations and translation of a free cylinder in a viscous confined flow. *Phys. Fluids*, 25(1):014102, 2013.

[11] Maria Veronica D'Angelo, Mario Cachile, Jean-Pierre Hulin, and Harold Auradou. Sedimentation and fluttering of a cylinder in a confined liquid. *Phys. Rev. Fluids*, 2 (10):104301, 2017.

[12] AS Dvinsky and Aleksander S Popel. Motion of a rigid cylinder between parallel plates in stokes flow: Part 1: Motion in a quiescent fluid and sedimentation. *Comput. & Fluids*, 15(4):391–404, 1987.

[13] Patricia Ern, Frédéric Risso, David Fabre, and Jacques Magnaudet. Wake-induced oscillatory paths of bodies freely rising or falling in fluids. *Annu. Rev. Fluid Mech.*, 44:97–121, 2012.

[14] R Di Felice. Review article number 47 hydrodynamics of liquid fluidisation. *Chem. Eng. Sci.*, 50:1213–1245, 1995.

[15] Járai-Szabó Ferenc and Zoltán Néda. On the size distribution of poisson voronoi cells. *Phys. A*, 385(2):518–526, 2007.

[16] Pedro C Fernandes, Frederic Risso, Patricia Ern, and Jacques Magnaudet. Oscillatory motion and wake instability of freely rising axisymmetric bodies. *J. Fluid Mech.*, 573: 479–502, 2007.

[17] Lionel Fiabane, Romain Volk, Jean-Francois Pinton, Romain Monchaux, Alain Cartellier, and Mickaël Bourgoin. Do finite-size neutrally buoyant particles cluster? *Phys. Scripta*, 2013(T155):014056, 2013.

[18] Audrey Filella, Patricia Ern, and Véronique Roig. Oscillatory motion and wake of a bubble rising in a thin-gap cell. *J. Fluid Mech.*, 778:60–88, 2015.

[19] Luciano Gianorio, Maria Veronica D'Angelo, Mario Cachile, Jean-Pierre Hulin, and Harold Auradou. Influence of confinement on the oscillations of a free cylinder in a viscous flow. *Phys. Fluids*, 26(8):084106, 2014.

[20] LG Gibilaro, R Di Felice, SP Waldram, and PU Foscolo. A predictive model for the equilibrium composition and inversion of binary-solid liquid fluidized beds. *Chem. Eng. Sci.*, 41(2):379–387, 1986.

[21] Jen-Bin Huang, Zen Chen, and Tsorng-Lin Chia. Pose determination of a cylinder using reprojection transformation. *Pattern Recognit. Lett.*, 17(10):1089–1099, 1996.

[22] Grinnell Jones and Wendell A Ray. The surface tension of solutions of electrolytes as a function of the concentration. iv. magnesium sulfate. *JACS*, 64(12):2744–2745, 1942.

[23] Ezra KT Kam, Fatma Jasam, and Mohammad Al-Mashan. Catalyst attrition in ebullated-bed hydrotreator operations. *Catal. Today*, 64(3):297–308, 2001.

[24] S Kressmann, C Boyer, JJ Colyar, JM Schweitzer, and JC Viguié. Improvements of ebullated-bed technology for upgrading heavy oils. *Oil & Gas Science and Technology*, 55(4):397–406, 2000.

[25] Yuk Man Lau, Karolin Müller, Salar Azizi, and Markus Schubert. Voronoï analysis of bubbly flows via ultrafast x-ray tomographic imaging. *Exp. Fluids*, 57(3):35, 2016.

[26] Andrew T Lee, Eduardo Ramos, and Harry L Swinney. Sedimenting sphere in a variable-gap hele-shaw cell. *J. Fluid Mech.*, 586:449–464, 2007.

[27] Xukun Luo, Peijun Jiang, and L-S Fan. High-pressure three-phase fluidization: Hydrodynamics and heat transfer. *AIChE J.*, 43(10):2432–2445, 1997.

[28] Jeremias Martinez, Jose L Sanchez, Jorge Ancheyta, and Richard S Ruiz. A review of process aspects and modeling of ebullated bed reactors for hydrocracking of heavy oils. *Cataly. Rev.*, 52(1):60–105, 2010.

[29] Romain Monchaux, Mickaël Bourgoin, and Alain Cartellier. Preferential concentration of heavy particles: a voronoï analysis. *Phys. Fluids*, 22(10):103304, 2010.

[30] Kak Namkoong, Jung Yul Yoo, and Hyoung G Choi. Numerical analysis of two-dimensional motion of a freely falling circular cylinder in an infinite fluid. *J. Fluid Mech.*, 604:33–54, 2008.

[31] Frédéric Risso. Theoretical model for k- 3 spectra in dispersed multiphase flows. *Phys. Fluids*, 23(1):011701, 2011.

[32] Véronique Roig, Matthieu Roudet, Frédéric Risso, and Anne-Marie Billet. Dynamics of a high-reynolds-number bubble rising within a thin gap. *J. Fluid Mech.*, 707: 444–466, 2012.

[33] RS Ruiz, F Alonso, and J Ancheyta. Pressure and temperature effects on the hydrodynamic characteristics of ebullated-bed systems. *Catal. Today*, 109(1):205–213, 2005.

[34] Daniel Schanz, Andreas Schröder, Sebastian Gesemann, Dirk Michaelis, and Bernhard Wieneke. Shake the box: a highly efficient and accurate tomographic particle tracking velocimetry (tomo-ptv) method using prediction of particle positions. 2013.

[35] Jean-Marc Schweitzer and Stéphane Kressmann. Ebullated bed reactor modeling for residue conversion. *Chem. Eng. Sci.*, 59(22-23):5637–5645, 2004.

[36] B Semin, Astrid Decoene, J-P Hulin, MLM François, and Harold Auradou. New oscillatory instability of a confined cylinder in a flow below the vortex shedding threshold. *J. Fluid Mech.*, 690:345–365, 2012.

[37] Benoit Semin, Jean-Pierre Hulin, and Harold Auradou. Influence of flow confinement on the drag force on a static cylinder. *Phys. Fluids*, 21(10):103604, 2009.

[38] Geoffrey I Taylor. Diffusion by continuous movements. *Proc. London Math. Soc. (3)*, 2(1):196–212, 1922.

[39] Ying H Tsang, Young-Ho Koh, and Donald L Koch. Bubble-size dependence of the critical electrolyte concentration for inhibition of coalescence. *J. Colloid Interface Sci.*, 275(1):290–297, 2004.

[40] Martin Anton van der Hoef, M van Sint Annaland, and JAM Kuipers. Computational fluid dynamics for dense gas-solid fluidized beds: a multi-scale modeling strategy. *China Part.*, 3(01n02):69–77, 2005.